

NON-EQUILIBRIUM CONDENSATION OF CARBON DIOXIDE
IN SUPERSONIC NOZZLES

by

Lt. Karl M. Duff, USN

S. B., Massachusetts Institute of Technology
(1957)

S. M., Massachusetts Institute of Technology
(1964)

Cambridge, Massachusetts

Submitted in Partial Fulfillment of
the Requirements for the Degree of

DOCTOR OF SCIENCE

in

MECHANICAL ENGINEERING

at the

MASSACHUSETTS INSTITUTE OF TECHNOLOGY

January 1966

Signature of Author

Department of Mechanical Engineering

Certified by

Thesis Supervisor

Accepted by

Chairman, Departmental Committee on Graduate Students

NON-EQUILIBRIUM CONDENSATION OF
CARBON DIOXIDE IN SUPERSONIC NOZZLES

by

Karl M. Duff

Submitted to the Department of Mechanical Engineering on January 10, 1966, in partial fulfillment of the requirements for the Degree of Doctor of Science.

ABSTRACT

Tests involving the condensation of CO_2 in three supersonic nozzles have been conducted. Data of streamwise pressure variation and local conditions at onset of condensation have been obtained and show that rate of expansion, as determined by nozzle geometry, has a significant influence on the supersaturation obtained prior to condensation.

Interferometric density measurements for non-condensing flow verified the applicability of 1-dimensional gas dynamics to the expansions, and the need for consideration of departure from perfect gas behavior of CO_2 . Non-condensing density-pressure measurements and total pressure measurements substantiated the use of the Plank Equation of State in the low temperature region of testing.

Classical nucleation and drop growth theory, as applied in this study to nozzle flow, will predict the conditions of supersaturation at onset of condensation reasonably well, provided small corrections to the flat film liquid surface tension of CO_2 are applied. These corrections amount to increases of from 17% to 38%, depending upon values of thermal and mass accommodation coefficients which are also applied.

The applied theory does not successfully predict the experimental streamwise variation in pressure caused by condensation, nor the extent of effects of nozzle geometry noted experimentally. These failings are thought to indicate inadequacies in drop growth theory, or in its application.

Thesis Supervisor: _____

Philip G. Hill

Title:

Associate Professor of Mechanical Engineering

BIOGRAPHICAL NOTES

The author was born February 18, 1936 in Fort Worth, Texas and received his high school diploma from Edmonds High School, Edmonds, Washington in June, 1953. He entered M.I.T. that fall and received his Bachelor of Science Degree in Mechanical Engineering in June 1957. After graduating from M.I.T., he entered Naval Officer's Candidate School at Newport, Rhode Island in September, 1957 and was commissioned in January, 1958. He served for three years aboard the U.S.S. Brown (DD-546) in the Pacific Fleet, and obtained the positions of Engineering Officer and Senior Watch Officer prior to completing his duty aboard. In June, 1961 he returned to M.I.T. under the Navy's post-graduate school program and in September, 1964 obtained a Master of Science Degree in Naval Architecture and Marine Engineering.

The author is a member of Pi Tau Sigma, honorary Mechanical Engineering Fraternity, and the American Society of Naval Engineers. In June, 1964 he received the Brand Award from the Society for having stood first in his class, course XIII-A, the post-graduate curricula entered into in 1961.

He is married to the former Gretchen M. Raddatz of La Jolla, California, and presently has one daughter, age one year.

ACKNOWLEDGEMENTS

I am indebted to my thesis advisor, Professor Philip G. Hill, Associate Professor at M. I. T., who originally conceived of this project, and who contributed throughout with his timely thought, comment and guidance. His sincere interest and effort played a significant role in its accomplishment.

Professor Edward S. Taylor, Director of the Gas Turbine Laboratory at M. I. T., in which the work took place, was particularly helpful with his continuing interest and advice, as were the other members of the author's thesis committee; Professor Ronald F. Probststein and Associate Professor Peter Griffith of the Department of Mechanical Engineering at M. I. T., and Professor Jack L. Kerrebrock of the Department of Aeronautics and Astronautics at M. I. T.

This work was carried out with the day-to-day interest and advice of the members of the teaching and research staff of the Gas Turbine Laboratory. The technical assistance of Mr. Thorvald Christensen was particularly helpful. Mr. Michael Kremmer designed and constructed Nozzle II used in the experiments.

Mrs. Madelyn M. Euvrard has contributed much in the way of her secretarial and other services, ranging from coffee to beach parties, and the author feels he has greatly benefited from his membership in her "brood". The final manuscript was the joint effort of many, and, in the absence of any other inspiration, would always serve to remind the author of a lasting debt to his loving wife, Gretchen.

The programmed computations were carried out with the assistance of the M. I. T. Computation Center's IBM 7094 digital computer, with many valuable contributions by Mrs. Joan Kukolich.

TABLE OF CONTENTS

	<u>Page</u>
Abstract	i
Acknowledgements	ii
Table of Contents	iii
Nomenclature	v
I. Introduction	1
II. Nozzle Flow Phenomena	3
A. Isentropic Effects	3
B. Wall and Boundary Layer Effects	3
C. Test Vapor Considerations	5
III. Experimental Investigations	8
A. Test Apparatus	8
B. Test Nozzles	9
C. Experimental Procedures	10
1. Pressure-Density Measurements	10
2. Stagnation Pressure Measurements	11
D. Non-Condensing Measurements	11
1. Real Gas Behavior	11
2. Pressure-Density Measurements	14
3. Normal Shock Total Pressure Measurements	15
4. Influence of Equation of State Upon Isentropes	17
E. Condensation Measurements	17
1. Pressure Profiles and Local Conditions at Onset of Condensation	17
2. Visual Observations	19
IV. Interpretation of Experimental Results	21
A. Nucleation Theory	21
1. General Form of Nucleation Rate Equation	21
2. Evaluation of Classical Nucleation Rate Equation	23
B. Drop Growth Theory	27
C. Application of Nucleation and Drop Growth Equations	30
D. Real Gas Effects	33
E. Results of Application of Theory to Condensation of CO ₂	35
1. Comparison of Theory and Experimental Data	35
2. Influence of Nucleation and Drop Growth Parameters on Theoretical Predictions	36
a) Onset of Condensation	37

TABLE OF CONTENTS Continued...

	<u>Page</u>
b) Profile Shapes	38
c) Downstream Moisture Formation	39
3. Influence of Contamination	40
V. Summary of Findings and Conclusions	42
A. Experimental Findings	42
B. Application of Nucleation and Condensation Theory	42
VI. Suggestions for Further Study	45
Bibliography	48
Appendix A - Figures and Tables	A1
Appendix B - Review of Nucleation Rate Equation Development	B1
Appendix C - Review of Development of Drop Growth Equations	C1
Appendix D - Modification of Foregoing Gas Dynamics, Nucleation and Drop Growth Equations for Departure from Perfect Gas During an Isentropic Expansion.	D1
Appendix E - A Closed Form Solution to the Momentum Integral Boundary Layer Equation Including Approximate Effects of Streamwise Density Variation	E1
Appendix F - Estimated Effect of Departure from 1-Dimensional Flow on Nozzle Throat Pressure Measurements	F1
Appendix G - Discussion of Interferometry Application to Two- Dimensional Nozzle Flow	G1
Appendix H - Programmed Computation Listings	H1
Appendix I - Estimation of Experimental Error	I1

NOMENCLATURE

A	Nozzle Flow Area
C_p	Specific Heat at Constant Pressure
C_v	Specific Heat at Constant Volume
g	Number of Molecules in a Droplet Cluster
g^*	Number of Molecules in a "Critical" Cluster
h	Specific Enthalpy
h_{fg}	Specific Enthalpy of Vaporization
H	Total Enthalpy
J	Number of Nuclei Produced per Unit Time per Unit Volume
k	Boltzman Constant
m	Molecular Weight
m'	"Effective" Molecular Weight
\dot{m}	Mass Flux, Particles/Unit Area-sec.
M	Mach Number
n	Number of Vapor Molecules/Unit Volume
n_i	Index of Refraction of a Vapor in State i
$N(g)$	Equilibrium Size Density Distribution of g-molecule Clusters
P, p	Static Pressure
P_o	Stagnation Pressure
P_o'	Stagnation Pressure behind a Normal Shock
P_∞, P_∞'	Flat Film Equilibrium Vapor Pressure
P_D	Droplet Equilibrium Vapor Pressure
Q	Heat
r	Droplet Radius
r^*	Helmholtz "Critical" Radius
R	Gas Constant
R'	Effective Gas Constant

s	Entropy
S	Fringe Shift, Number of Fringes
t	Time
T	Static Temperature
T_0	Stagnation Temperature
T_D	Drop Temperature
T_R	Temperature of Molecules Reflected from a Droplet
u	Streamwise Velocity
U_{fd}	Internal Energy of a Droplet
v	Specific Volume
V	Total Volume
x	Streamwise Variation of Distance in Nozzle
y	Vertical Cross-Stream Variation of Distance in Nozzle
z	Horizontal Cross-Stream Variation of Distance in Nozzle
α	Thermal Accommodation Coefficient
γ	Ratio of Specific Heats
γ'	Effective Ratio of Specific Heats
δ	Boundary Layer Thickness
ϵ	Defined in Appendix B, page B2.
η	Quasi-Equilibrium Droplet Density Distribution
θ	Angle, Radians
λ	$h_{fg}/C_p T$
λ_0	Wave Length of Interferometer Light Source - 5461 \AA
μ	Mass Fraction of Condensed Moisture
ξ	Condensation (Mass Accommodation) Coefficient
ρ	Local Density
ρ_0	Stagnation Density

ρ_L	Droplet (Cluster) Density
σ	Drop Surface Tension
σ_∞	Liquid Flat Film Surface Tension
τ	$1/T$
ϕ	Free Energy per Molecule (Subscripts; L = Liquid, V = Vapor)
Φ	Total Free Energy of g Molecules
z	Distance z Between Optical Glass Side Walls, Nozzle I.

I. INTRODUCTION

In recent years, increasing attention has been given to the problem of homogeneous nucleation and condensation of supersaturated vapors.

Particular interest has arisen in connection with high temperature, low vapor pressure fluids, capable of high Carnot efficiencies in power plant application. The possible space application of systems employing alkali metals, and recent reports of experiments involving the flow of sodium and potassium through nozzles^{43,54} underlines the need to understand the condensation behavior of these gases well enough to provide a basis for optimum turbine and cycle design.

Early investigations in cloud chambers showed that, after initial expansions and settling had removed dust particles and other nuclei, subsequent expansions into the saturated region would result in the spontaneous formation of a condensation cloud at some limiting expansion ratio. In the absence of other nucleation sites, it was concluded that such clouds were the result of homogeneous nucleation of the super-saturated vapor. Similar condensation occurs in vapors expanded in nozzles, where rates of expansion are generally much more rapid than those of cloud chambers.

Despite extensive literature on the subject, there exists little agreement as to the correct formulation of nucleation and drop growth rates, and within the theoretical framework there exist many other uncertainties regarding the fluid properties pertinent to numerical evaluation. Experimental work is relatively limited in terms of range of test conditions, and numbers of fluids tested. Although a variety of gases have been studied in cloud chamber expansions, applicable and informative studies of nozzle expansions are somewhat sparse outside of steam and airborne water vapor for which both cloud chamber and nozzle data is extensive.^{7,62,63,66 & 67} This data as well as the cloud chamber data for several other vapors tends to substantiate

so-called "classical"^{5,18,23} nucleation theory, as opposed to revised models of nucleation theory offered by more recent authors, as a better means of predicting condensation behavior. However, there is doubt regarding the extent to which cloud chamber data may be applied to the determination of nucleation rates, and too little data outside of water vapor has been obtained for flow in nozzles to allow a comprehensive test of theory over a variety of gases.

The purpose of this work has been to extend the limits of existing experimental data involving condensation in nozzles, through experimentation with CO_2 , to study by means of a computational program the predictions of existing theory and make some judgments regarding the importance of the various physical parameters and uncertainties pertaining thereto, and to reduce these uncertainties to a point where a valid comparison of existing theory and experimental results can be made for CO_2 .

II. NOZZLE FLOW PHENOMENA

Converging-diverging nozzles lend themselves particularly nicely to the study of condensation behavior of gases. Following are some of the aspects of gas behavior in nozzle flow and features which recommend it as a means of experimental study of condensation.

A. Isentropic Effects

It is general knowledge that for sufficiently high pressure ratios, an ideal gas will expand isentropically in a converging-diverging nozzle, becoming sonic at the point of minimum flow area and supersonic downstream, with continuously increasing velocities and decreasing pressures, densities and temperatures all along the expansion. A non-ideal gas behaves similarly, and depending upon the stagnation conditions, the extent of the expansion, and the properties of the vapor being tested, the isentrope may approach saturation conditions of pressure and temperature. As illustrated on the T-S diagram of Figure 1, it is possible for conditions to exist for certain gases when the opposite may be true and an isentropic expansion will result only in increasing the degree of superheat of the vapor (i.e. as with many of the FREONS). However, in most cases it is a simple matter to devise stagnation conditions which result in the rapid arrival of the gas to conditions of supersaturation during its isentropic expansion. For a supersonic nozzle a few inches in length expansion time is of the order 10^{-4} seconds.

B. Wall and Boundary Layer Effects

In all real gases there are departures from ideal non-viscous behavior which must be considered. Fortunately, in nozzle flow these effects are easily accounted for, provided fully developed flow does not occur. Viscous effects are accounted for by considering the nozzle flow to be an isentropic expansion contained between wall boundary layers. The boundary layers are greatly influenced by the shape of the pressure gradient and are generally

depressed to a very small minimum value near the most critical point, the geometric throat. Further, viscous and recovery effects on the nozzle walls will keep the wall temperature close to stagnation value in the absence of very strong wall cooling or heating, and, at decreased downstream pressures, is adequate guarantee that there will be no condensation of liquid on the walls which could interfere with the mid-stream process.

In experimentation where nozzle size might be limited by mass flow or other restrictions, considerations of Reynold's Numbers and boundary layer thicknesses which may be expected in the throat region are important since large boundary layers in relation to nozzle size could invalidate the assumption of an isentropic region of flow. A means of estimating the boundary layer thickness in the throat region of a supersonic nozzle was devised (Appendix E) and showed good agreement with interferometric photos that the boundary layers involved in the CO₂ experiments of this investigation were about .006" at the nozzle throat. In all nozzles tested this was less than 11% of the throat width. Additional discussion of boundary layer treatment in this investigation is included later.

The isentropic region between boundary layers may be described by one-dimensional gas dynamics, and, by means of measurement of some vapor property (such as static pressure) along the nozzle, a complete time-history of the expansion may be obtained.

Condensation in a nozzle expansion has been shown by many investigations to have a large influence on the thermodynamic properties of the fluid. In particular, the static pressure records large variation from the non-condensing profile as a result of the heat released by moisture formation. For the addition of heat to an ideal gas, it may be shown that

$$\frac{dP}{P} = \frac{\gamma M^2}{1-M^2} \left[\frac{dA}{A} - \frac{dQ}{C_p T} \right]$$

For water vapor, it is easily estimated that at $M = 2$, a formation of 1% moisture at constant area is accompanied by about 7% variation in static pressure. As is later shown, it is possible to detect the onset of condensation at about .1% presence of moisture through simple static pressure measurements.

It may be seen from the above equations that pressure variation is increased by establishing conditions such that condensation occurs with Mach Number close to unity.

Willmarth and Nagamatsu,⁶⁴ and Arthur,³ have shown that the ratio P/P'_0 plotted against the streamwise variation of P'_0/P_0 is an even more sensitive indicator of condensation, where P is the measured static pressure, P'_0 is the measured total pressure behind a normal shock, and P_0 is the original stagnation pressure.

An important consideration in any system designed to test homogeneous nucleation theory is the possible effects of contamination. As will be shown later, nozzle expansions from superheated to supersaturated state proceed in such an extremely short time that spontaneous nucleation will produce nuclei many orders of magnitude greater in number than those which could be present in the form of dust or other particles and the amount of moisture formed on such contaminants is entirely negligible. As will also be mentioned later, an exception to this is the case of a pre-condensing vapor.

The preceding observations indicate that, with fairly simple instrumentation of a nozzle system, it is possible to obtain a complete history of a gas expansion and any condensation occurring within, with the reasonable assumption that no outside influences exist which would invalidate testing of homogeneous nucleation and drop growth theory in the same system.

C. Test Vapor Considerations

The selection of a vapor for testing is subject to the following

considerations. First, a large number of vapors are toxic, reactive to instrumentation materials, or do not exist as vapors at conditions most convenient for laboratory testing. Second, the state relations and other properties of many are so poorly defined, that application to any meaningful test of theory would be ill-founded. Neither of these considerations would be restrictive if the condensation data for a particular vapor were particularly needed, or if a test of theory were incidental to the experimental data. Third, two particular properties are desirable in a test vapor, both of which are more common to gases of low molecular weight. The first has been mentioned previously, and involves the shape of the coexistence line in relation to the isentrope. A preferred test gas has a coexistence line having rapid convergence with the isentrope. Also, the measure of heat release resulting from condensation compared with that needed to alter its vapor properties is important. This may be expressed through the parameter h_{fg}/C_p , for which typical values for various gases are presented in Table 1. Variations in the gas properties caused by condensation are increased with larger values of this parameter. A more applicable use of these values is, as seen from Equation 1, the form $h_{fg}/C_p T$ at the test conditions of interest. For vapors such as alkali metals, higher values of h_{fg}/C_p are decreased in significance due to the high temperatures of the gas.

CO_2 was selected for this study because it satisfies all the foregoing criteria and in addition may be obtained in high purity at relative low cost, thus allowing its use in a system not necessitating recovery after expansion. Also, such physical properties as CO_2 vapor pressure, liquid surface tension, and solid and liquid density, necessary in the application of theory, are well established and readily available in numerous publications of physical property data.

Discussion of the application of these properties, and details of the theoretical mechanism and behavior of condensation are presented later.

The question could be raised concerning possible non-equilibrium of energy modes of CO_2 during such a rapid expansion. Kantrowitz³⁰ has shown that this would not be a problem with CO_2 in this case since 1) vibrational energy modes are not activated at the low temperatures of experimental test conditions and 2) the relaxation time constant of vibration is considerably less ($\approx 10^{-6}$ sec.) than that of the gas expansion. Camac¹⁰ has recently formulated the pressure-temperature dependence of CO_2 vibrational relaxation time and his expression also yields times of the order 10^{-6} sec. in the region of experimental testing.

III. EXPERIMENTAL INVESTIGATIONS

A. Test Apparatus

Industrial Welding CO₂ having very high (moisture content less than .0045% by weight) purity was introduced via a manifold from a bank of nine 50 lb cylinders to a needle valve used for regulation of flow rate (See Figure 2). Thence the flow entered a stagnation tank and then the test nozzle. Exhaust was to atmosphere in earlier tests and later to a steam ejector system maintaining about 23" Hg. of vacuum. This modification facilitated lower minimum stagnation pressures without the interference of compression shock systems in the supersonic test section. Nine cylinders were employed in order to obtain a large mass flow source providing nearly constant conditions to the nozzles for extended periods of flow, despite the quasi-steady nature of the "blow-down" method.

The stagnation tank contained a calibrated pressure gauge and, extending into the flow just upstream of the nozzle entrance, a copper-constantan thermocouple using an ice reference. A 100 inch 25-tube mercury filled manometer board was used in connection with static wall taps to determine pressure readings along the nozzle. Pressure data was recorded by polaroid photograph of the manometer board. Test time durations were of the order of 1 minute.

The stagnation tank had a removable end plate and contained screens which allowed the packing of large amounts of steel wool inside a nylon filter bag upstream of the nozzle entrance. (Figure 5) When high stagnation temperatures were desired (i.e. non-condensing tests) an electric heating tape wrapped around the stagnation tank was energized and the steel wool used for heat storage and thermal inertia to decrease the rate of the temperature transient. When low temperatures were desired, the steel wool was removed and the heating tape not used.

B. Test Nozzles

Two test nozzles were employed for experimental measurements, henceforth referred to as Nozzle I and Nozzle II.

Nozzle I appears schematically in Figure 7 and in photos in Figures 6 and 9. It featured two removable parallel side walls which were plates of optical glass, used for interferometric measurements. By exchanging one of the plates for an identical metal one containing pressure taps, static pressure profiles could be obtained and the flow observed simultaneously through the remaining glass wall. Slotted "O-rings" provided sealing of the side walls. The nozzle was made wide in comparison to its height in order to minimize any contribution to error caused by boundary layer effects of the side walls on the interferometric measurements. This error was later estimated to be less than .2% of the measured densities.

The nozzle shape was also intended to provide nearly 2-dimensional flow, and in fact, interferometric photos to be discussed later show the flow to be effectively 1-dimensional between boundary layers. A region of isentropic flow was thus obtained between the boundary layers, which were of thickness $\approx .005'' - .007''$ at the throat (Appendix E).

Pressure Taps in Nozzle I were spaced .2" apart, and later during the program, additional taps, resulting in .1" spacing, were added in the test section region.

Nozzle II is illustrated in Figures 8 and 10 and featured hinged upper and lower nozzle walls which could be placed at arbitrary angles between the fixed parallel side walls. This facilitated variable expansion rates in the test section, depending on the divergence angle of the test section, and it was hoped to thus establish a "best" angle of divergence to obtain the most informative pressure profiles. Since pressure variations due to heat addition approach maximum when Mach

Number approaches 1.00, it was expected that this result would be obtained for a very low angle of divergence.

Static pressure taps located in the side wall were located .25 inches apart for early runs, after which a new test plate with taps .1 inches apart in the test region was substituted.

C. Experimental Procedures

1. Pressure-Density Measurements

Tests were conducted using two persons and the following procedure.

1) The needle valve was opened until the approximate value of desired stagnation pressure was obtained.

2) One observer maintained a null-balance on the thermocouple-potentiometer circuit, while the other, manning a tripod-mounted polaroid camera, observed the manometer board.

3) When the manometer board reached a steady state, a polaroid photo was taken of the manometer board by the second observer while the first recorded the stagnation gauge pressure and terminated the null-balancing procedure on the thermocouple potentiometer.

4) The reading of the potentiometer at time of photograph was converted to a stagnation temperature reading, and the polaroid display of the pressure data developed, and all pertinent data involving the test run affixed to it (including local barometric pressure).

Interferometer runs were made in a similar manner, except for the use of 5" x 7" sheet film in the built-in camera of the interferometer, and requiring only the potentiometer null-balance prior to recording data.

Discussion of interferometry theory and the methods applied in this investigation plus related references are presented in Appendix G.

2. Stagnation Pressure Measurements

The stagnation pressure behind a normal shock was measured by means of a .030" O.D. pitot tube extending upstream from a micrometer mounted on the elbow downstream of the nozzle. (See Figure 6) All measurements were made on Nozzle I, by visually aligning (with the aid of lighting, and machinist's templates) the tip of the tube with the center of the corresponding wall tap with which static pressure was measured. Since the location of the shock was actually located a small distance upstream, a correction was made to the static pressure reading corresponding to this distance, (about .63 tube diameters at Mach 1.65 and about .30 tube diameters at Mach 2.45, decreasing further as Mach Number increases.)⁵⁵ Upstream stagnation pressures were measured with the calibrated gauge in the stagnation tank. As in the case of the static pressure profile measurements, photographs of the manometer board were taken simultaneously with stagnation temperature and pressure measurements, after steady pressure readings and a null potentiometer reading were obtained.

Total pressure measurements were made with all manometer tubes disconnected except the following 1) pitot tube 2) static wall tap at tip of pitot tube 3) throat static wall tap (recorded only for supplementary purposes).

Discussion and estimates of possible experimental error are contained in Appendix I.

D. Non-Condensing Measurements

1. Real Gas Behavior

It became necessary to consider the departure from perfect gas behavior of CO₂ near the very outset of this investigation, since one of the objects of experimental work was to compare the agreement of measured density profiles with measured pressure profiles. Failure to consider the proper

p-v-T relation for reduction of interferometric data resulted in considerable error in the density profile. It also introduced doubt as to how the proper density ratios should be converted to the corresponding isentropic pressure ratios for purposes of making comparison between measurements.

Existing tabulated properties of CO_2 also showed that the degree of departure from perfect gas behavior for CO_2 (as reflected by the compressibility factor, $z = \frac{Pv}{RT}$) increased markedly near the saturated region, and that the values of compressibility factor could easily be as low as .9 during an expansion. Also, existing tables did not extend to pressures and temperatures low enough to make adequate determination of what the real gas behavior of CO_2 is.

Since a meaningful test of the nucleation and drop growth predictions which were to follow must rest on the most precisely accurate information available regarding the gas dynamics, and since, as will be shown, the predictions are quite sensitive to errors in this respect, it was decided to establish the real gas behavior of CO_2 through use of an applicable equation of state.

Unfortunately, though the literature abounds with work, much of it recent, on high pressure and temperature properties of CO_2 ,^{4,11,24,26,28,33,51, & 59} it was possible to find only one equation of state that is applicable in the lower P-T range of these experiments, that being Plank's⁴⁷ (1929), which fits the data of Lowry and Erikson,³⁹ and Maass and Mennie⁴¹ very well. Comparison of Plank's Equation of State and of their data is shown in Figure 14, showing maximum disagreement of about .1% of $\frac{Pv}{RT}$. For comparison, the equation of State of Martin & Hou, and Benedict, Webb, and Rubin, applied well outside their applicable region to the area of experimental interest, vary by as much as 10% from Plank's.

Plank's equation is stated and was applied as follows:

$$v = \frac{RT}{p} + \frac{(.0825 + .0012657p) \times 10^3}{(.01T)^3} \quad (2)$$

Using the relations:

$$\left(\frac{\partial h}{\partial p}\right)_s = v = \frac{1}{\rho} \quad (3)$$

$$dh = \left(\frac{\partial h}{\partial T}\right)_p dT + \left(\frac{\partial h}{\partial p}\right)_T dp \quad (4)a$$

$$= C_p dT + \left(\frac{\partial(v\tau)}{\partial \tau}\right)_p dp \quad (4)b$$

where $\tau = \frac{1}{T}$, it is possible to use the zero pressure value³⁴ for C_p in the result

$$h = \int_0^T C_p dT + \int_0^p \left[\frac{\partial(v\tau)}{\partial \tau}\right]_p dp \quad (4)c$$

The right hand term may be evaluated from the equation of state and hence it is possible to determine enthalpy at any desired pressure and temperature. To determine an isentrope, equation (3) is used and the change in h calculated for an arbitrary change in p . Thence, knowing new values of p and h , the corresponding value of T may be determined, either through the use of pre-calculated enthalpy tables, or by iterative integration of equation (4)_c. It is then a simple matter to calculate the new value of density from equation (2) and to thus determine a series of pressure, temperature, and density ratios along an isentrope for any given set of stagnation conditions.

Table 2 contains values of enthalpies calculated in this manner. Agreement within .1° to .3°K occurs at the juncture of those presented by Din.¹⁵

In addition to the comparison of pressure and density measurements, it was decided to apply an additional experimental test to the ability of the Plank Equation of State to predict the behavior of CO₂ gas dynamics in regions of low pressure and temperature yet below its known region of applicability, (0°C to -70°C). Measurement of the normal shock pressure

characteristics were made and compared with the predictions of "real" gas dynamics. For this purpose, it was necessary to include a computation scheme for solution of the continuity, momentum, energy, and state equations across a normal shock and to return along a new isentrope to the new stagnation conditions. A listing of this computation procedure is given in Appendix H.

2. Pressure-Density Measurements

Photographs of two interferometer fringe patterns for non-condensing flow are seen in Figures 11 and 12 and the resulting densities given in Table 3 and 4. The photographs are marked by an extended region of near vertical interference fringes between the upper and lower nozzle walls, indicating that this region is in 1-dimensional flow, and that the boundary layers are quite small (approximately .006" at the throat).

Results of the two sets of measured density and the corresponding pressure profiles of Nozzle I are shown in Figures 15a, 15b and 16a, 16b. Each comparison has been illustrated in two ways. Figures 15a and 16a show the density and pressure profiles in relation to nozzle position. Pressures have been directly measured and plotted at their tap locations. Measured density ratios have been converted to their corresponding pressure ratios through use of the real gas isentropic values based on the experimental stagnation conditions.

Figures 15b and 16b show the same data plotted in somewhat different form, illustrating the theoretical isentropic values of P/P_0 vs. ρ/ρ_0 and those values of P/P_0 and ρ/ρ_0 which were measured at identical points in the nozzle. On Figure 16b, the corresponding perfect gas conversion from density to pressure (based on zero pressure value of C_p/C_v) is also shown.

Figures 15 and 16 show very good agreement between measured pressures and densities, and those predicted from the Plank Equation of State. The fact that the conversion of density to pressure is not very significantly affected by the use of the equation of state rather than perfect gas relations, is indicated by the close proximity of the perfect gas line in Figure 16b, where the applied ratio of specific heats is the zero pressure value at stagnation temperature, $\gamma = 1.28$. However, it should be emphasized that even this use of the perfect gas approximations is preceded by the use of real gas p-v-T relations in the reduction of interferometric fringe shift data to obtain values of density. The only noticeable departure from exact real gas agreement consistent to both tests occurs near the throat region where the measured pressures are slightly higher (≈ 1.8 " Hg) than those values based on measured density. This departure is concluded to be due to departure from 1-dimensional flow over the boundary layer of the lateral side walls in this region and an approximate numerical estimate of this effect in good agreement with the noted error is made in Appendix F.

Attempts to apply the interferometer to direct study of condensation were frustrated by increasing fluctuation and blurring of the interference fringes as stagnation pressure was increased. This effect was apparently due to thermal turbulence. Above pressures of 85 psia, complete blurring resulted upstream of the throat, although the interference bands again became visible downstream, where acceleration of the flow dampens the effects of turbulence. Consequently, no density profiles involving condensation were obtained although photographs of the condensation ice cloud showing the interference fringes within were obtained.

3. Normal Shock Total Pressure Measurements

A more sensitive test of the Plank Equation of State predictions versus those of perfect gas was made by applying each to the gas dynamics

of normal shock behavior and comparing experimental results with theoretical predictions based on the experimental stagnation conditions of each test.

Results of experimental normal shock measurements are shown in Figure 17, using the display of Willmarth and Nagamatsu, and Arthur, who made similar measurements for Nitrogen and Helium.^{64,3} The predictions computed with Plank's Equation of State are shown in Figure 18. Test series No. 2 was taken with a great deal of regard for better accuracy in pitot tube positioning and establishment of steady state readings prior to taking data, with a resulting decrease in the amount of scatter. One-dimensional perfect gas predictions are shown for reference in the lines of constant γ , the appropriate zero pressure value for most of the test conditions being about $\gamma = 1.28$. It is seen that the real gas predictions are considerably more accurate than those of perfect gas in predicting the normal shock characteristics of CO_2 , although there still exists some departure of the experimental results from those predicted with the Plank Equation of State. The experimental results indicate behavior very close to that of a perfect gas having a value of $\gamma = 1.40$. However, this is misleading, since treatment of CO_2 as a perfect gas, using this value of ratio of specific heats, does not successfully correlate the pressure-density measurements, or correctly predict local temperatures along an isentrope. In terms of the measured properties, the experiment indicated about 2% larger values of stagnation pressure behind the normal shock than those predicted.

Despite the above mentioned lack of complete agreement between Plank's Equation of State and measured normal shock pressure characteristics, it appears that such a "real gas" treatment of the gas dynamics is a considerably better description than perfect gas and so warranted application to the prediction of local conditions along the isentrope.

4. Influence of Equation of State Upon Isentropes

The influence of real gas treatment to the computation of CO_2 isentropes has quite a significant effect upon the values of local temperature calculated. Figures 19 and 20 compare two typical perfect gas isentropes with those predicted using Plank's Equation of State. These curves indicate that an error of 5°K could easily occur by attempting to describe the isentrope by a constant ratio of specific heats, and that a decrease in stagnation temperature could cause errors of possibly 10°K if one isentrope were applied to all experimental test conditions.

The resulting uncertainty in predicted nucleation rate, depending upon location within the supersaturated region, can be seen by referring to the classical nucleation rate profiles for CO_2 illustrated in Figure 21. Errors of 15 orders of magnitude could easily occur.

E. Condensation Measurements

1. Pressure Profiles and Local Conditions at Onset of Condensation

Results of experimental measurements involving condensation in Nozzle I, pressure tap plates 1 & 2 are shown in Figures 22 and 23. Results of Nozzle II, pressure tap plate 1 are shown in Figure 24, and of the same nozzle using pressure tap plate 2 in Figures 25 through 30. Figures 24, 25, 26, 27 and 28 are for Nozzle II at an included divergence angle of approximately 2.2° while Figures 29 & 30 are for Nozzle II at an angle of 0.80° . For convenience and due to manometer board limitations, pressure ratios are expressed in terms of the pressure at the tap nearest the throat, but may be easily converted to total pressure ratio. Data for each Figure is adjoined in Tables 5 through 13.

All experimental profiles showed a marked occurrence of pressure variation from non-condensing values at the point of occurrence of

condensation (verified visually in Nozzle I). By noting the pressure ratio at which condensation occurs, it is possible to determine the local conditions at occurrence using the isentropic relations for the equation of state previously discussed. Based on the range of applicability of Plank's Equation of State and comparison with the tables of Din,¹⁵ it is estimated that temperatures in the vicinity of 190°K are accurate to within .3°K and temperatures in the region of 160°K accurate to perhaps 1° or 2°K. A plot of these points for all three nozzle geometries tested is shown in Figure 31.

Several characteristics of the condensation profiles and the local conditions at point of occurrence may be noted.

First, the shape of the profiles contain no sharp minimum at the point of occurrence of condensation such as those noted in the condensation of pure water vapor.^{7,23} i.e. it is not appropriate to speak of condensation shock in this case, since the formation of moisture occurs along an extended region.

Second it appears that pressure level (or temperature level, or some dependent property) may influence the shape of the profile, i.e. the rate of formation of moisture, to some extent since the shapes of the condensation profiles appear to be more "spread out" for high stagnation pressures than for low stagnation pressures. See Figure 27. These effects are not explainable in terms of gas dynamics influences, and the cause is not apparent.

Third, a very definite influence of nozzle geometry upon the point of onset of condensation occurs, as seen in Figure 31. The rapid rate of nozzle divergence and expansion of Nozzle I results in higher supersaturation ratios and relatively greater delay of condensation. Progressively decreasing the rate of expansion through decrease of nozzle divergence

results in earlier condensation. Comparative geometry and non-condensing pressure profiles of the three nozzles may be seen in Figure 32.

Fourth, the extremely low rate of divergence of Nozzle II in the 0.80° case (subsonic flow results at about 0.50° divergence) results in notable axial fluctuation of the pressure profile data (Figure 29) and some scatter of the point of onset of occurrence of condensation. (Figure 31) It should be remembered that differential changes in gas properties are proportional to $(1/1-M^2)$ and that at the pressure ratios present in these tests Mach Number remains very close to unity. ($M = 1.25$ at $P/P_0 \approx .40$). Also, as heat of condensation is released, Mach Number is driven even closer to unity. This is coupled with the fact that at low angles of divergence, the value of the negative pressure gradient is greatly decreased, downstream of the throat, from those values which existed for the other two test nozzles. This would tend to create more rapid boundary layer growth and greater departure from 1-dimensional flow in the narrow angle case. It might be expected that larger departures from 1-dimensional flow, plus the magnifying effects of near unity Mach Numbers could contribute to larger pressure fluctuations.

2. Visual Observations

Experimental observations indicated that the pressure hump accompanying condensation occurred at a point coincident with the appearance of the ice cloud.

This at first seemed at variance with the expectation that pressure variation should occur prior to the appearance of visible condensate, due to the theoretically small sizes of forming nuclei. ($r \sim 10^{-7}$ cm).

Yellot's^{66,67} investigation of condensing steam was also accompanied by visual observation of the water cloud coincident with the location of onset of condensation as determined by pressure measurements. He

reported that this observation remained valid despite changes which resulted in the axial shift of condensation in the nozzle. The same was true in this investigation.

It is also mentioned that the data illustrated a very high degree of consistency and reproduceability, that illustrated in Figures 24 through 28 involving three separate sets of measurements over a period of six months, each set being separated by nozzle dismantlement, cleaning, and pressure tap plate alterations.

IV. INTERPRETATION OF EXPERIMENTAL RESULTS

As discussed in Sections I and II, there are reasons for supposing that the process of nozzle condensation is one involving homogeneous nucleation within the super-saturated vapor. The purpose of this section is to discuss homogeneous nucleation theory and the subsequent drop growth process and apply these processes to nozzle expansions for the purpose of testing the ability of existing theory to interpret the experimental results of CO₂ condensation. Attention is given to the physical properties upon which nucleation and drop growth theory depend, and to the uncertainties which exist in the applicable values of these properties as well as to the theory itself.

A. Nucleation Theory

A review of classical nucleation theory, following the development of Frenkel¹⁹ is presented in Appendix B. For more comprehensive review of theory see Reference Numbers 5,6,12,18,38,56,58,65 and 68. The discussion of Yang,⁶⁵ accomplished while working under P.P. Wegener at Yale University, is particularly thorough.

1. General Form of Nucleation Rate Equation

The rate of production of nuclei in a supersaturated vapor has been shown by various authors to be of the form*

$$J = A \cdot \exp\left(\frac{-\Delta G^*}{KT}\right) \quad (5)$$

where J = number of nuclei produced per unit time per unit volume,

ΔG^* = free energy of formation of a critical cluster (a cluster in unstable equilibrium with its supersaturated vapor)

And A is proportional to the incident flux of vapor molecules on a critical-sized cluster.

$$A = C_n \left[\frac{P}{\sqrt{2\pi mKT}} \right] 4\pi r^*{}^2 \quad (6)$$

* See Appendix B for a review of nucleation theory development

The value of C varies somewhat as derived in the classical treatments of Volmer,⁵⁸ Becker and Doring,⁶ Frenkel,¹⁹ Barnard,⁵ Yang⁶⁵ and others. Though variations of one to two orders of magnitude occur over the range of values presented, the effect on nucleation rate is small, since for only a small additional expansion along a nozzle, the value of J can easily vary by 5 - 10 orders of magnitude. Since the change in local conditions is small for a variation in nucleation rate of this sort and, in fact, is scarcely noticeable for 1 to 2 order of magnitude variations in J , the differences in classical treatments of the theory are not significant.

In the classical treatments of the theory, the nucleus is considered as a stationary object, and the free energy of formation is merely:

$$\Delta G = 4\pi r^2 \sigma - gKT \ln \frac{P}{P_\infty} \quad (7)$$

where the first term is the work of formation of surface area for a liquid having surface tension σ , and the second is the constant-temperature free energy change of g molecules which change state from vapor at P, T to saturated liquid at T . P_∞ is the flat film vapor pressure of the liquid at temperature T .

The critical cluster^(*) is that for which the function ΔG is a maximum, and results in

$$\ln \frac{P}{P_\infty} = \frac{2m\sigma}{\rho_L KTr^*} \quad (8)$$

Using the procedure presented by Frenkel, for which the value of c becomes

$$c = \left[\frac{\ln P/P_\infty}{6\pi g^*} \right]^{1/2} \quad (9)$$

the expression for nucleation rate is

$$J = \left(\frac{P}{KT} \right)^2 \frac{m}{\rho_L} \left(\frac{2\sigma}{\pi m} \right)^{1/2} \exp \left[\frac{-4\pi\sigma r^{*2}}{3KT} \right] \quad (10)$$

As mentioned, Yang has shown that the results of the authors previously mentioned yield expressions for classical nucleation that are much alike (in some cases identical) and which yield quantitative predictions that are not significantly different.

More recent authors have pointed out the need for inclusion of additional terms to the free energy of formation of a critical cluster, which account for the fact that the cluster may have translational, rotational and vibrational energy modes. Kuhrt, Rodebush⁵³ Lothe and Pound,³⁸ and Courtney^{12,13} have treated this problem but reach widely different conclusions as to the effect upon nucleation rate. The postulated correction factors for this "gassification" of the condensed clusters range from 10^4 to 10^{20} , depending on the treatment and molecular configuration chosen.

More recently, Feder, Russell, Lothe and Pound¹⁸ have jointly made a very comprehensive review of this problem, and offered some new thoughts on the subject. For water vapor, they conclude that the effects of gassification are equivalent to a correction factor of about 10^{15} , but admit that this is not borne out by cloud chamber data. In general, such experimental data as does exist tends to more strongly verify classical theory^{5,23} than the improved gassified theory, despite strong arguments for the greater theoretical validity of the latter.

2. Evaluation of Classical Nucleation Rate Equation

Essentially the same physical properties appear both in the exponential and pre-exponential terms of the nucleation rate equation. Of course, uncertainties in these properties will effect the calculated value of nucleation rate chiefly through the exponential. By substitution for the value of r^* it is seen that the exponential is

$$\exp\left[\frac{-4\pi\sigma r^{*2}}{3KT}\right] = \exp\left[\frac{-4\pi}{3} \left(\frac{2m}{\rho_L \ln P/P_\infty}\right)^2 \left(\frac{\sigma}{KT}\right)^3\right] \quad (11)$$

In evaluating this term correctly it is clear that four physical properties of the vapor must be known: 1) the liquid drop surface tension 2) local temperature 3) liquid drop density and 4) local supersaturation ratio.

Much attention has been given to the applicable values of surface energy for small droplets. However, here again there is little agreement as to what corrections should be made to flat film values to take account of the effect of droplet curvature, and the sign of the correction is itself a subject of controversy.

Effects of curvature are considered by some to cause a surface tension decreasing with drop radius such as in the Kirkwood-Buff Equation.

$$\sigma = \frac{\sigma_{\infty}}{(1 + 2\delta/r)} \quad (12)$$

where δ is a length, nearly constant, lying between .25 and 0.6 of the molecular radius.

In addition, Stever and Rathbun⁵⁶ have calculated a correction to take account of the radius dependency of surface tension which also results in a decrease for small radii. Compared with uncorrected surface tension these corrections lead to lower energies of formation of nuclei and hence higher nucleation rates for the same supersaturated conditions.

However, Oriani and Sundquist,⁴⁴ predict an increase in surface energy of about 25% in the case of water, using an analysis based on the breaking of intermolecular bonds. A bonding model used by Benson and Shuttleworth, however, predicts a 15% reduction in surface energy of correspondingly small water ice crystals. Bogdonoff and Lees,⁸ also using considerations of binding energies of sodium and of nitrogen obtained a correction that results in larger critical clusters and also larger energies of formation, hence lower nucleation rates from the uncorrected case. For lack of a more

definite indication of the effects of small droplet sizes, most investigators use the flat film value of surface energy, and estimate the effects on the theoretical predictions of departure from it.

An additional uncertainty in surface energy occurs with CO_2 due to the fact that, at pressures below its ice point, 75.1 psia, it apparently condenses in the form of ice crystals rather than liquid droplets. Bondi⁹ has shown that for metal crystals, which involve valence bonding, increases in surface energy from the liquid value are closely proportional to the heat of fusion and, depending also on the crystal planes involved, amount to increases of about 25% for those metals which he discusses. He further presumes that for molecular solids one might expect increases of from approximately 1/8 to 1/3 these amounts.

In the case of some gases there is doubt as to the proper value of droplet density to be applied. Though density does not vary too rapidly with temperature, there is doubt, in the case of CO_2 , as to whether solid or liquid density should be used. Although the CO_2 may condense as ice particles, there is some argument for use of liquid density in order to be consistent with the spherical geometry and liquid surface energy applied to the liquid drop model, and in the absence of any knowledge of CO_2 crystal surface energies. Also, studies of Dorsch and Hacker¹⁶ with very small water droplets indicated that the spontaneous freezing temperature decreases rapidly with decreasing droplet size. (Figure 33) This might tend to justify doubt on the reality of attempting to distinguish the difference between liquid and solid states at droplet sizes of critical clusters. [For CO_2 , typical critical radii are of 7.5×10^{-8} cm to 10^{-7} cm (about 30 - 50 molecules) at supersaturation ratios of the order of 10, where noticeable quantities of moisture are condensed. Typical nucleation rates are 10^{17} to 10^{21} nuclei/cm³ - sec.]

Figure 34 illustrates existing data on vapor pressures of CO_2 in the region of experimental condensation, and the computational approximations used in the condensation calculations. Accuracy of the vapor pressure data and the approximation below temperatures of about 180°K is uncertain, but is probably within 5% for higher temperatures. Supersaturation ratio may be determined within these limits of accuracy for a given local pressure if the temperature is also known.

Surface tension is considered to be described for flat film liquid by the function $\sigma_\infty = 5.00 - .193T(^{\circ}\text{C})$ dynes./cm, based on data of References 21, 27, and 50, for which a linear dependence of σ_∞ on T down to 220°K is justified. An alternative function $\sigma = 75\left(1 - \frac{T}{T_c}\right)^{1.25}$ (Reference 27) yields values of σ_∞ which vary by only 2% to 9%, in the 200°K to 160°K region of interest, from those of the linear function above.

Knowledge of local temperature, previously discussed, is important in evaluating the nucleation rate equation, not only because of its presence as a cubic in the exponent, but because the other variables are also dependent in value upon temperature. Effects of uncertainty in temperature do not cancel appreciably in their influence upon theoretical nucleation rate. At 200°K , a 1% error in temperature will result in about a 2% error of the opposite sign in surface tension and hence about a 3% error in the ratio σ/T for CO_2 . These effects were illustrated in the earlier discussion of the potential uncertainty of local temperature unless an equation of state is used to determine the isentrope for CO_2 . It is possible that some past applications of theory to experimental condensation data have erred through failure to consider these real gas effects.

Departures from perfect gas behavior affect the evaluation of the free energy required for the formation of a critical cluster, and also the drop growth relations dealt with in the following section, since both nucleation

and drop growth developments are based on perfect gas assumptions. This problem is dealt with in Section IVD, following the discussion of drop growth theory, and the application of nucleation and drop growth to condensation in nozzles.

B. Drop Growth Theory

Subsequent to the production of nuclei, additional formation of moisture will occur through the growth of the clusters due to vapor impingement. Nuclei may by this process grow to radii of up to about an order of magnitude greater than their original size, depending upon two important drop growth parameters introduced below. In the theoretical treatment, the distinction between nucleation and commencement of drop growth treatment is somewhat artificial, as it is necessary to establish some size of cluster at which the nucleated droplet exists and may commence growing. Becker and Doring have shown that at a cluster radius 1.3 times critical, the probability of clusters continuing to grow reaches better than 99%, and hence it is considered that this is a reasonable starting point for the application of drop growth equations. (Note: Computations showed that results were relatively insensitive to this starting radius.)

The growth of a droplet depends predominantly on two factors: 1)The rate of condensing mass flux 2)The rate of droplet energy transfer to the vapor environment.

It would appear that the first factor is itself a description of the drop growth process, but in actuality, it is greatly dependent upon not only local vapor conditions, but also the difference between droplet and vapor conditions. Both of these are strongly influenced by the second factor.

Two coefficients are defined to describe this behavior:

ξ = Condensation Coefficient. The fraction of impinging vapor molecules which are absorbed at the drop surface.

α = Thermal Accommodation Coefficient. The fractional temperature change which takes place in the reflected portion of incident molecules.

$$\alpha = \frac{T_R - T}{T_D - T} \quad (13)$$

Temperature variation across the droplet is assumed to be negligible, and the droplet is assumed to be spherical.

Based on mass and energy balance considerations presented and developed in Appendix C the following drop growth equations are obtained.

Conservation of Mass

$$\rho_L 4\pi r^2 \frac{dr}{dt} = 4\pi r^2 \left(\frac{\xi P}{(2\pi RT)^{1/2}} - \frac{\xi P_D}{(2\pi RT_D)^{1/2}} \right) \quad (14)$$

Conservation of Energy

$$\begin{aligned} 4/3\pi r^3 \rho_L C \frac{dT_D}{dt} + 4\pi r^2 \frac{dr}{dt} \rho_L U_{FD} = \beta(2RT) - \xi\beta_D(2RT_D) \\ - (1 - \xi)\beta_D R [T + \alpha(T_D - T)] \end{aligned} \quad (15)$$

These equations may be reduced, respectively, to

$$\frac{dr}{dt} = \frac{\xi}{\rho_L} (\beta - \beta_D) \quad (16)$$

$$0 = 2\xi \left(1 - \frac{\beta_D}{\beta} \frac{T_D}{T}\right) - 2(1 - \xi)\alpha \left(\frac{T_D}{T} - 1\right) - \xi \left(1 - \frac{\beta_D}{\beta}\right) \left(\frac{\gamma}{\gamma - 1}\right) (\lambda - 1) \quad (17)$$

where $\lambda = \frac{\gamma - 1}{\gamma} \frac{hfg}{RT}$

$$\beta = \frac{P}{(2\pi RT)^{1/2}} \quad \beta_D = \frac{P_D}{(2\pi RT_D)^{1/2}}$$

And P_D is the equilibrium vapor pressure for a spherical liquid drop of temperature T_D in an environment of temperature T_D .

$$P_D = P_\infty(T_D) \exp\left(\frac{2\sigma}{\rho_L RT_D r}\right) \quad (18)$$

In the further application of these equations to streamwise growth of drops in a nozzle, additional assumptions are made. First, for an

acceptably simple computation scheme it is convenient to treat droplets of uniform size, where the radius is an average based either on surface area or volume. Ignoring the effects of coagulation, there is evidence that the actual distribution of drop sizes is narrow, and that the average droplet treatment does not introduce appreciable error.

One possible error that may occur as a result of the above assumption becomes likely when the supersaturation ratio P/P_{∞} , is reduced so rapidly as a result of condensation, that droplets, which have recently nucleated and begun to grow, will suddenly be of size less than the critical cluster size. In this case, considerable re-evaporation would occur among the smaller droplets of the actual size distribution, and the treatment of an "average" droplet does not account for this.

Relative motion between droplets and the gas stream is ignored, and though this is generally accepted, it may be possible that the same translational modes of energy required by recent authors in nucleation theory might also affect to some degree such things as incident mass and energy fluxes upon newly formed nuclei.

Values of α and ξ have been presented by numerous investigators for several vapors, excluding CO_2 . Although earlier presented values of ξ were fairly low, there has been more recent substantiation of values close to 1.00 for most materials, including liquid metals, the previous errors having been caused by neglect of surface temperature depressions and the effects upon evaporation flux. However, there is also indication that molecules of higher dipole moment tend to have lower values of ξ , as with liquid water for which Alty and MacKay,^{1,2} and Prueger⁴⁹ present values of less than $\xi = .04$. The influence of crystallization upon ξ may also be large, as Tschudin presents a value close to unity for water ice. Effects

of surface contamination and surface diffusion barriers (to recently evaporated particles due to insufficient vacuum and mean free path lengths,) are also thought to play a role in experimentation which tends to lower apparent values of ξ . No experimental values of ξ have been measured for CO_2 , which has a dipole moment of about 1.5 compared with 80.0 for that of water.

The thermal accommodation coefficient for vapors and their liquids is generally accepted to be around unity. However, values may be much lower between vapors and solids, as Wachman⁶⁰ indicates for gases on clean metal surfaces. For CO_2 , the value of α for the vapor and its solid crystal is unknown, and there is uncertainty as to which of the two situations above is the most applicable description.

Departures from perfect gas behavior also influence drop growth. Again, correct values of local temperature and supersaturation ratio will be influenced, and the perfect gas assumptions used in treating mass and energy balances leading to equations (16) and (17) may require modification.

In this study, considerable attention has been given to the behavior and influence of the above mentioned factors.

C. Application of Nucleation and Drop Growth Equations

The predicted effects of moisture formation during a nozzle expansion are determined by applying the time rate release of heat to the gas dynamics of the related expansion. By considering the process with respect to variable nozzle position, rather than time, a result is obtained which can be directly compared with experiment.

Interferometric measurements of density variations in the nozzle verified that the flow between boundary layers is in fact one-dimensional and allows the use of the one-dimensional gas dynamics relations;

Continuity

$$\dot{m} = \frac{\rho A u}{1 - \mu} \quad (19)$$

Momentum

$$-A dp = \dot{m} du \quad (20)$$

Energy

$$C_p dT + u du = h_{fg} d\mu \quad (21)$$

where \dot{m} is the mass rate of flow through the nozzle, μ the mass fraction of condensed moisture, u is the streamwise velocity of the vapor, and ρ , P , and T are the vapor density, pressure and temperature, respectively. A is the effective area of flow between boundary layer thickness, and is determined experimentally for non-condensing flow.

The rate of moisture formation is determined as follows and assumes the droplet velocities to be those of the vapor. A nucleus of radius r_0 formed at some point x_0 will grow to a larger size at some future time and distance x .

$$r = r_0 + \int_{x_0}^x \frac{1}{u} \frac{dr}{dt} dx \quad (22)$$

and the surface area will be

$$a = 4\pi \left[r_0 + \int_{x_0}^x \frac{1}{u} \frac{dr}{dt} dx \right]^2 \quad (23)$$

For a rate of growth $\frac{dr}{dt}$ predicted by drop growth, the increase in liquid mass per droplet will be

$$\rho_L a dr = \rho_L 4\pi \left[r_0 + \int_{x_0}^x \frac{1}{u} \frac{dr}{dt} dx \right]^2 \frac{dr}{dt} \frac{1}{u} dx \quad (24)$$

And the fractional moisture change that occurs at x for the

$$dn_0 = J(x_0) A(x_0) \left[\frac{dx_0}{u_0} \right] dx_0 \text{ particles formed in the volume } A(x_0) dx_0 \text{ is}$$

$$d\mu_0 = \frac{dn_0 \rho_L a dr}{(\rho_0 A_0 dx_0) / (1 - \mu_0)} = \frac{J(x_0) A(x_0) \frac{dx_0}{u_0} dx_0 \rho_L 4\pi \left[r_0 + \int_{x_0}^x \frac{1}{u} \frac{dr}{dt} dx \right]^2 \frac{dr}{dt} \frac{dx}{u}}{(\rho_0 A_0 dx_0) / (1 - \mu_0)} \quad (25)$$

Inclusion of the drop growth on all previously formed nuclei necessitates integrating the right hand term over all x_0 . Noting that

$\dot{m} = \rho_o A_o u_o / 1 - \mu_o$ and considering also the moisture produced through additional nucleation at x , there results

$$\begin{aligned} \frac{d\mu}{dx} &= \int_0^x J(x_o) \left(\frac{A(x_o) dx_o}{u} \right) \frac{\rho_L 4\pi}{\dot{m}} \left[r_o + \int_{x_o}^x \frac{1}{u} \frac{dr}{dt} dx \right]^2 \frac{dr}{dt} dx_o \\ &+ \frac{4\pi r^*{}^3}{3} \frac{\rho_L}{\dot{m}} J(x) A(x) \\ &= \frac{4\pi \rho_L}{\dot{m}} \left[\int_0^x \left(r_o + \int_{x_o}^x \frac{1}{u} \frac{dr}{dt} dx \right)^2 J(x_o) A(x_o) \frac{1}{u} \frac{dr}{dt} dx_o \right. \\ &\left. + 1/3 r^3 J(x) A(x) \right] \end{aligned} \quad (26)$$

For nuclei generally only slightly larger than critical size, the theoretical drop growth rate is essentially independent of size.²³ Hence $\frac{dr}{dt}$ is assumed to have a value equal to that for large drops. Also, since it is practically impossible to keep account of the radii of each group of growing nuclei which formed at each section dx , it is assumed that the droplets can be represented by the "surface-area averaged" radius of droplets. As previously mentioned, volume averaging has little influence on the results. In addition, Lundgren has given experimental evidence that the actual size distribution of particles condensed in a nozzle expansion is quite narrow.

The foregoing equations are reduced to the following form for use with a Runge-Kutta-Merson integration procedure along the expansion path. (The detailed listing of computation procedure may be seen in Appendix H).

$$dY_1 = 8\pi JA$$

$$dY_2 = Y_1 \frac{dr}{dt} + r^* dY_1$$

$$dY_3 = Y_2 \frac{dr}{dt} + JA(4\pi r^*{}^2)$$

$$dY_4 = \frac{d\mu}{dx} = \frac{\rho_L}{\dot{m}} \left[Y_3 \frac{dr}{dt} + JA \left(\frac{4\pi r^*{}^3}{3} \right) \right]$$

$$dY_5 = \frac{dP}{dx} = P \left[\left(\lambda - \frac{1}{1-\mu} \right) d\mu - \frac{1}{A} \frac{dA}{dx} \right] / \left[1 - (1-\mu) \left(\frac{Y}{\gamma} - \frac{1}{\gamma M^2} \right) \right]$$

$$dY_6 = \frac{dT}{dx} = T \left[\lambda d\mu + \frac{Y-1}{\gamma} (1-\mu) \frac{dP}{P} \right]$$

$$dY_7 = \frac{dM}{dx} = M \left[- \frac{(1-\mu)}{\gamma M^2} \frac{dP}{P} - \frac{dT}{2T} \right]$$

where

$$\lambda = h_{fg}/C_p T$$

$$\gamma = C_p/C_v$$

$$M = u/\sqrt{\gamma RT}$$

Initial values of the stagnation conditions, physical properties of the vapor and its liquid, values of α and ξ , and calculation starting point are given for each computation. Effects of contamination may also be considered by giving non-zero values to $Y(1)$, $Y(2)$ and $Y(3)$, based on an initial concentration and size of contaminant. Effects of possible droplet energy modes upon free energy of cluster formation ("gassified" behavior of droplets - page 23) may be considered by multiplying nucleation rate by constant arbitrary factors, equivalent to the values proposed by various authors.

The various sub-routines of the listed computation scheme accomplish the determination of such things as the change in nozzle area, vapor and liquid properties, supersaturation ratios and solution to the drop growth equations when step-wise changes are made along the stream of the expansion. An error estimation is made for each computation and the size of the step, dx , is adjusted to reduce the error bounds to within the desired limits.

D. Real Gas Effects

The preceding developments of nucleation and drop growth theory and application to nozzle condensation computations assume perfect gas behavior during the expansion. However, as earlier discussion illustrated, experimental measurements were being made for which values of $\frac{Pv}{RT}$ which were considerably less than unity. Consequently, the computational scheme was modified so that the effects of departure from perfect gas behavior could also be considered.

A feature of an isentropic expansion which facilitates fairly simple corrections to the gas dynamics, drop growth and nucleation equations is the

fact that for this particular thermodynamic process, the compressibility factor remains fairly constant, changes of less than 2% in the value of z generally occurring for expansion pressure ratios of 10 or more. This was found to be true for several other gases, including ammonia, and for CO_2 is valid throughout the superheated and supersaturated regions for which compressibility factors are in excess of about .88. Using this fact, it may be shown (Appendix D) that the following relations are approximately true for an isentropic expansion.

$$\frac{Pv}{RT} = z = \text{constant} \quad (27)$$

$$\gamma' = \frac{\gamma}{1 + (\gamma-1)(1-z)} = \frac{dP}{d\rho} \left(\frac{\rho}{P} \right) \quad (28)$$

$$R' = \frac{Rz}{m} = zR \quad (29)$$

where γ' and R' are the effective ratio of specific heats and gas constant, respectively, that are applicable. It should be noted here, that the nucleation rate is effected in the following manner;

$$J \propto \exp \left(\frac{-4\pi\sigma r^*2}{3KT} \right); \quad r^* = \frac{2m\sigma}{\rho_L zKT \ln P/P_\infty}$$

due to the change in free energy required to form a critical cluster.

To apply these effects to the perfect gas relations of the condensation computations, two additional steps were necessary. First, modifications which allowed for use of a variable ratio of specific heats ($\gamma = \gamma(T)$) were made. Second, each set of stagnation conditions which was to be placed in the condensation scheme first had its "real" isentrope, z , and effective isentropic exponent $\gamma'(T)$ determined, and from these the $\gamma(T)$ which corresponded to z and γ' . Computation input was $\gamma(T)$ and correction (compressibility factor) z . This resulted in an isentrope, providing the correct values of P vs. T being employed in each condensation calculation, plus the use of effective values of γ and R in the drop growth and nucleation calculations. Additional details of this procedure are presented in Appendix D.

E. Results of Application of Theory to Condensation of CO₂

1. Comparison of Theory and Experimental Data

Data shown in Table 14 and Fig. 31 illustrate the local conditions at the occurrence of condensation for each of the experimental tests made. Local temperature was determined through computation of the isentrope for each test case, using the procedure discussed on page 13 based on Plank's Equation of State for CO₂. Reference to Figure 35 illustrates that .1% presence of moisture is a convenient and reasonable criteria for theoretical onset of condensation. Comparing the data and the predictions of theory involved two main comparisons; 1) The location of the onset of condensation, defined as the theoretical occurrence of .1% moisture, and 2) The shape of the pressure profiles. For lack of better knowledge, α , ξ and $\frac{\sigma}{\sigma_{\infty}}$ were originally assumed to be unity. Specific comparisons were made of the predictions of 1) Classical nucleation theory 2) Droplet "gassification" corrections to the theory 3) "Real" gas vs. perfect gas treatment of the classical theory (to determine whether or not a simplified approach, containing known errors, might yet yield a better prediction of observed behavior.) 4) Use of liquid vs. solid droplet density and 5) the predictions of the theory in nozzles of different geometry. Figures 36 through 39 illustrate these comparisons and support the following conclusions:

1) All predictions based on values of σ/σ_{∞} , α and ξ of unity predict condensation at considerably lower supersaturation ratios than those observed experimentally.

2) Real Gas treatment of the classical theory yields a closer prediction than perfect gas treatment, and the "gassification" corrections are in the wrong direction. (Fig. 36)

3) Use of liquid rather than solid droplet density yields a prediction nearer to experimental results, lacking any better knowledge of

what corrections might be applied to surface energies of small CO_2 crystals. (Fig. 37)

4) The unmodified theory does extremely poorly in predicting any effects of nozzle geometry. (Fig. 38)

5) The shape of condensation profiles predicted by values of α and ξ of unity are in extreme disagreement with those observed experimentally. (Figs. 45 and 46)

2. Influence of Nucleation and Drop Growth Theory on Theoretical Predictions.

It is concluded that homogeneous nucleation and drop growth theory fail in their ability to predict observed condensation behavior of CO_2 , unless some modification in values of the nucleation and drop growth parameters σ , ρ_L , α , and ξ can be independently established. Toward better understanding of how these parameters influence predicted condensation phenomena, and with the idea in mind of finding corrections for the prediction of CO_2 condensation, a series of calculations based on arbitrary variations of σ , ρ_L , α and ξ were made.

Figures 39 and 40 show typical pressure profiles for condensation of CO_2 , for various condensation and thermal accommodation coefficients. Shown in the lower portion of the figures is the nucleation rate, indicating how nucleation rate remains high for longer duration when drop growth is retarded. This results in condensation clouds of greater particle density and smaller particle size than in the case of ready drop growth. In addition, smaller total deflection in the static pressures (from non-condensing), indicating lesser amounts of moisture, exist for the downstream portions of profiles having lower drop growth parameters.

An important observation in these figures is that, beyond a certain reduction in the drop growth parameters, appreciable proportions of moisture

may be present primarily from nucleation. This is manifested in the form of a so-called "ramp" deflection in the pressure profile to which additional drop growth effects are super-imposed. Thus, for example in Figure 39, for an assumed α of .10, variations in ξ from 1.0 to .3 and then to .1 have progressively less effect on the point of departure of the condensation curve, and for lower values of ξ , the nucleation "ramp" becomes increasingly apparent. The same behavior occurs for decreasing values of α , (shown for an assumed value of $\xi = .04$) in Figure 40. It would be possible to obtain a deflection curve involving only nucleation, if drop growth were set at zero.

Figure 41 illustrates the influence of increasing or decreasing the nucleation rate by changing the free energy of formation of nuclei. Indicated are variations in the surface energy from flat film liquid value, though similar changes may be introduced by varying the droplet density ρ_L . The important parameter in the nucleation rate exponent is (ρ^3/ρ_L^2) , since, with knowledge of temperature and supersaturation ratio, the uncertainties of surface energy corrections, small cluster densities, and non-spherical geometry may all be contained in this term.

Two interesting features may be noted in Figure 41. First is the effects of higher downstream velocities, which tend to "wash out" the curves further downstream, and second, the important observation that, for α and ξ of unity, condensation results in a return to near-equilibrium conditions, seen by the fact that condensation commencing at any point in the nozzle results in the same pressure deflection immediately further downstream.

a) Onset of Condensation

As the previous figures suggest, influence of the drop growth coefficients upon the point of onset of condensation is relatively small compared to that caused by changes in surface tension. However, uncertainties in α

and ξ still have appreciable effect upon values of surface energy necessary to bring the predictions of theory into agreement with experiment. Figures 42, 43, and 44 show the corrections to flat film surface tension necessary to provide agreement between theory and experiment (based on fitting the data of nozzle I(2.20°)). If the uncertainty in the values of α and ξ for CO_2 crystals, is given limits of from perhaps .01 to 1.0 for each, then the respective surface energy corrections necessary may range from about 20% to 38% increases in the flat film surface tension. For the absolute lower bound of uncertainty on α and ξ of zero, the necessary correction in surface energy is reduced to +17%.

It is noted in these figures that the theoretical effects of nozzle geometry are increased to some extent by use of small, but non-zero values of the drop growth parameters, but that the theory in all cases predicts less effect than that recorded experimentally.

b) Profile Shapes

Figure 45 illustrates the pressure profiles for a single expansion corresponding to the same values of α and ξ , and corresponding σ determined above, and indicates an additional distinct failing of the theory in its description of the early stages of condensation. It is apparently impossible to reconcile the experimental downstream pressure deflections, which indicate a considerable degree of supersaturation, or departure from equilibrium, with the apparent rates of formation of moisture immediately after onset. When drop growth parameters are adjusted to bring theoretical profiles into agreement regarding the amount of downstream pressure deflection, then the upstream theoretical rate of formation of moisture lags considerably behind the experimental results.

This problem may result from some of the approximations discussed in the numerical calculations, or may in fact indicate some physical "arrest"

of the condensation process, perhaps due to decreasing mass or thermal accommodation characteristics of crystals which grow rapidly colder during their passage downstream.

c) Downstream Moisture Formation

For purposes of calculating the amounts of carbon dioxide that will form, or the downstream pressure variations which will occur during a nozzle expansion of CO_2 , the following parameters were determined, having arbitrarily set thermal accommodation coefficient, α , at unity. These results, as a best description of the three nozzles, the profiles shown in Figures 46, 47, 48 and 49 for $\alpha = 1.0$, $\xi = .00008$, $\rho_L = 1.18 \text{ gm/cm}^3$, $\rho/\rho_\infty = 1.18$. These drop growth parameters have no physical significance, and are presented only as an aid in determining approximate amounts of CO_2 moisture formation subsequent to the occurrence of condensation in a nozzle expansion.

The best compromise to profile shape soon after onset has been a recipe which yields theoretical profiles lagging behind and below the experimental data early in the condensation, and which then pass slightly to the other side of the data by about the same amount for the remainder of the profile.

The condensation data of Nozzle II (0.80) indicates the presence of ~~so~~ some cyclic axial variation in the pressure ratios of all profiles. This suggests that at this narrow angle, some departure from 2-dimensional flow may be interfering with the condensation process. Friction, or compression shocks may be creating these fluctuations, and would also result in decreased supersaturation ratios in this region, offering a possible explanation as to why considerably less moisture is forming than the recipe predicts for that nozzle.

3. Influence of Contamination

Computations attempting to determine the influence of contamination of vapor in nozzles were carried out at intervals during this investigation. Original calculations were based on perfect gas assumptions and values of α , ξ , and $\frac{\sigma}{\sigma_{\infty}}$ of unity, in an attempt to establish whether or not condensation could possibly be due to reasonable amounts of contamination present in the test vapor. Such contaminants might be present in the form of dust, charged particles, or the result of an earlier condensation of some other vapor. Contamination of this sort would be expected to cause earlier condensation than would occur if the test vapor were perfectly homogeneous.

Junge²⁷ presents data for typical size density distributions of contamination in atmosphere. Upper limits of particle concentration in dirty atmosphere of a large city reach values of $5 \times 10^5 \text{ cm}^{-3}$ for particles of size less than 10^{-5} cm (.1 micron), about 10^3 cm^{-3} for sizes from .1 to 1.0 microns and 1.0 cm^{-3} for particles exceeding one micron in size.

Typical profiles of supersaturation obtained for increasing concentrations of contamination with microscopic particles are shown in Fig. 50. Beyond a limiting concentration of particles, (depending on size) the supersaturation ratio obtains lesser and lesser values, until the flow reaches a state where it is close to equilibrium throughout the expansion, due to the ready formation of moisture on contaminant particles.

Subsequent to the establishment of the "recipe" described in the previous section, additional computations for both microscopic and macroscopic contamination were made.

The results are shown graphically in Figures 51 and 52, and are briefly summarized:

- 1) Micron-sized particles in excess of $10^8 / \text{cm}^3$ are required to influence the theoretical condensation of CO_2 . This is at least 5 orders of

magnitude larger than upper atmospheric concentrations of particles of this size.

2) Microscopic particles, such as might occur from the precondensation of another vapor, of size the order of 10^{-7} cm are required in excess of $10^{12}/\text{cm}^3$ to influence theoretical condensation of CO_2 .

3) No appreciable difference between empirically fitted real and perfect gas theories results.

4) The difference between amounts of contamination necessary to influence condensation in the rapid expansion of Nozzle I and the slow expansion of Nozzle II (0.80°) is approximately one order of magnitude, independent of particle size.

5) The empirically fitted recipe predicts necessary concentrations of particles roughly two orders of magnitude larger than that predicted using values of α , ξ , and σ/σ_∞ of unity.

When the curves of Fig 52 are replotted in terms of $\left[\log_{10} \frac{V_{\text{CNTAM}}}{V_{\text{TOTAL}}} \right]$, the two curves tend to move together, since the first curve to drop downward represents larger volume contamination. This results in fairly localized values of supersaturation ratio at occurrence of condensation as a function of *volume* contamination, regardless of particle size.

Applying the volume amounts of contamination of CO_2 in nitrogen presented by Willmarth and Nagamatsu,⁶⁴ and Arthur,³ a computation of the predicted effects of theoretical influence of contamination on nitrogen was made, using values of α , ξ , and α/α_∞ of unity and perfect gas assumptions for nitrogen. The results are shown in Figure 53, for various size particles typical of cluster sizes for CO_2 , indicating reasonably good agreement with their data. This is taken to indicate some substantiation of the above calculations for contamination in CO_2 , perhaps within one or two orders of magnitude of the calculated contamination levels needed to influence homogeneous condensation.

V. SUMMARY OF FINDINGS AND CONCLUSIONS

A. Experimental Findings

1. Consistent data regarding the supersaturation of CO_2 at onset of condensation plus the shape of pressure profiles has been obtained for three different nozzles.
2. Interferogram photographs and an approximate theoretical estimation show agreement that the boundary layer in the nozzle throat was of the order .006" and substantiates the treatment of flow in the mid-stream as 1-dimensional isentropic flow.
3. Departures from perfect gas behavior by CO_2 in the P-T range tested are significant, and must be accounted for in the calculation of local conditions along an isentropic expansion. Density and static pressure measurements plus total pressure measurements for non-condensing flow indicate that the Plank Equation of State gives a good description of low temperature CO_2 behavior.
4. Rates of CO_2 expansion, as determined by nozzle geometry have a large influence upon the degree of supersaturation obtained prior to occurrence of condensation.

B. Application of Nucleation and Condensation Theory

1. Classical nucleation and drop growth theory, as applied herein, will reasonably predict the conditions at which onset of CO_2 condensation occurs, if flat film liquid surface energies are corrected by amounts within suggested ranges of uncertainty for small droplets or crystals. In these calculations a droplet density equal to that of CO_2 liquid at the triple point, 1.18 gm/cm^3 , has been assumed.
2. The appropriate correction to surface energy is dependent upon the values of mass and thermal accommodation coefficients, ξ and α , and has a correction uncertainty of about 21% of flat film values for maximum possible

uncertainty in ξ and α . ($\frac{\sigma}{\sigma_{\infty}} = 1.17$ for $\xi = \alpha = 0.0$; $\frac{\sigma}{\sigma_{\infty}} = 1.38$ for $\xi = \alpha = 1.0$.) Consequently, the applicable value of the parameter (σ^3/ρ_L^2) to be applied to the nucleation rate equation corresponds to values of $(\sigma^3/\rho_L^2)(\rho_{L_0}^2/\sigma_{\infty}^3)$ which lie between the limits $(1.17)^3$ and $(1.38)^3$ where $\rho_{L_0} = 1.18$ gm./cm³ and σ_{∞} is the linear temperature dependent function $\sigma_{\infty} = 5.00 - .193T(^{\circ}\text{C})$ dyne/cm.

3. Pressure profiles obtained experimentally indicate that considerably less moisture is forming than that necessary to return the mixture of vapor and condensate to near equilibrium values, or zero supersaturation downstream of the onset of condensation. Values of ξ and α necessary to produce agreement between the theory and experiment in this respect require that one or both of these parameters be considerably less than what are thought to be minimal values (about .01, for each.)

4. Even at their best empirical fit, classical nucleation and drop growth theory as applied herein do not seem to provide any means of describing the exact shape of the pressure profiles obtained experimentally or the extent of effects of geometry noted experimentally. These failings, in addition to that of B3, above, are thought to indicate inadequate or incorrect assumptions in the treatment of the drop growth calculations.

5. Application of the so-called "gassification" corrections to classical nucleation theory results in corrections in the wrong direction, unless even larger corrections in the surface energy of formation of CO₂ ice crystals (than indicated above) can be established. Use of solid, rather than liquid, droplet density in the parameter (σ^3/ρ_L^2) further increases the necessary corrections to surface energies required to provide agreement with experiment.

6. The influence of dirt particles or other foreign particles on the

condensation of CO_2 , and probably most other gases, may be completely disregarded in supersonic nozzles, unless the particles result from the precondensation of another gas in the stream. Amounts of micron-sized particles necessary to influence CO_2 condensation are about five orders of magnitude in excess of upper atmospheric limits of concentration, and particles of the order of 20 \AA are necessary in excess of about 10^{12} particles/cm.³ to influence homogeneous nucleation and condensation. Testing the condensation of nitrogen with pre-condensed particles of CO_2 in quantities mentioned by Willmarth and Nagamatsu, and Arthur, yields theoretical predictions which are in reasonable agreement with their experimental observations.

7. Additional knowledge of thermal and mass accommodation coefficients are necessary to allow better testing of homogeneous nucleation and condensation theory. In addition, comprehensive testing of the theory will await some better establishment of surface energy corrections for small particles. Until this information becomes available and an established treatment of nucleation and drop growth can be applied with confidence to many vapors, "recipe" fitting may provide the best means for predicting nozzle condensation behavior.

VI. SUGGESTIONS FOR FURTHER STUDY

One of the greatest difficulties in application of experimental results to a meaningful test of theoretical predictions results from the uncertainties in value of many of the important variables and parameters contained in nucleation and drop growth theory. Consequently, any methods or devices of experimentation which would decrease any of the uncertainties, or the effects of uncertainty, of such quantities as σ , ρ_L , α , ξ , local temperature and the gas dynamics in general would be of great assistance. One means of proceeding in this direction is to contain the test gas within large quantities of another gas which is non-condensing in the region of interest of the test gas, and whose gas properties are well-known, preferably being as near those of a perfect gas as possible. An immediate benefit of this is to provide a means of accurately determining local properties at all points of the isentrope with ease, since, the temperature of the test gas should be that of the ideal "carrier" gas, which dominates the gas dynamics. Second, the influence of thermal accommodation is greatly reduced due to the fact that the huge preponderance of incident molecules upon the surface of a formed droplet are those of "carrier" gas, and hence are reflected. The drop is consequently kept at or nearly at environmental temperature regardless of the value of α . Hence, there are advantages to be gained by testing gases for which these uncertainties exist (the huge preponderance of all gases) in a carrier stream of such gases as nitrogen, helium, or dry air. Several complications arise from this method, including the need for very precise measurement of mass fraction of test gas in the mixture, and more sensitive instrumentation to detect the lessened effects of condensation upon the gas properties.

Highly steady flow systems would aid in obtaining the accuracy necessary.

With regard to some of the uncertainties pertaining to CO_2 , it would be of considerable interest to determine whether or not the experimental behavior of condensation is influenced by establishing liquid rather than ice formation of condensate particles. This could presumably be accomplished by raising pressure levels to a point where condensation occurs above the ice point, 75.1 psia. This would necessitate stagnation pressure in the range of 175 - 250 psia, mass rates of flow and a source of CO_2 which are proportionally larger, heavier construction of some important fixtures in the system, (such as the stagnation tank) and a means of pressure profile procurement other than manometer board.

It is felt that interferometric means of study offer enough advantages, particularly with more toxic or reactive gases, to warrant further application to study of condensation in nozzles. The inability to distinguish interference lines in the upstream region of the nozzle encountered at high pressure levels in this investigation could possibly be solved by facilitating higher camera shutter speeds (1/150 sec., the maximum possible, was used in these studies) or by establishing wall temperatures which are close to stream stagnation temperature. Two-dimensional nozzles, where interferometric study could be successfully employed, would decrease the problems of instrumentation and would be readily adaptable to studies of light scattering and polarization, yielding experimental information regarding droplet sizes. Interferometric photos involving condensation, although not applied in this report, were obtained, and showed interference bands very clearly within the region of condensation,

this region being marked plainly by the decreased light intensity resulting from the presence of the ice cloud.

Light scattering or other techniques which yield information regarding the average size of the ice particles at their initial appearance and after subsequent downstream growth would be very useful. Since, as previously mentioned, there is some indication that nucleation is the major contributor to moisture in its early stages of formation for CO_2 , this information might be directly related to the critical cluster size of CO_2 .

Additional investigation of crystal thermal and mass accommodation coefficients would be of help in further establishing the apparent indication from this investigation that either one or both have very low values for crystalline CO_2 at low temperatures. The carrier gas technique previously mentioned could isolate the influence of α and might facilitate a better means of studying ξ and its role in condensation.

BIBLIOGRAPHY

1. Alty, T. - "The Interaction of Vapor Molecules with a Crystal Surface" - Proc. Roy. Soc. (London) - Vol. 161A, pp. 68 - 79, (1937).
2. Alty, T. and MacKay, C. A. - "The Accommodation Coefficient and the Evaporation Coefficient of Water" - Proc. Roy. Soc. (London) - Vol. 149A, pp. 104 - 116, (1935)
3. Arthur, P. D. - "Effects of Impurities on the Supersaturation of Nitrogen in a Hypersonic Wind Tunnel" - Ph.D. Thesis - California Institute of Technology, (1952).
4. Bailey, Harry E. - "Equilibrium Thermodynamic Properties of Carbon Dioxide" - NASA, SP-3014, (1963).
5. Barnard, A. J. - Proc. Roy. Soc. (London) - AZZO, p. 132, (1953).
6. Becker, R. and Woring, W. - Ann. der Physics - Vol. 25, p. 719, (1935).
7. Binnie, A. M. and Green, T. R. - Proc. Roy. Soc. (London) - Vol. 181, p. 134, (1942).
8. Bogdonoff, S. M. and Lees, L. - "Study of the Condensation of the Components of Air in Supersonic Wind Tunnels" - Part I: "Absence of Condensation and Tentative Explanation" - Princeton Univ. Aeronaut. Eng. Lab. Rept. #146, (1949).
9. Bondi, A. - "The Spreading of Liquid Metals on Solid Surfaces" - Chem. Rev., Vol. 52, No. 2, pp. 417 - 458, April 1953.
10. Camac, M. - "CO₂ Relaxation Processes in Shock Waves" - AVCO RR 194, (BSD-TDR-64-96), October 1964.
11. Chen, L. H. - "Thermodynamic Properties of CO₂, Papers, Lafayette, Indiana - pp. 358 - 369, (1959) or (Electric Boat, Groton, Conn. - GA 1038, p. 157, (1959)).
12. Courtney, W. G. - Jour. Chemistry and Physics - Vol. 34, p. 2018, (1962).
13. Courtney, W. G. - "Re-Examination of Nucleation and Condensation of Water" (not yet published).
14. Dean, R. C. Jr., - *Aerodynamic Measurements*, M. I. T. Gas Turbine Laboratory - Chapter IX: DeFrate, Barry and Bailey - "Optical Techniques", pp. 167 - 208, (1952).
15. Din, F. - *Thermodynamic Functions of Gases* - Vol. 1 - British Oxygen Co., Ltd., (1956).
16. Dorsch, R. G. and Hacker, P. T. - "Photomicrographic Investigation of Spontaneous Freezing Temperatures of Supercooled Water Droplets" - NACA TN-2142, July 1950.
17. Faro, I., Small, T. R. and Hill, F. K. - Jour. Applied Physics - Vol. 34, p. 40, (1952).

18. Feder, J.*, Russell, K. C. **, Lothe, J., Pound, G. M. - "Homogeneous Nucleation and Growth of Droplets in Vapors"; toward partial fulfillment of degrees - (*) Cand. Real., Fysik Institute, Univ. of Oslo; (**) Ph.D., Fac. of Eng. & Sci., Carnegie Institute of Technology, (1964).
19. Frenkel, J. - *Kinetic Theory of Liquids* - Oxford Univ. Press, (1946).
20. General Dynamics Corp., Liquid Carbonics Div. - "Physical Properties of Carbon Dioxide and Temperature-Entropy Chart" - Tech. Bulletin #48.
21. *Handbook of Chemistry and Physics*, 45th. Ed., Chemical Rubber Co., (1964).
22. Hill, P. G., Witting, H. and Demetri, E. P. - ASME Trans., Jour. of Heat Transfer - p. 303, November 1963.
23. Hill, P. G. - "Homogeneous Nucleation of Supersaturated Water Vapor in Nozzles" - M. I. T. Gas Turbine Laboratory Report #78, January 1965.
24. Hilsenrath, J.; Becket, C. W.; Benedict, W. S.; Fana, L.; Hoge, H. J.; Masi, J. F.; Nuttal, R. L.; Touloukian, Y. S. and Wooley, H. W. - "Tables of Thermal Properties of Gases" - NBS Cir. 564, U. S. Dept. of Commerce, (1955).
25. Hirth, J. P. - Ann. N. Y. Academy of Science - Vol. 101, p. 805, (1963).
26. Holley, Worlton and Zeigler - Compressibility Factors - from the Beattie-Bridgman Equation for H_2 , N_2 , O_2 , CO_2 , NH_3 , and other gases - U. S. Atomic Energy Commission, Los Alamos, La-2271, 51 pp., (1959).
27. *International Critical Tables* - McGraw-Hill Book Co., New York -(1926-30).
28. Jorgensen, L. H. and Redmond, R. J. - Charts for Equilibrium Flow Properties of CO in Hypervelocity Nozzles - NASA SP-3015, (1965).
29. Junge, C. E. - *Air Chemistry & Radioactivity* - Academic Press (1963).
30. Kantrowitz, A. R., - "Effects of Heat Capacity Lag in Gas Dynamics" - NACA Wartime Report L-457, January 1944.
31. Kantrowitz, A. R. and Huber, P. W. - "Heat Capacity Lag in Turbine Working Fluids" - NACA Wartime Report L-21, May 1944.
32. Kantrowitz, A. R., - Physics Review - Vol. 77, p. 572, (1950).
33. Katkhe, O. I. - "Equation of State of CO" - (Eng. Inst. Merchant Marine, Odessa) - Inshener, Fiz. Zhur., Akad. Nauk Belorus, S. S. R. - Vol. 1, No. 5, pp. 95 - 98, (1958).
34. Keenan, J. H. and Kaye, J. - *Gas Tables* - Wiley & Sons, Inc. - New York - (1948).
35. Kennedy, G. C. - American Journal of Science - 252, 225, (1954).

36. Ladenburg, R., Van Voorhis, C. C. and Winckler, J. - "Interferometric Study of Supersonic Phenomena" - NavOrd Report 69-46, (1946).
37. Liley, P. E. - Jour. Chem. and Eng. Data - Vol. 4, No. 3, p. 238, July 1959.
38. Lothe, J and Pound, G. M. - Jour. Chemistry & Physics - Vol. 36, p. 2080, (1962).
39. Lowry and Erikson - Jour. Am. Chem. Soc. - Vol. 49, p. 2729, (1927).
40. Maass, O. and Barnes - Proc. Roy. Soc. (London) - Ser. A., Vol. 111, p. 224, (1926).
41. Maass, O. and Mennie, J. H. - Proc. Roy. Soc. (London) - Ser. A., Vol. 110, p. 198, (1926).
42. Matheson Company Inc. - *Matheson Gas Data Book* - James Grey, Inc. (1961).
43. Nichols, L. R., Nozek, S. M, Winzig, C. H. and Goldman, L. J. - "Experimental Determination of Sodium Vapor Expansion Characteristics with Inert Gas Injection Pressure Measuring Technique" - NASA TN D-2276, April 1964.
44. Oriani, R. A. and Sundquist, B. E. - Jour. Chemistry & Physics - Vol. 38, p. 2082, (1963).
45. Oswatitsch, K. - Z. Angew. Math. und Mech. - Vol. 22, p. 1, (1942).
46. Paul, B. - ARS Journal - Vol. 32, No. 9, p. 1321, (1962).
47. Plank, R. and Kuprianoff, J. - Z. Ges. Kaiteind. Beih. - Vol. 1, No. 1, (1929).
48. Probststein, R. F. - "Time Lag in the Self-Nucleation of a Supersaturated Vapor" - Jour. Chem. Physics - Vol. 19, No. 5, p. 619, May 1951.
49. Prueger, W. - "Die Verdampfungsgeschwindigkeit der Fluessigkeiten" - Z. Physik - Vol. 115, pp. 202 - 244, (1940).
50. Quinn, E. L. and Jones, C. L. - *Carbon Dioxide* - Reinhold Publishing Co. - New York, (1936).
51. Raymond, J. L. - "Thermodynamic Properties of Carbon Dioxide to 24,000°K with Possible Application to the Atmosphere of Venus" - RM-2292, The Rand Corporation, November 1958.
52. Reisse, R. - Jour. Chemistry & Physics - Vol. 20, p. 1216, (1952).
53. Rodebush, W. H. - Ind. and Eng. Chem. - Vol. 44, No. 6, p. 1289, June 1952.
54. Rossbach, R. J. - "Critical Flow of Potassium Vapor Through Instrumented Converging-Diverging Nozzle" - ASME Rep. 65-GTP-22, January 1965.

55. Shapiro, A. H. - *Dynamics and Thermodynamics of Compressible Fluid Flow* - Ronald Press - New York - Vol. II, p. 887, (1953).
56. Stever, H. G. and Rathbun, K. C. - "Theoretical and Experimental Investigation of Condensation of Air in Hypersonic Wind Tunnels" - NACA Tech. Note 2559, (1951).
57. Stodola, A. - *Steam and Gas Turbines* - McGraw-Hill Pub. Co. - pp. 117 - 128, 1034 - 1073, (1927).
58. Volmer, M. and Flood, H. - Z. Phys. Chem. - Vol. A170, p. 273, (1934).
59. Vukalovich, M. P. and Altunin, V. V. - "Experimental Research on PVY Relation of CO₂" - Teploenergetika, Vol. 6, No. 11, pp. 58 - 65, (1959).
60. Wachman, H. Y. - "The Thermal Accommodation Coefficient: A Critical Survey" - ARS Journal, Vol. 32, pp. 2 - 12, (1962).
61. Wakeshima, H. - Phys. Soc. of Japan - Vol. 10, No. 2, p. 141, (1955).
62. Wegener, P. P. - "Condensation Phenomena in Nozzles" - AIAA Preprint No. 63, p. 509, (1963).
63. Wegener, P. P. and Pouring, A. A. - Physics of Fluids - Vol. 7, p. 352, (1964).
64. Willmarth, W. W. and Magamatsu, H. T., - Jour. Applied Physics - Vol. 23, p. 1089, (1952).
65. Yang, W. T. - "A Study of Homogeneous Nucleation from Vapor to Droplets" Doctoral Dissertation - Yal University, (1963).
66. Yellott, J. I. - Trans. ASME, Vol. 56, p. 411, (1934).
67. Yellott, J. I. and Holland C. K. - Trans. ASME, Vol. 59, p. 171, (1937).
68. Zeldovich, J. J. - Exp. Theor. Phys. (USSR), Vol. 12, p. 525, (1942).

APPENDIX A.LIST OF FIGURES AND TABLES

Figure 1	Typical Co-Existence Lines Versus Isentropic Expansion Paths	A1
Table 1	Typical Values of h_{fg}/C_p for Various Gases	A2
Figure 2	Schematic Arrangement of Test Apparatus	A3
Figure 3	General View of Test Apparatus	A4
Figure 4	Stagnation Tank, Pressure Gauge and Thermocouple Location	A5
Figure 5	Stagnation Tank with End Plate Removed, Showing Screen and Filter Bag Containing Steel Wool	A6
Figure 6	Nozzle I Showing Total Pressure Tube in Test Position	A7
Figure 7	Assembly View and Geometry of Nozzle I	A8
Figure 8	Detail of Nozzle II	A9
Figure 9	Nozzle I; Disassembled, Showing Optical Glass and Metal Pressure Tap Plate Side Walls, and Metal Clamp Bars	A10
Figure 10	Nozzle II; Disassembled, Showing Hinged Upper and Lower Walls, and Pressure Tap Plates 1 and 2	A11
Figure 11	Interferometric Photographs for Test 1 of Density Profiles	A12
Figure 12	Interferometric Photographs for Test 2 of Density Profiles	A13
Figure 13	Graphical Representation of Determination of Fringe Shifts - Test No. 1	A14
Figure 14	Comparison of the Plank Equation of State and Data Upon Which It Was Formulated	A15
Table 2	Carbon Dioxide Enthalpy Tables	A16
Table 3	Interferometric Measurement and Calculation of Density (Test No. 1)	A19
Table 4	Interferometric Measurement and Calculation of Density (Test No. 2)	A20
Figure 15a	Nozzle I Profiles of Measured Pressure Ratio and Isentropically Converted Measured Density Ratio, Test No. 1	A21
Figure 15b	Measured Versus Theoretical Pressure and Density Ratios, Test No. 1	A22
Figure 16a	Nozzle I Profiles of Measured Pressure Ratio and Isentropically Converted Measured Density Ratio, Test No. 2	A23
Figure 16b	Measured Versus Theoretical Pressure and Density Ratios, Test No. 2	A24

Figure 17	Experimental Normal Shock Characteristics of CO ₂	A25
Figure 18	Predicted Normal Shock Characteristics of CO ₂ -- Plank Equation of State	A26
Figure 19	Comparison of Predicted CO ₂ Isentropes	A27
Figure 20	Comparison of Predicted CO ₂ Isentropes	A28
Figure 21	Constant Nucleation Rate Profiles of Classical Nucleation Theory for CO ₂ , $\frac{\sigma}{\sigma_{\infty}} = 1.00$	A29
Figure 22	Experimental Pressure Ratio Profiles. Nozzle I, Pressure Plates 1 & 2	A30
Table 5	Pressure Data for Figure No. 22	A31
Figure 23	Experimental Pressure Ratio Profiles. Nozzle I, Pressure Plates 1 & 2	A32
Table 6	Pressure Data for Figure No. 23	A33
Figure 24	Experimental Pressure Ratio Profiles. Nozzle II, Pressure Plate 1, Angle of Divergence = 2.18°	A34
Table 7	Pressure Data for Figure No. 24	A35
Figure 25	Experimental Pressure Ratio Profiles. Nozzle II, Pressure Plate 2, Angle of Divergence = 2.18°	A36
Table 8	Pressure Data for Figure No. 25	A37
Figure 26	Experimental Pressure Ratio Profiles. Nozzle II, Pressure Plate 2, Angle of Divergence = 2.22°	A38
Table 9	Pressure Data for Figure No. 26	A39
Figure 27	Experimental Pressure Ratio Profiles. Nozzle II, Pressure Plate 2, Angle of Divergence = 2.22°	A40
Table 10	Pressure Data for Figure No. 27	A41
Figure 28	Experimental Pressure Ratio Profiles. Nozzle II, Pressure Plate 2, Angle of Divergence = 2.22°	A42
Table 11	Pressure Data for Figure No. 28	A43
Figure 29	Experimental Pressure Ratio Profiles. Nozzle II, Pressure Plate 2, Angle of Divergence = 0.80°	A44
Table 12	Pressure Data for Figure No. 29	A45
Figure 30	Experimental Pressure Ratio Profiles. Nozzle II, Pressure Plate 2, Angle of Divergence = 0.80°	A46
Table 13	Pressure Data for Figure No. 30	A47
Figure 31	Condensation Data. Local Conditions at Onset of Condensation	A48
Table 14	Experimental Data. Local Conditions at Onset of Condensation	A49
Figure 32	Comparison of Nozzle Geometries and Non-Condensing Pressure Profiles	A50
Figure 33	Spontaneous Freezing Temperature of Supercooled Water Droplets on Platinum and Copper Surfaces	A51

Figure 34	Low Temperature Vapor Pressure Values	A52
Figure 35	Presence of Moisture in a Typical Condensation Profile	A53
Figure 36	Onset of Condensation, Nozzle II, Comparison of Theory and Experiment	A54
Figure 37	Influence Upon Theory of Use of Liquid Versus Solid Droplet Density. Nozzle II(2.20°)	A55
Figure 38	Predicted Influence of Nozzle Geometry on Occurrence of Condensation. Using $\xi, \alpha, \sigma/\sigma_\infty$ of Unity. $\rho_L = 1.18 \text{ gm/cm}^3$	A56
Figure 39	Influence of Mass Accommodation Coefficient on Condensation of CO_2 , (Theoretical)	A57
Figure 40	Influence of Thermal Accommodation on Theoretical Condensation of CO_2	A58
Figure 41	Theoretical Influence of Surface Tension on Condensation of CO_2	A59
Figure 42	Theoretical Occurrence of .1% Moisture for $\alpha = \xi = 1.00$, Corrected Surface Tension $\sigma/\sigma_\infty = 1.38$	A60
Figure 43	Theoretical Occurrence of .1% Moisture for $\alpha = \xi = .01$, Corrected Surface Tension $\sigma/\sigma_\infty = 1.20$	A61
Figure 44	Theoretical Occurrence of .1% Moisture for $\alpha = \xi = 0.0$, Corrected Surface Tension $\sigma/\sigma_\infty = 1.17$	A62
Figure 45	Comparison of Experimental and Theoretical Pressure Profiles for Various ξ and α	A63
Figure 46	Comparison of Empirically Fitted Theoretical Condensation and Experimental Data - Nozzle I. $\alpha = 1.0, \xi = .00008, \sigma/\sigma_\infty = 1.18$	A64
Figure 47	Comparison of Empirically Fitted Theoretical Condensation and Experimental Data, Nozzle II (2.20°) Pressure Tap Plate No. 1. $\alpha = 1.00, \sigma/\sigma_\infty = 1.18, \xi = .00008$	A65
Figure 48	Comparison of Empirically Fitted Theoretical Condensation and Experimental Data - Nozzle II (2.20°) $\alpha = 1.0, \xi = .00008, \sigma/\sigma_\infty = 1.18$	A66
Figure 49	Comparison of Empirically Fitted Theoretical Condensation and Experimental Data - Nozzle II (0.80°) $\alpha = 1.0 \xi = .00008, \sigma/\sigma_\infty = 1.18$	A67
Figure 50	Theoretical Influence of Contamination on Condensation of CO_2	A68
Figure 51	Theoretical Influence of Macroscopic Contamination on Condensation of CO_2 , Using Theory Empirically Fitted to Homogeneous Condensation Data	A69
Figure 52	Theoretical Influence of Microscopic Contamination on Condensation of CO_2 , Using Theory Empirically Fitted to Homogeneous Condensation Data. $\xi = .00008, \sigma/\sigma_\infty = 1.18, \rho_L = 1.18 \text{ GM./CM}$	A70

Figure 53	Theoretical Effect of CO ₂ Contamination on Nitrogen Condensation. Supersaturation at .1% Moisture	A71
Table 15	Values of γ_a , γ_b and z Used to Match Real Gas Isentropes	A72

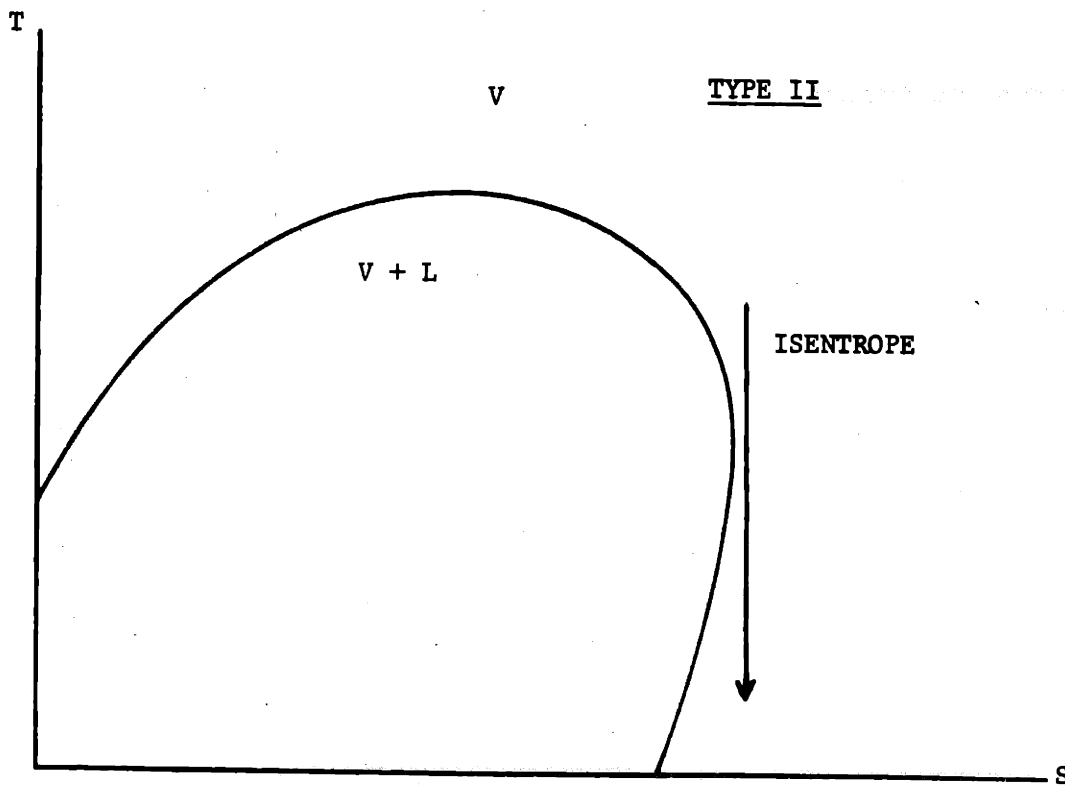
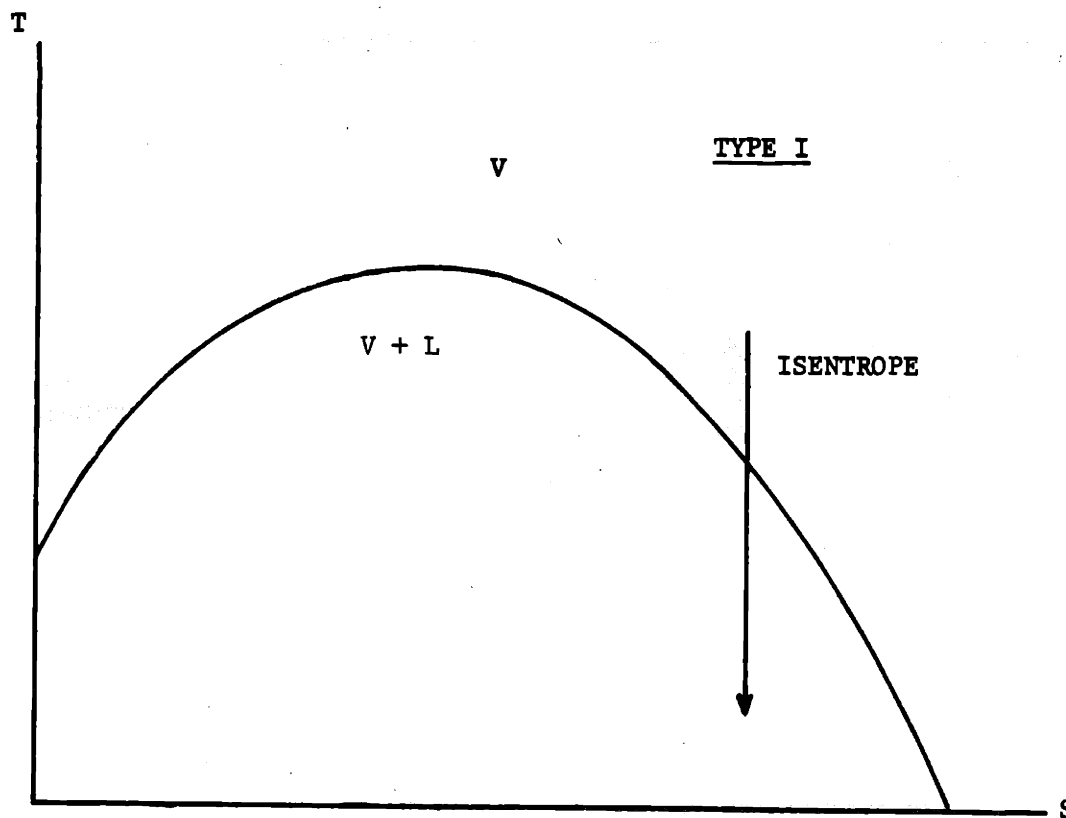


FIGURE 1, TYPICAL CO-EXISTENCE LINES VERSUS ISENTROPIC EXPANSION PATHS.

TABLE 1
TYPICAL VALUES OF h_{fg}/C_p FOR VARIOUS GASES

<u>FLUID</u>	(h_{fg}) Lat. Heat of Vap. <u>BTU/lbm</u>	C_p Specific Heat <u>BTU/lbm-°F</u>	h_{fg}/C_p	<u>T_s @ 1 atm</u>
C_2H_6O (Ethyl Al.)	406	.342 ✕	1.19×10^3	173 °F
CH_4O (Methyl Al.)	482	.295 ✕	1.63×10^3	152 °F
H_2O	840	.445 ✕	1.89×10^3	212 °F
C_6H_6 (Benzene)	172	.280 °F	6.15×10^2	175.3 °F
$CHCl_2F$ (Genetran 21)	140.15	.140 °F	1.01×10^3	48 °F
NH_3 (Ammonia)	589.4	.523 °F	1.12×10^3	- 28 °F
BCl_3 (Boron Chloride)	68.8	.127 °F	5.4×10^2	54.5 °F
Butene-1	168	.382 °F	4.4×10^2	20.7 °F
Butene-2	179	.375 °F	4.78×10^2	38.7 °F
CO_2	247	.198 °F	1.24×10^3	-109.3 °F
Freon-22	100	.152 °F	6.6×10^2	- 41 °F
Difluoroethylene	276	.224 °F	1.23×10^3	-117 °F
Dimethylamine	252	.374 °F	6.74×10^2	44.4 °F
Ethyl Chloride	164	.244 °F	6.74×10^2	54.3 °F
Ethylene Oxide	250	.268 °F	9.31×10^2	51.3 °F
Isobutane	158	.355 °F	4.46×10^2	10.9 °F
Methyl Acetylene	234	.357 °F	6.55×10^2	- 9.6 °F
Monethylamine	260	.330 °F	7.87×10^2	61.8 °F
Monmethylamine	358	.320 °F	1.12×10^3	20.6 °F
SO_2	171	.117 °F	1.45×10^3	14 °F
Freon-11	78.3	.135 °F	5.8×10^2	74.8 °F

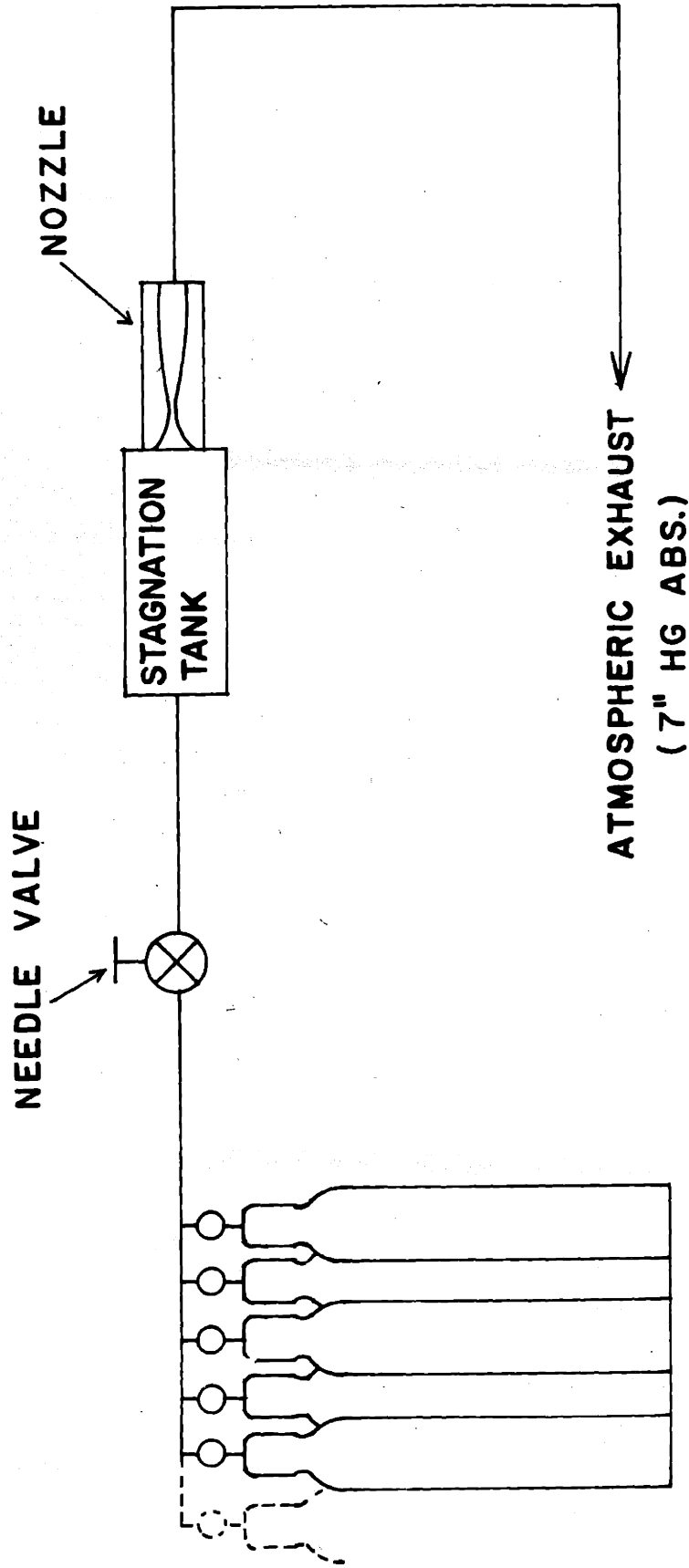


FIG 2 SCHEMATIC ARRANGEMENT OF TEST APPARATUS

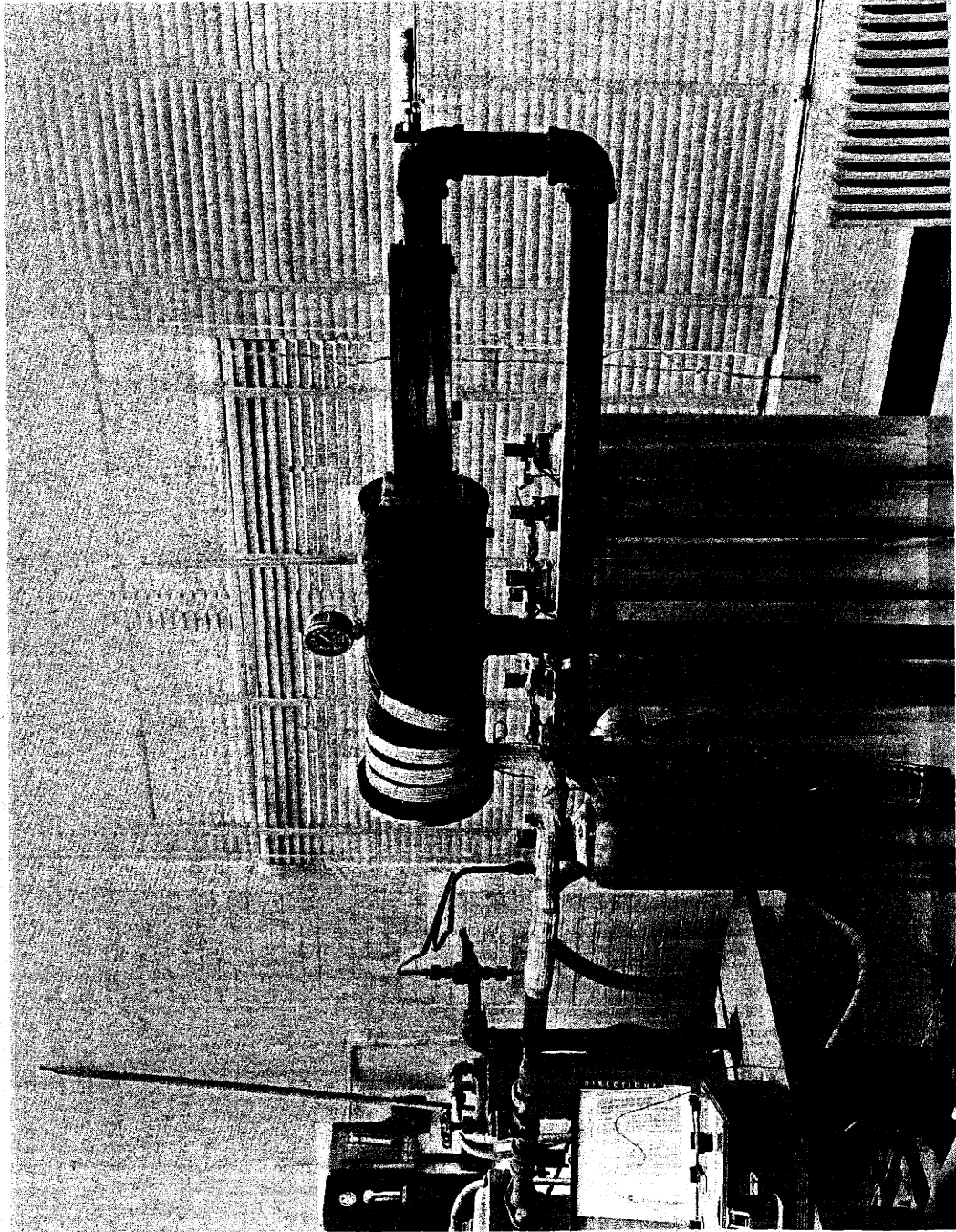


FIGURE 3, GENERAL VIEW OF TEST APPARATUS

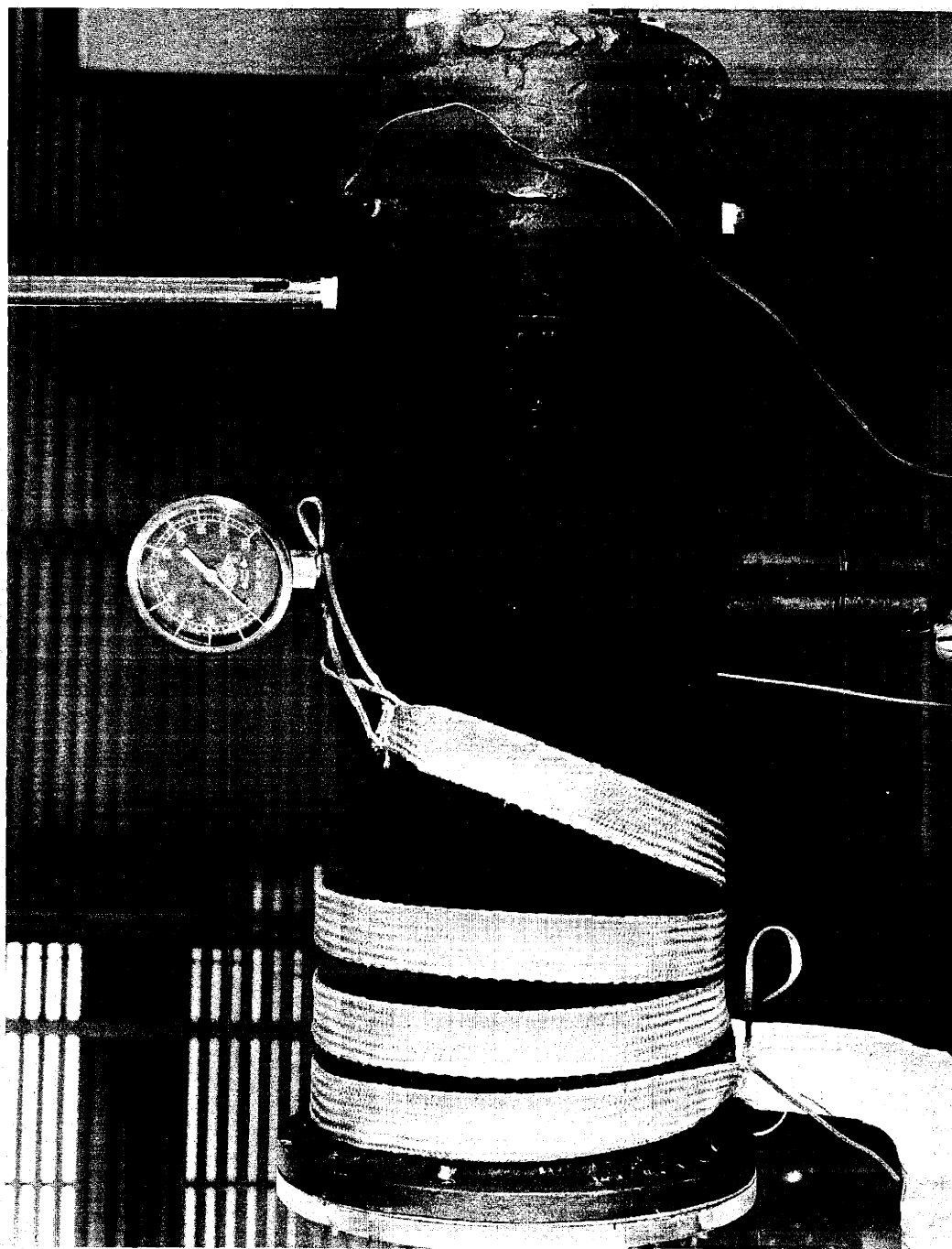


FIGURE 4, STAGNATION TANK, PRESSURE GAUGE AND THERMOCOUPLE LOCATION.

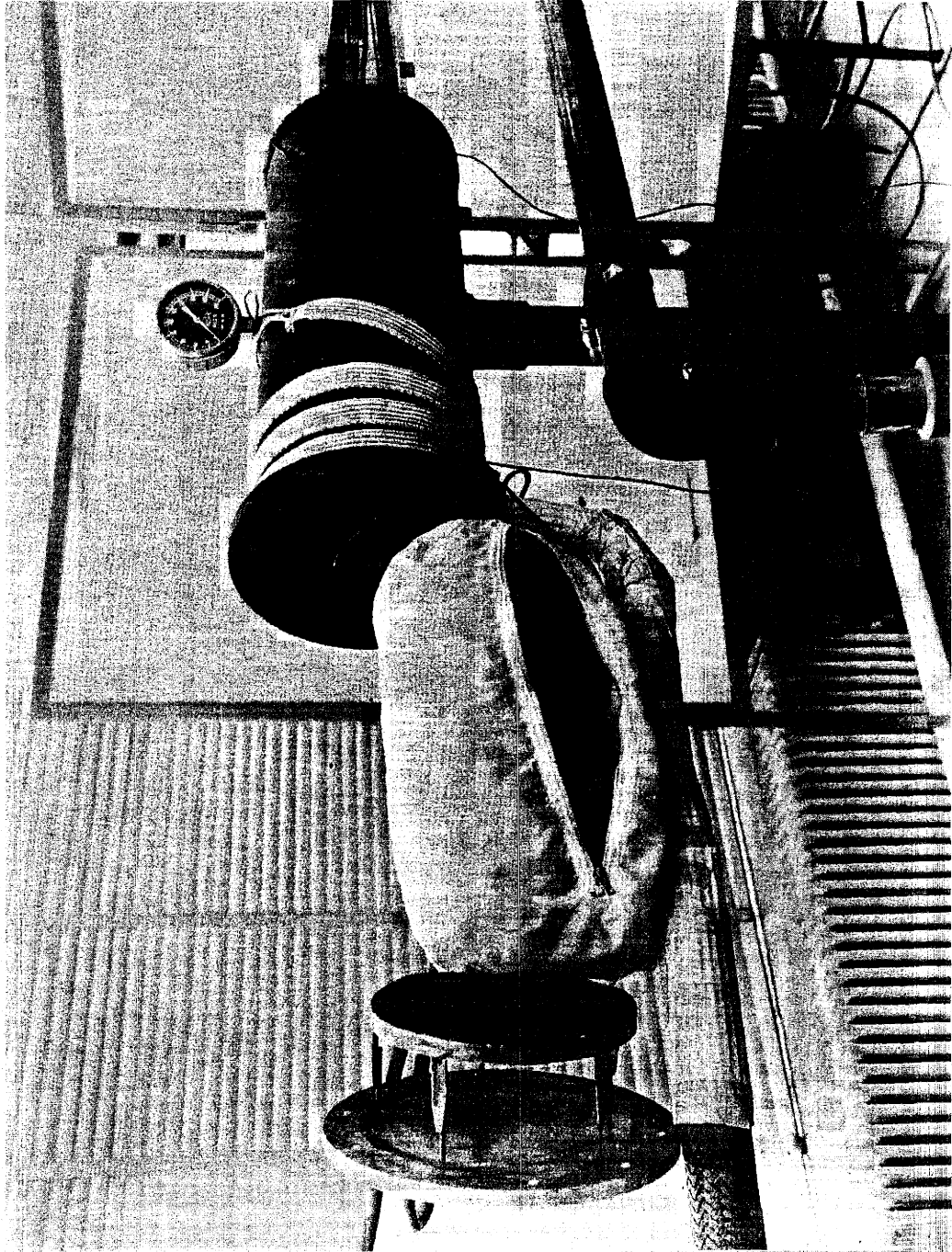


FIGURE 5, STAGNATION TANK WITH END PLATE REMOVED, SHOWING SCREEN AND FILTER BAG CONTAINING STEEL WOOL.

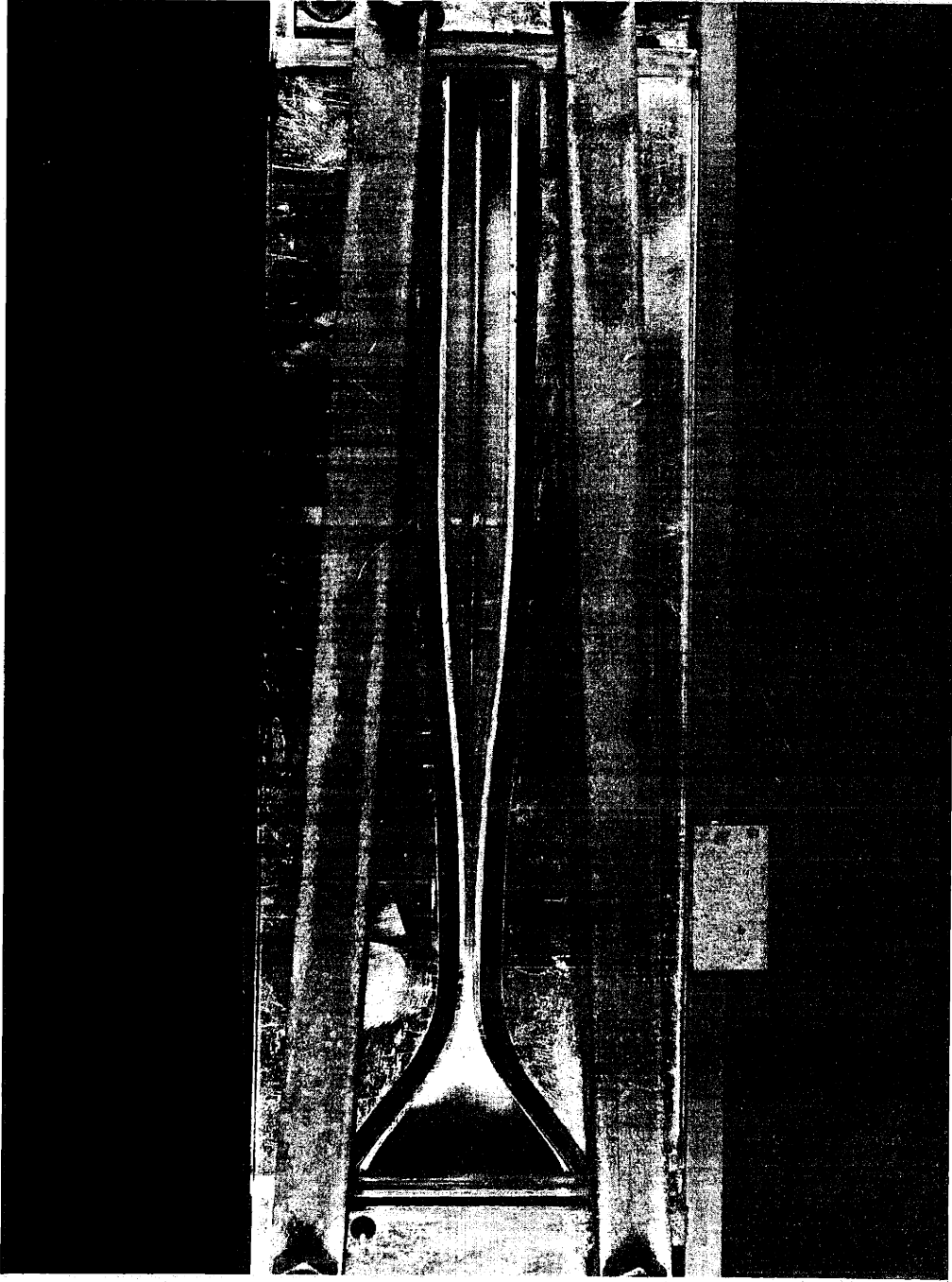
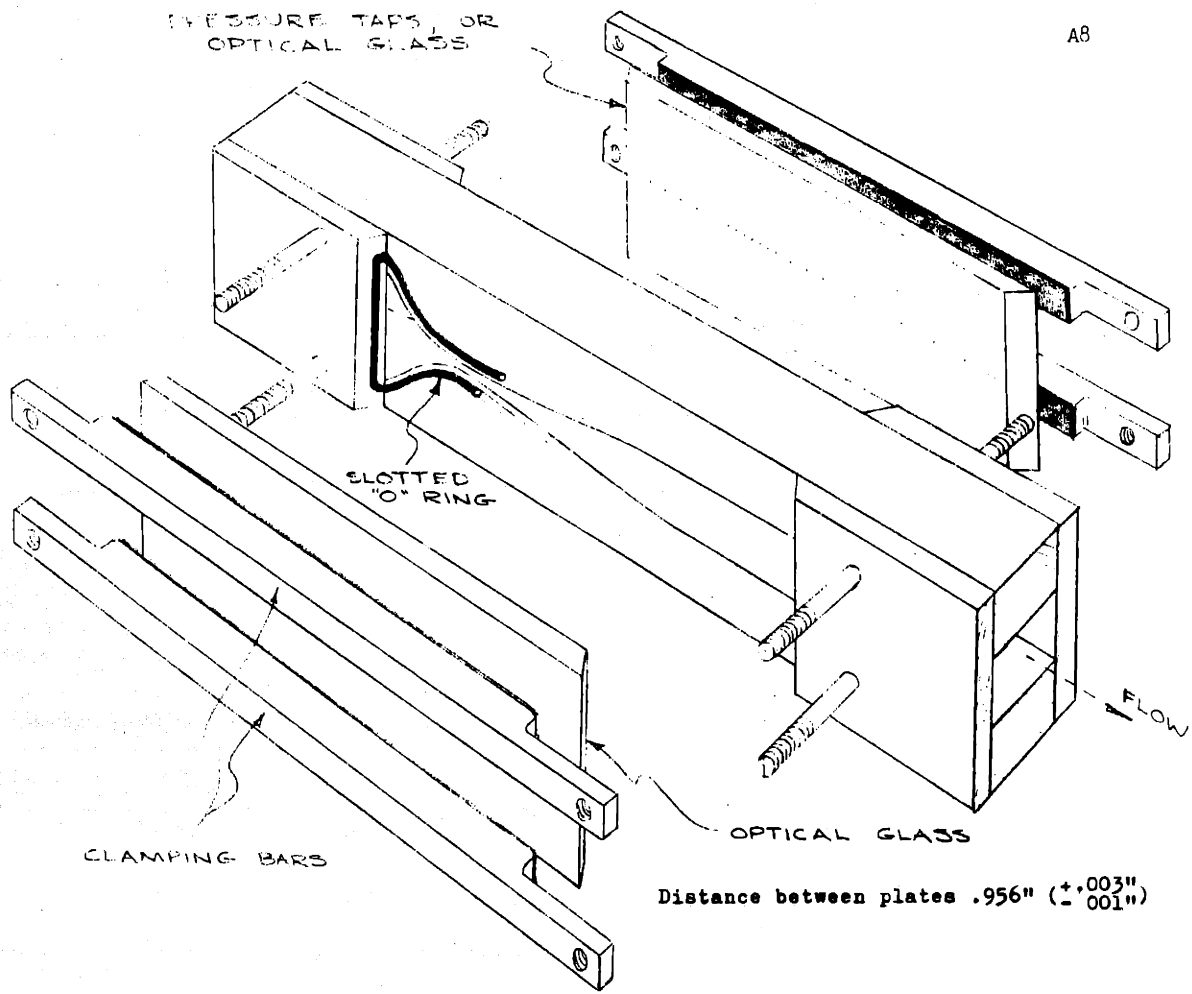


FIGURE 6, NOZZLE I SHOWING TOTAL PRESSURE TUBE IN TEST POSITION.



$x(\pm .005)$	b	x	b	x	b	x	b	x	b
0	1.0	1.11	.101	1.325	.055	2.07	.074	3.11	.225
.63	.550	1.15	.090	1.350	.054	2.15	.078	3.23	.250
.84	.300	1.165	.086	1.400 \pm .015	.0531 \pm .0001	2.21	.086	3.51	.300
.89	.250	1.190	.078	1.500	.054	2.27	.090	3.86	.358
.92	.225	1.200	.074	1.570	.055	2.38	.101	4.27	.404
.95	.200	1.220	.069	1.620	.056	2.46	.110	4.67	.428
.97	.175	1.235	.066	1.670	.057	2.52	.120	5.20	.432
1.01	.150	1.250	.063	1.735	.060	2.63	.135	on	"
1.04	.135	1.270	.060	1.820	.063	2.71	.150		
1.07	.120	1.290	.057	1.920	.066	2.84	.175		
1.09	.110	1.305	.056	1.990	.069	2.98	.200		

FIGURE 7, ASSEMBLY VIEW AND GEOMETRY OF NOZZLE I.

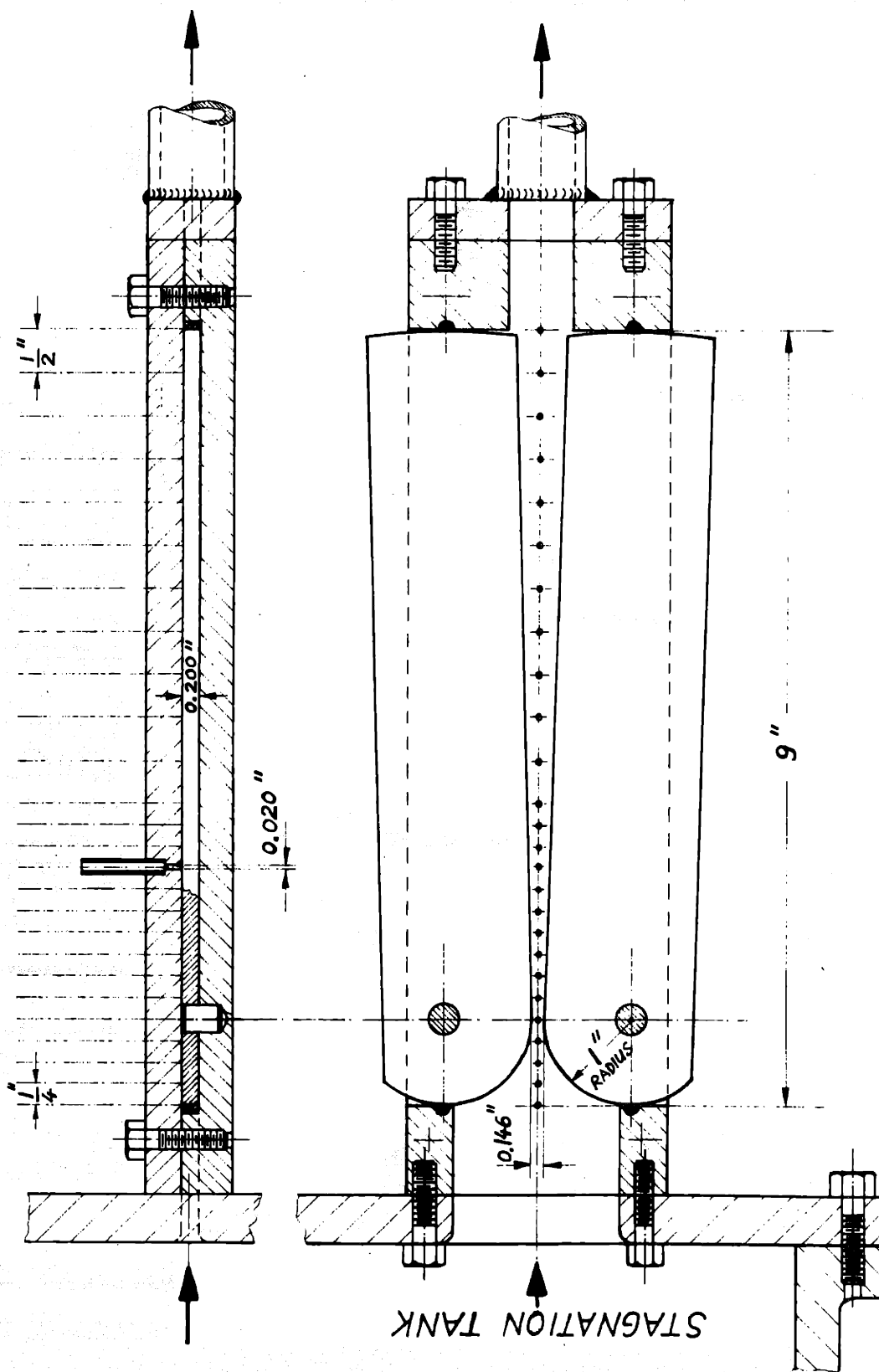


FIGURE 8, DETAIL OF NOZZLE II

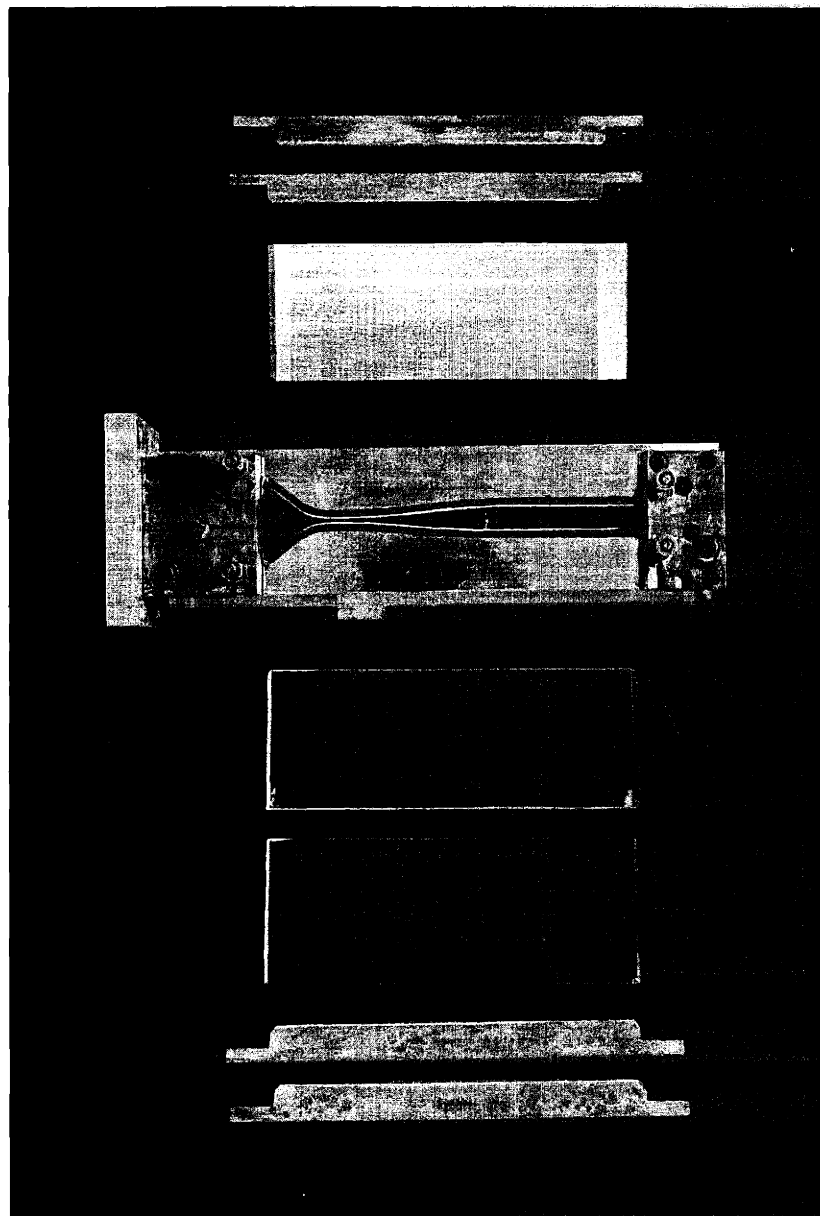


FIGURE 9, NOZZLE I; DISASSEMBLED, SHOWING OPTICAL GLASS AND METAL PRESSURE TAP PLATE SIDE WALLS, AND METAL CLAMP BARS.

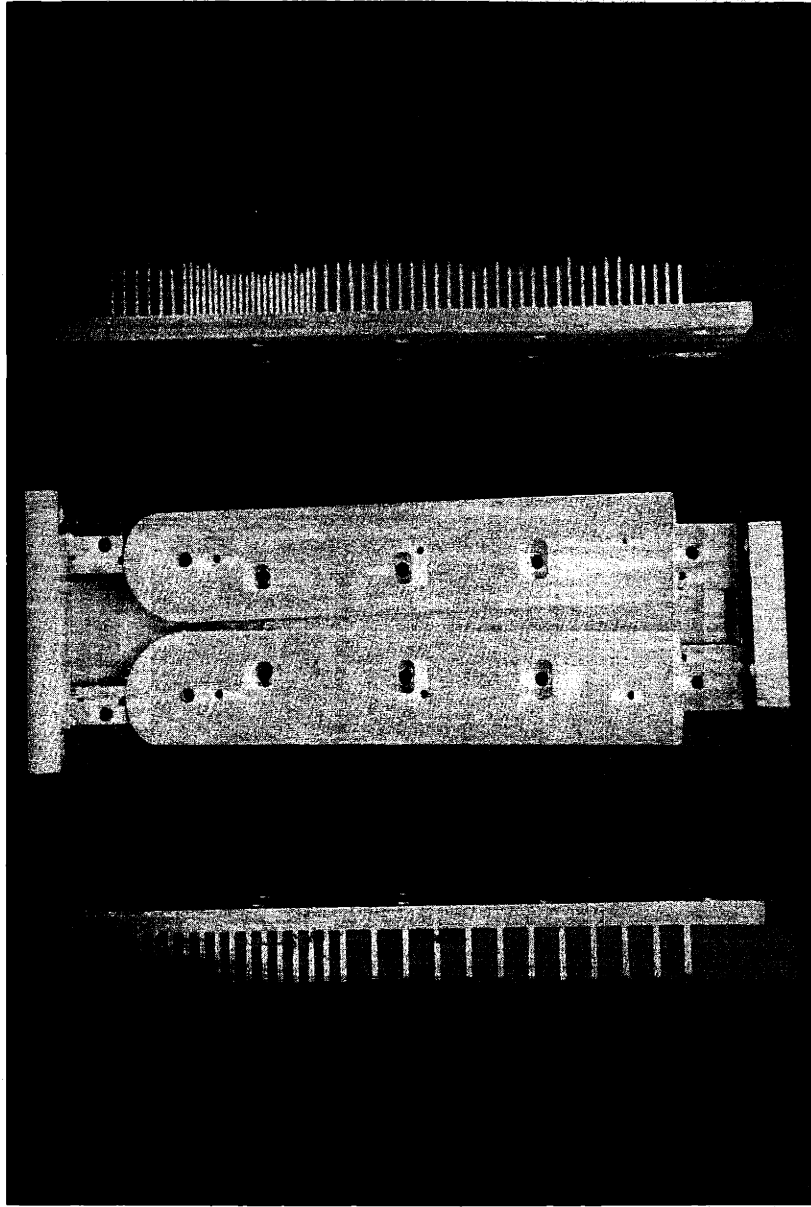
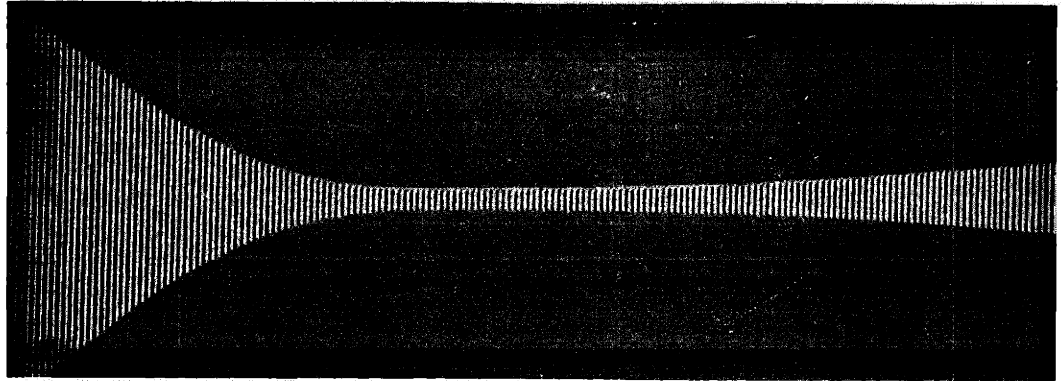
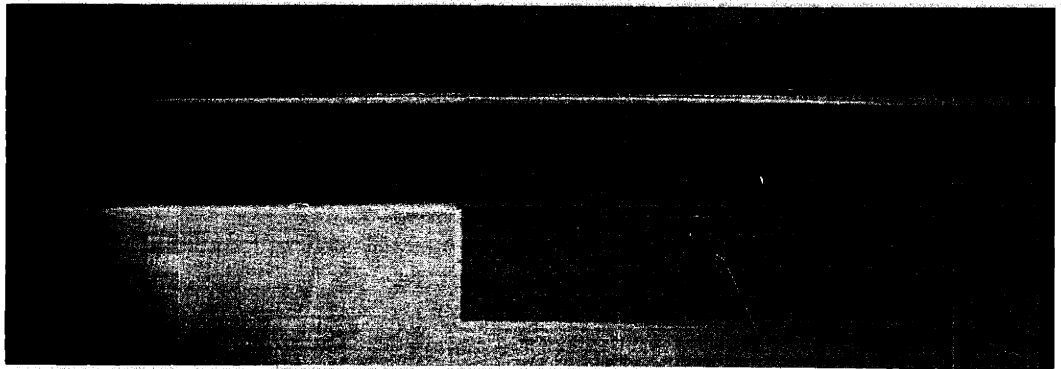


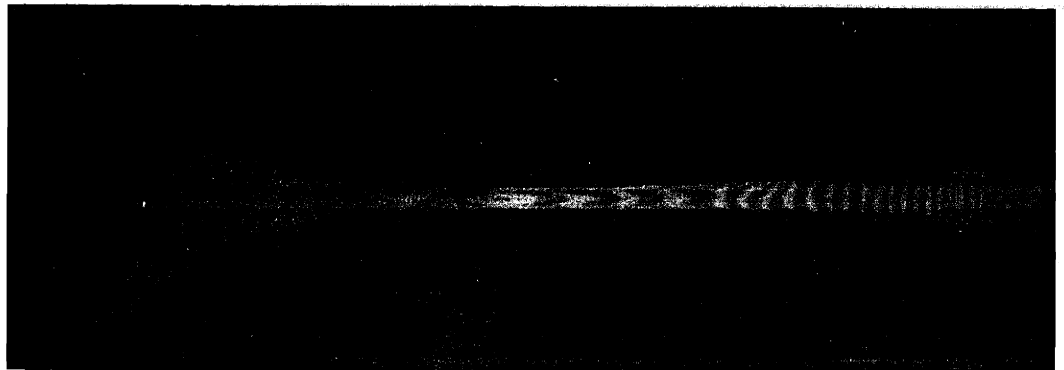
FIGURE 10, NOZZLE II; DISASSEMBLED, SHOWING HINGED UPPER AND LOWER WALLS, AND PRESSURE TAP PLATES 1 AND 2.



(A) NO FLOW

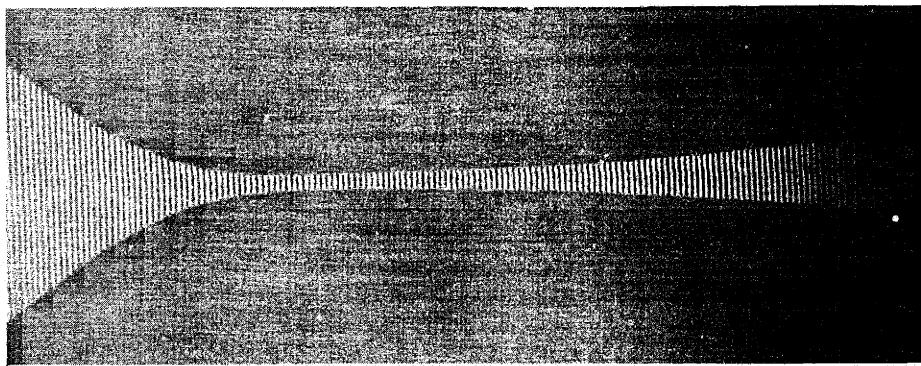


(B) SCALING PLATE (1.00")

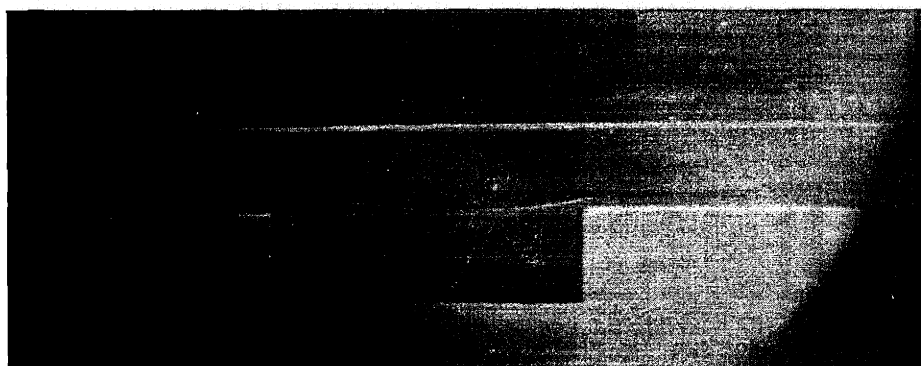


(C) FLOW, SHOWING SHIFT IN INTERFERENCE BANDS

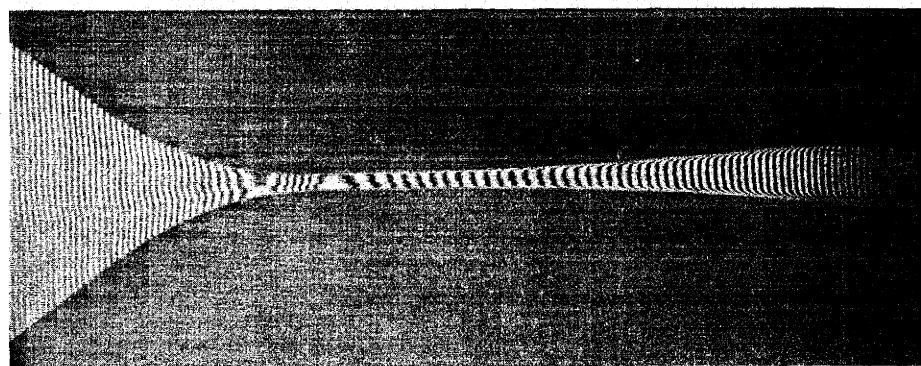
FIGURE 11, INTERFEROMETRIC PHOTOGRAPHS FOR TEST 1 OF DENSITY PROFILES.



(A) NO FLOW



(B) SCALING PLATE (1.00")



(C) FLOW, SHOWING SHIFT IN INTERFERENCE BANDS

FIGURE 12, INTERFEROMETRIC PHOTOGRAPHS FOR TEST 2 OF DENSITY PROFILES.

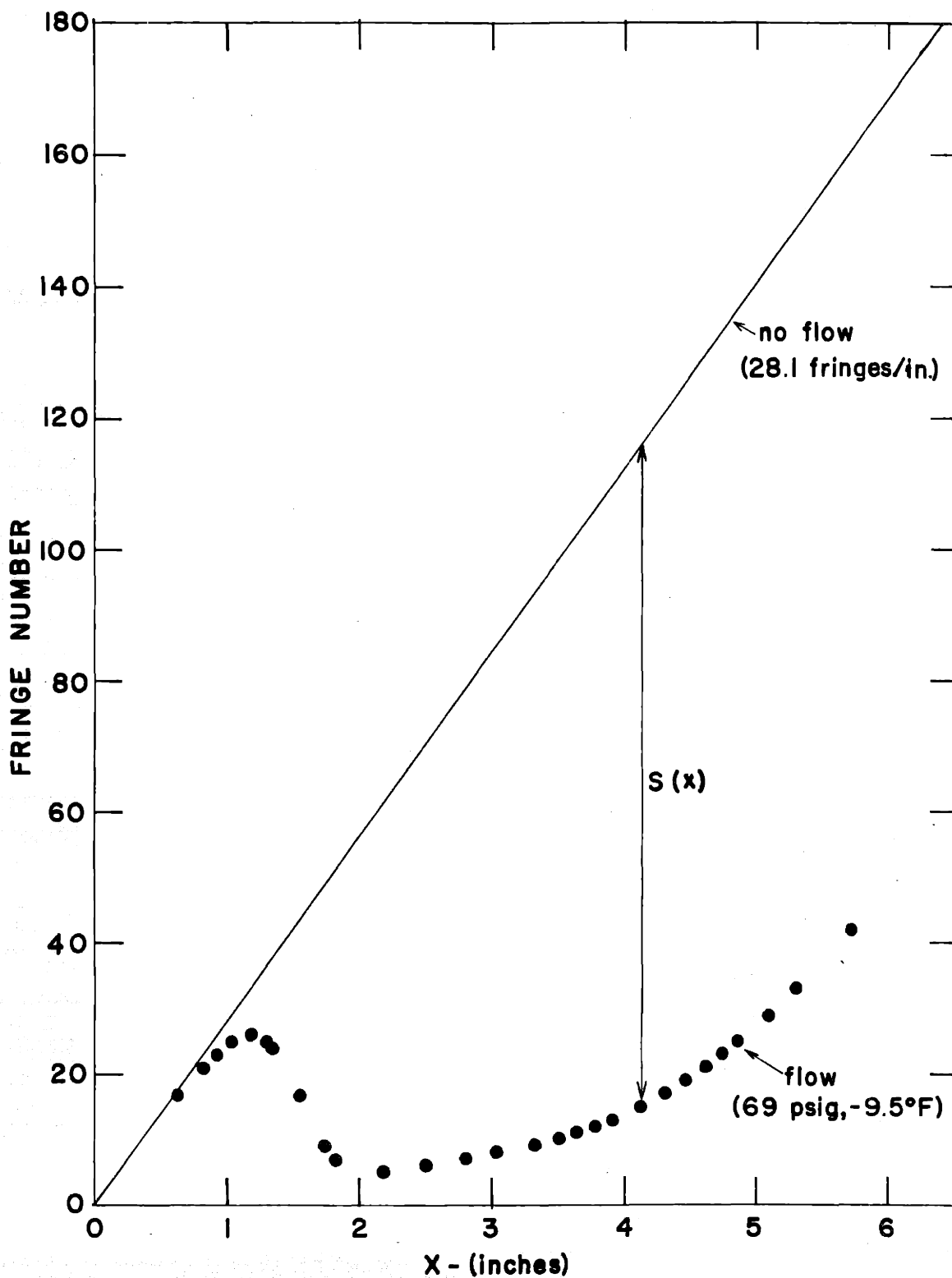


FIG 13 GRAPHICAL REPRESENTATION OF DETERMINATION OF FRINGE SHIFTS - TEST NO 1

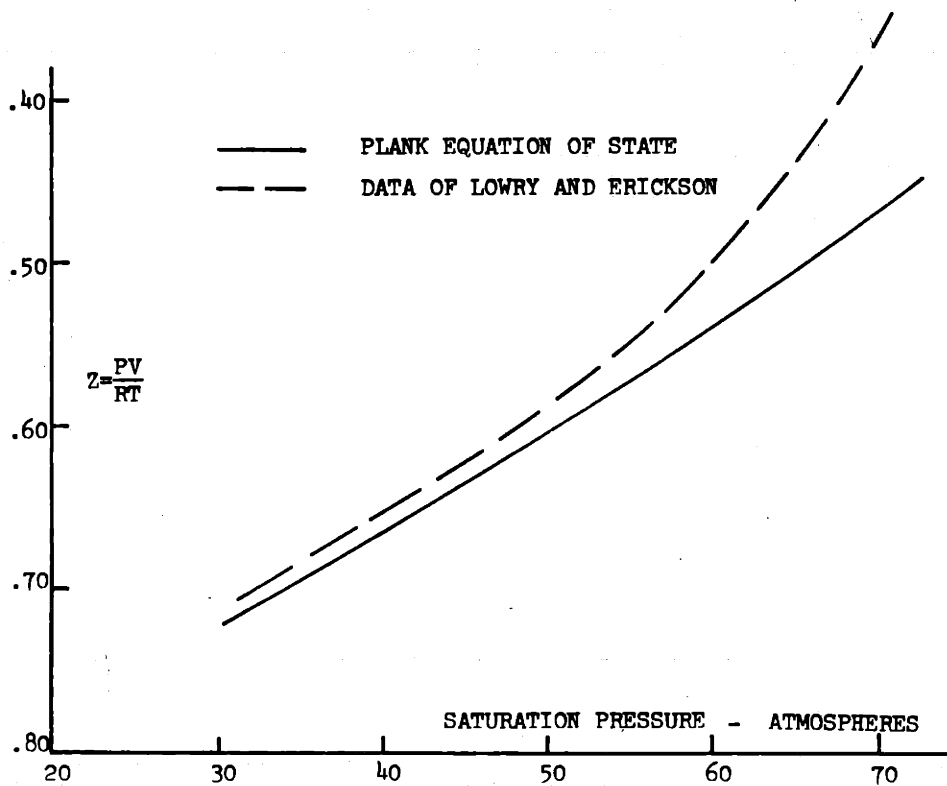
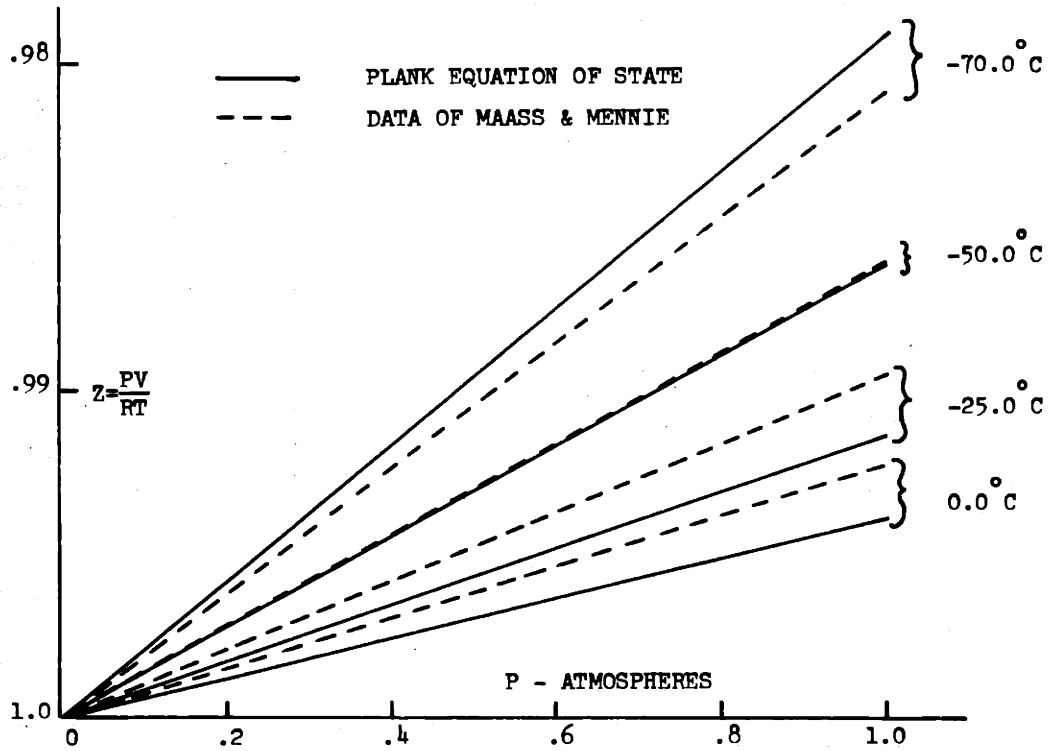


FIGURE 14, COMPARISON OF THE PLANK EQUATION OF STATE AND DATA UPON WHICH IT WAS FORMULATED

TABLE 2

CARBON DIOXIDE ENTHALPY TABLESEnthalpy in cal/gm, p in atm, T in deg K

p	T = <u>100.0</u>	<u>110</u>	<u>120</u>	<u>130</u>	<u>140</u>	<u>150</u>
.5	154.03	156.83	159.19	161.35	163.36	165.29
1.0	149.60	153.61	156.78	159.50	161.92	164.14
1.5	145.10	150.33	154.33	157.63	160.45	162.98
2.0	140.54	147.01	151.84	155.72	158.97	161.79
2.5	135.91	143.64	149.64	153.79	157.46	160.60
3.0	131.21	140.22	146.77	151.83	155.93	159.38
3.5	126.45	136.76	144.17	149.85	154.38	158.15
4.0	121.62	133.24	141.54	147.83	152.80	156.90
4.5	116.73	129.68	138.88	145.79	151.21	155.63
5.0	111.77	126.07	136.17	143.72	149.59	154.34
5.5	106.74	122.41	133.43	141.63	147.95	153.04
6.0	101.64	118.70	130.66	139.50	146.29	151.72
6.5	96.48	114.94	127.85	137.35	144.61	150.39
7.0	91.26	111.14	125.00	135.17	142.91	149.04
7.5	85.96	107.29	122.12	132.96	141.19	147.67
8.0	80.60	103.39	119.20	130.73	139.44	146.28
8.5	75.18	99.44	116.25	128.46	137.67	144.87
9.0	69.68	95.44	113.25	126.17	135.88	143.45
9.5	64.13	91.39	110.23	123.85	134.07	142.01
10.0	58.50	87.30	107.16	121.51	132.24	140.56
10.5	52.81	83.16	104.06	119.13	130.38	139.08
11.0	47.05	78.97	100.93	116.73	128.51	137.59
11.5	41.23	74.73	97.76	114.30	126.61	136.08
12.0	35.34	70.44	94.55	111.85	124.69	134.56
12.5	29.38	66.10	91.30	109.36	122.75	133.02

p	T = <u>160</u>	<u>170</u>	<u>180</u>	<u>190</u>	<u>200</u>	<u>210</u>
.5	167.16	168.99	170.81	172.63	174.44	176.28
1.0	166.23	168.23	170.19	172.10	174.01	175.90
1.5	165.29	167.47	169.55	171.57	173.56	175.52
2.0	164.34	166.69	168.91	171.04	173.11	175.14
2.5	163.37	165.90	168.26	170.49	172.65	174.75
3.0	162.39	165.10	167.59	169.94	172.18	174.35
3.5	161.40	164.29	166.92	169.38	171.71	173.95
4.0	160.39	163.46	166.24	168.81	171.23	173.54
4.5	159.37	162.63	165.55	168.23	170.74	173.13
5.0	158.33	161.78	164.85	167.65	170.25	172.71
5.5	157.28	160.92	164.14	167.06	169.75	172.29
6.0	156.22	160.05	163.42	166.46	169.25	171.86
6.5	155.14	159.17	162.70	165.85	168.73	171.42
7.0	154.05	158.28	161.96	165.23	168.22	170.98
7.5	152.94	157.38	161.21	164.61	167.69	170.54
8.0	151.83	156.47	160.46	163.98	167.16	170.08
8.5	150.69	155.54	159.69	163.34	166.62	169.63
9.0	149.55	154.60	158.92	162.69	166.07	169.16
9.5	148.39	152.65	158.13	162.04	165.52	168.69
10.0	147.21	152.70	157.34	161.38	164.96	168.22

<u>p</u>	<u>160</u>	<u>170</u>	<u>180</u>	<u>190</u>	<u>200</u>	<u>210</u>
10.5	146.02	151.72	156.54	160.71	164.40	167.74
11.0	144.82	150.74	155.73	160.03	163.83	167.25
11.5	143.61	149.75	154.91	159.34	163.25	166.76
12.0	142.38	148.74	154.08	158.65	162.67	166.27
12.5	141.13	147.73	153.24	157.95	162.07	165.76

<u>p</u>	<u>T = 220</u>	<u>230</u>	<u>240</u>	<u>250</u>	<u>260</u>	<u>270</u>
.5	178.12	179.99	181.87	183.77	185.70	187.65
1.0	177.80	179.71	181.63	183.56	185.51	187.48
1.5	177.48	179.43	181.38	183.35	185.33	187.32
2.0	177.15	179.15	181.14	183.13	185.14	187.15
2.5	176.81	178.86	180.89	182.92	184.95	186.98
3.0	176.48	178.56	180.63	182.69	184.75	186.81
3.5	176.13	178.27	180.38	182.47	184.56	186.64
4.0	175.78	177.97	180.12	182.24	184.36	186.46
4.5	175.43	177.66	179.85	182.01	184.15	186.28
5.0	175.07	177.35	179.58	181.78	183.95	186.10
5.5	174.71	177.04	179.31	181.54	183.74	185.92
6.0	174.34	176.72	179.04	181.30	183.53	185.73
6.5	173.97	176.40	178.76	181.06	183.31	185.55
7.0	173.59	176.08	178.47	180.81	183.10	185.35
7.5	173.21	175.75	178.19	180.56	182.88	185.16
8.0	172.82	175.41	177.90	180.31	182.66	184.97
8.5	172.43	175.07	177.61	180.05	182.43	184.77
9.0	172.03	174.73	177.31	179.79	182.21	184.57
9.5	171.63	174.39	177.01	179.53	181.98	184.36
10.0	171.22	174.04	176.70	179.26	181.74	184.16
10.5	170.81	173.68	176.40	179.00	181.51	183.95
11.0	170.40	173.32	176.09	178.72	181.27	193.74
11.5	169.98	172.96	175.77	178.45	181.03	183.53
12.0	169.55	172.59	175.45	178.17	180.78	183.31
12.5	169.12	172.22	175.13	177.89	180.54	183.10

<u>p</u>	<u>T = 280</u>	<u>290</u>	<u>300</u>	<u>310</u>	<u>320</u>	<u>330</u>
.5	189.62	191.60	193.63	195.67	197.70	199.82
1.0	189.47	191.47	193.51	195.57	197.61	199.74
1.5	189.33	191.34	193.40	195.46	197.52	199.65
2.0	189.18	191.21	193.28	195.36	197.42	199.57
2.5	189.03	191.08	193.16	195.25	197.33	199.48
3.0	188.88	190.94	193.04	195.14	197.23	199.39
3.5	188.73	190.81	192.92	195.03	197.13	199.30
4.0	188.57	190.67	192.80	194.92	197.03	199.21
4.5	188.41	190.53	192.67	194.81	196.93	199.12
5.0	188.25	190.38	192.54	194.70	196.83	199.03
5.5	188.09	190.24	192.41	194.58	196.72	198.94
6.0	187.92	190.09	192.28	194.46	196.62	198.84
6.5	187.76	189.94	192.15	194.34	196.51	198.74
7.0	187.59	189.79	192.02	194.22	196.40	198.65
7.5	187.42	189.64	191.88	194.10	196.29	198.55
8.0	187.24	189.49	191.74	193.98	196.18	198.45
8.5	187.07	189.33	191.60	193.85	196.07	198.35
9.0	186.89	189.17	191.46	193.73	195.96	198.24
9.5	186.71	189.01	191.32	193.60	195.84	198.14

<u>p</u>	<u>280</u>	<u>290</u>	<u>300</u>	<u>310</u>	<u>320</u>	<u>330</u>
10.0	186.53	188.85	191.17	193.47	195.72	198.03
10.5	186.34	188.69	191.03	193.34	195.61	197.93
11.0	186.16	188.52	190.88	193.21	195.49	197.82
11.5	185.97	188.35	190.73	193.07	195.37	197.71
12.0	185.78	188.19	190.58	192.94	195.25	197.60
12.5	185.59	188.01	190.43	192.80	195.12	197.49

TABLE 3
INTERFEROMETRIC MEASUREMENT AND CALCULATION OF DENSITY

Test No. 1

$$T_0 = -9.5^\circ\text{F}$$

$$P_0 = 83.7 \text{ psia}$$

No Flow: Average 28.1 fringes/inch

$$\frac{\lambda}{l} = \frac{5461 \times 10^{-8}}{(.956)(2.54)} = 2248 \times 10^{-8}$$

Photograph Scale: 2.35 in./in.

$$\rho_0 = \frac{P}{zRT} = .806 \text{ lbm/ft}^3$$

$$G\rho_0 = N_0 - 1 = (.3673 \times 10^{-2})(.806) = 296.0 \times 10^{-5}$$

<u>Fringe Number</u>	<u>x_{photo}</u>	<u>S(x)</u>	<u>$\frac{S\lambda}{l} \times 10^5$</u>	<u>$(n_0 - 1) - S \lambda / l$</u>	<u>ρ / ρ_0</u>	<u>x_{nozzle}</u>
0	0	0	0			
1	.035					
9	.335	0	0			
17	.630	.46	1.035	294.96	.997	.268
21	.810	1.45	3.26	292.74	.990	.345
23	.920	2.50	5.62	290.38	.982	.392
25	1.040	3.82	8.59	287.41	.971	.442
26	1.180	6.8	15.3	280.7	.949	.502
25	1.300	11.1	25.0	271.0	.916	.552
24	1.350	13.5	30.4	265.6	.897	.574
17	1.550	26.2	58.9	237.1	.801	.659
9	1.730	39.2	88.2	207.8	.702	.735
7	1.820	43.8	98.6	197.5	.668	.774
5	2.180	56.0	126.0	170.0	.575	.918
6	2.510	64.4	145.0	151.0	.510	1.067
7	2.805	71.8	161.8	134.2	.454	1.192
8	3.030	77.1	173.6	122.4	.414	1.289
9	3.315	84.1	189.3	106.7	.360	1.410
10	3.510	88.6	199.5	96.5	.326	1.492
11	3.630	91.0	204.8	91.2	.308	1.545
12	3.765	94.0	211.5	84.5	.2855	1.602
13	3.900	96.7	217.7	78.3	.2645	1.660
15	4.120	101.0	226.3	69.7	.2355	1.753
17	4.310	104.2	234.6	61.4	.2072	1.833
19	4.460	106.5	239.8	57.2	.1933	1.899
21	4.610	108.7	244.5	51.5	.1740	1.960
23	4.740	110.4	248.6	47.4	.1601	2.018
25	4.860	111.7	251.3	44.7	.1510	2.067
29	5.09	114.2	257.2	38.8	.1311	2.165
33	5.30	116.1	261.5	34.5	.1165	2.253
42	5.72	119.0	267.8	28.2	.0953	2.453

TABLE 4
INTERFEROMETRIC MEASUREMENT AND CALCULATION OF DENSITY

A20

Test No. 2

$$T_o = 117.0^\circ\text{F}$$

$$P_o = 58.7 \text{ psia}$$

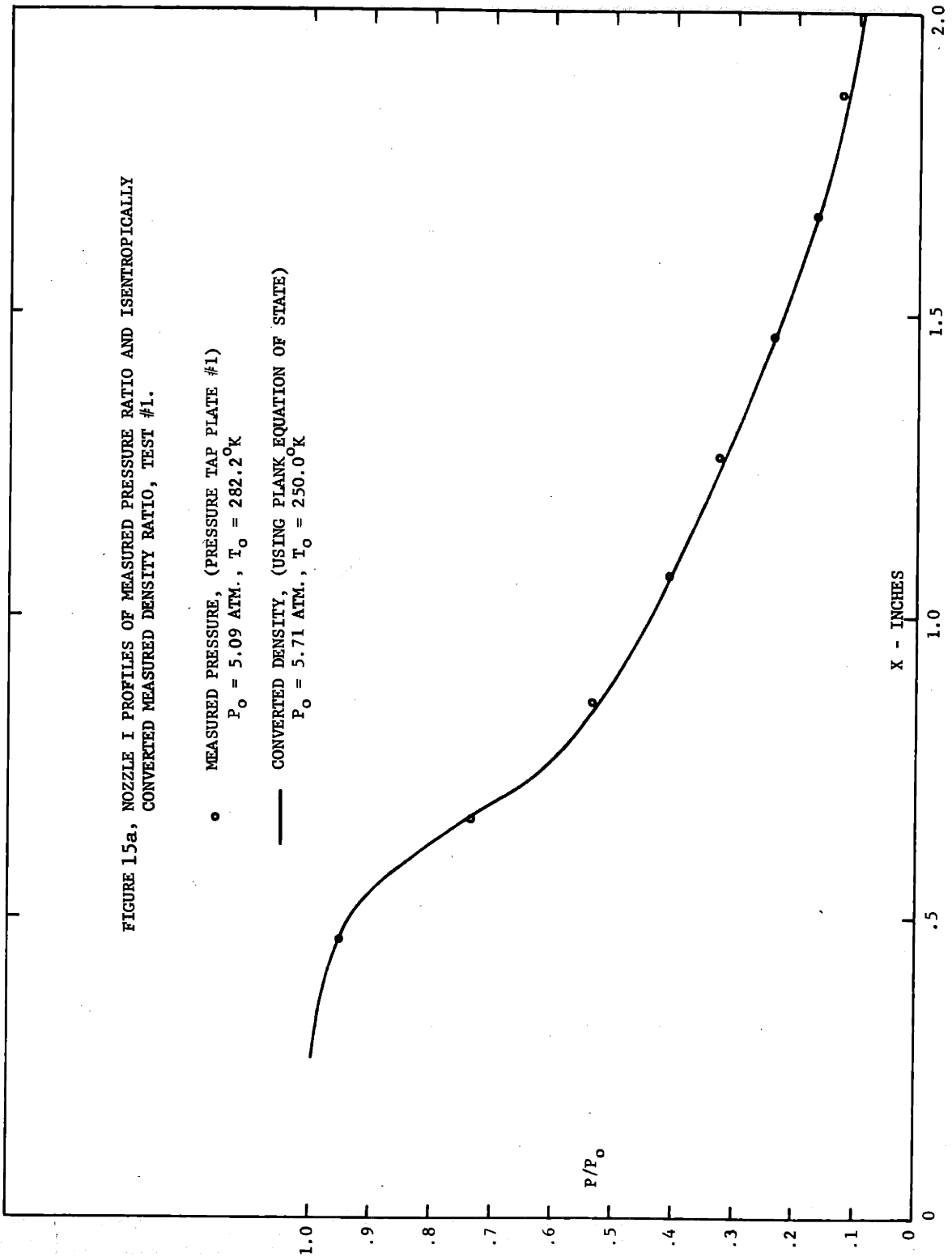
$$\rho_o = \frac{P}{zRT} = .4235 \text{ lbm/ft}^3$$

$$\frac{\lambda}{l} = \frac{5461 \times 10^{-8}}{2.54(.970)} = 2.215 \times 10^{-5}$$

$$Gp_o = N_o - 1 = (.3673 \times 10^{-2})(.4235) = 155.6 \times 10^{-5}$$

f (flow)	x _{photo}	f (no flow)	S	$\frac{S\lambda}{l} \times 10^5$	$Gp_o - S\lambda/l$	ρ/ρ_o	x _{nozzle}
0	0	0	0	0	155.6	1.000	0
8	.295	8.5	.5	1.10	154.5	.994	.160
12	.455	13.1	1.1	2.4	153.2	.986	.248
14	.545	15.7	1.7	3.8	151.8	.975	.297
16	.650	18.7	2.7	6.0	149.6	.961	.354
17	.715	20.6	3.6	8.0	147.6	.949	.389
18	.850	24.4	6.4	14.2	141.4	.910	.462
17	.945	27.2	10.2	22.6	133.0	.855	.514
16	1.000	28.8	12.8	28.4	127.2	.819	.545
14	1.085	31.3	17.3	38.4	117.2	.754	.590
13	1.135	32.8	19.8	43.9	111.7	.718	.617
12	1.195	34.7	22.7	50.3	105.3	.677	.650
12	1.380	39.8	27.8	61.6	94.0	.604	.751
13	1.520	44.3	31.3	69.4	86.2	.555	.827
14	1.625	47.5	33.5	74.3	81.3	.523	.883
16	1.795	52.6	36.6	81.1	74.5	.479	.975
18	1.945	57.0	39.0	86.4	69.2	.445	1.057
20	2.110	61.9	41.9	92.9	62.7	.403	1.147
22	2.260	66.4	44.4	98.5	57.1	.367	1.228
24	2.420	71.1	47.1	104.5	51.1	.329	1.315
26	2.580	75.9	49.9	110.7	44.9	.289	1.402
28	2.725	80.1	52.1	115.5	40.1	.258	1.482
30	2.860	84.1	54.1	120.0	35.6	.229	1.555
32	2.980	87.8	55.8	123.6	32.0	.206	1.620
34	3.100	91.1	57.1	126.6	29.0	.186	1.685
36	3.210	94.4	58.4	129.3	26.3	.169	1.745
40	3.415	100.4	60.4	133.8	21.8	.141	1.857
44	3.600	105.8	61.8	137.0	18.6	.120	1.958
48	3.785	111.3	63.3	140.3	15.3	.099	2.060
52	3.950	116.0	64.0	141.8	13.8	.089	2.148
60	4.245	124.6	64.6	143.2	12.4	.080	2.308

FIGURE 15a, NOZZLE I PROFILES OF MEASURED PRESSURE RATIO AND ISENTROPICALLY CONVERTED MEASURED DENSITY RATIO, TEST #1.



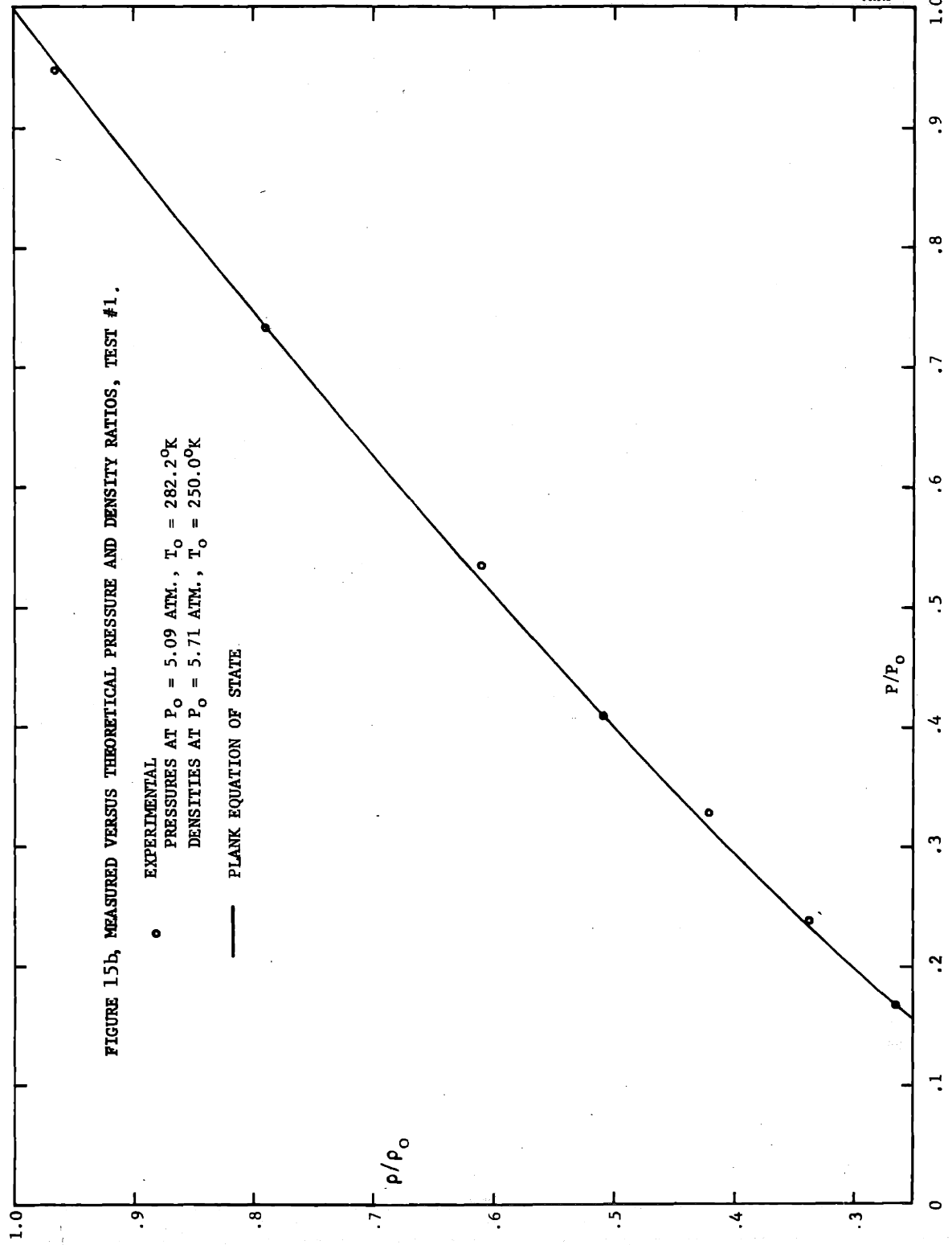


FIGURE 15b, MEASURED VERSUS THEORETICAL PRESSURE AND DENSITY RATIOS, TEST #1.

• EXPERIMENTAL

PRESSURES AT P₀ = 5.09 ATM., T₀ = 282.2°K

DENSITIES AT P₀ = 5.71 ATM., T₀ = 250.0°K

— PLANK EQUATION OF STATE

FIGURE 16a, NOZZLE I PROFILES OF MEASURED PRESSURE RATIO AND ISENTROPICALLY
CONVERTED MEASURED DENSITY RATIO, TEST #2.

• MEASURED PRESSURE, (PRESSURE TAP PLATE #2)
 $P_0 = 3.83 \text{ ATM.}, T_0 = 315.0^\circ\text{K}$

— CONVERTED DENSITY (USING PLANK EQUATION OF STATE)
 $P_0 = 4.00 \text{ ATM.}, T_0 = 320.5^\circ\text{K}$

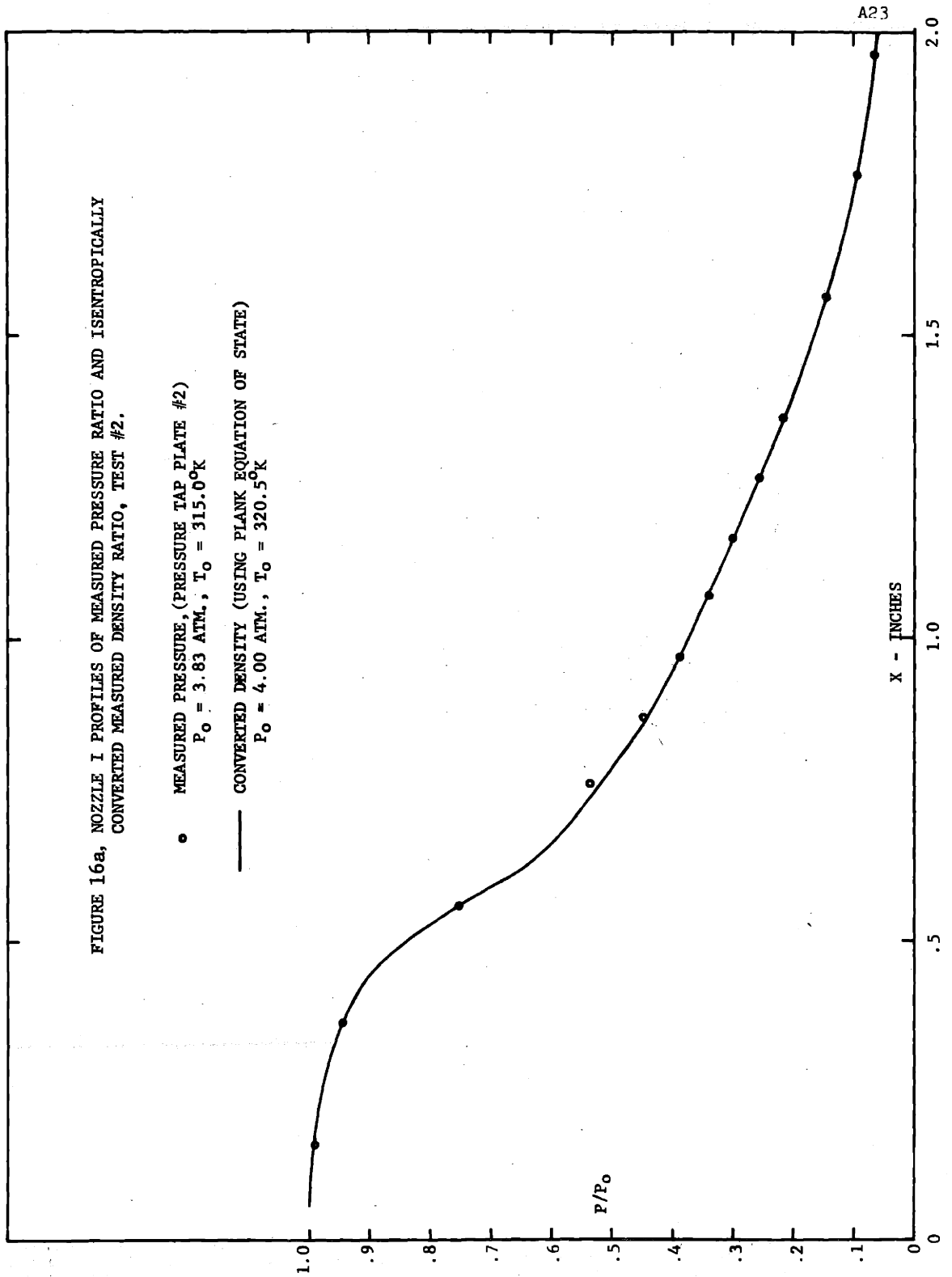
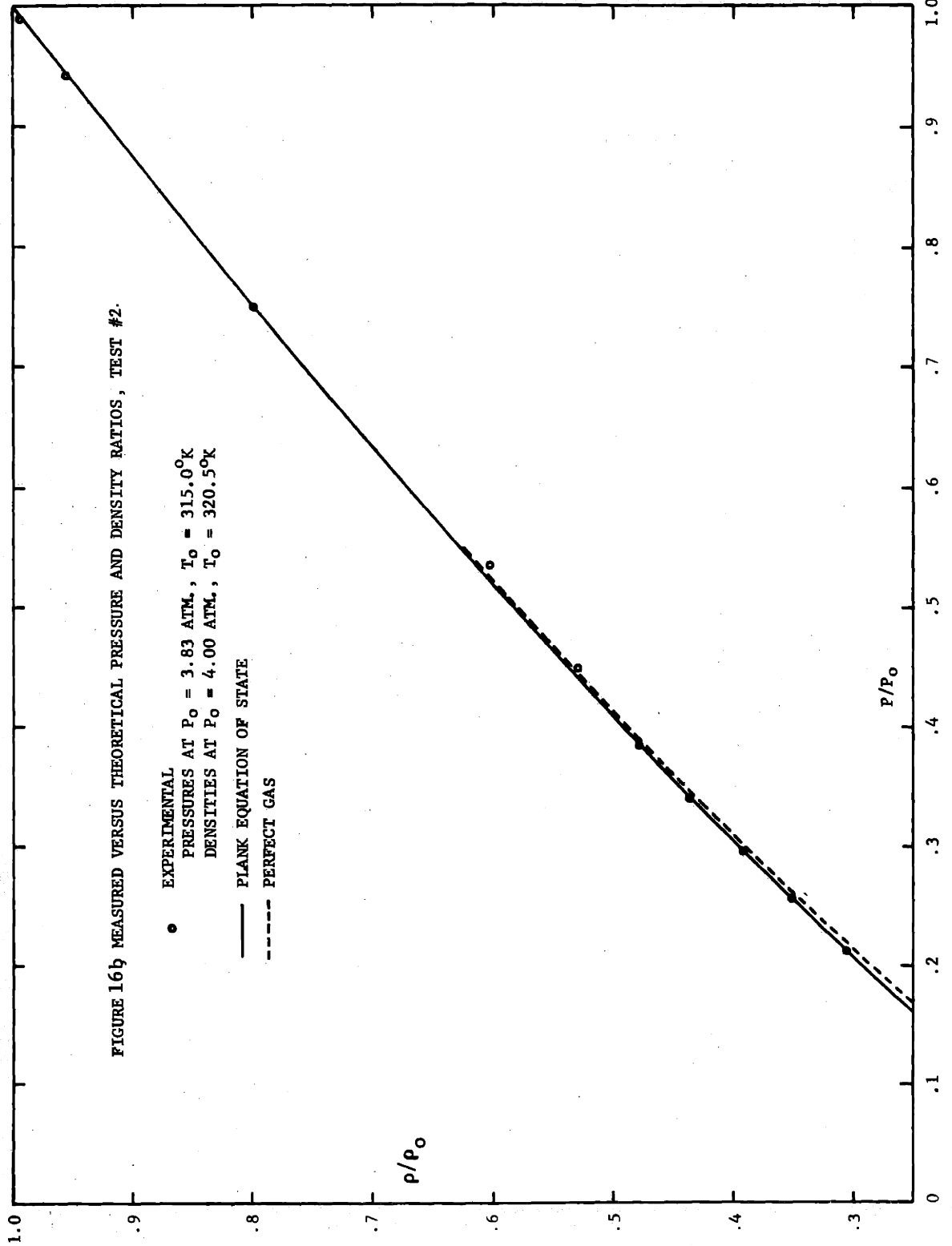
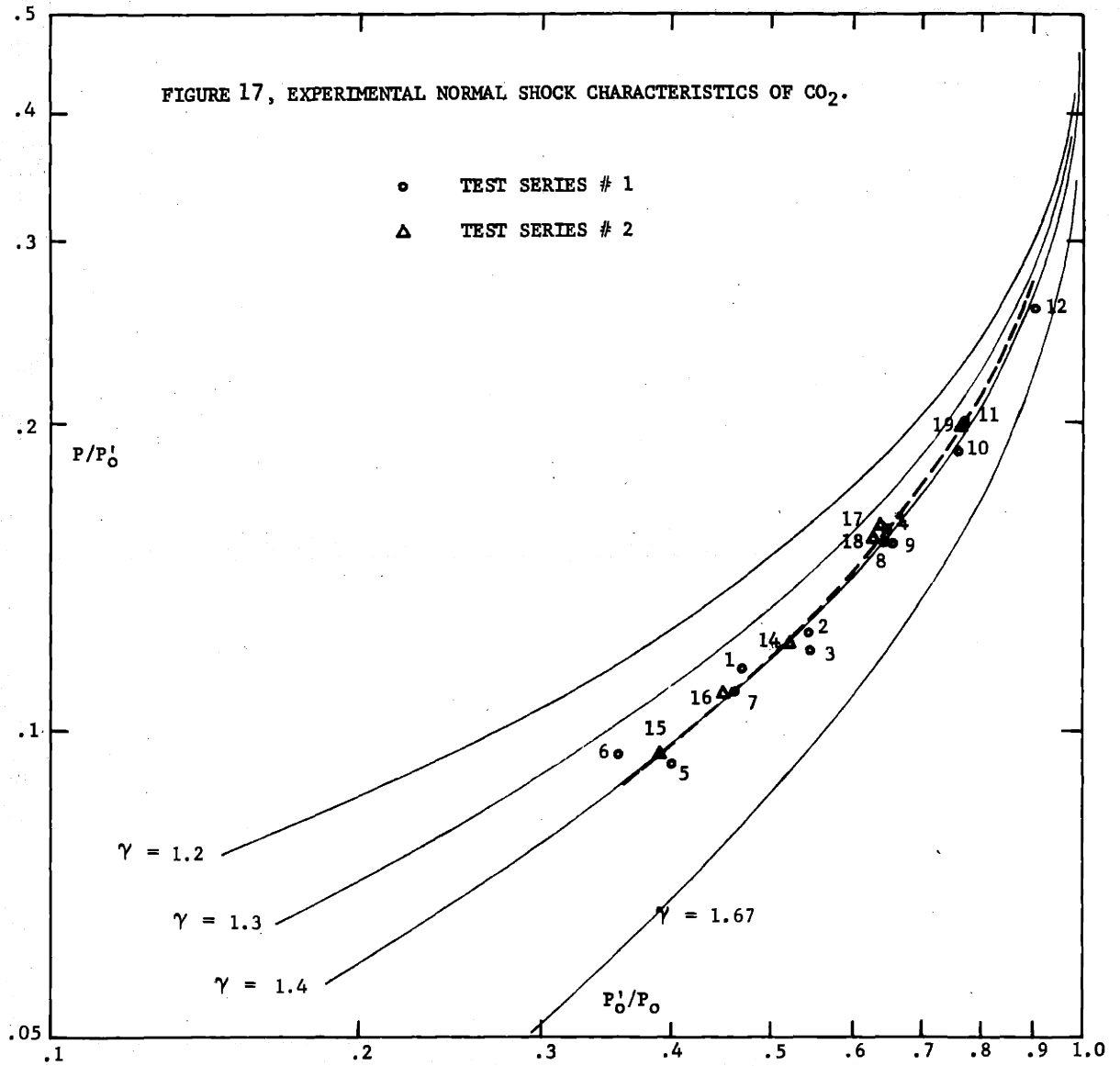
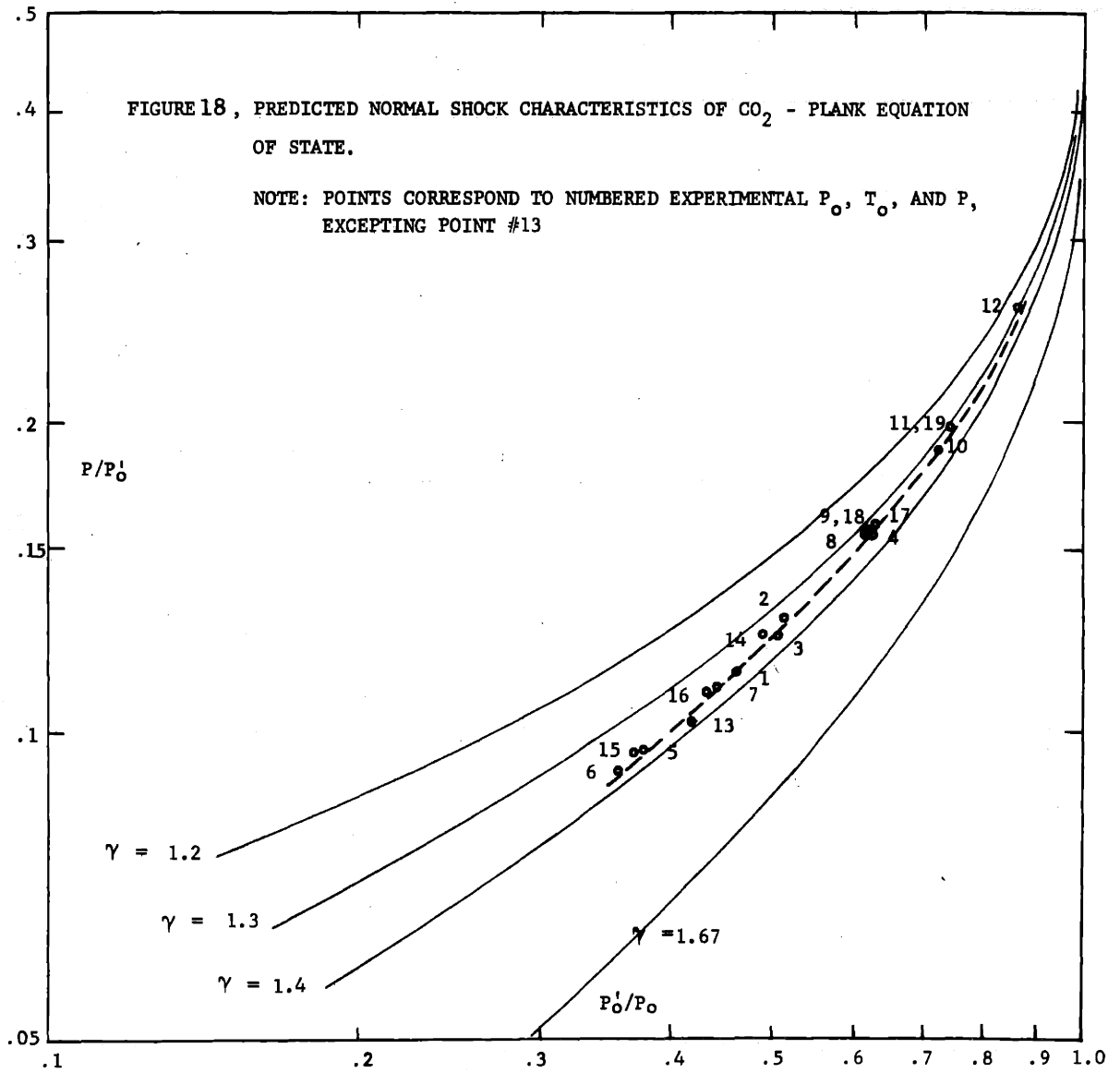


FIGURE 16b MEASURED VERSUS THEORETICAL PRESSURE AND DENSITY RATIOS, TEST #2.







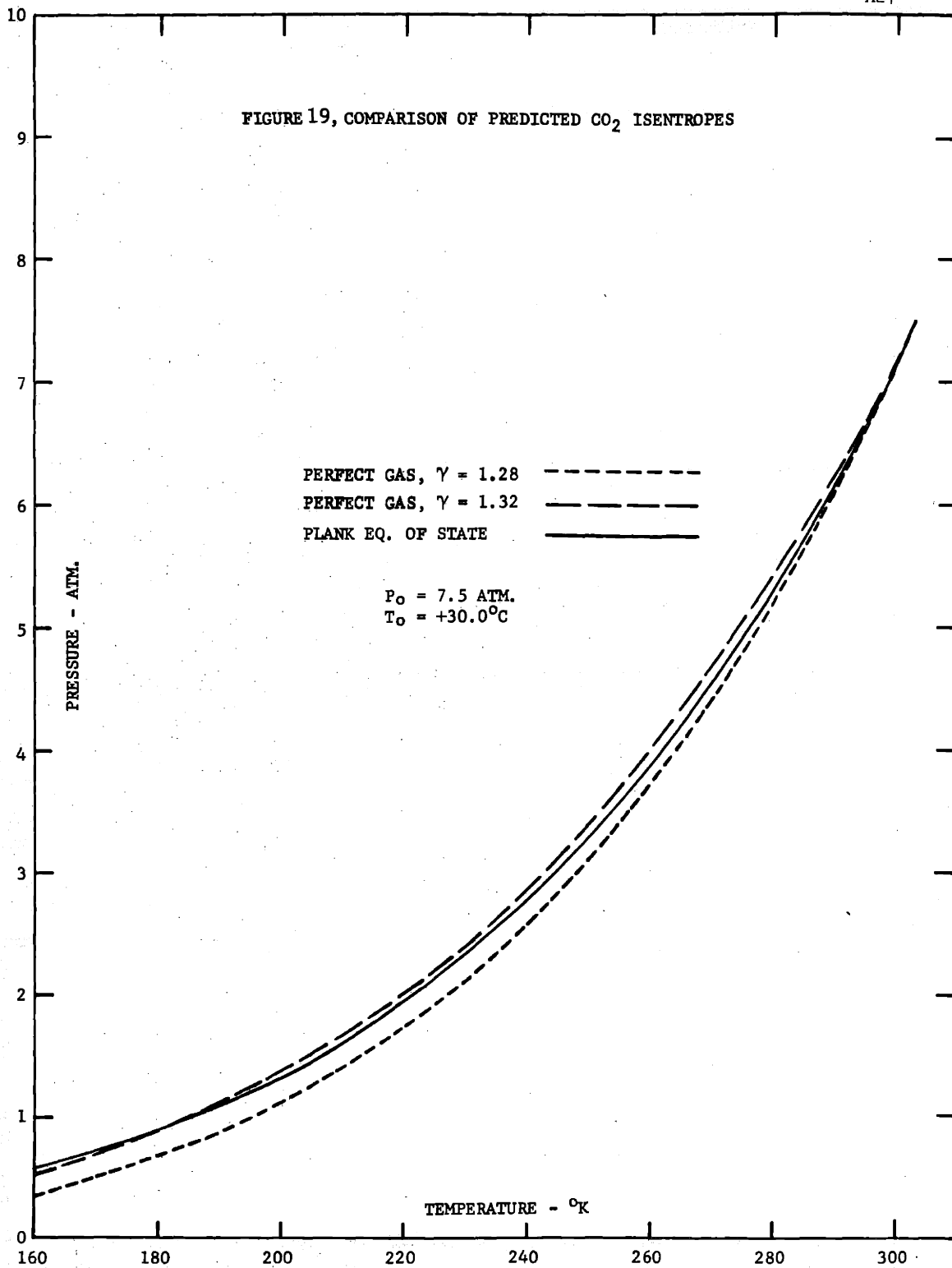
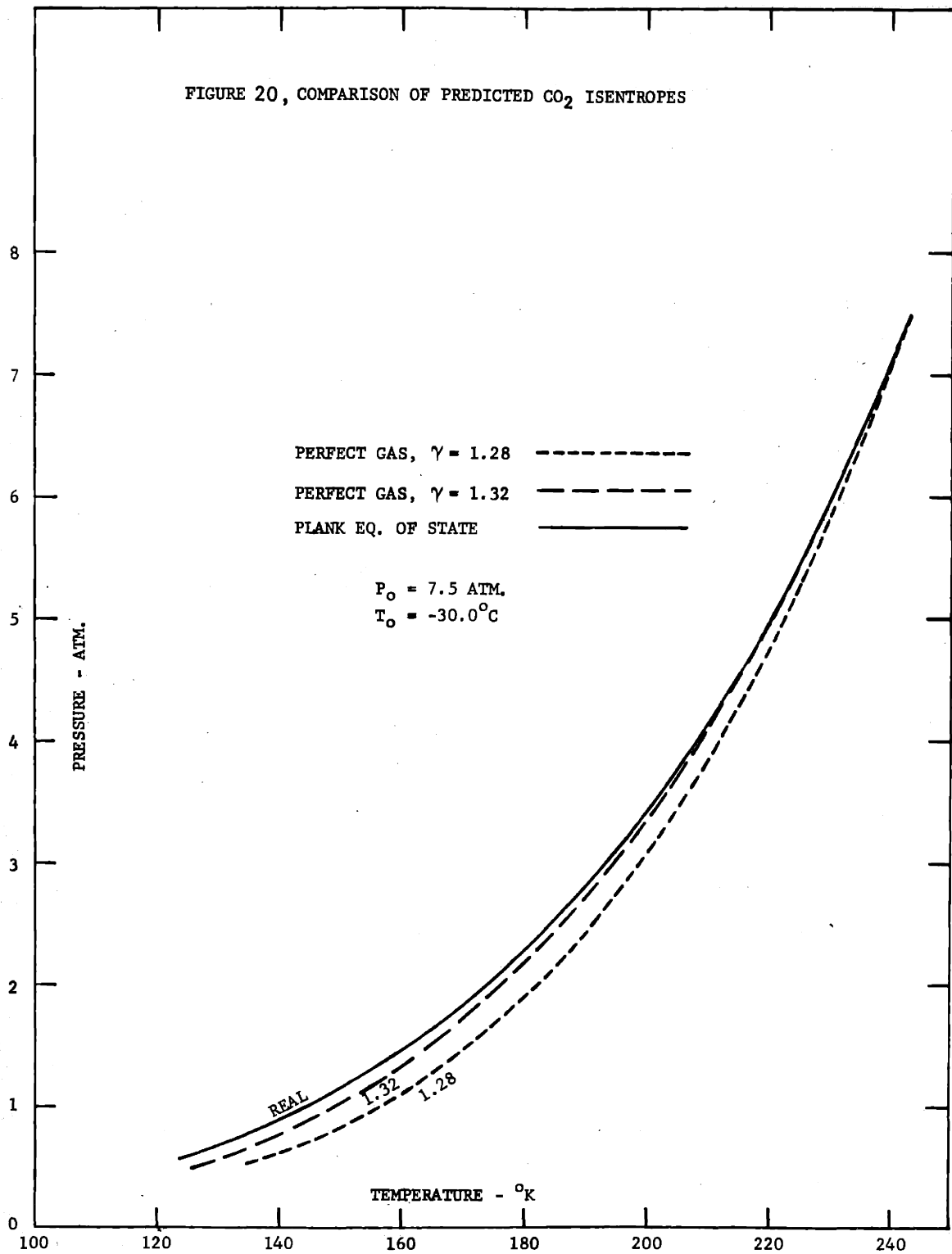
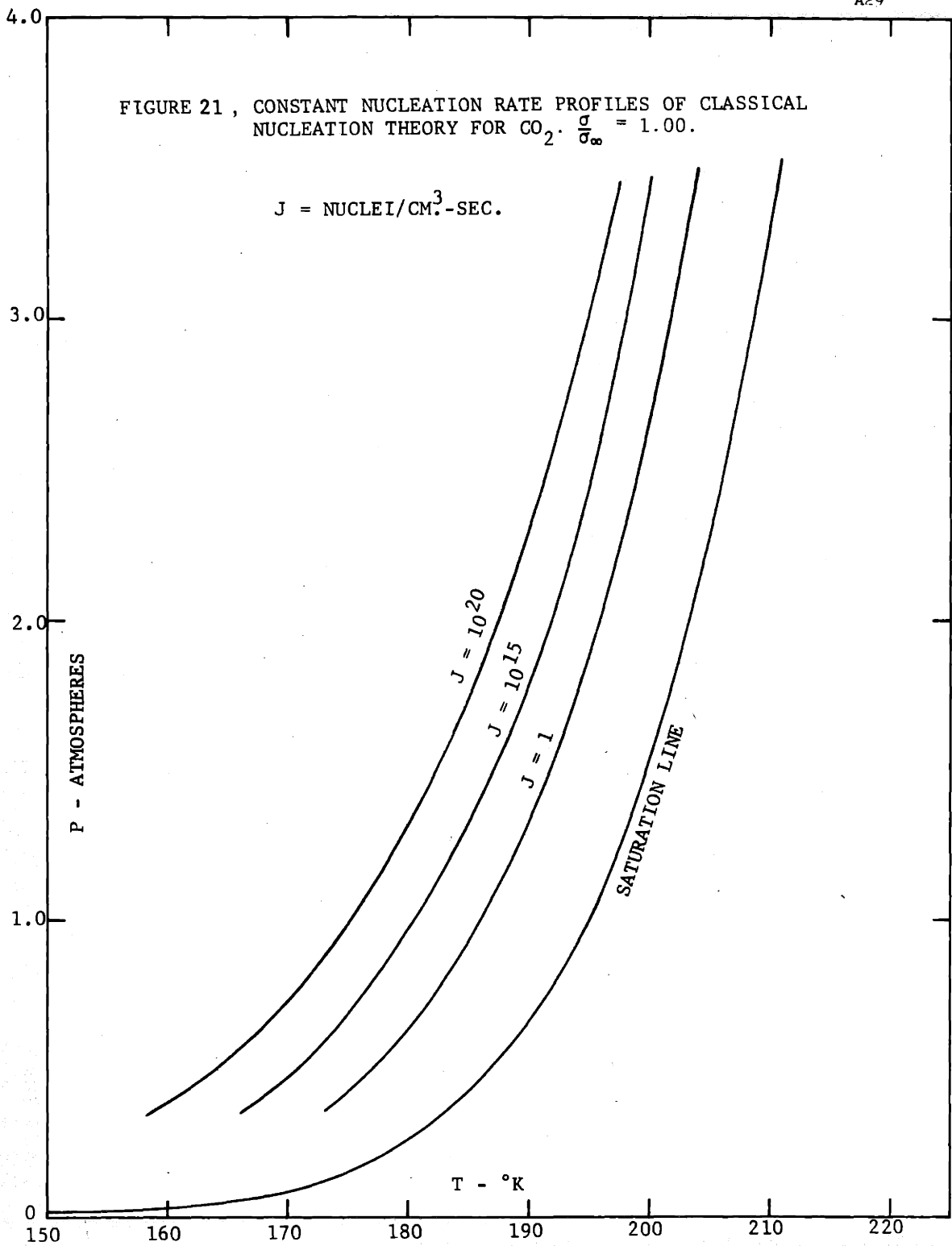


FIGURE 20, COMPARISON OF PREDICTED CO₂ ISENTROPES



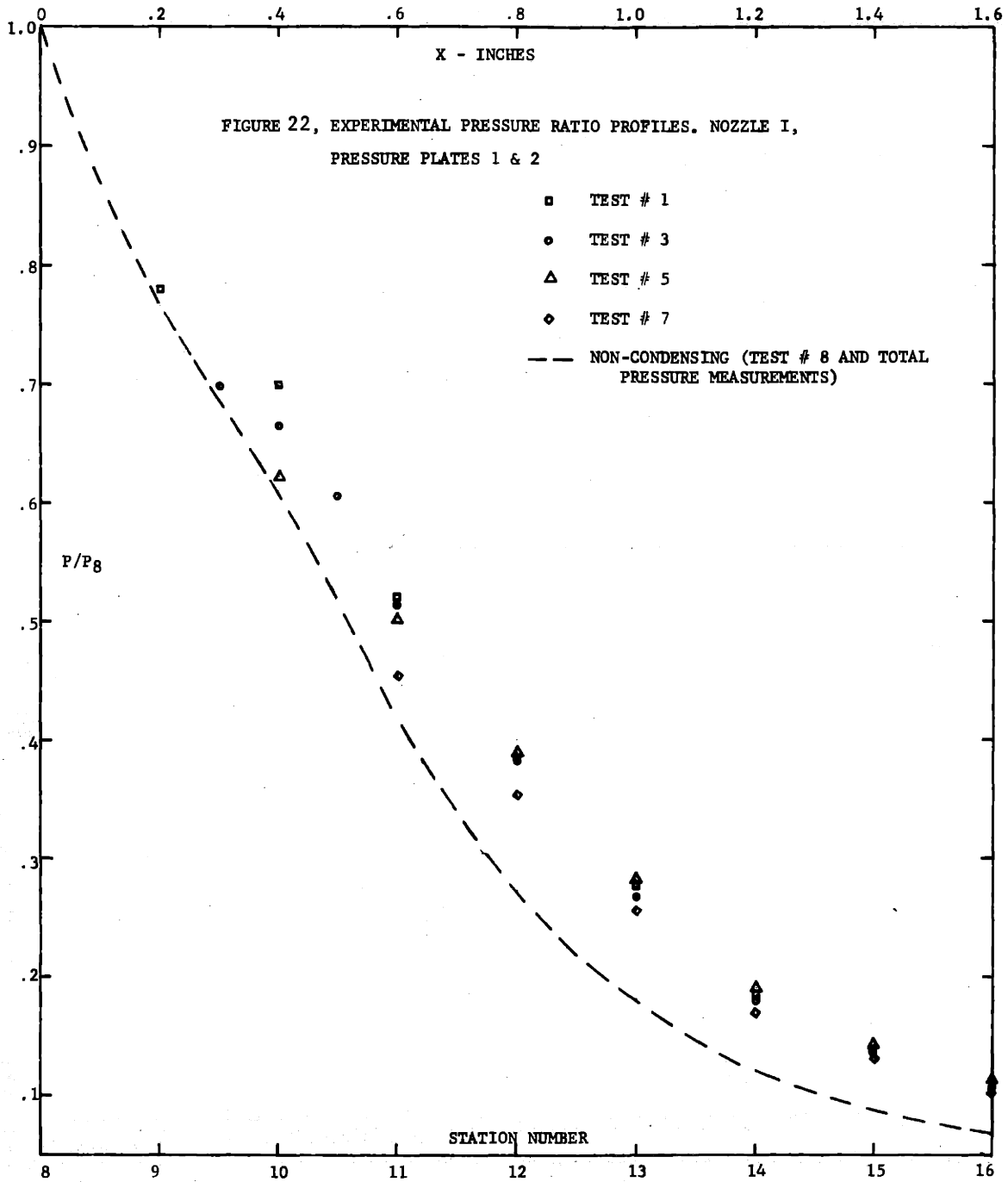


TABLE 5
Pressure Data for Figure No. 22

Station No.	Run No. 1 _I		Run No. 3 _I		Run No. 5 _I		Run No. 7 _I		Run No. 8 _I	
	P ("Hg)	P/P ₈	P ("Hg)	P/P ₈	P ("Hg)	P/P ₈	P ("Hg)	P/P ₈	P ("Hg)	P/P ₈
8	122.2	1.000	122.3	1.000	112.4	1.000	81.6	1.000		
8½			107.0	.874						
9	95.4	.780	93.5	.764	86.0	.765	62.6	.767		
9½			85.6	.699						
10	85.4	.699	81.5	.665	70.0	.622	50.7	.621		
10½			74.1	.605						
11	63.5	.519	63.1	.515	56.3	.501	37.0	.453		
12	47.3	.388	47.0	.384	43.9	.390	28.8	.353		
13	33.8	.276	33.0	.269	31.8	.282	21.0	.257		
14	22.6	.185	22.1	.180	21.5	.191	13.8	.169		
15	17.0	.139	16.7	.1364	16.6	.1453	10.7	.131		
16	13.0	.106	12.8	.1045	12.6	.1120	8.4	.103		
17	10.8	.0884	10.8	.0880	10.4	.0925	10.8	.132		
18	10.0	.0818	10.0	.0815	9.5	.0844	12.2	.149		
19	9.3	.0761			8.9	.0793				
20	8.9	.0728			8.6	.0765				
21	8.3	.0678			8.4	.0748				
22	7.9	.0646			8.6	.0765				
23	7.6	.0621								
24	6.8	.0556								

See Table 6

Run No. 7_I
P = 152.7 "Hg
o (calculated)
T_o = -35° F ± 5° F

Run No. 5_I
P = 104.7 psia
T_o = -45° F ± 2

Run No. 3_I
P = 228.5 "Hg
(calculated)
T_o = -47.2° F

Run No. 1_I
P_o = 112.2 psia
T_o = 50.6° F

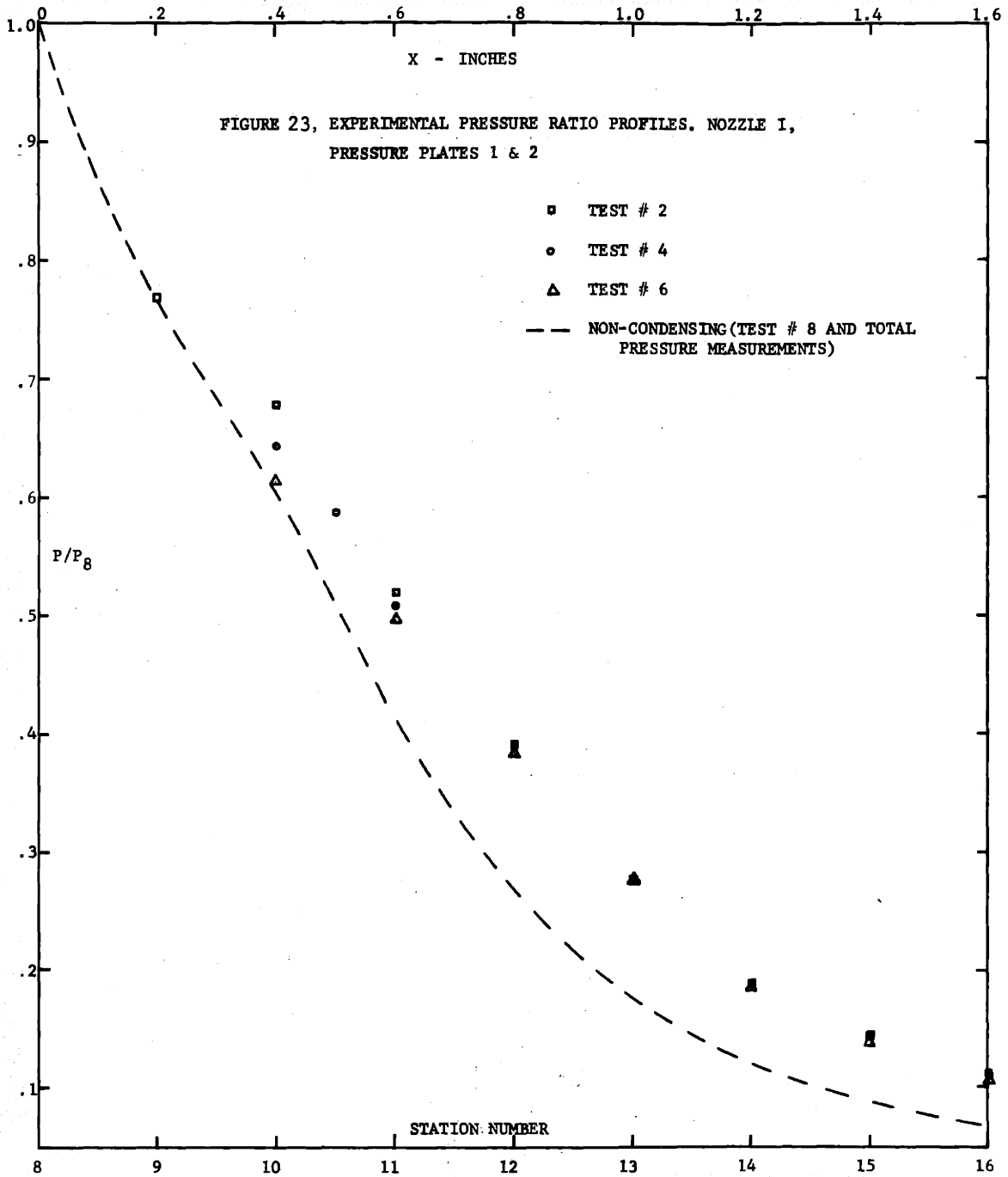


TABLE 6
Pressure Data for Figure No.23

Station No.	Run No. 2 _I		Run No. 4 _I		Run No. 6 _I		Run No. 8 _I	
	P("Hg)	P/P ₈	P("Hg)	F/P ₈	P("Hg)	P/P ₈	P("Hg)	P/P ₈
	122.7	1.000	129.0	1.000	105.8	1.000	81.6	1.000
7½			118.4	.884				
8			104.7	.766				
8½	94.5	.770	90.8	.885	80.8	.764	62.4	.765
9			81.2	.644				
9½			76.4	.588				
10	83.1	.677	68.8	.511	65.1	.615	50.0	.611
10½			60.6	.390				
11	63.8	.520	46.3	.278				
12	48.0	.391	32.9	.186				
13	34.0	.277	22.1	.142				
14	22.8	.186	16.8	.107				
15	17.0	.1385	12.7	.0885				
16	13.0	.106	10.5	.0793				
17	10.8	.088	9.4					
18	9.9	.0806	9.3					
19	9.4	.0765	8.8					
20	9.1	.0740	8.3					
21	8.7	.0708	7.8					
22	8.3	.0675	7.8					
23	7.8	.0635	7.8					
24	7.0	.0570	9.2					
25	7.3							

*Indicates improved values determined from subsequent total pressure tests.

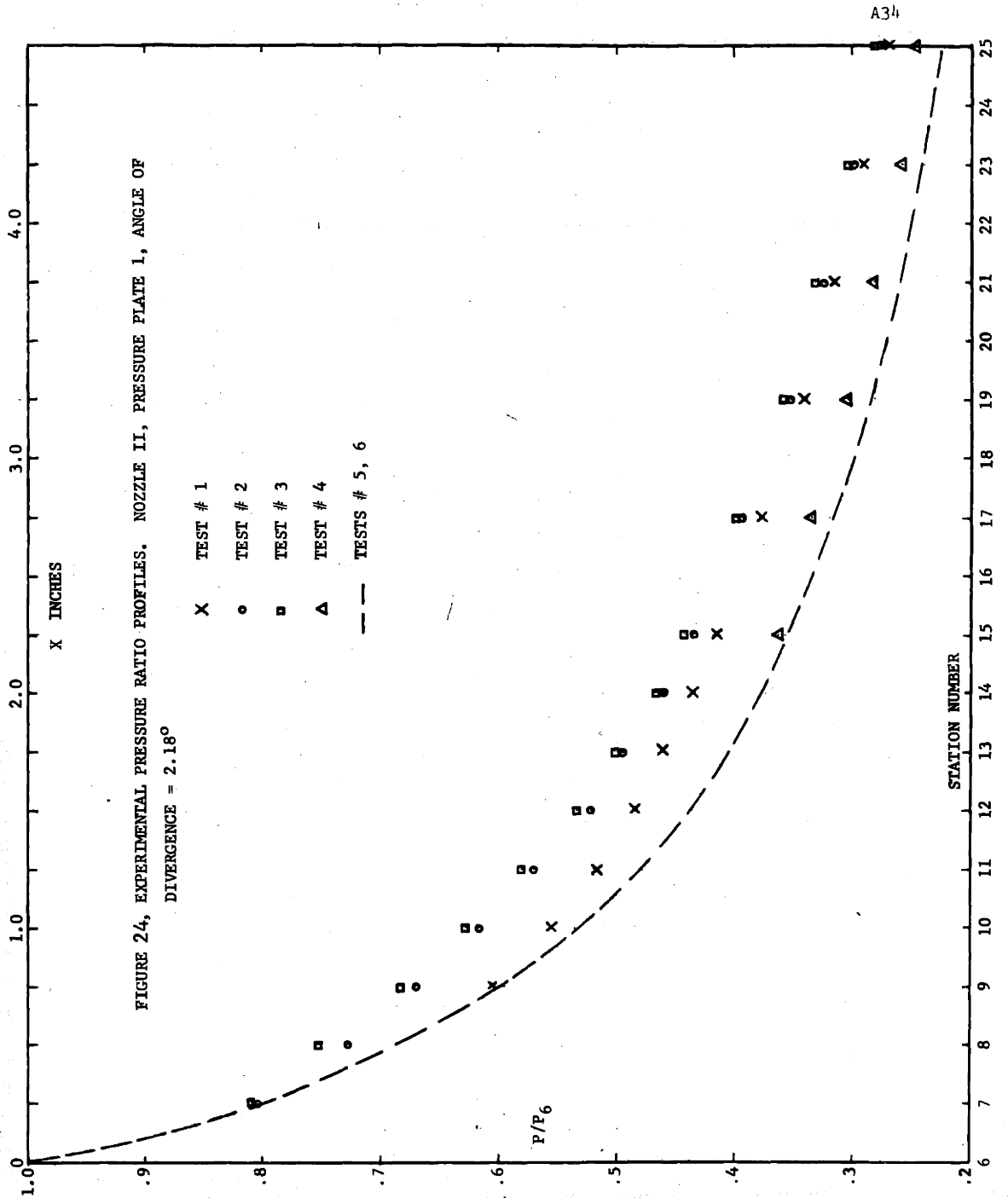
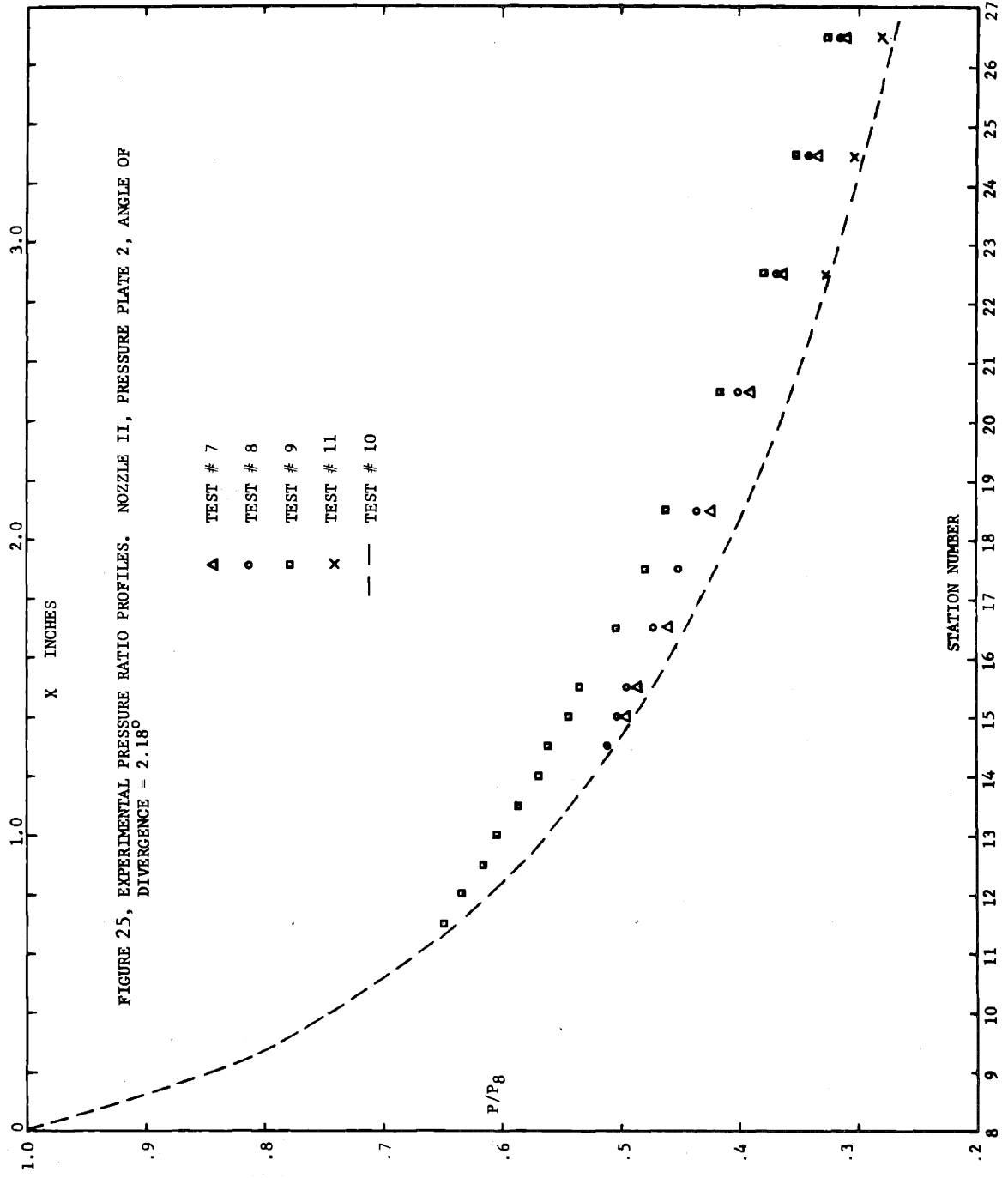


TABLE 7
Pressure Data for Figure No. 24

Tube No.	Test No. 1 ^{II}		Test No. 2 ^{II}		Test No. 3 ^{II}		Test No. 4 ^{II}		Test No. 5 ^{II}		Test No. 6 ^{II}	
	P	P/P ₆	P	P/P ₆	P ₀ =114.7 psia T ₀ =-27.7°F	P ₀ =117.7 psia T ₀ =-41.1°F	P ₀ =117.7 psia T ₀ =-45.0°F	P ₀ =108.2 psia T ₀ =+9.0°F	P ₀ =113.7 psia T ₀ =72.0°F	P ₀ =113.7 psia T ₀ =72.0°F	P ₀ =96.7 psia T ₀ =100.4°F	P ₀ =96.7 psia T ₀ =100.4°F
6	127.0	1.000	130.4	1.000	130.4	1.000	118.1	1.000	124.9	1.000	105.6	1.000
7	101.9	.801	104.9	.804	105.4	.809	94.5	.801	100.0	.801	84.3	.799
8	87.8	.691	94.9	.727	98.0	.752	81.2	.689	85.8	.687	72.5	.687
9	76.8	.605	87.1	.669	89.1	.684	70.7	.599	74.5	.596	62.9	.595
10	70.6	.556	80.3	.616	81.9	.628	63.8	.540	66.9	.535	56.5	.535
11	65.6	.517	74.2	.570	75.7	.580	56.7	.480	59.8	.478	50.6	.479
12	61.6	.485	68.0	.521	69.5	.533	51.6	.437	54.2	.434	46.1	.436
13	58.5	.461	64.4	.494	65.4	.501	48.2	.409	50.5	.404	42.8	.405
14	55.2	.435	59.9	.459	60.8	.466	44.2	.374	46.6	.373	39.7	.376
15	52.7	.415	56.6	.434	57.6	.442	42.7	.362	44.5	.356	37.7	.357
16	47.7	.376	51.1	.392	51.9	.398	39.3	.333	39.7	.318	33.6	.318
17	43.1	.340	45.7	.351	46.5	.358	35.7	.302	35.0	.280	29.7	.281
18	39.9	.314	42.3	.324	43.1	.331	33.0	.280	32.2	.258	27.3	.258
19	36.8	.290	39.0	.299	39.5	.303	30.3	.257	29.7	.238	25.3	.239
20	34.0	.268	35.9	.275	36.5	.280	28.8	.244	27.8	.2225	23.6	.223
21	32.3	.254	34.0	.261	34.4	.264			26.1	.209	22.2	.210
22	30.3	.239	32.2	.248					24.5	.196	20.8	.197



STATION NUMBER

TABLE 8
Pressure Data for Figure No. 25

Tube No.	Sta. No.	Run No. 7 II			Run No. 8 II			Run No. 9 II			Run No. 10 II			Run No. 11 II		
		P_0	T_0	P/P8	P_0	T_0	P/P8	P_0	T_0	P/P8	P_0	T_0	P/P8	P_0	T_0	P/P8
3	8	80.7 psia	-30.6°F	1.000	86.2 psia	-37.8°F	1.000	114.7 psia	-33.6°F	1.000	84.7 psia	112.7 psia	129.4	-1.5°F	1.000	
4	8½	85.3		.921	90.8		.919	119.9		.919	89.3		119.0		.919	
5	9	78.4		.846	83.1		.845	110.2		.845	81.9		109.2		.844	
6	9½	72.8		.787	77.2		.782	103.1		.790	76.2		102.2		.789	
7	10	69.0		.745	73.3		.741	96.4		.740	72.6		96.4		.745	
8	10½	65.1		.703	68.9		.696	91.9		.706	68.6		90.9		.702	
9	11	61.3		.662	65.1		.659	86.7		.667	65.2		86.2		.666	
10	11½	58.5		.632	62.2		.630	84.2		.649	61.9		82.2		.635	
11	12	56.4		.609	59.6		.603	82.1		.632	59.6		78.5		.606	
12	12½	54.0		.583	57.1		.578	79.8		.615	57.1		75.6		.584	
13	13	52.1		.562	55.2		.559	78.4		.604	55.0		72.6		.561	
14	13½	50.4		.544	53.5		.541	76.0		.585	53.0		70.2		.542	
15	14	47.9		.518	51.0		.516	73.8		.567	50.8		67.1		.519	
16	14½	46.6		.503	50.4		.510	72.8		.560	48.8		64.9		.501	
17	15	45.7		.493	49.5		.494	70.6		.542	47.8		63.1		.488	
18	15½	44.7		.483	48.8		.494	69.5		.533	46.7		61.7		.476	
19	16	42.2		.456	46.5		.471	65.5		.502	43.3		57.2		.442	
20	16½	40.3		.435	44.4		.449	62.2		.477	40.8		54.4		.420	
21	17	39.0		.421	42.9		.434	59.8		.460	38.5		51.0		.394	
22	18	36.0		.389	39.3		.398	54.0		.414	34.6		46.0		.355	
23	20	33.6		.363	36.3		.367	49.3		.378	31.4		42.2		.326	
24	22	30.7		.332	33.7		.341	45.8		.352	28.9		39.1		.302	
25	26	28.5		.308	31.1		.315	42.4		.326	26.5		36.3		.281	

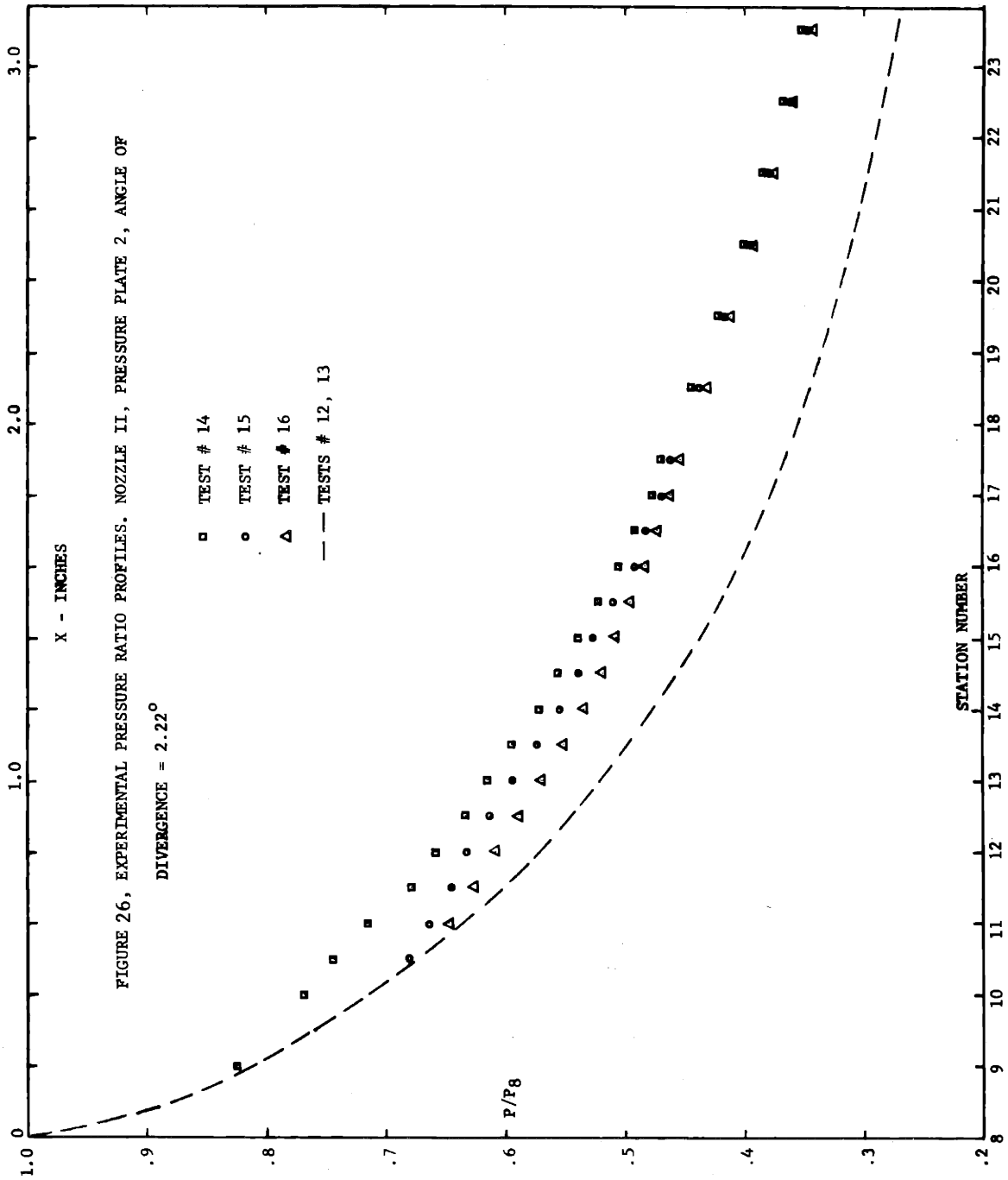


TABLE 9
Pressure Data for Figure No. 26

Tube No.	Station	Test No. 12 ^{II}		Test No. 13 ^{II}		Test No. 14 ^{II}		Test No. 15 ^{II}		Test No. 16 ^{II}	
		P_o	T_o	P_o	T_o	P_o	T_o	P_o	T_o	P_o	T_o
		106.2 psia	146.7°F	96.2 psia	126°F	135.2 psia	37.0°F	103.2 psia	43.2°F	112.2 psia	39.0°F
		P/P_8	P/P_8	P/P_8	P/P_8	P/P_8	P/P_8	P/P_8	P/P_8	P/P_8	P/P_8
1	8	119.3	1.000	108.5	1.000	127.4	*	116.9	1.000	127.3	1.000
2	9	96.9	.811	88.1	.812	118.6	.827	96.4	.825	105.3	.826
3	10	85.1	.713	77.1	.711	114.6	.769	87.6	.716	91.3	.712
4	10½	80.2	.672	72.6	.670	110.1	.744	79.5	.680	86.3	.673
5	11	75.6	.634	68.5	.631	104.5	.715	77.5	.663	83.0	.647
6	11½	71.4	.598	64.7	.596	101.4	.678	75.2	.644	80.1	.625
7	12	68.3	.572	61.8	.569	97.5	.658	73.7	.631	77.9	.607
8	12½	65.0	.545	58.8	.542	94.7	.632	71.5	.612	75.5	.589
9	13	62.4	.523	56.3	.519	91.6	.614	69.2	.593	73.0	.569
10	13½	60.6	.508	54.7	.505	87.9	.594	66.9	.572	70.5	.550
11	14	54.7	.459	49.4	.455	85.6	.570	64.6	.553	68.4	.533
12	14½	53.8	.451	48.6	.448	83.1	.555	62.9	.538	66.4	.517
13	15	52.0	.436	46.9	.432	80.4	.538	61.3	.525	64.9	.506
14	15½	50.4	.422	45.7	.421	77.6	.521	59.4	.508	62.9	.494
15	16	48.7	.408	43.4	.400	75.6	.503	57.3	.490	61.2	.481
16	16½	47.0	.394	42.3	.390	73.5	.490	56.2	.481	60.0	.471
17	17	44.7	.375	40.3	.372	72.2	.476	54.7	.468	58.5	.460
18	17½	43.6	.366	39.5	.364	70.2	.468	53.7	.460	57.5	.452
19	18½	40.9	.343	36.7	.338	68.2	.442	50.9	.436	54.6	.429
20	19½	39.2	.328	35.5	.327	64.9	.420	48.4	.414	52.2	.410
21	20½	38.1	.319	34.5	.318	61.6	.399	46.1	.394	49.6	.390
22	21½	35.1	.294	32.0	.295	59.1	.383	44.2	.378	47.8	.375
23	22½	34.3	.287	31.1	.286	56.6	.367	42.2	.361	45.6	.358
24	23½	32.5	.272	29.5	.272	54.2	.352	40.5	.347	43.6	.342
25	24½	32.8	.275	29.6	.273	52.0	.337	39.0	.334	42.0	.330

* Assumed Station 8 Total Pressure Ratio $P_8/P_o = .560$

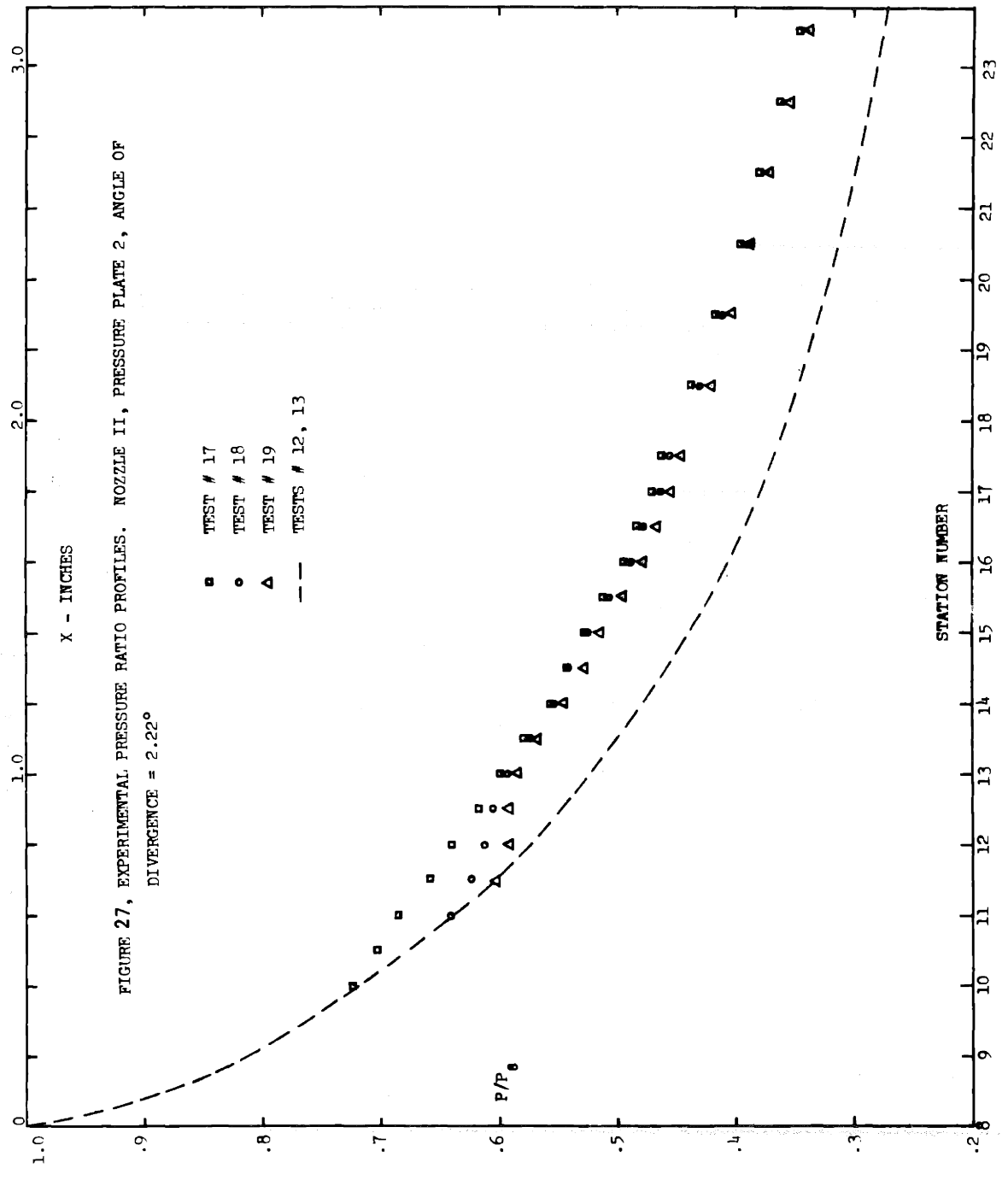


FIGURE 27, EXPERIMENTAL PRESSURE RATIO PROFILES. NOZZLE II, PRESSURE PLATE 2, ANGLE OF DIVERGENCE = 2.22°

X - INCHES

- TEST # 17
- TEST # 18
- △ TEST # 19
- TESTS # 12, 13

P/P_0

STATION NUMBER

TABLE 10

Pressure Data for Figure No. 27

Tube No.	Station	Test No. 17 _{II}		Test No. 18 _{II}		Test No. 19 _{II}		Test No. 12 _{II}		Test No. 13 _{II}	
		P_o	T_o	P_o	T_o	P_o	T_o	P_o	T_o	P_o	T_o
		112.7 psia	-42.0°F	84.7 psia	-47.2°F	84.2 psia	-43.0°F				
		P("Hg)	P/P ₈	P("Hg)	P/P ₈	P("Hg)	P/P ₈	P("Hg)	P/P ₈	P("Hg)	P/P ₈
1	8	127.9	1.000	95.4	1.000	72.1	1.000				
2	9	105.6	.826	78.7	.825	59.4	.825				
3	10	92.4	.723	68.3	.716	51.9	.719				
4	10½	89.6	.701	64.2	.673	48.5	.673				
5	11	87.4	.684	61.1	.640	46.0	.638				
6	11½	84.0	.657	59.3	.622	43.5	.603				
7	12	81.7	.640	58.3	.611	42.5	.590				
8	12½	78.7	.616	57.6	.604	42.5	.590				
9	13	76.4	.598	56.4	.591	42.1	.584				
10	13½	73.9	.578	54.6	.572	40.9	.567				
11	14	71.0	.555	52.8	.553	39.2	.544				
12	14½	69.1	.541	51.6	.541	38.0	.527				
13	15	67.2	.526	50.0	.524	36.9	.512				
14	15½	65.1	.510	48.2	.505	35.6	.494				
15	16	62.9	.492	46.4	.486	34.3	.476				
16	16½	61.6	.482	45.5	.476	33.5	.465				
17	17	59.9	.469	44.1	.462	32.6	.452				
18	17½	58.8	.460	43.2	.453	32.0	.444				
19	18½	55.6	.435	40.9	.429	30.2	.419				
20	19½	53.0	.415	39.1	.410	28.9	.401				
21	20½	50.4	.394	37.0	.388	26.7	.370				
22	21½	48.3	.378	35.3	.370	23.8	.330				
23	22½	46.1	.361	33.7	.353	23.0	.319				
24	23½	44.1	.345	32.3	.338	21.1	.293				
25	24½			31.2	.327	20.7	.287				

(See Table 9)

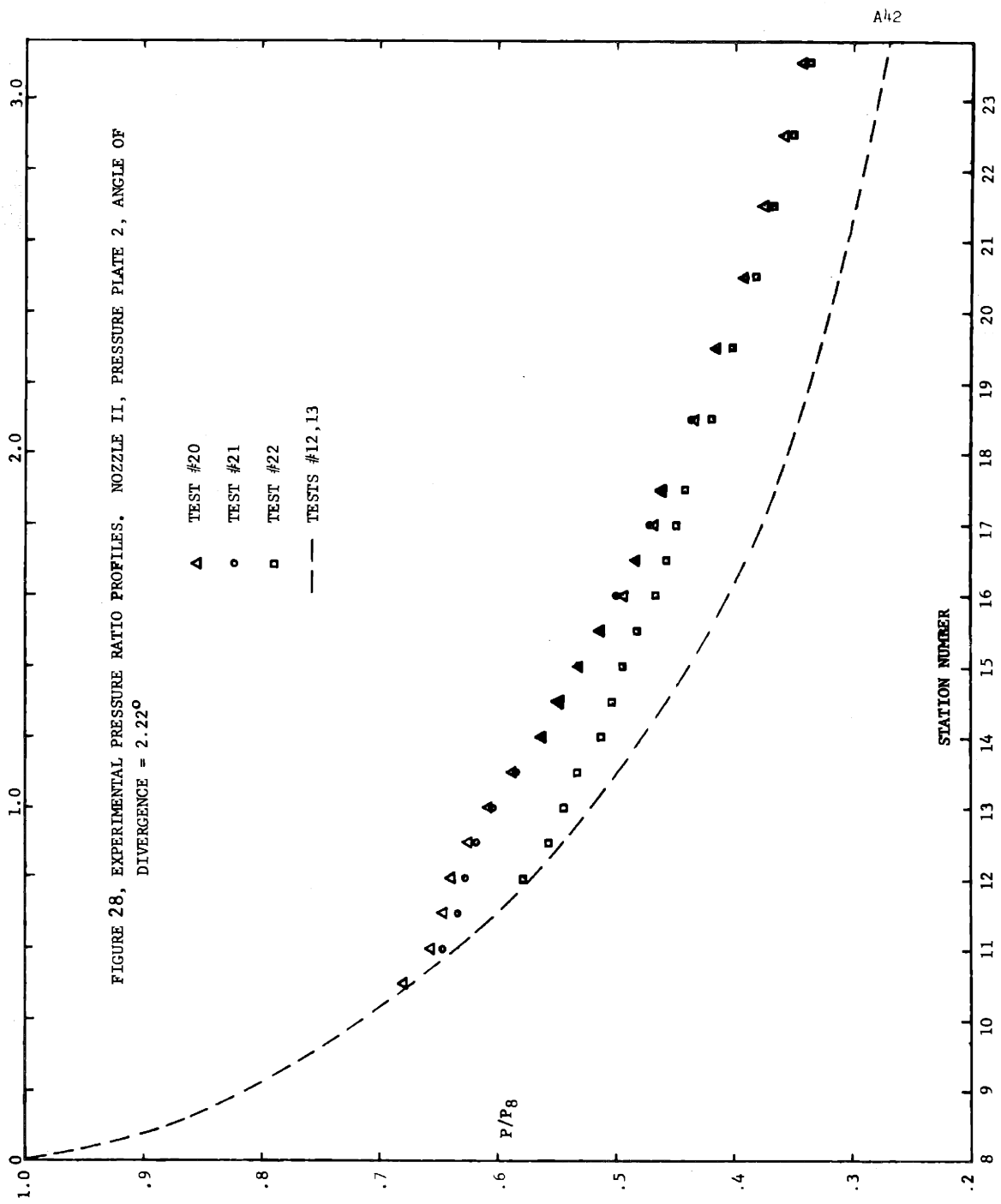


TABLE II
Pressure Data for Figure No. 28

Tube No.	Station	Test No. 20 ^{II}		Test No. 21		Test No. 22 ^{II}		Test No. 12 ^{II}		Test No. 13 ^{II}	
		P ("Hg)	P/P ₈	P ("Hg)	P/P ₈	P ("Hg)	P/P ₈	P ("Hg)	P/P ₈	P ("Hg)	P/P ₈
		P ₀ = 95.2 psia		P ₀ = 90.2 psia		P ₀ = 108.7 psia					
		T ₀ = -44.0°F		T ₀ = -44.5°F		T ₀ = -27.5°F					
1	8	107.2	1.000	101.6	1.000	123.3	1.000				
2	9	88.6	.826	83.8	.825	102.0	.826				
3	10	76.8	.716	72.8	.716	88.4	.716				
4	10½	72.7	.679	68.4	.673	83.2	.675				
5	11	70.3	.656	65.7	.647	78.8	.639				
6	11½	69.1	.645	64.3	.633	74.2	.601				
7	12	68.4	.638	63.7	.627	71.2	.577				
8	12½	66.8	.623	62.8	.618	68.6	.556				
9	13	65.0	.606	61.3	.604	67.0	.543				
10	13½	62.8	.586	59.2	.583	65.5	.531				
11	14	60.2	.561	57.0	.561	63.1	.511				
12	14½	58.7	.548	55.5	.546	61.9	.502				
13	15	56.7	.529	53.9	.530	60.7	.492				
14	15½	54.8	.511	52.0	.512	59.1	.480				
15	16	52.7	.492	50.6	.498	57.4	.465				
16	16½	51.6	.481	48.9	.481	55.3	.456				
17	17	50.0	.466	47.8	.470	55.2	.447				
18	17½	49.1	.458	46.8	.460	54.2	.440				
19	18½	46.2	.431	44.3	.436	51.4	.417				
20	19½	44.1	.411	42.0	.413	49.3	.400				
21	20½	42.0	.392	39.5	.389	46.8	.380				
22	21½	40.1	.374	36.8	.362	45.0	.365				
23	22½	38.4	.358	35.3	.347	43.0	.349				
24	23½	36.8	.343	33.0	.325	41.1	.333				
25	24½	35.4	.330	32.0	.315	39.7	.324				

(See Table 9)

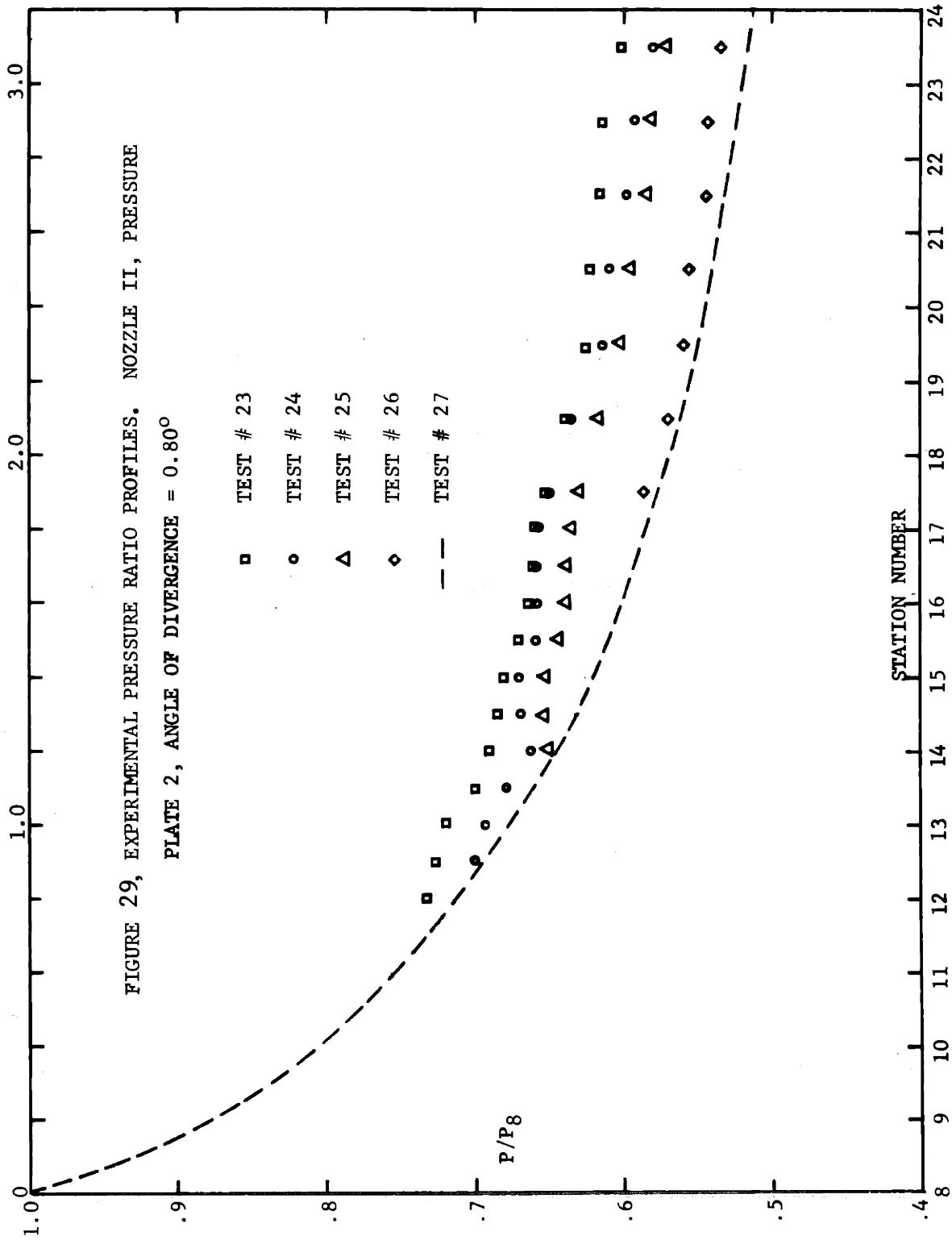


TABLE 12
Pressure Data for Figure No. 29

Tube No.	Station	Test No. 23 _{II} P ₀ =128.2 psia T ₀ =-40.6°F	Test No. 24 _{II} P ₀ =121.7 psia T ₀ =-39.9°F	Test No. 25 _{II} P ₀ =131.7 psia T ₀ =-32.9°F	Test No. 26 _{II} P ₀ =101.7 psia T ₀ =-26.5°F	Test No. 27 _{II} P ₀ =93.7 psia T ₀ =-1.0°F
		P("Hg) P/P ₈	P("Hg) P/P ₈	P("Hg) P/P ₈	P("Hg) P/P ₈	P("Hg) P/P ₈
1	8	*	*	*	129.8	119.7
2	9	131.1	124.7	134.7	114.0	105.2
3	10	127.9	121.0	131.3	104.3	96.4
4	10½	124.4	117.3	127.1	101.4	93.5
5	11	119.9	113.1	122.2	98.0	90.6
6	11½	120.0	110.7	119.8	94.4	87.5
7	12	119.0	108.8	116.8	92.3	85.5
8	12½	117.5	107.6	114.8	90.0	83.3
9	13	114.1	105.2	111.9	87.8	81.1
10	13½	111.5	103.9	109.1	85.3	79.1
11	14	112.2	103.9	109.7	82.4	76.0
12	14½	109.4	102.4	109.5	82.1	75.7
13	15	108.6	102.0	108.0	81.1	74.7
14	15½	108.2	101.8	107.3	79.2	72.9
15	16	107.9	101.8	106.8	77.9	71.6
16	16½	106.7	100.7	105.9	77.2	71.0
17	17	104.5	98.3	103.6	76.1	69.8
18	17½	102.3	95.8	101.1	75.7	68.9
19	18	102.0	94.5	99.7	72.5	67.1
20	19	100.4	92.6	98.0	71.4	65.6
21	20	100.4	91.9	97.7	70.5	64.6
22	21	98.4	89.9	95.7	63.6	63.6
23	22	96.4	87.6	93.6	63.2	63.2
24	23				61.6	61.6
25	24				60.7	60.7

* Assumed Station 8 Total Pressure Ratio P₈/P₀ = .627

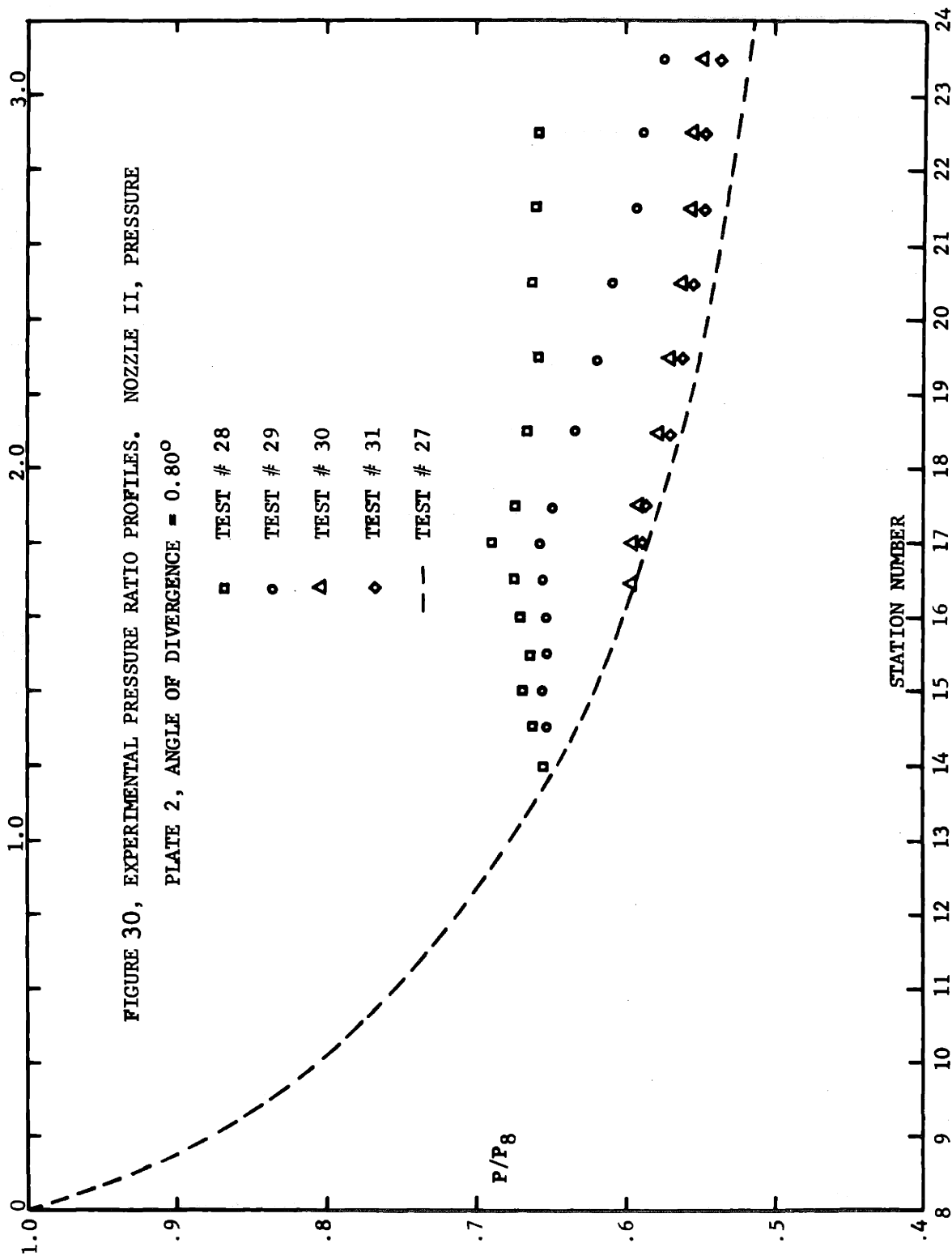


TABLE 13

Pressure Data for Figure No. 30

Tube No.	Station	Test No. 28 ^{II}		Test No. 29 ^{II}		Test No. 30 ^{II}		Test No. 31 ^{II}		Test No. 27 ^{II}
		P ₀	T ₀	P ₀	T ₀	P ₀	T ₀	P ₀	T ₀	
		91.7 psia	-53.2°F	101.2 psia	-40.1°F	115.7 psia	-29.0°F	96.2 psia	-31.6°F	
		P("Hg)	P/P ₈	P("Hg)	P/P ₈	P("Hg)	P/P ₈	P("Hg)	P/P ₈	
1	8	*	*	*	*	*	*	123.1	1.000	
2	9	93.2	.805	103.7	.804	129.0	.875	108.2	.878	
3	10	90.6	.779	100.7	.780	118.0	.800	99.0	.805	
4	10½	88.1	.757	97.7	.758	114.9	.779	96.3	.493	
5	11	84.9	.729	94.4	.732	112.3	.761	93.1	.756	
6	11½	83.3	.715	92.2	.715	107.2	.728	89.7	.729	
7	12	81.0	.695	90.0	.698	105.0	.712	87.7	.713	
8	12½	79.7	.685	88.2	.684	102.2	.694	85.4	.693	
9	13	77.5	.665	85.6	.664	99.9	.678	83.2	.676	
10	13½	76.0	.653	83.1	.644	97.0	.659	81.1	.659	
11	14	76.9	.660	83.9	.651	94.0	.638	78.5	.638	
12	14½	77.6	.666	84.3	.654	93.5	.635	78.1	.635	
13	15	77.1	.662	83.7	.649	92.2	.626	77.3	.628	
14	15½	77.8	.668	83.8	.650	90.1	.611	75.2	.611	
15	16	78.3	.672	84.1	.653	88.7	.602	74.2	.603	
16	16½	80.2	.689	84.0	.652	87.9	.596	73.3	.595	
17	17	78.3	.672	83.2	.646	87.1	.591	72.3	.587	
18	17½	77.3	.664	81.1	.630	86.6	.588	71.8	.583	
19	18	76.4	.656	79.0	.613	84.8	.575	69.9	.568	
20	19	76.8	.659	77.8	.604	83.2	.565	68.5	.556	
21	20	76.7	.658	75.9	.589	82.5	.560	67.5	.548	
22	21	76.5	.656	75.1	.583	81.4	.552	66.4	.539	
23	22	74.1	.636	73.5	.570	80.1	.544	66.5	.540	
24	23	71.8	.616	71.7	.556	78.9	.536	65.3	.531	
25	24							64.4	.524	

(See Table 12)

* Assumed Station 8 Total Pressure Ratio P₈/P₀ = .627

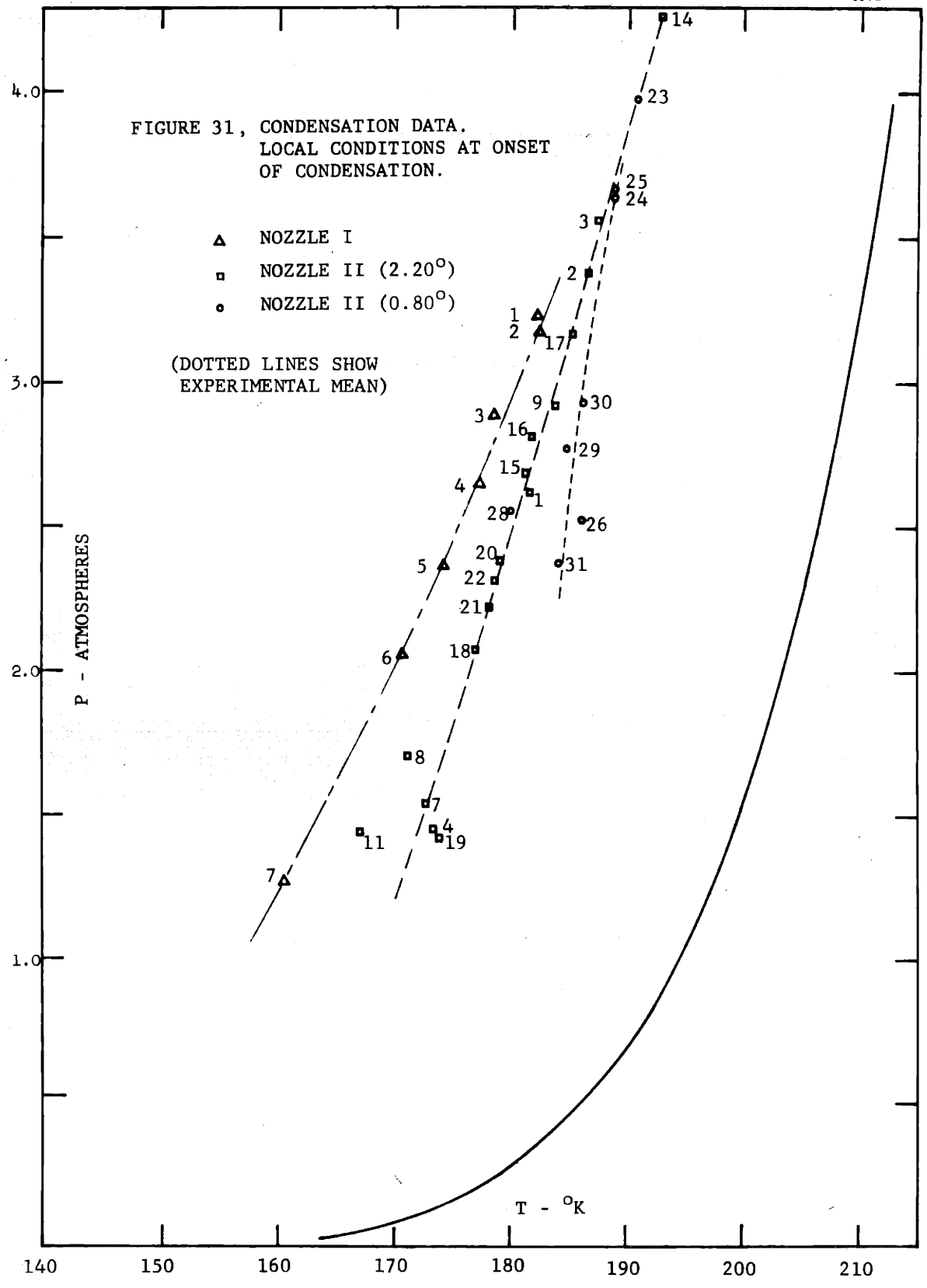


TABLE 14
EXPERIMENTAL DATA
LOCAL CONDITIONS AT ONSET OF CONDENSATION

Run	P _o (atm)	T _o °K	z _o	P (atm)	T °K	z
1I	7.64	227.2	.892	3.23	182.5	.889
2I	7.67	228.6	.895	3.18	182.6	.892
3I	7.66	229.1	.896	2.89	178.7	.892
4I	7.42	230.3	.902	2.66	177.3	.898
5I	7.04	230.3	.907	2.37	174.5	.903
6I	6.65	230.3	.913	2.06	170.8	.908
7I	5.14	230.3	.934	1.26	160.8	.927
1II	7.81	239.9	.913	2.62	181.9	.910
2II	8.01	232.4	.897	3.38	186.9	.895
3II	8.01	230.3	.893	3.56	187.6	.891
4II	7.36	260.0	.942	1.46	173.5	.938
5II			Non-Condensing			
6II			Non-Condensing			
7II	5.47	238.3	.939	1.54	172.9	.935
8II	5.87	234.4	.929	1.71	171.3	.925
9II	7.81	236.6	.907	2.92	184.1	.905
10II			Non-Condensing			
11II	7.66	254.6	.934	1.45	167.2	.929
12II			Non-Condensing			
13II			Non-Condensing			
14II	9.19	234.8	.886	4.25	193.1	.884
15II	7.02	231.3	.909	2.69	181.3	.906
16II	7.63	233.6	.905	2.84	181.8	.902
17II	7.66	232.0	.901	3.17	185.5	.899
18II	5.76	231.1	.926	2.07	178.2	.923
19II	4.37	231.4	.946	1.43	174.1	.942
20II	6.48	230.9	.916	2.39	179.2	.912
21II	6.14	230.5	.920	2.23	178.3	.915
22II	7.40	240.0	.918	2.31	178.7	.914
23II	8.72	232.8	.888	4.00	191.0	.886
24II	8.28	233.1	.895	3.64	189.2	.893
25II	8.95	237.0	.893	3.68	189.2	.891
26II	6.92	240.6	.925	2.52	185.5	.922
27II			Non Condensing			
28II	6.24	225.7	.911	2.57	185.1	.907
29II	6.88	233.0	.914	2.77	185.1	.911
30II	7.86	239.2	.911	2.93	186.4	.909
31II	6.54	237.8	.925	2.58	184.2	.923

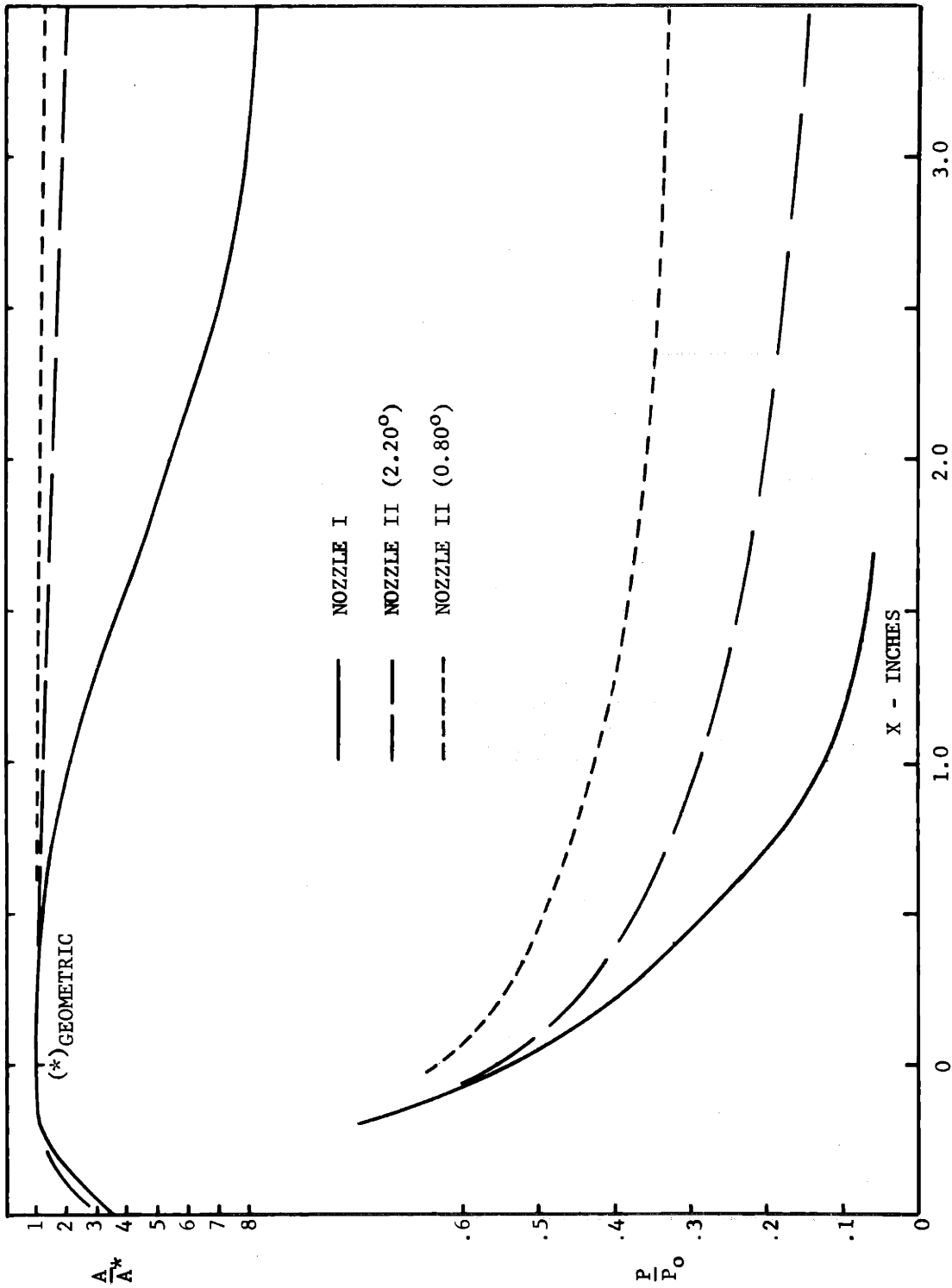


FIGURE 32, COMPARISON OF NOZZLE GEOMETRIES AND NON-CONDENSING PRESSURE PROFILES.

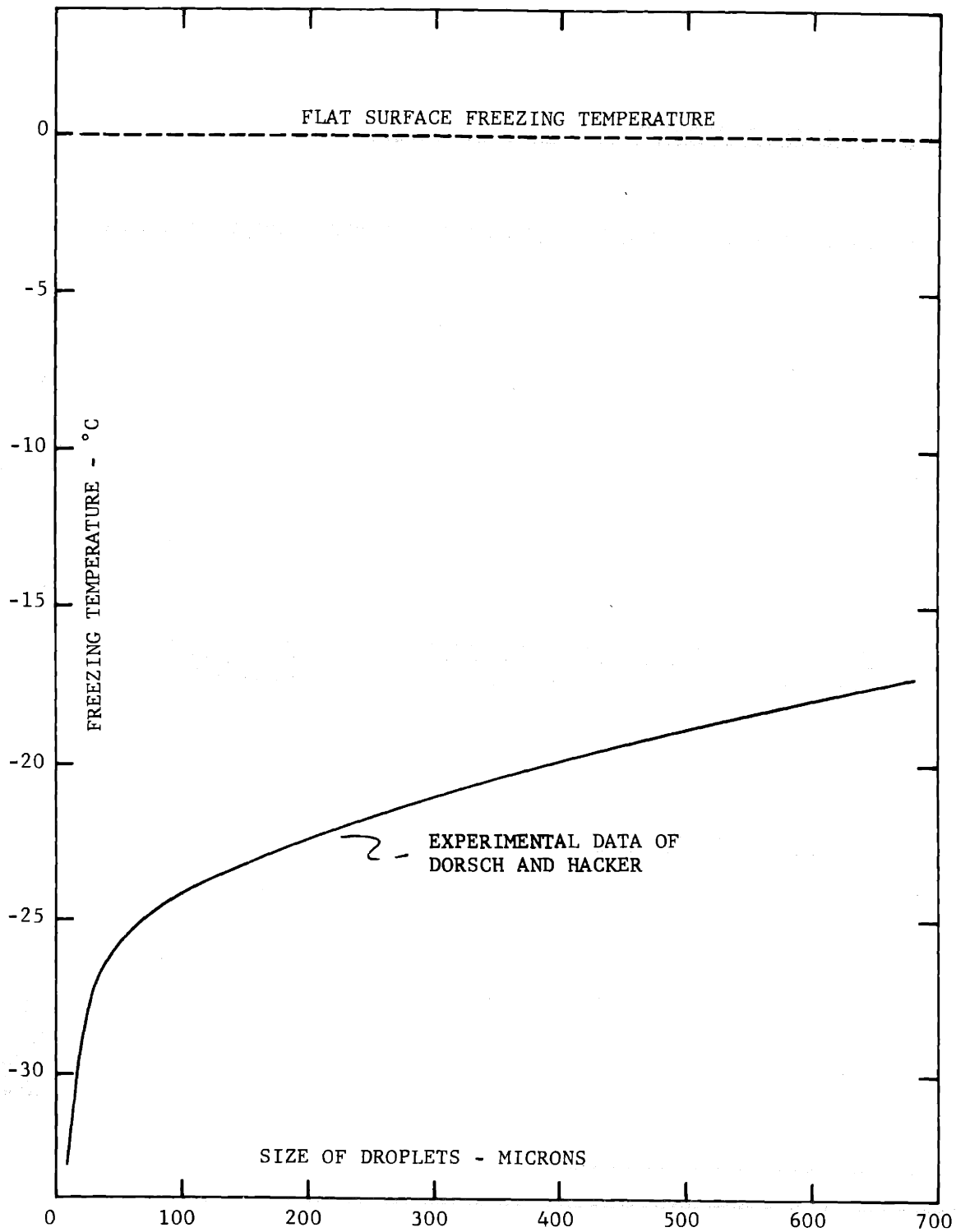


FIGURE 33, SPONTANEOUS FREEZING TEMPERATURE OF SUPERCOOLED WATER DROPLETS ON PLATINUM AND COPPER SURFACES.

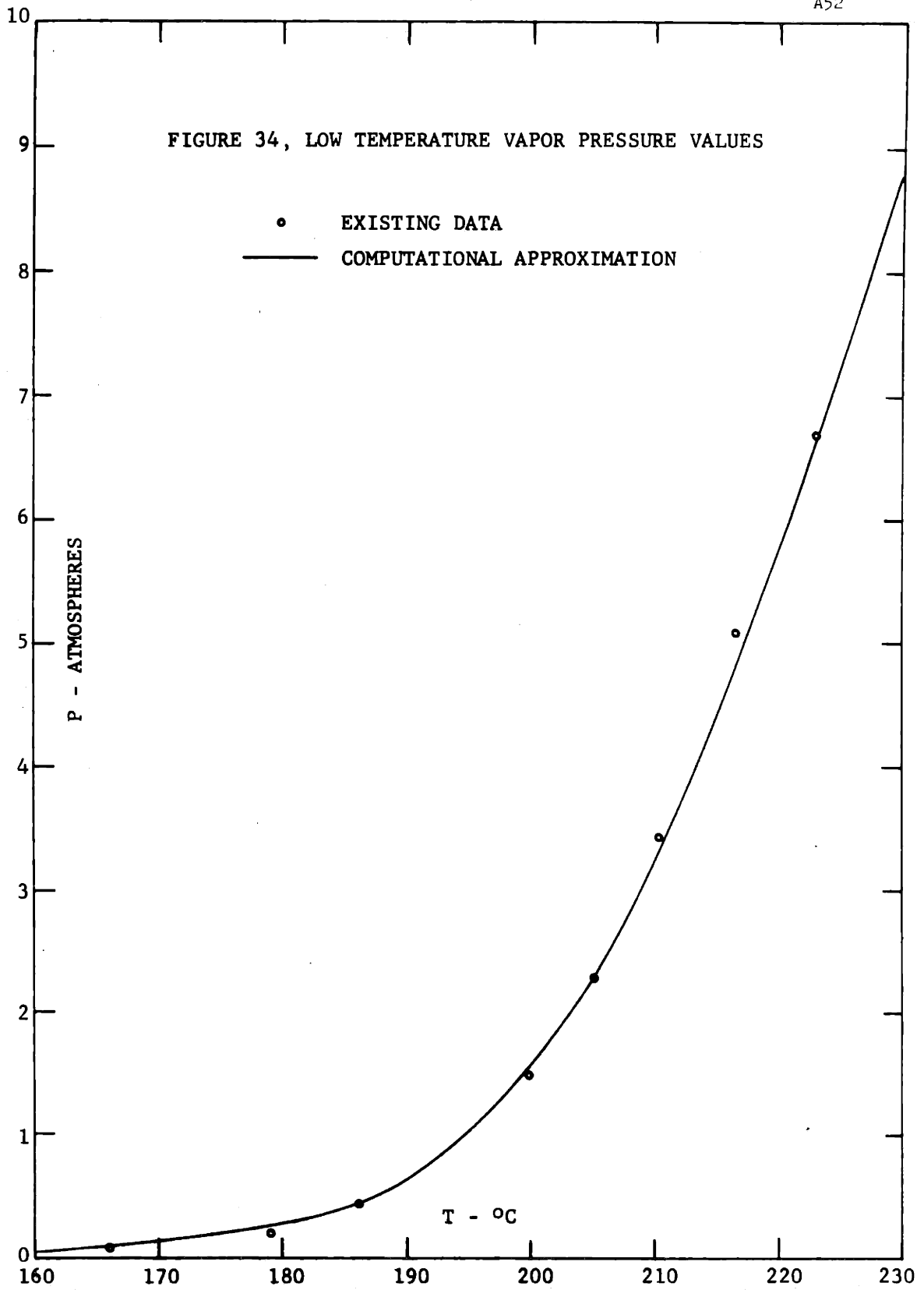


FIGURE 35, PRESENCE OF MOISTURE IN A TYPICAL CONDENSATION PROFILE.

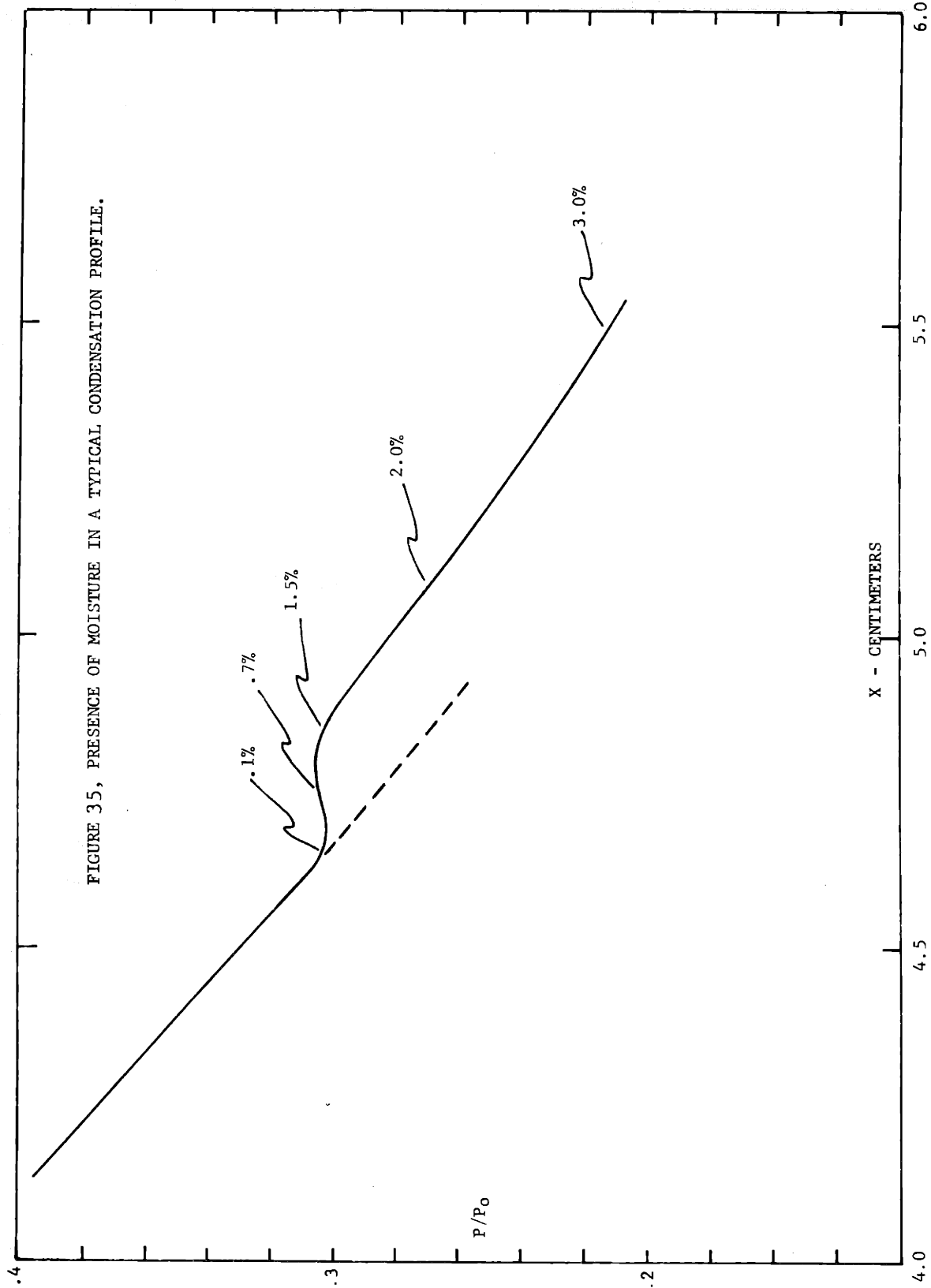
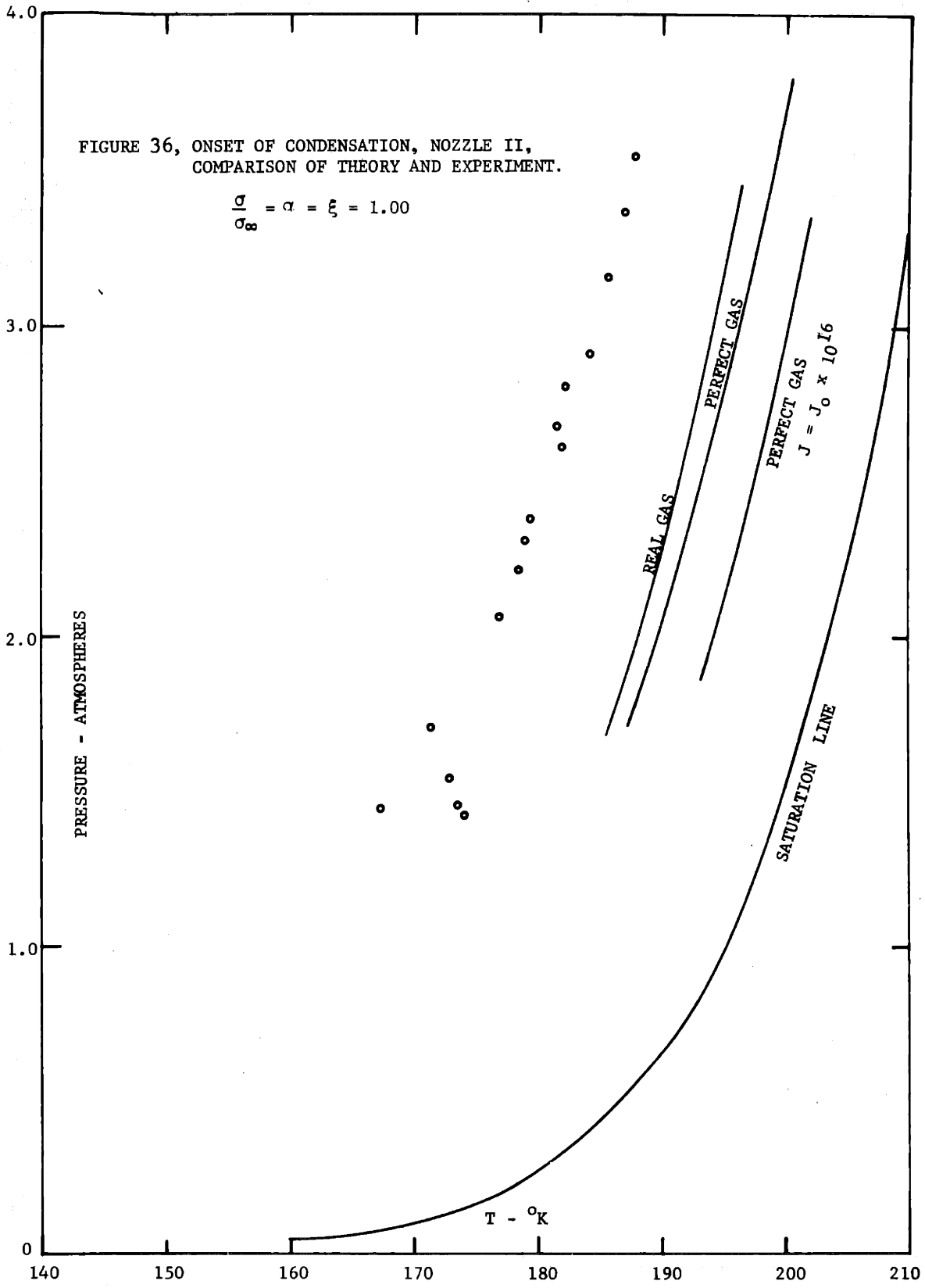
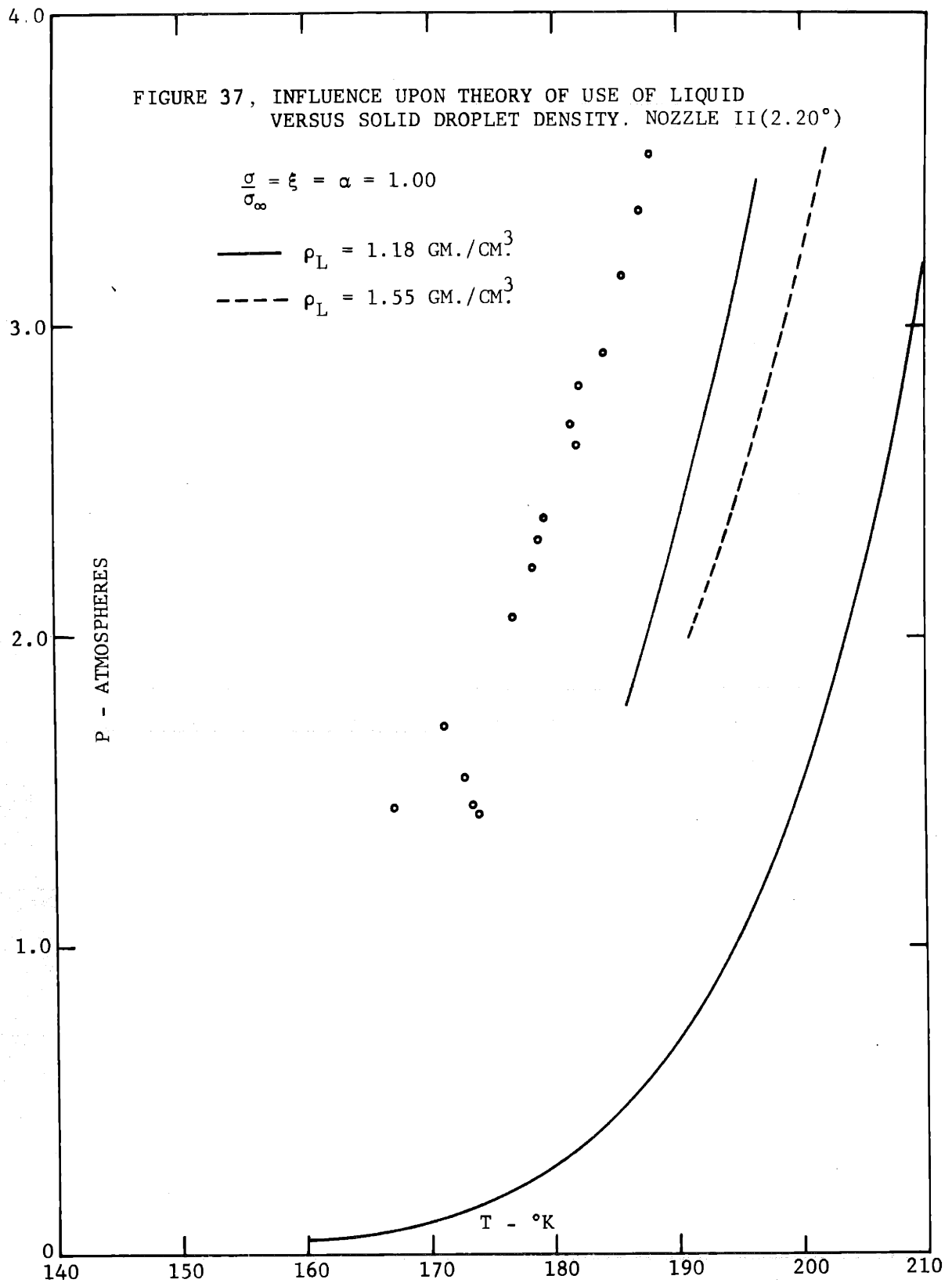


FIGURE 36, ONSET OF CONDENSATION, NOZZLE II,
COMPARISON OF THEORY AND EXPERIMENT.

$$\frac{\sigma}{\sigma_8} = \alpha = \xi = 1.00$$





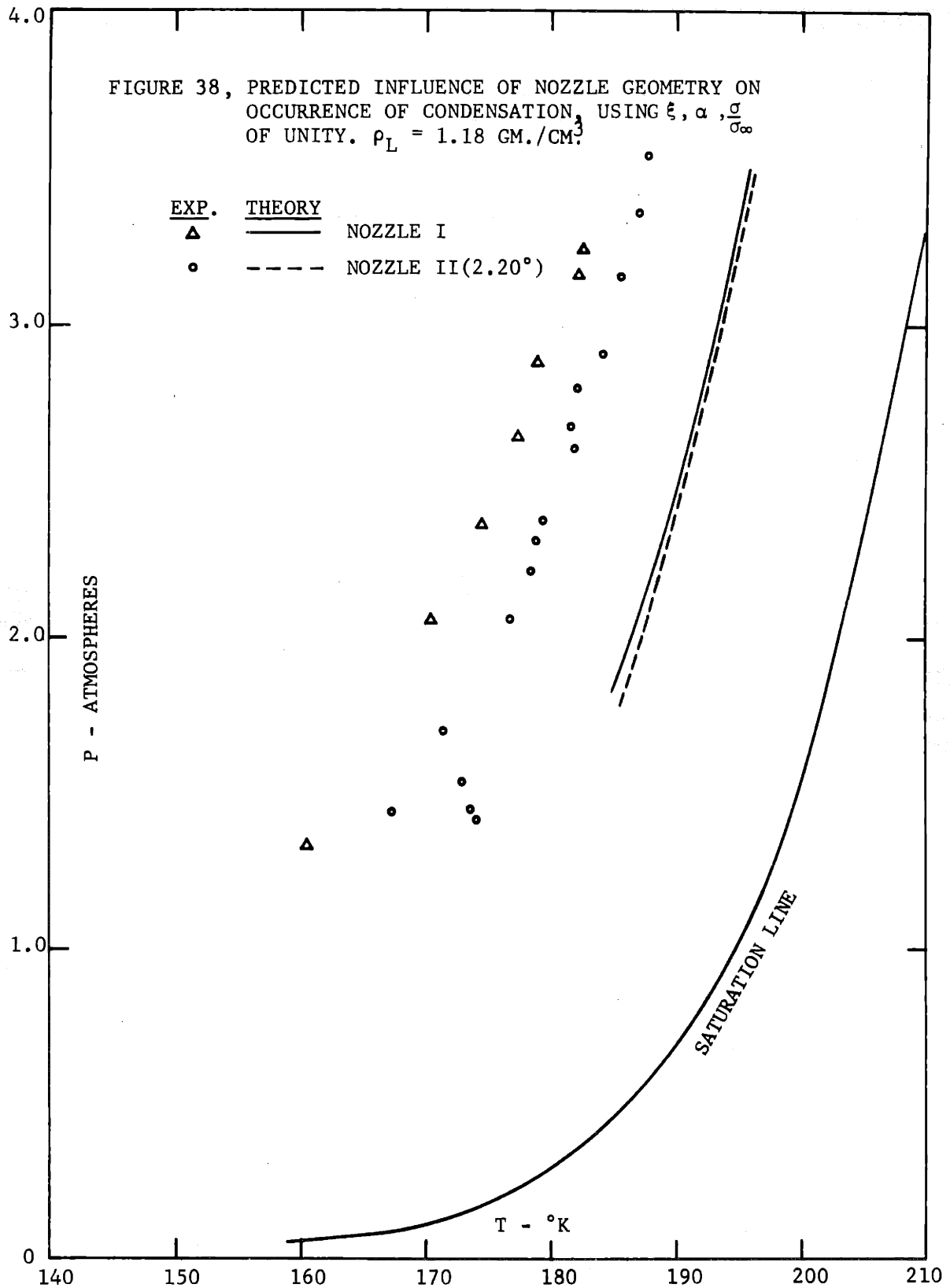


FIGURE 39, INFLUENCE OF MASS ACCOMMODATION COEFFICIENT ON CONDENSATION OF CO₂, (THEORETICAL).

$T_0 = -26.0 \text{ C}$ $\rho_L = 1.18 \text{ GM./CM.}^3$
 $P_0 = 5.39 \text{ ATM.}$
 $\frac{\sigma}{\sigma_\infty} = 1.00$
 $\alpha = .10$

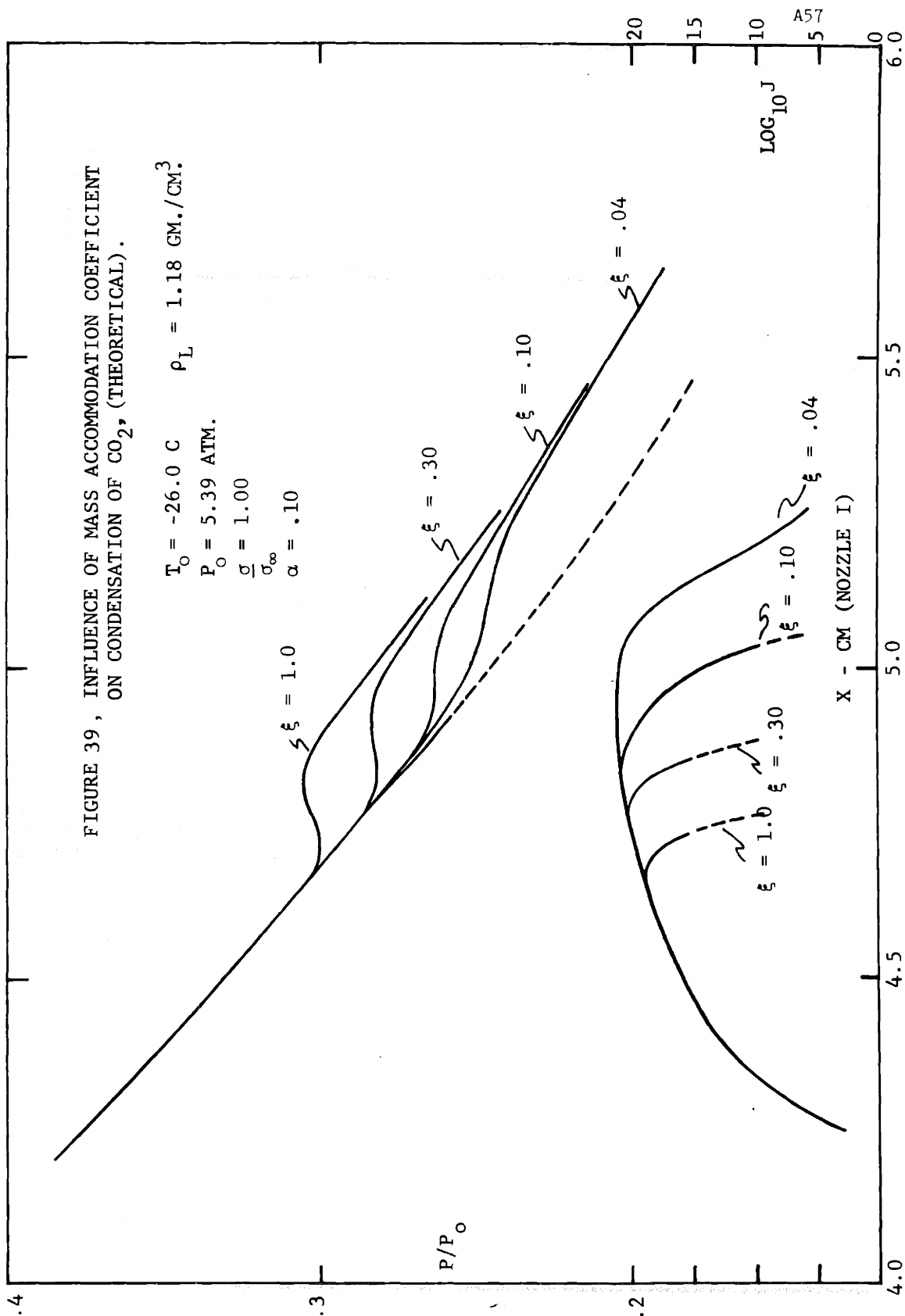


FIGURE 40, INFLUENCE OF THERMAL ACCOMMODATION ON THEORETICAL CONDENSATION OF CO₂.

$P_0 = 5.39 \text{ ATM.}$
 $T_0 = -26.0^\circ\text{C}$
 PERFECT GAS, $\gamma = 1.32$
 $\xi = .04, \rho_L = 1.18, \frac{\sigma}{\sigma_\infty} = 1.00$

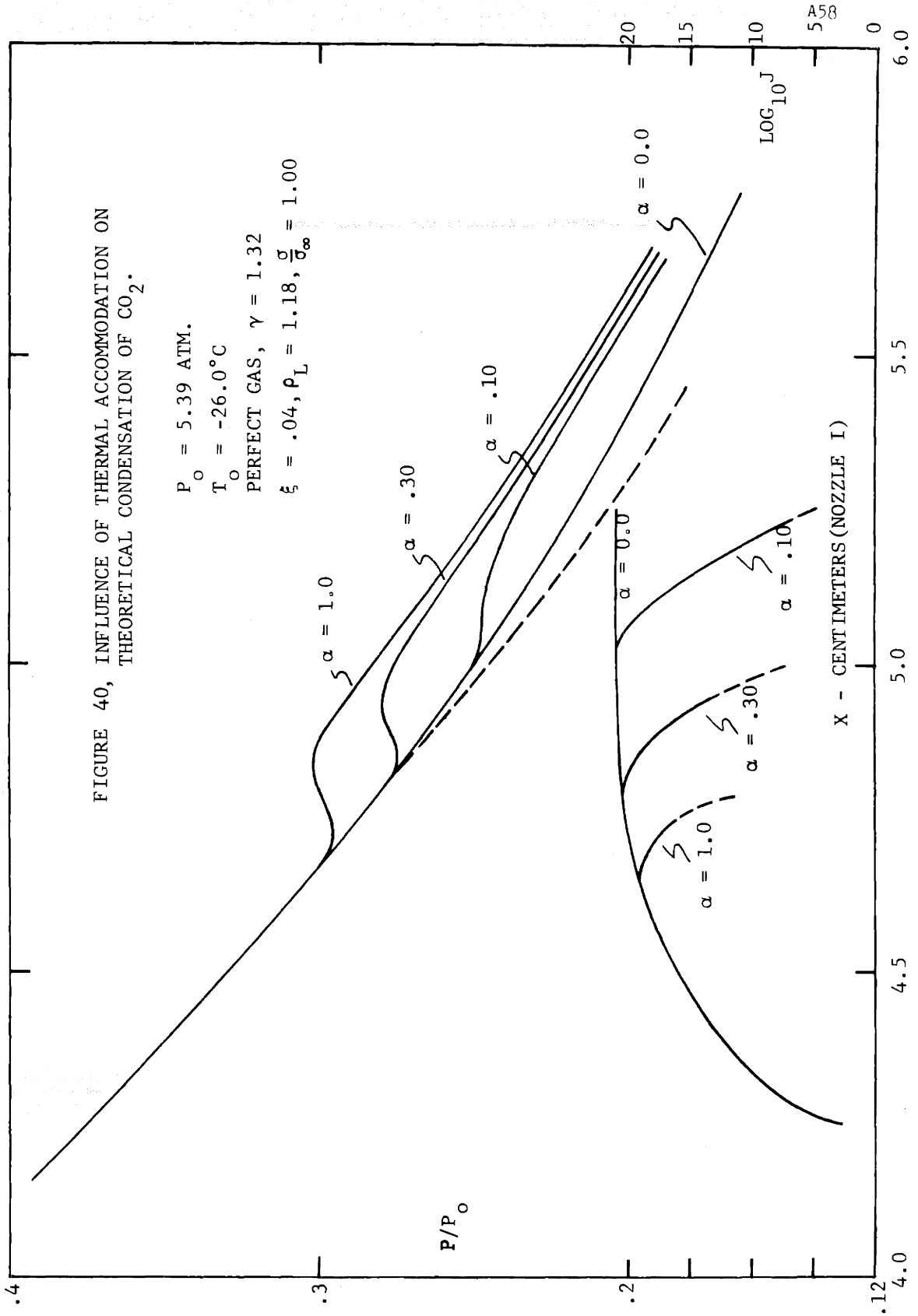
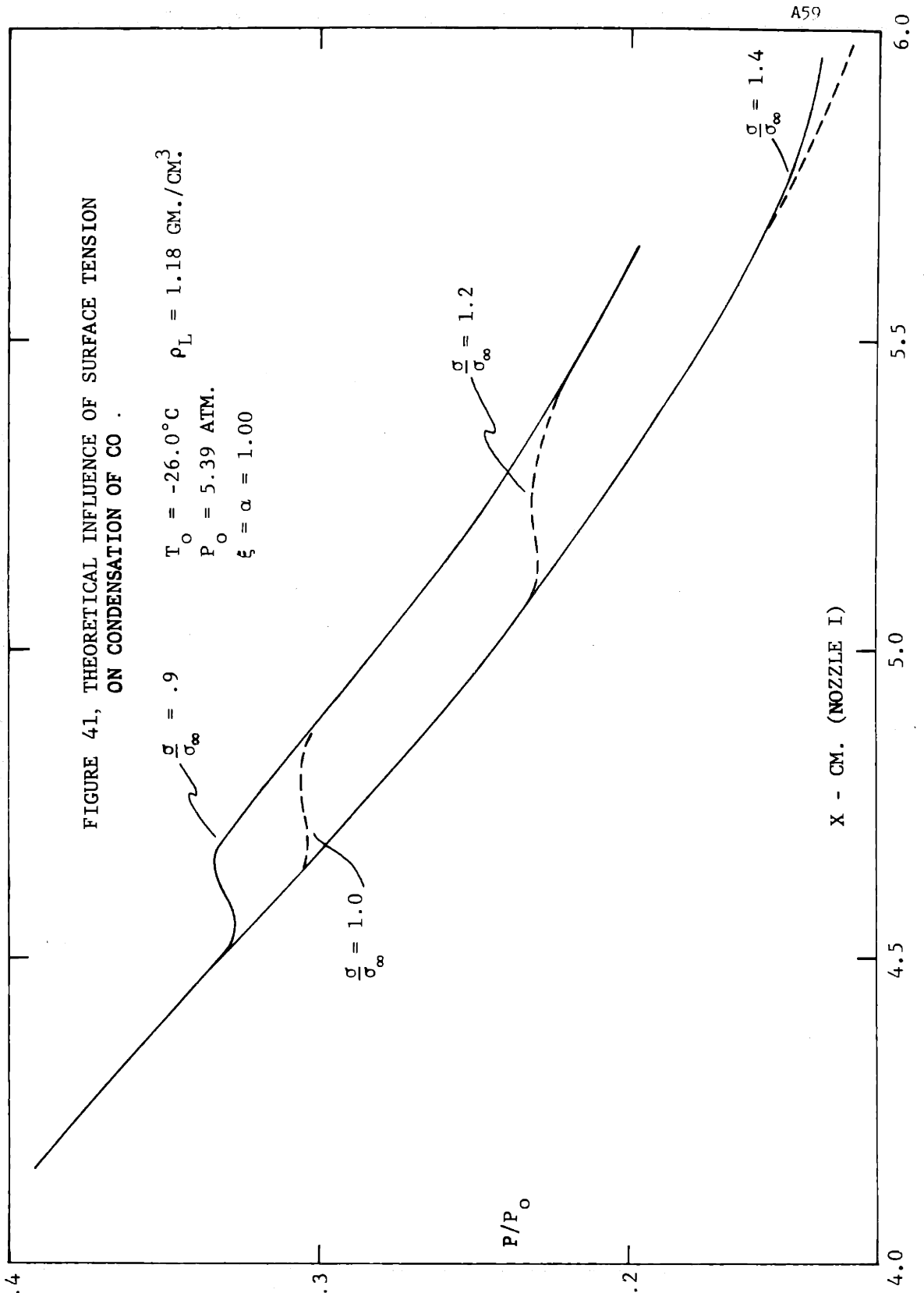
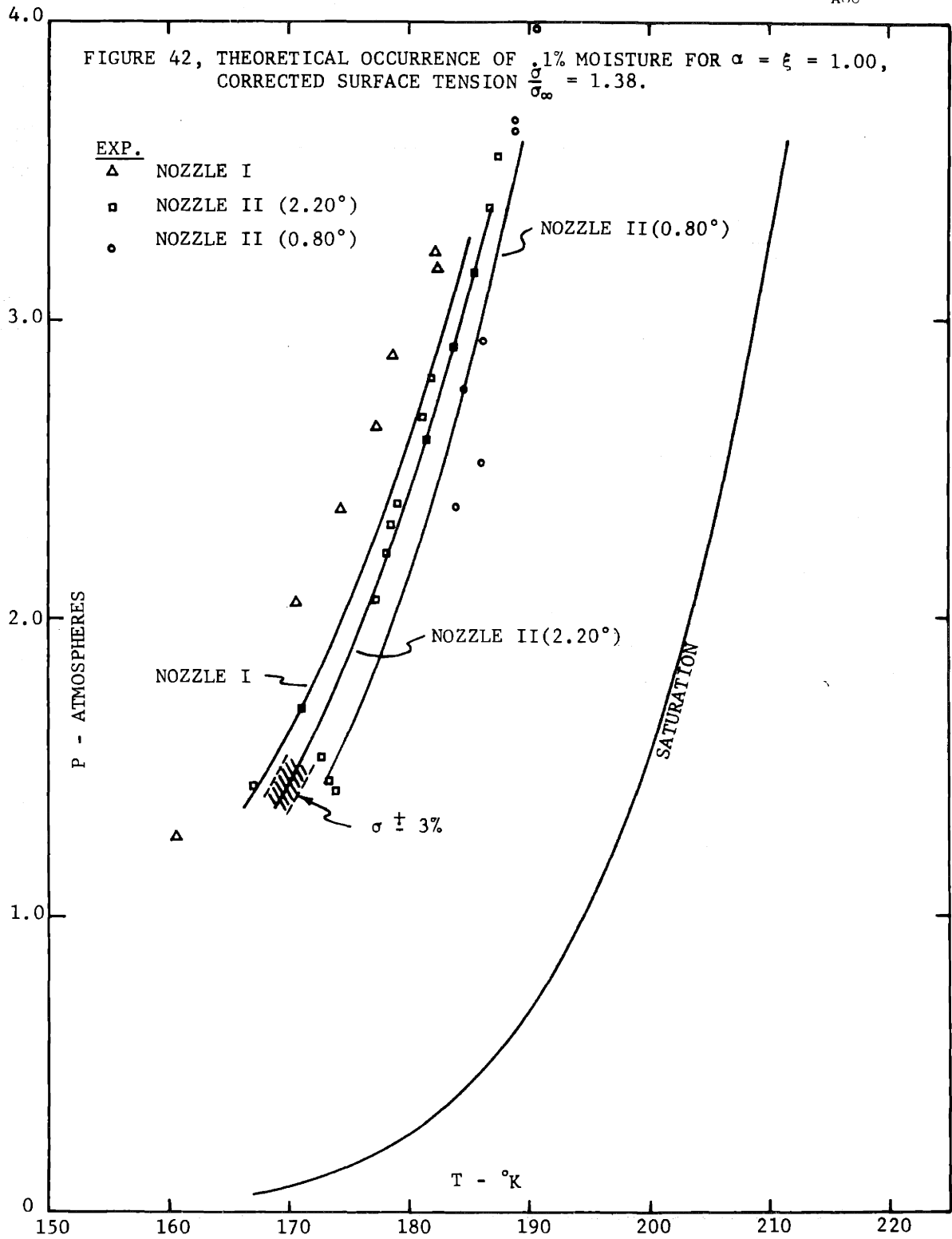
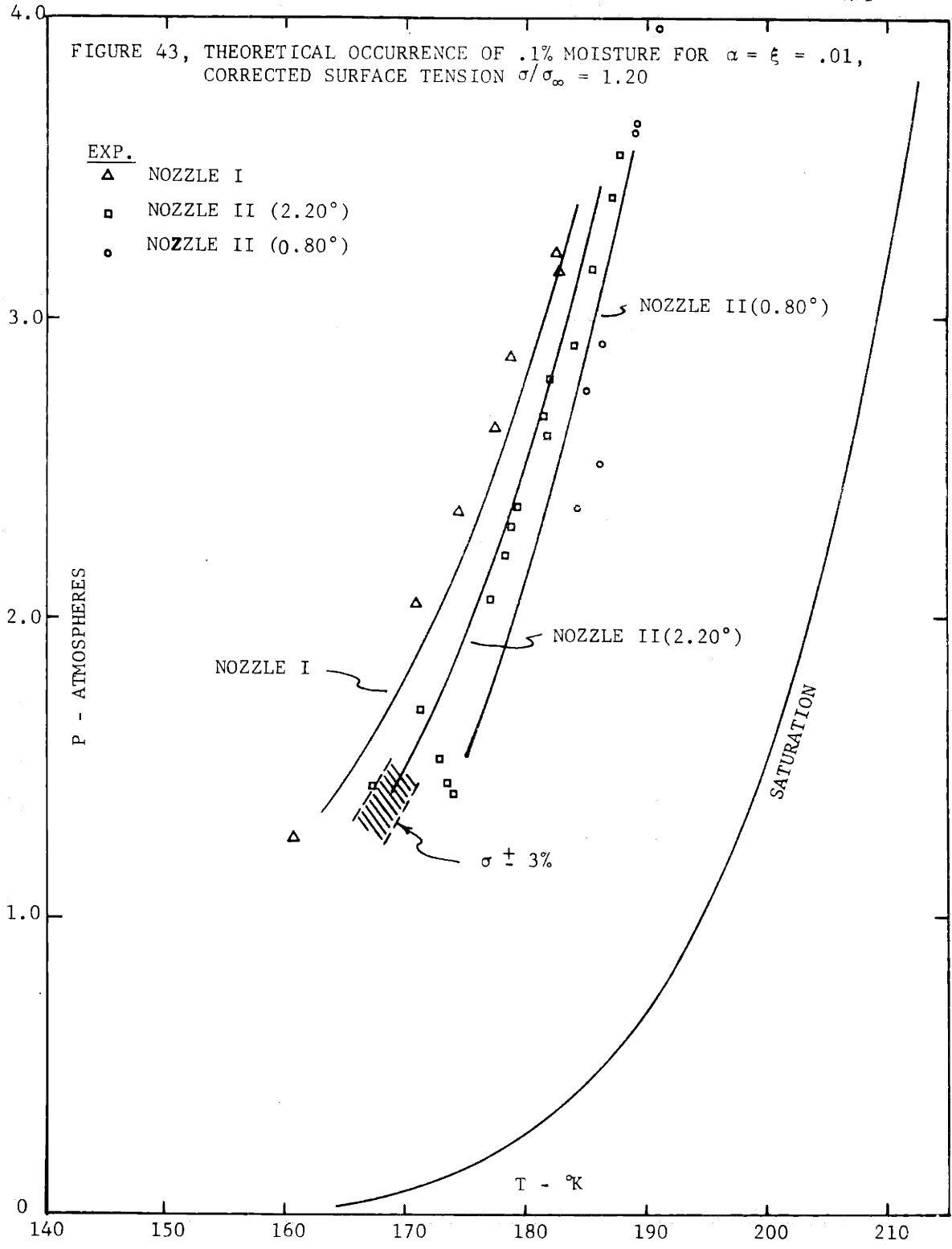


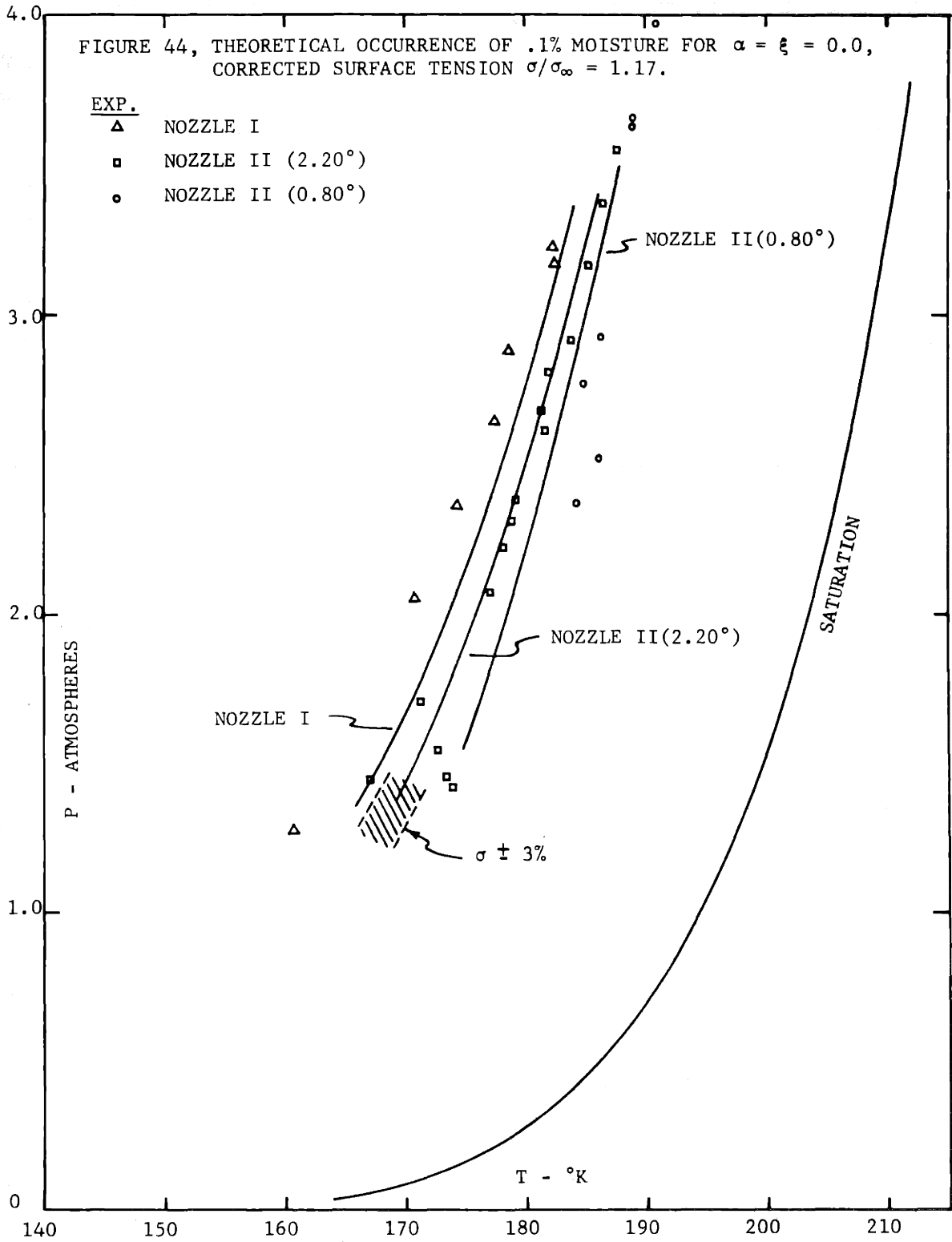
FIGURE 41, THEORETICAL INFLUENCE OF SURFACE TENSION ON CONDENSATION OF CO .

$T_0 = -26.0^\circ\text{C}$ $\rho_L = 1.18 \text{ GM./CM.}^3$
 $P_0 = 5.39 \text{ ATM.}$
 $\xi = \alpha = 1.00$









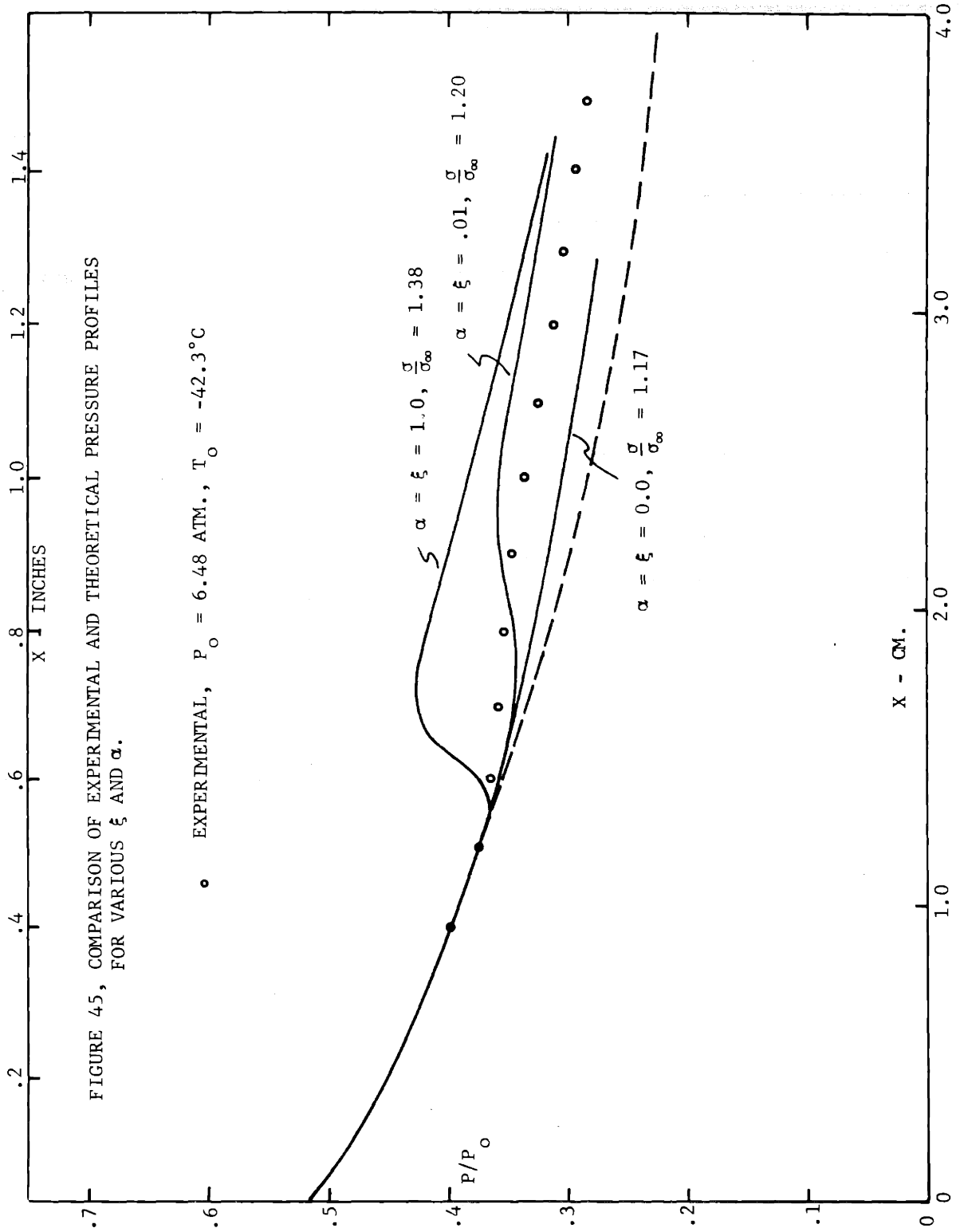
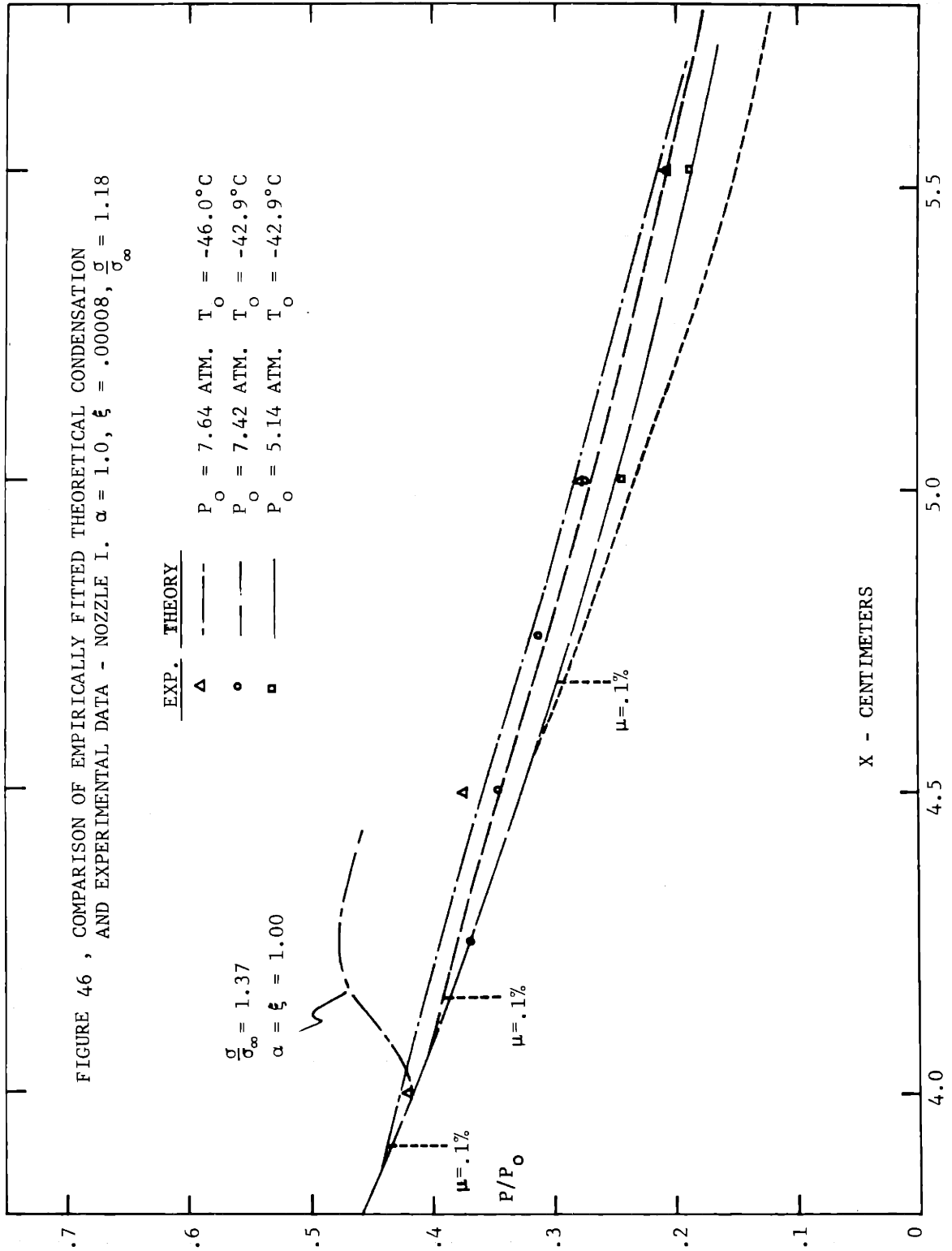


FIGURE 46 , COMPARISON OF EMPIRICALLY FITTED THEORETICAL CONDENSATION AND EXPERIMENTAL DATA - NOZZLE I. $\alpha = 1.0$, $\xi = .00008$, $\frac{\sigma}{\sigma_\infty} = 1.18$



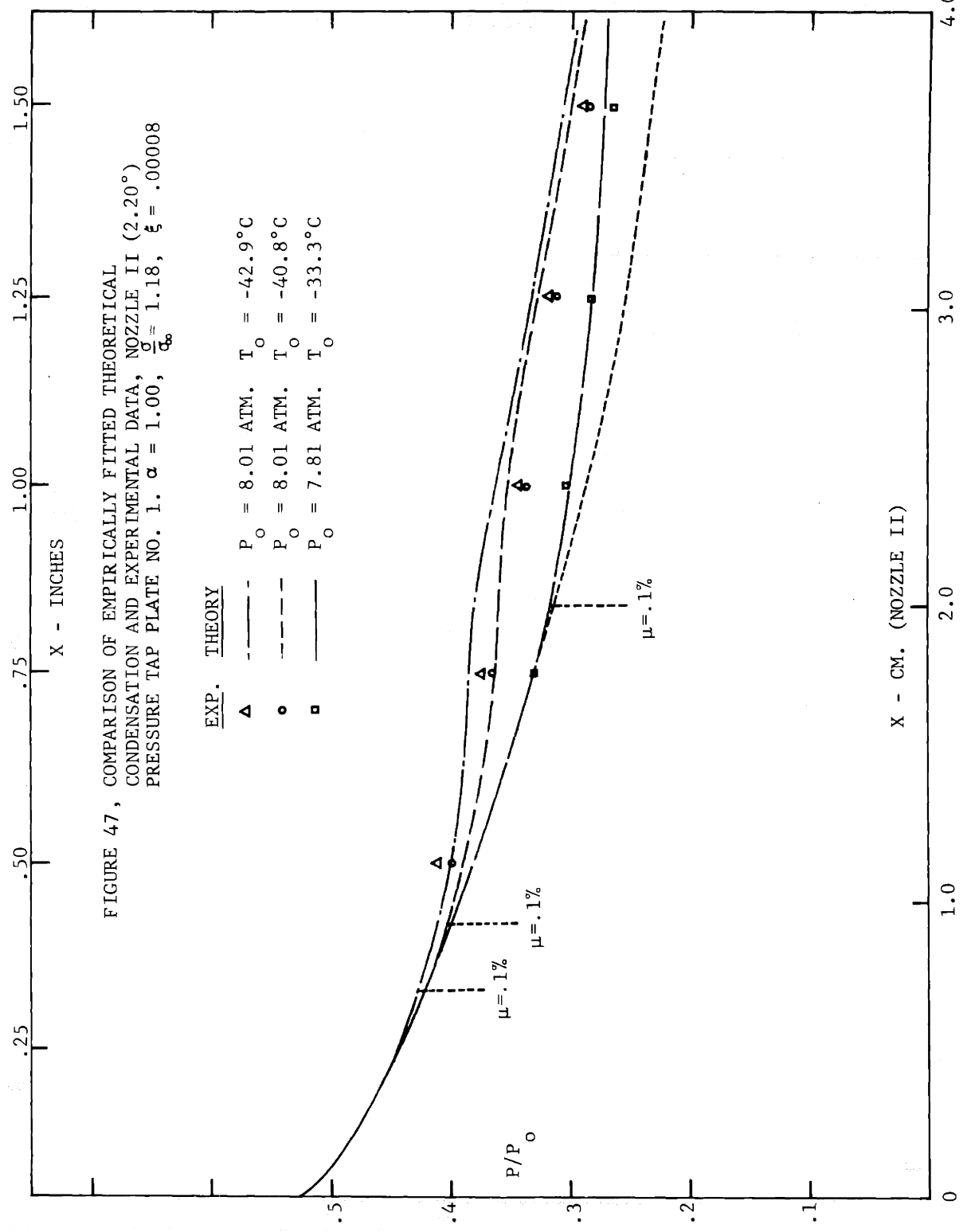
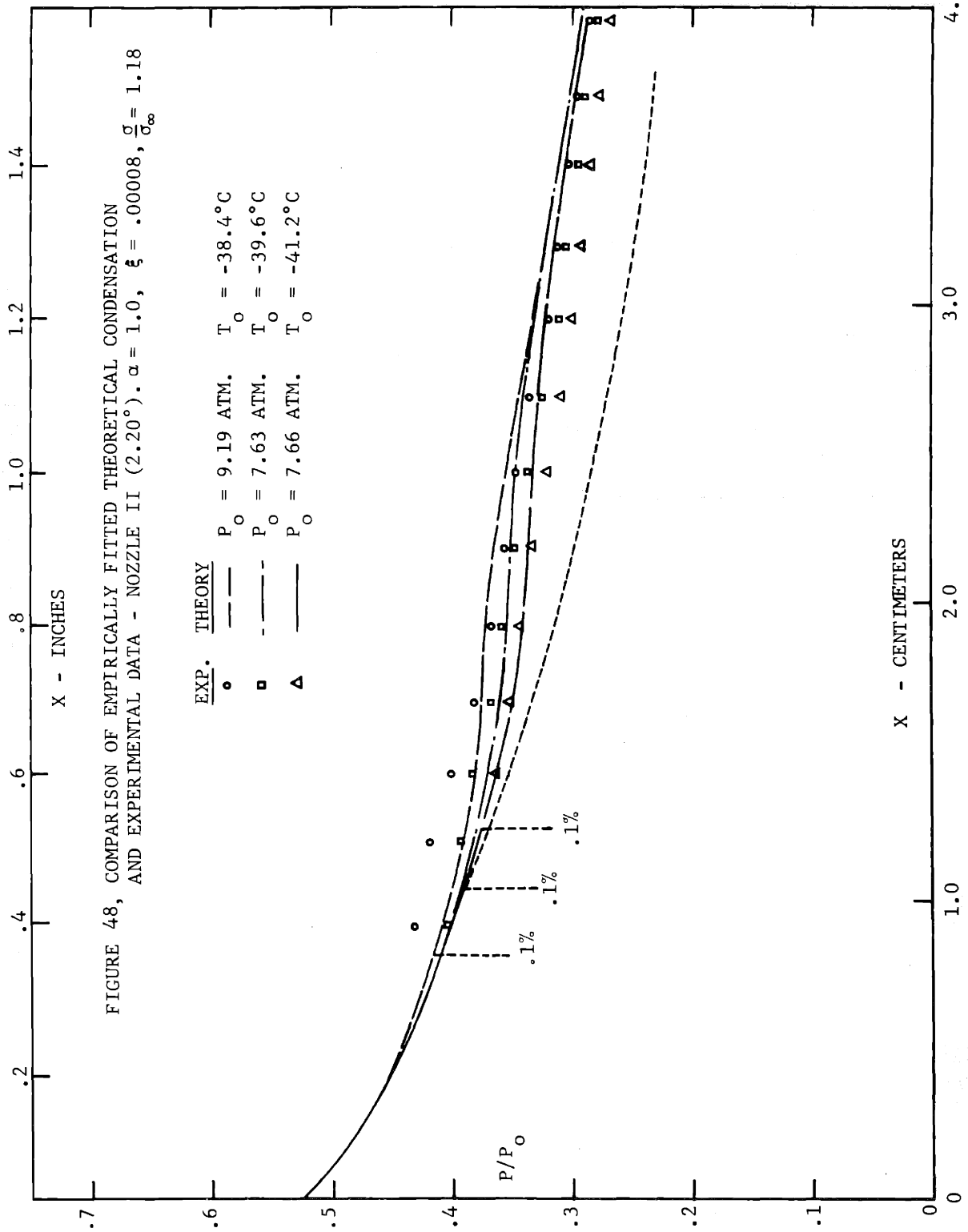


FIGURE 47, COMPARISON OF EMPIRICALLY FITTED THEORETICAL CONDENSATION AND EXPERIMENTAL DATA, NOZZLE II (2.20°) PRESSURE TAP PLATE NO. 1. $\alpha = 1.00$, $\alpha_\infty = .00008$

EXP. THEORY

- Δ - - - - $P_0 = 8.01$ ATM. $T_0 = -42.9^\circ\text{C}$
- \circ - - - - $P_0 = 8.01$ ATM. $T_0 = -40.8^\circ\text{C}$
- \square — — — $P_0 = 7.81$ ATM. $T_0 = -33.3^\circ\text{C}$

X - CM. (NOZZLE II)



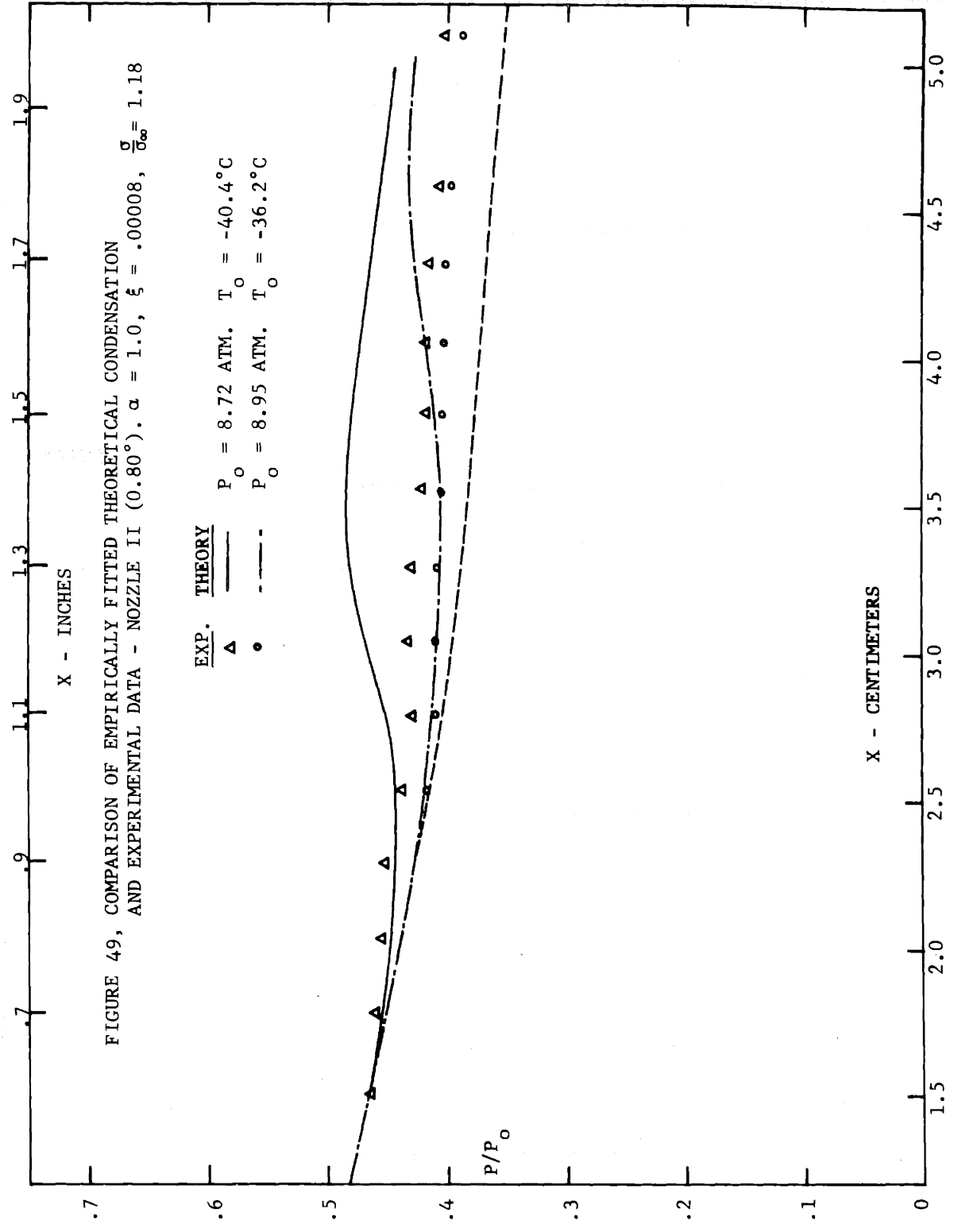
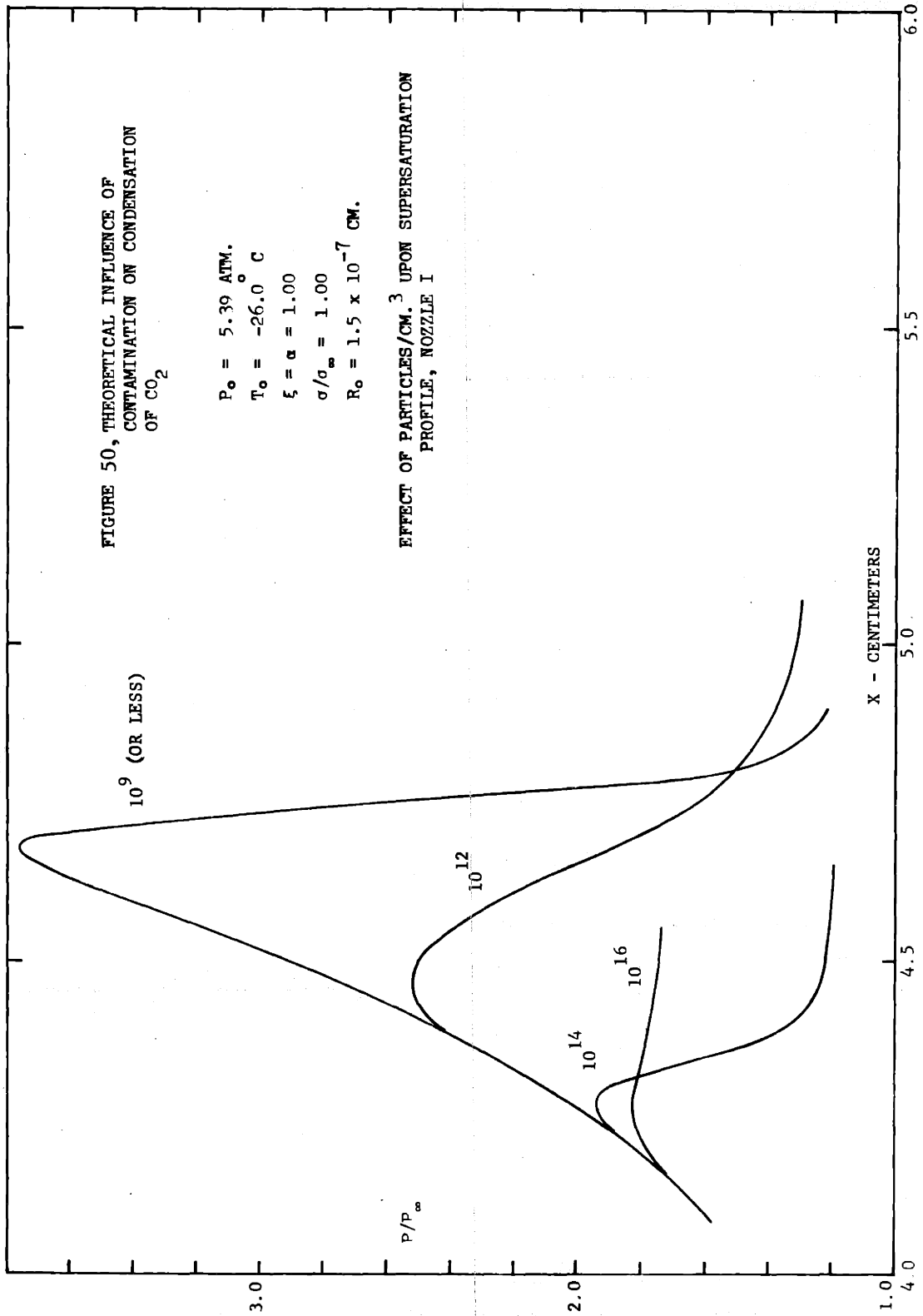
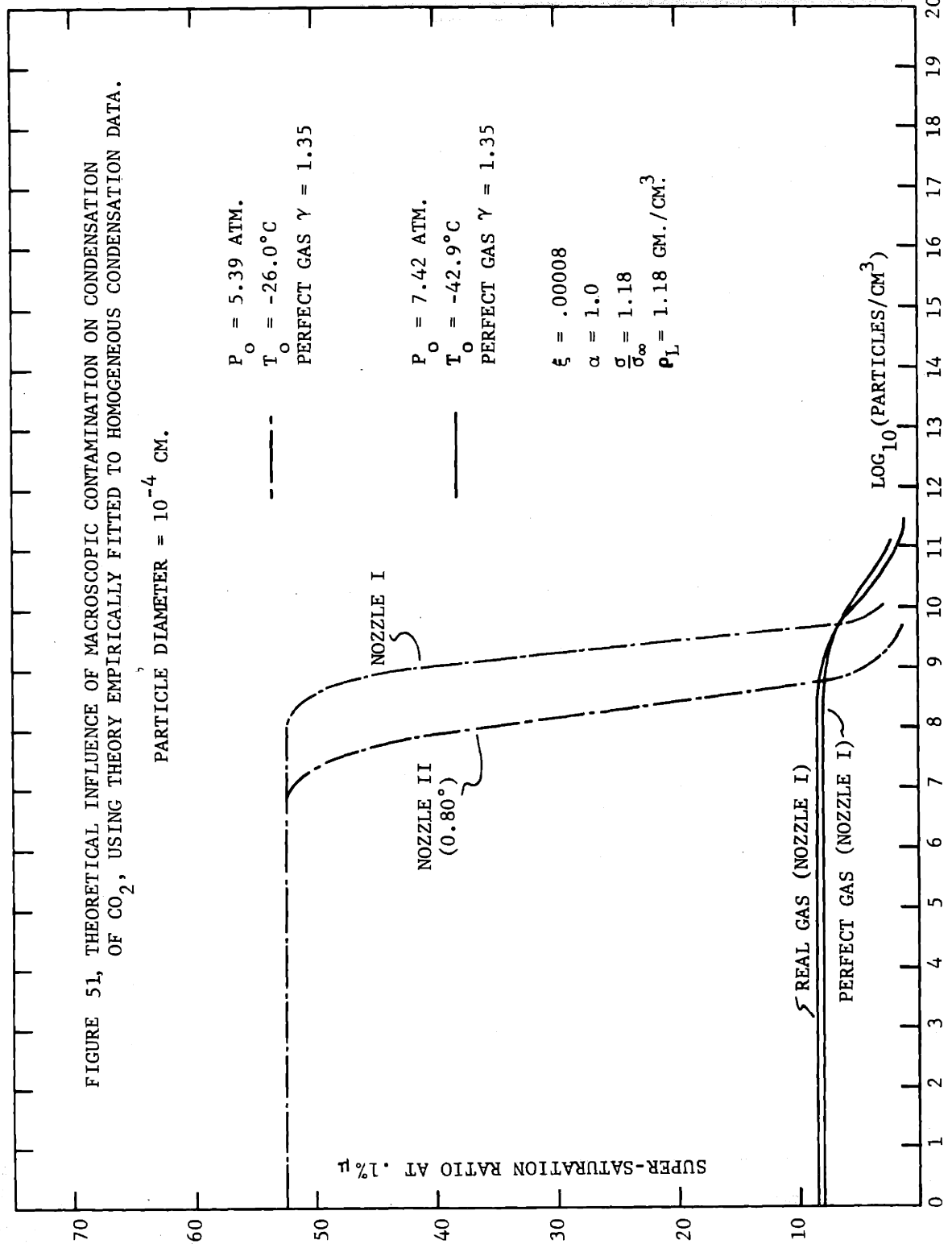


FIGURE 49, COMPARISON OF EMPIRICALLY FITTED THEORETICAL CONDENSATION AND EXPERIMENTAL DATA - NOZZLE II (0.80°). $\alpha = 1.0$, $\xi = .00008$, $\frac{\sigma}{\sigma_{\infty}} = 1.18$

EXP. THEORY
 Δ ———— $P_0 = 8.72$ ATM. $T_0 = -40.4^\circ\text{C}$
 \circ - - - - $P_0 = 8.95$ ATM. $T_0 = -36.2^\circ\text{C}$





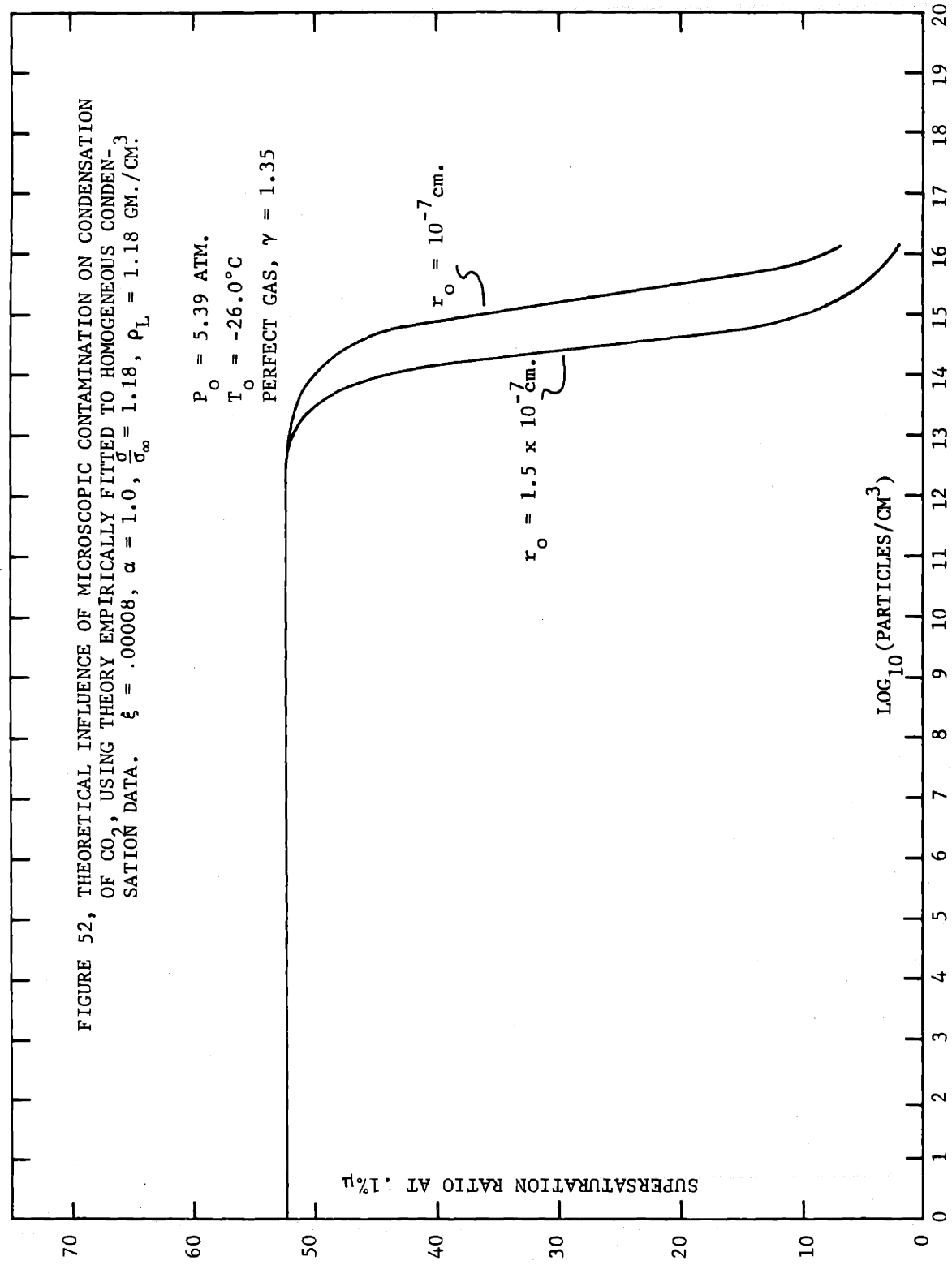


FIGURE 53, THEORETICAL EFFECT OF CO₂ CONTAMINATION ON NITROGEN CONDENSATION. SUPERSATURATION AT .1% MOISTURE.

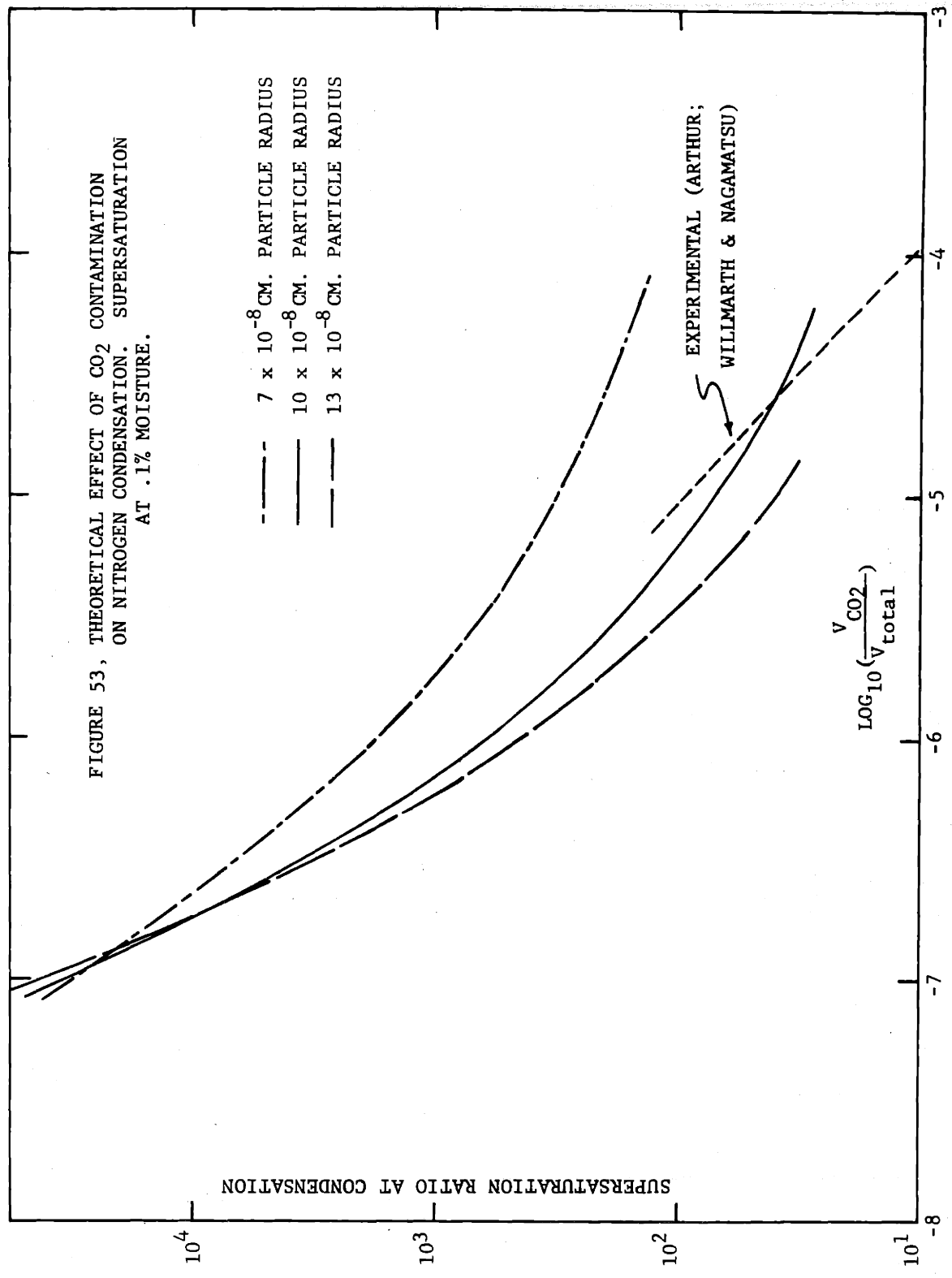


TABLE 15

VALUES OF γ_a , γ_b and z USED TO MATCH REAL GAS ISENTROPES

Run	P_0 (atm)	T_0 °K	γ_a	γ_b	z
1 _I	7.64	227.2	1.3736	.000400	.8902
2 _I	7.67	228.6	1.3717	.000407	.8949
3 _I	7.66	229.1	1.3685	.000431	.8932
4 _I	7.42	230.3	1.3643	.000442	.8988
5 _I	7.04	230.3	1.3597	.000449	.9045
6 _I	6.65	230.3	1.3539	.000481	.9101
7 _I	5.14	230.3	1.3403	.000560	.9314
1 _{II}	7.81	239.9	1.3557	.000453	.9114
2 _{II}	8.01	232.4	1.3711	.000401	.8949
3 _{II}	8.01	230.3	1.3735	.000398	.8906
4 _{II}	7.36	260.0	1.3342	.000505	.9416
7 _{II}	5.47	238.3	1.3335	.000536	.9367
8 _{II}	5.87	234.4	1.3419	.000500	.9277
9 _{II}	7.81	236.6	1.3606	.000445	.9057
11 _{II}	7.66	254.6	1.3415	.000455	.9335
14 _{II}	9.19	234.8	1.3795	.000376	.8841
15 _{II}	7.02	231.3	1.3566	.000469	.9067
16 _{II}	7.63	233.6	1.3614	.000450	.9031
17 _{II}	7.66	232.0	1.3675	.000397	.8990
18 _{II}	5.76	231.1	1.3435	.000500	.9247
19 _{II}	4.37	231.4	1.3278	.000570	.9438
20 _{II}	6.48	230.9	1.3515	.000483	.9141
21 _{II}	6.14	230.5	1.3477	.000500	.9183
22 _{II}	7.40	240.0	1.3513	.000465	.9167
23 _{II}	8.72	232.8	1.3782	.000387	.8857
24 _{II}	8.28	233.1	1.3718	.000394	.8937
25 _{II}	8.95	237.0	1.3768	.000358	.8917
26 _{II}	6.92	240.6	1.3457	.000390	.9232
28 _{II}	6.24	225.7	1.3544	.000488	.9083
29 _{II}	6.88	233.0	1.3551	.000455	.9118
30 _{II}	7.86	239.2	1.3566	.000456	.9098
31 _{II}	6.54	237.8	1.3440	.000493	.9237

APPENDIX BREVIEW OF NUCLEATION RATE EQUATION DEVELOPMENT

The following is a review of the classical nucleation rate equation as developed by J. Frenkel⁽¹⁹⁾. Although Frenkel was not the first to investigate nucleation theory, his result is not greatly different from earlier authors mentioned in the text, and his method provides relatively straightforward consideration of the important aspects and assumptions in classical nucleation theory

Frenkel's droplet model was based on Volmer's⁽⁵⁸⁾ earlier model of droplets as generalized molecules, neglecting intermolecular forces, and his method of development was based on that of Zeldovich⁽⁶⁸⁾. He showed that the distribution of clusters of vapor molecules, resulting from the kinetic interaction of the molecules could be described by a Boltzmann distribution. That is, that (in equilibrium)

$$N(g) = N_0 \exp(-\Delta\phi/KT) \quad (B-1)$$

where N_0 = total number of molecules

$$\phi = H - TS$$

$\Delta\phi = \phi_L - \phi_V$ = change in free energy of a group of (g) free molecules when forming a liquid embryo.

Several simplifying assumptions of debatable validity are made at this point. First, the droplet model is taken to be a liquid sphere, having surface energy described by the flat-film liquid surface tension (or some corrected function thereof). Second, the total change in free energy is assumed to be the work of formation of the surface of the droplet, plus the change in free energy resulting from the change in state of g molecules condensing from vapor to liquid, with the spherical droplet assumed to be stationary in the vapor system, and having no rotational or vibrational energy. This is the important distinction between classical and more recent "gassified"

droplet models of nucleation theory. Third, the droplet is assumed to form at environmental temperature, an assumption which may also be invalid⁽³²⁾.

Using these assumptions, and defining ϕ as the free energy per molecule, $\Delta\phi$ can then be written:

$$\Delta\phi = g(\phi_L - \phi_V) + 4\pi r^2\sigma \quad (\text{B-2})$$

$$= -T(\Delta S) + 4\pi r^2\sigma$$

$$= -gKT \ln \frac{p}{p_\infty} + 4\pi r^2\sigma \quad (\text{B-3})$$

where p_∞ equals the flat surface equilibrium pressure of a formed embryo of (g) molecules and p is the existing local pressure.

Hence,

$$N(g) = N_0 \exp\left(g \ln \frac{p}{p_\infty} - \frac{4\pi r^2\sigma}{KT}\right) \quad (\text{B-4})$$

Saying that:

$$gm = \frac{4}{3}\pi r^3\rho_L \quad (\text{B-5})$$

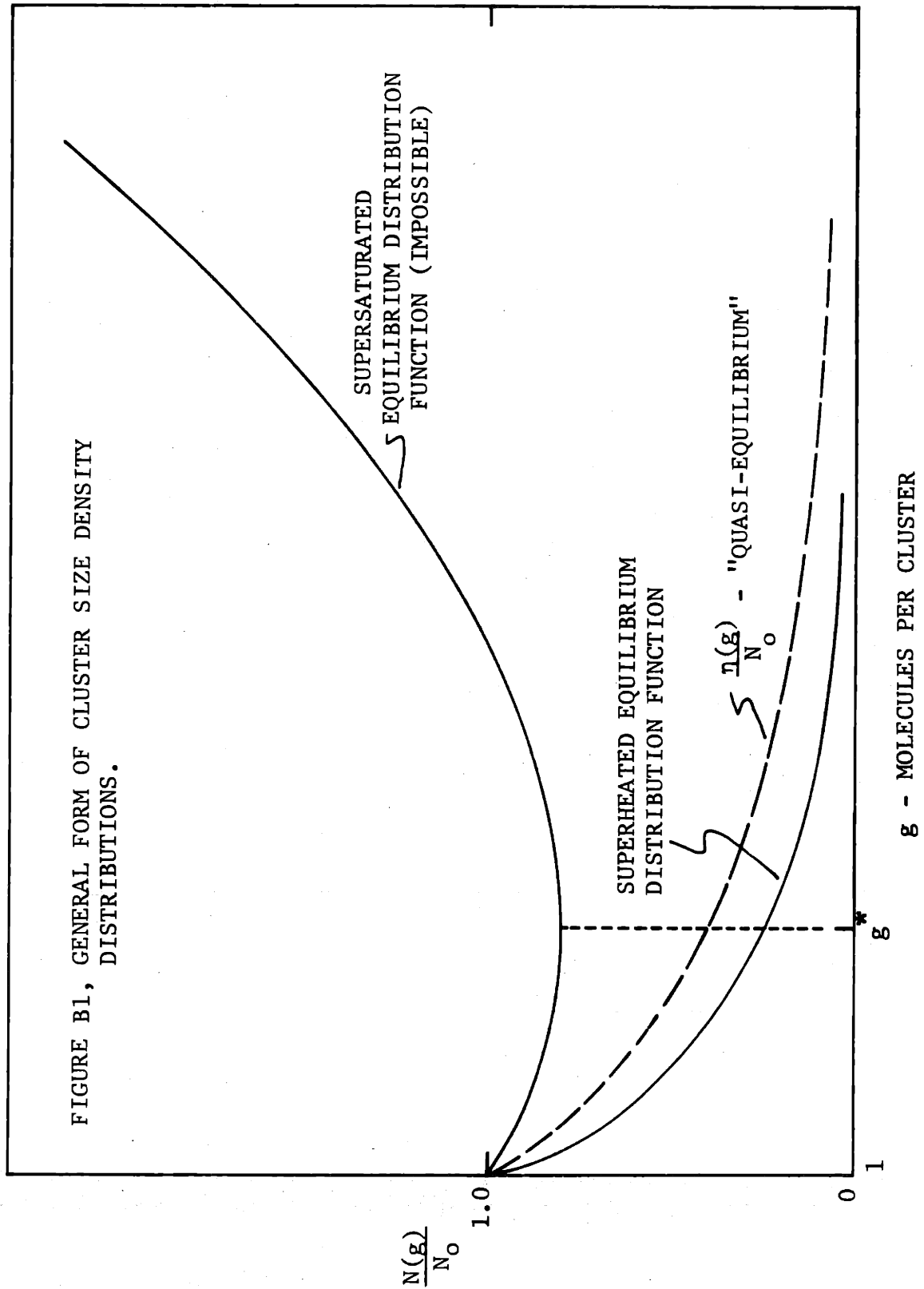
yields

$$N(g) = N_0 \exp\left\{g \ln \frac{p}{p_\infty} - \frac{4\pi\sigma}{KT} \left(\frac{3gm}{4\pi\rho}\right)^{2/3}\right\} \quad (\text{B-6})$$

$$= N_0 \exp\left\{g \ln \frac{p}{p_\infty} - \left(\frac{\epsilon}{KT}\right) g^{2/3}\right\}$$

where $\epsilon = 4\pi\sigma\left(\frac{3m}{4\pi\rho}\right)^{2/3}$

Inspection of Eq. (B-6) shows that a reasonable equilibrium distribution results when p is less than p_∞ , that is, in a superheated vapor. However, in a supersaturated vapor, an unreasonable and, in fact, impossible equilibrium distribution is predicted as seen in Fig. (B-1), since it predicts $N(g) \rightarrow \infty$ as $g \rightarrow \infty$. Acknowledging that an equilibrium distribution of drop sizes is unreasonable under supersaturated conditions, early authors treated the system as one in a state of quasi-equilibrium, where droplets are imagined to be removed after reaching some size larger than the critical radius, r^* , which occurs at the maximum of the supersaturated free energy change. This maximum in $\Delta\phi$ (minimum in $N(g)$) occurs when;



$$\frac{d}{dg} (\Delta\phi) = 0 = -KT \ln \frac{p}{p_\infty} + \frac{2}{3} \epsilon g^{-1/3}$$

$$KT \ln \frac{p}{p_\infty} = \frac{2}{3} \epsilon g^{-1/3}$$

$$\Delta\phi_{\max} = \frac{1}{3} \epsilon g^{2/3} = \frac{4}{3} \pi r^2 \sigma$$

Then

$$\Delta\phi_{\max} = -gKT \ln \frac{p}{p_\infty} + 4\pi r^2 \sigma = \frac{4}{3} \pi r^2 \sigma \quad (\text{B-7})$$

Hence

$$KT \left(\frac{4}{3} \pi r^3 \frac{\rho_L}{m} \right) \ln \frac{p}{p_\infty} = \frac{8}{3} \pi r^2 \sigma$$

$$\ln \frac{p}{p_\infty} = \frac{2m\sigma}{\rho_L KT r^*} \quad (\text{B-8})$$

Equation (B-8) is the Kelvin-Helmholtz expression describing the conditions under which a liquid drop may remain in equilibrium with its vapor phase. The radius (r^*) and the number (g^*) of atoms of a critical embryo are thus determined. A variation of r (or g) in either direction results in a decrease of free energy from the maximum, and consequently the drop is in unstable equilibrium at this point.

In considering the quasi-equilibrium state, and ignoring interaction between nuclei, it is said that nucleation rate is the net rate at which particles of a given size (g) are formed. To maintain quasi-equilibrium, it is further assumed the net rate at which ($g+1$)-sized droplets are formed from (g)-sized droplets is equal to the rate at which (g)-sized droplets are formed from ($g-1$)-sized droplets, and so on. That is, nucleation rate is independent of g , in order that the number of droplets of any size remains constant and the rate at which droplets of larger size are imagined to be removed is also equal to the nucleation rate. Correspondingly, it is imagined that single molecules are added to the system at a rate equal to the depletion due to nucleation.

Using this model then, and assuming that growth of nuclei is due only to interaction with free molecules, the nucleation rate is

$$J(g+1, t) = \beta s(g) \times n(g, t) - \gamma(g+1) s(g+1) n(g+1, t) \quad (\text{B-9})$$

where β = rate at which molecules strike unit surface area.

$\gamma(g)$ = rate at which molecules leave the surface per unit area

$n(g, t)$ = distribution of non-equilibrium drops

$s(g)$ = surface area of a g -sized drop.

Assuming that no effects of droplet curvature exist, and neglecting the cluster motion,

$$\beta = \frac{p}{(2\pi mKT)^{1/2}}$$

Also, it is said that if nucleation rate were zero, then the non-equilibrium (or quasi-equilibrium) distribution would in that case have to be equal to the equilibrium distribution $N(g)$. This is easy enough to see in the superheated case, but perhaps a bit difficult to accept when $N(g)$ is the fictitious mathematical result corresponding to supersaturation.

Applying this, when $J(g, t) = 0$

$$\gamma(g+1) s(g+1) n(g+1) = \beta s(g) n(g)$$

when $n(g) = N(g)$

Hence,

$$\gamma(g+1) s(g+1) N(g+1) = \beta s(g) N(g)$$

and Equation (B-9) becomes

$$J(g, t) = \beta s(g) N(g) \left[\frac{n(g, t)}{N(g)} - \frac{n(g+1, t)}{N(g+1)} \right] \quad (\text{B-10})$$

Here some rather notable simplifications and manipulations facilitate a solution to (B-10). For large values of (g) where these functions may be treated as continuous, this is approximately:

$$J(g, t) = \beta s(g) N(g) \frac{d}{dg} \left(\frac{n}{N} \right)$$

Hence, since it is assumed that $J(g, t) = J(t)$

$$\int d\left(\frac{n}{N}\right) = -\frac{J}{\beta} \int \frac{dg}{s(g) N(g)} \quad (\text{B-11})$$

Using the boundary conditions

$$(a) \frac{n}{N} = 1.0 \text{ at } g = 1 \quad (b) \lim_{g \rightarrow \infty} \frac{n}{N} = 0$$

One obtains

$$J = \frac{\beta}{\int_1^{\infty} \frac{dg}{sN}} \quad (B-12)$$

Since $\frac{1}{N} = \frac{1}{N_0} \exp \left[\frac{\Delta\phi}{KT} \right]$ has a sharp maximum in the vicinity of $g = g^*$, it is possible to approximate (B-12) as:

$$J = \frac{\beta s(g^*) N_0}{\int_1^{\infty} \exp(\Delta\phi/KT) dg} \quad (B-13)$$

Using Equations (B-5), (B-6) and (B-8), the exponent may be written:

$$\begin{aligned} \frac{\Delta\phi}{KT} &= -g \ln \frac{p}{p_{\infty}} + \frac{\epsilon}{KT} g^{2/3} \\ &= -g \left[\frac{2m\sigma}{\rho_L KT r^*} \right] + \frac{4\pi\sigma}{KT} \left[\frac{3m}{4\pi\rho_L} \right]^{2/3} g^{2/3} \\ &= A \left[3(g/g^*)^{2/3} - 2(g/g^*) \right] \end{aligned}$$

where

$$\begin{aligned} A &= \frac{\sigma m}{\rho_L KT} \left(\frac{4\pi\rho_L}{3m} \right)^{1/3} g^{*2/3} \frac{4\pi\sigma r^{*2}}{3KT} \\ J &= \int_1^{\infty} \exp \left\{ A \left[3(g/g^*)^{2/3} - 2(g/g^*) \right] \right\} dg \quad (B-14) \end{aligned}$$

This integral occurs in the Becker and Doring, and Frenkel derivations, and can be solved approximately with the introduction of

$$\Omega = (g/g^*)^{1/3} - 1 \quad (B-15)$$

Since the integrand of (B-14) has a very sharp maximum e^A at $g = g^*$, the important values of Ω are small, and the limits of the integral may be taken at $+\infty$ and $-\infty$.

$$\text{Also, since } (g/g^*)^{2/3} = \Omega^2 + 2\Omega + 1$$

$$dg = 3(1 + \Omega)^2 g^* d\Omega$$

$$\text{And } 3(g/g^*)^{2/3} - 2(g/g^*) = -3\Omega^2 - 2\Omega + 1$$

The integral may be written approximately

$$\begin{aligned} &3g^* e^A \int_{-\infty}^{\infty} (1 + \Omega)^2 \exp(-3A\Omega^2 - 2A\Omega^3) d\Omega \\ &= 3g^* e^A \int_{-\infty}^{\infty} \exp(-3A\Omega^2) d\Omega \end{aligned}$$

$$= 3g^* e^A (\pi/3A)^{1/2} \quad (B-16)$$

Hence, the nucleation rate finally becomes

$$J = \frac{\beta s(g^*) N_0}{g^*} \left[\frac{A}{3\pi} \right]^{1/2} \exp(-A) \quad (B-17)$$

with

$$N_0 = p/KT$$

$$\beta = p/(2\pi mKT)^{1/2}$$

$$s(g^*) = \frac{\epsilon (g^*)^{2/3}}{\sigma}$$

and with the definitions of ϵ and A , (B17) can be shown equivalent to

$$J = \left(\frac{p}{KT} \right) \frac{m}{\rho} \left(\frac{2\sigma}{\pi m} \right)^{1/2} \exp\left(\frac{-4\pi\sigma r^{*2}}{3KT} \right) \quad (B-18)$$

This is an expression of the number of nuclei formed per unit volume per unit time, due to the existence of a non-equilibrium distribution $n(g)$. By assuming (J) was independent of (g) as Becker and Doring did, it was evaluated using only the boundary conditions of $n(g)$ and the properties of $\Delta\phi(g)$.

Discussion and criticism of Eq. (B-17), and of the importance of its various constituent values is contained in the text.

APPENDIX CREVIEW OF DEVELOPMENT OF DROP GROWTH EQUATIONS

The following development follows the method of Oswatitch⁽⁴⁵⁾ in considering the necessary conservation of mass and energy of growing droplets. Included are a correction of average incident energy to be $2RT$ rather than $3/2RT$, and with generalized non-unity values of both mass and thermal accommodation. An important assumption is that molecular velocity distribution are Maxwellian before *and* after collision and accommodation with the droplet surface.

Consider a drop of temperature T_D in an atmosphere p and T . It has an incident mass flux equal to

$$\frac{p}{(2\pi RT)^{1/2}}$$

with a proportion ξ (condensation coefficient) condensing and the rest being reflected. Since the drop is very small, its temperature is assumed to be constant throughout. The mass transfer from the drop is equal to that which would be incident in an environment T_D and p_D , the equilibrium values of temperature and pressure, where

$$\ln \frac{p_D}{p_{\text{sat}}(T_D)} = \frac{2m\sigma}{\rho_L K T r}$$

Hence, the mass flux per unit area passing out through the surface is

$$\frac{\xi p_D}{(2\pi R T_D)^{1/2}}$$

Thus, the conservation of mass may be written

$$\rho_L 4\pi r^2 \left(\frac{dr}{dt}\right) = 4\pi r^2 \left[\frac{\xi p}{(2\pi RT)^{1/2}} - \frac{\xi p_D}{(2\pi R T_D)^{1/2}} \right]$$

$$\text{or} \quad \frac{dr}{dt} = \frac{\xi}{(2\pi R)^{1/2}} \left(\frac{p}{T^{1/2}} - \frac{p_D}{T_D^{1/2}} \right) \quad (\text{C-1})$$

assuming that ξ is constant, or at most, a function of the drop temperature only.

Considerations of energy conservation are made after first defining the

the thermal accommodation coefficient, involving the change in temperature of reflected incident molecules.

$$\alpha = \frac{T_{\text{refl.}} - T}{T_D - T} \quad \text{(Thermal Accommodation Coefficient)} \quad \text{(C-2)}$$

The energy flux to the drop is, per unit area

$$\frac{p}{(2\pi RT)^{1/2}} [2RT]$$

and the energy leaving, upon reflection

$$\frac{(1 - \xi)p}{(2\pi RT)^{1/2}} \{2R [T + \alpha(T_D - T)]\}$$

In addition, the evaporating mass flux carries energy

$$\frac{\xi p_D}{(2\pi RT_D)^{1/2}} [2RT_D]$$

assuming the evaporating mass flux also to be Maxwellian.

The rate of change of droplet internal energy is

$$\frac{4}{3} \pi r^3 \rho_L c \frac{dT_D}{dt} + 4\pi r^2 \frac{dr}{dt} \rho_L U_{fD}$$

$$U_{fD} = h_{fD} = \frac{\gamma}{\gamma - 1} RT - h_{fg}$$

Hence, conservation of energy requires,

$$\frac{4}{3} \pi r^3 \rho_L c \frac{dT_D}{dt} + 4\pi r^2 \frac{dr}{dt} \rho_L \left(\frac{\gamma}{\gamma - 1} RT - h_{fg} \right) =$$

$$\beta(2RT) - \xi \beta_D(2RT_D) - (1 - \xi) \beta 2R [T + \alpha(T_D - T)]$$

$$\text{or} \quad \frac{\rho_L c}{3RT} \cdot \frac{dT_D}{dt} = 2\beta \xi \left[1 - \frac{\beta_D}{\beta} \frac{T_D}{T} \right] - (1 - \xi) \beta \left[2\alpha \left(\frac{T_D}{T} - 1 \right) \right] - \frac{\rho_L}{RT} \frac{dr}{dt} \left[\frac{\gamma}{\gamma - 1} RT - h_{fg} \right]$$

$$\text{where} \quad \beta = \frac{p}{(2\pi RT)^{1/2}} \quad \beta_D = \frac{p_D}{(2\pi RT_D)^{1/2}}$$

An order of magnitude analysis shows that the left hand term is small compared to the last term on the right hand side. Taking typical values;

$$\begin{array}{lll} r \sim 10^{-7} \text{ cm} & h_{fg}/c_p T \sim 3 & \\ c \sim .3 \text{ cal/gm } ^\circ\text{K} & R \sim .045 \text{ cal/gm } ^\circ\text{K} & T \sim 250^\circ\text{K} \\ \gamma/(\gamma - 1) \sim 4 & dT_D/dr \sim 7 \times 10^7 \text{ } ^\circ\text{K/cm} & \end{array}$$

$$\frac{rc \frac{dT_D}{dr}}{(3RT) \left(\frac{\gamma}{\gamma - 1} \right) \left(\frac{h_{fg}}{C_p T} - 1 \right)} = .008 \sim 10^{-2}$$

This signifies that the energy required to change the droplet temperature during the expansion is much less than the latent heat imparted from condensing incident molecules. Neglecting this term, the energy equation becomes:

$$0 = 2\xi \left(1 - \frac{\beta_D}{\beta} \frac{T_D}{T} \right) - 2(1 - \xi) \alpha \left(\frac{T_D}{T} - 1 \right) + \frac{\rho_L}{\beta} \frac{dr}{dt} \left(\frac{\gamma}{\gamma - 1} \right) (\lambda - 1)$$

where $\lambda = \frac{h_{fg}}{C_p T}$

Since $\frac{dr}{dt} = \frac{\xi}{\rho_L} (\beta - \beta_D)$ (C-1)

The energy equation can be further reduced to

$$0 = \left(1 - \frac{\beta_D}{\beta} \frac{T_D}{T} \right) - \alpha \left(\frac{1}{\xi} - 1 \right) \left(\frac{T_D}{T} - 1 \right) + \frac{1}{2} \left(1 - \frac{\beta_D}{\beta} \right) \left(\frac{\gamma}{\gamma - 1} \right) (\lambda - 1)$$
 (C-3)

Solution to the drop growth equations involves an iterative determination of drop temperature, T_D , from Eq. (C-3) and the resulting value of growth rate from Eq. (C-1).

An interesting indication of the importance of considering both mass and energy balance may be seen by closer inspection of Eqs. (C-1) and (C-3).

It is seen that the requirement for a drop to grow is that

$$\frac{dr}{dt} = \frac{\xi \beta}{\rho_L} \left(1 - \frac{\beta_D}{\beta} \right) > 1 \quad \therefore \frac{\beta_D}{\beta} < 1$$
 (C-4)

Re-arranging Eq. (C-3) into the form:

$$\frac{\beta_D}{\beta} \left[\frac{T_D}{T} + \frac{1}{2} \left(\frac{\gamma}{\gamma - 1} \right) (\lambda - 1) \right] = 1 - \alpha \left(\frac{1}{\xi} - 1 \right) \left(\frac{T_D}{T} - 1 \right) + \frac{1}{2} \left(\frac{\gamma}{\gamma - 1} \right) (\lambda - 1)$$

we obtain

$$\frac{\beta_D}{\beta} = \frac{\left[1 + \frac{1}{2} \left(\frac{\gamma}{\gamma - 1} \right) (\lambda - 1) \right] - \alpha \left(\frac{1}{\xi} - 1 \right) \left(\frac{T_D}{T} - 1 \right)}{\frac{T_D}{T} + \frac{1}{2} \left(\frac{\gamma}{\gamma - 1} \right) (\lambda - 1)}$$
 (C-5)

It is clear that whenever $T_D > T$ the denominator of Eq. (C-5) is always greater than the numerator. Hence from Eq. (C-4) the droplet will grow. Even in the most unfavorable case, that of $\alpha = 0$, where the drop temperature becomes much hotter than the surrounding environment, the value of β_D/β will remain less than unity and the drop will grow. This is really a proof of the intuitive fact that a droplet of size greater than critical radius must continue to grow in a supersaturated environment. Conversely when $T_D < T$, β_D/β is greater than unity and the drop evaporates, supporting our knowledge that evaporating liquids are cooler than their superheated environments.

APPENDIX D.MODIFICATION OF FOREGOING GAS DYNAMICS, NUCLEATION AND DROP GROWTH
EQUATIONS FOR DEPARTURE FROM PERFECT GAS DURING AN ISENTROPIC
EXPANSION.

The following corrections introduced into the perfect gas relations to account for departure from perfect gas behavior are based on the empirical observation that compressibility factor $z = Pv/RT$ is almost constant during an isentropic expansion. This is illustrated by Table 15 which lists the values of P , T and z for all of the condensation tests of this investigation. Changes in z generally encountered were less than .5% from stagnation pressure to maximum supersaturation prior to condensation. This in effect allows introduction of "effective" perfect gas relations,

$$Pv = R' T \quad \text{where } R' = zR \quad (D-1)$$

and the gas dynamics are affected accordingly:

$$\begin{aligned} Tds = 0 &= C_p dT - vdp \\ &= C_p \frac{pdv}{Rz} + \frac{vdp}{Rz} - vdp \\ &= \frac{\gamma}{\gamma-1} \left[-\frac{d\rho}{\rho} + \frac{dp}{p} \right] - \frac{\gamma-1}{\gamma} \frac{dp}{p} \end{aligned}$$

$$\text{Hence } \frac{d\rho}{\rho} = \frac{dp}{p} \left[1 - z \left(\frac{\gamma-1}{\gamma} \right) \right] = \frac{dp}{p} \left(\frac{1}{\gamma'} \right) \quad (D-2)$$

Hence, the isentropic relations of a perfect gas may be modified by replacing γ with γ' as defined in equation (D-2).

Similarly, the free energy of formation of a nucleus is modified as follows. The free energy change from vapor to liquid of (g) molecules (added to the free energy of surface formation in the classical droplet model) is

$$d\phi = dH - d(TS)$$

If it is assumed that the nucleus forms at environmental temperature.

$$dH = SdT = 0$$

$$d\phi = -TdS = vdp = zRT \cdot \frac{dp}{p}$$

$$\phi_2 - \phi_1 = zgkT \ln \frac{p_2}{p_1} = -zgkT \ln \frac{p}{p_\infty}$$

or, the total change in free energy of formation of a classical model droplet becomes

$$\phi_2 - \phi_1 = -zgkT \ln \frac{p}{p_\infty} + 4\pi r^2 \sigma$$

By proceeding as in Appendix B, it can be further shown that

$$\Delta\phi_{\max} = \frac{4}{3} \pi r^2 \sigma \quad \text{at } r = r^*$$

and

$$\ln \frac{p}{p_\infty} = \frac{2m\sigma}{\rho_L zKTr^*}$$

These, plus the corrections to the drop growth equations, may be introduced to the perfect gas equations by the simple substitutions

$$m' = \frac{m}{z} \tag{D-3}$$

$$\gamma' = \frac{\gamma}{1 + (\gamma - 1)(1 - z)} \tag{D-4}$$

In a computation involving condensation of a "real" gas, it is necessary to first determine the real isentrope, determined through use of the equation of state as mentioned in the text.

From this, by use of the equation of state and Equation D2, respectively, z and γ' are established at all points of the expansion and it is then a simple matter to determine the value of γ to be entered into the computation. The value of z is taken as the mean of stagnation and condensation values (indicated in Table 14) and a linear, temperature dependent approximation to γ between the same two points is made,

$$\gamma = \gamma_a - \gamma_b T(^{\circ}\text{C})$$

where values of γ_a and γ_b are given in Table 15.

Consequently, the computation scheme treats a value of γ which will yield the real isentropic exponent γ' when treated with the corrections (D-3) and (D-4). This matches the isentrope prior to condensation with the best

estimate of local conditions and calculates corrected nucleation and drop growth rates within the theoretical framework of perfect gas.

Perfect gas calculations may be made by simply setting $z = 1.00$, and entering the desired value of $\gamma = \gamma_a, \gamma_b = 0$.

It might be pointed out that the compressibility factor begins to vary more rapidly after condensation commences, and that the computation scheme ignores this. Some error in profile shapes may result, but probably are no more in doubt than those resulting from perfect gas treatment. The value of this treatment lies in its attempt at establishment of the best estimate of conditions and behavior at the point of *onset* of condensation.

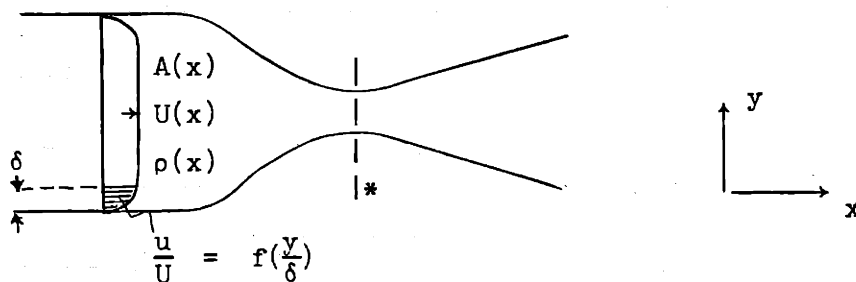
Another possibility for the consideration of real gas behavior in condensation would be to completely rewrite the entire processes of nucleation, drop growth and gas dynamics in terms of an equation of state, as was done for the non-condensing isentropes and total pressure computations. This could only be done by greatly increasing the complexity of an already complex computation and at the cost of excluding the many perfect gas relationships which so greatly simplify the mathematical treatment of condensation in gas flow processes.

APPENDIX E. A CLOSED FORM SOLUTION TO THE MOMENTUM INTEGRAL BOUNDARY LAYER EQUATION INCLUDING APPROXIMATE EFFECTS OF STREAMWISE DENSITY VARIATION

In most cases involving the study of boundary layers, effects of changing density are negligible. However, in such cases as nozzle flow, where sonic velocities are approached or exceeded, acceleration forces due to the presence of the density gradient become appreciable, and near the throat of a supersonic nozzle are of the same order as those due to area change in their influence on main stream velocity and hence boundary layer growth. A study of the momentum integral equation has revealed that a closed form solution is possible for both laminar and turbulent flow. In the laminar case, an extremely simple form of solution is possible, enabling one to determine estimates of boundary layer growth and depression in supersonic nozzles, using only slide-rule calculations.

If it is assumed that density and pressure vary in the direction of flow, but not across the boundary layer, the momentum integral equation may be written as follows:

$$\frac{d}{dx} \rho \int_0^{\delta} (U - u) u dy + \rho \frac{dU}{dx} \int_0^{\delta} (U - u) dy = \tau_{y=0} \quad (E-1)$$



For the general case, it is assumed that

$$u/U = f(y/\delta) \quad (E-2a)$$

$$\tau_0/\rho U^2 = a_1 \left(\frac{y}{U\delta}\right)^{1/n} \quad (E-2b)$$

Then, Equation (1) may be reduced to:

$$b_1 \frac{d}{dx} (\rho \delta U^2) + b_2 \rho \delta U \frac{dU}{dx} = a_1 \left(\frac{v}{U\delta}\right)^{1/n} \rho U^2 \quad (E-3)$$

where b_1 , b_2 and a_1 are dependent upon the assumed profile.

Equation (E-3) may be manipulated to appear in the form:

$$\frac{b_1}{2} \frac{d(\delta^2)}{dx} + \delta^2 \left[\frac{2b_1 + b_2}{U} \frac{dU}{dx} + \frac{b_1}{\rho} \frac{d\rho}{dx} \right] = a_1 \left(\frac{v}{U\delta}\right)^{1/n} \delta$$

or

$$\frac{d(\delta^2)}{dx} + \delta^2 \left[\frac{C_1}{U} \frac{dU}{dx} + \frac{2}{\rho} \frac{d\rho}{dx} \right] = C_2 \left(\frac{v}{U\delta}\right)^{1/n} \delta \quad (E-4)$$

$$\text{where } C_1 = \frac{2(2b_1 + b_2)}{b_1} \quad C_2 = \frac{2a_1}{b_1}$$

Equation (E-4) may be put into integrable form by using the integration factor:

$$m = C \int P dx; \quad P dx = C_1 \frac{dU}{U} + 2 \frac{d\rho}{\rho}$$

Hence, m takes the convenient form:

$$m = U^{C_1} \rho^2 \quad (E-5)$$

$$\text{or, more conveniently } m = \left(\frac{U}{U_0}\right)^{C_1} \left(\frac{\rho}{\rho_0}\right)^2$$

and the new form of the differential equation is:

$$\frac{d}{dx} (m\delta^2) = mQ \quad (E-6)$$

$$\text{where } Q = C_2 \left(\frac{v}{U\delta}\right)^{1/n} \delta$$

Hence

$$\begin{aligned} \frac{d}{dx} (m\delta^2) &= C_2 m \left(\frac{v}{U}\right)^{1/n} \delta^{1-1/n} \\ &= C_2 m \left(1 - \frac{n-1}{2n}\right) \left(\frac{v}{U}\right)^{1/n} (m\delta^2)^{\frac{n-1}{2n}} \end{aligned}$$

$$\text{and: } (m\delta^2)^{-\left(\frac{n-1}{2n}\right)} \frac{d}{dx} (m\delta^2) = C_2 m \frac{n+1}{2n} \cdot \left(\frac{v}{U}\right)^{1/n}$$

Integrating, one finally obtains:

$$\left[(m\delta^2)^{\frac{n+1}{2n}} \right]_{x_0}^x = \frac{C(n+1)}{2n} \int_{x_0}^x m^{\frac{n+1}{2n}} \left(\frac{v}{U}\right)^{1/n} dx \quad (E-7)$$

Equation (E-7) is the most general form of solution to the momentum integral equation, approximately valid for a compressible gas in either a laminar or turbulent boundary layer.

It should be noted that the integrating factor m can often be more conveniently expressed as follows:

$$pdx = \left[C_1 \left(-\frac{dA}{A} - \frac{d\rho}{\rho} \right) + 2 \frac{d\rho}{\rho} \right]$$

$$m = e^{\int p dx} = A^{-C_1} \rho^{2-C_1}$$

or, more conveniently:

$$m = \left(\frac{A}{A^*} \right)^{-C_1} \left(\frac{\rho}{\rho_0} \right)^{2-C_1} \quad (E-8)$$

Laminar Boundary Layer

Considering Equation (E-7) for the case of a laminar boundary layer,

where $n = 1$, we immediately have:

$$\left[m\delta^2 \right]_{x_0}^x = C_2 \int_{x_0}^x m \left(\frac{v}{U} \right) dx \quad (E-7a)$$

Assuming that viscosity μ is nearly constant and substituting for m with

Equation (8) yields:

$$\begin{aligned} \delta^2 &= \frac{C_2 \mu}{m} \int_{x_0}^x m \left(\frac{1}{\rho U} \right) dx + \frac{m_0}{m} \delta_0^2 \\ &= C_2 \mu \left(\frac{A}{A^*} \right)^{C_1} \left(\frac{\rho}{\rho_0} \right)^{C_1-2} \int_{x_0}^x \left(\frac{A}{A^*} \right)^{-C_1} \left(\frac{\rho}{\rho_0} \right)^{2-C_1} \left(\frac{1}{\rho U} \right) dx + \frac{m_0}{m} \delta_0^2 \end{aligned}$$

Further, for a nozzle: mass flow rate = constant = $\rho U A = \rho^* U^* A^*$

Hence:

$$\delta^2 = \left\{ \frac{C_2 \mu}{\rho^* U^*} \left(\frac{A}{A^*} \right)^{C_1} \left(\frac{\rho}{\rho_0} \right)^{C_1-2} \int_{x_0}^x \left(\frac{A}{A^*} \right)^{1-C_1} \left(\frac{\rho}{\rho_0} \right)^{2-C_1} dx \right\} + \frac{m_0}{m} \delta_0^2 \quad (E-9)$$

Equation (E-9) is the specialized form of Equation (E-7) for a laminar boundary layer. Reviewing Equations (E-3) and (E-4), it is seen that the constants C_1 and C_2 will depend on the polynomial used to approximate the shape of the boundary layer velocity profile.

For flow in a nozzle, (A/A^*) is known and (ρ/ρ_0) can be easily determined. Hence, the function:

$$F = m \left(\frac{A}{A^*} \right) = \left(\frac{A}{A^*} \right)^{1-C_1} \left(\frac{\rho}{\rho_0} \right)^{2-C_1} \quad (\text{E-10})$$

may be also easily determined and plotted. The integral may be determined by the area under the curve F , and at any point, x :

$$\delta^2 = K_1 m^{-1} \int_{x_0}^x F dx + \frac{m_0}{m} \delta_0^2$$

For $\delta_0 = 0$ at $x = 0$:

$$\delta^2 = K_1 m^{-1} \int_{x_0}^x F dx \quad (\text{E-9a})$$

where $K_1 = \frac{C_2 \mu}{\rho^* U^*}$

Equation (E-6) was applied to a nozzle of known geometry, using the assumption:

$$\frac{u}{U} = \frac{2y}{\delta} - \left(\frac{y}{\delta} \right)^2$$

for which $C_1 = 9$ $C_2 = 30$

At first glance, the assumption of a laminar boundary layer may seem unjustified. However, Launder^(R1) has shown that turbulent boundary layers under sufficiently negative pressure gradients will revert to a definite laminar form. Also, for the conditions of this calculation the observed boundary layer at the nozzle throat was such that the boundary layer Reynolds Number was about 2000 at the throat. This is less than the transition value and would indicate that a reversion to a laminar form could have taken place^(R1). Hence, the laminar assumption is not unreasonable.

Calculations were made according to Table I for CO₂ at stagnation conditions of 84 psia and -10°F, according to the corresponding values.

$$F = (A/A^*)^{-8} (\rho/\rho_0)^{-7} \quad p_0 = 84 \text{ psia}$$

$$K_1 = \frac{30\mu}{\rho * U^*} \quad \text{for CO}_2 \text{ at } T_0 = -10^\circ\text{F}$$

Results of calculations are shown in Figure E1.

At the conditions noted above and for the nozzle in question, limited interferometer data provided visual means of measuring the boundary layer thickness, and four values are shown in Figure E1. These observations are estimated to be accurate $\pm 15\%$.

Also shown in Figure 1, to assist in estimating the relative size of the boundary layer, are those values of uniform flow flat plate laminar boundary layers calculated for the densities and velocities at the entrance and throat of the nozzle, respectively.

It is seen that the limited experimental data seems to agree well with the approximate calculation of boundary layer thickness. More experimental data is necessary for a more thorough evaluation.

The extremely small boundary layers resulting in the pressure gradients which occur when compressibility becomes important make it appear that further interferometer observations would be an advisable method of gaining such data if it is not readily available in the literature.

The fact that the past "history" of the boundary layer has a greatly decreased effect on the value of boundary layer thickness in the region of rapid acceleration is quite apparent both from the curve in Figure 1 and from inspection of the equations. Equation (E-9) shows that the value of δ_0^2 , which exists at the beginning of integration must be multiplied by the ratio m_{x_0}/m_x . Hence, if the value of m increases appreciably, as it does when flow area A and density ρ decrease, then the term $(m_{x_0}/m_x)\delta_0^2$ contributes

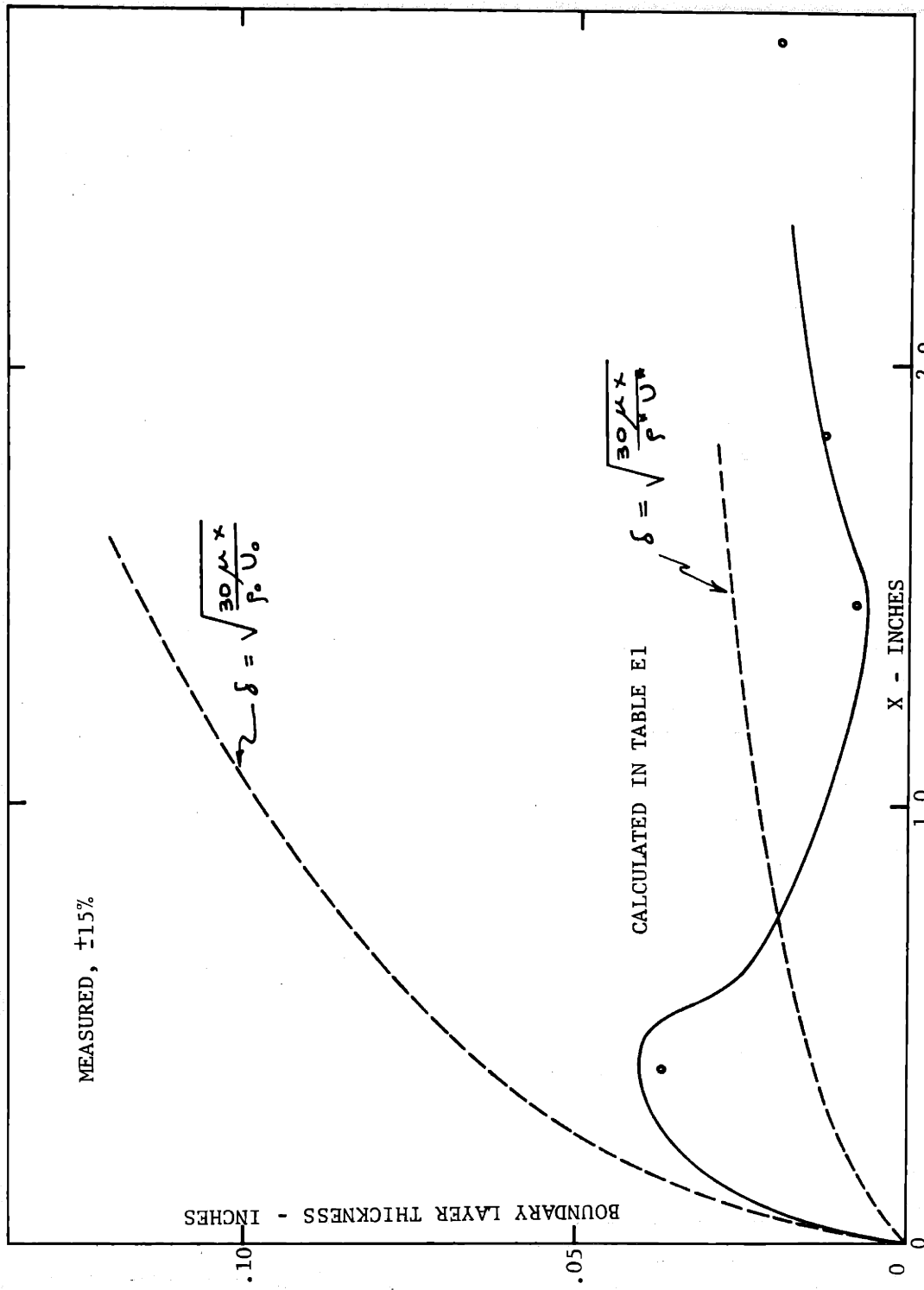


FIGURE E1, COMPARISON OF BOUNDARY LAYER APPROXIMATIONS AND INTERFEROMETRIC MEASUREMENTS IN A TWO-DIMENSIONAL SUPERSONIC NOZZLE.

little when added to the integral term.

The fact that one is limited to an assumed boundary layer velocity profile during an integration does not restrict the possibility of breaking the flow into regions, and applying Equation (E-9) to different velocity profiles (i.e. different constants C_1 and C_2) over the various intervals of x , with relative ease.

Turbulent Boundary Layer

It is apparent that Equation (E-7) is readily applicable to turbulent boundary layers in its present form, merely by selecting the expressions desired for Equations (E-2a) and (E-2b), that is, the velocity profile and wall shear dependence.

However, since most persons are accustomed to referring to turbulent boundary layer behavior in terms of momentum thickness θ , and shape factor $H = \delta^*/\theta$, it is worthwhile to re-derive Equation (E-7) in terms of θ and H .

$$\frac{d}{dx} \rho \int_0^{\delta} (U - u)u dy + \rho \frac{dU}{dx} \int_0^{\delta} (U - u) dy = \tau_0$$

$$\frac{d}{dx} (\rho U^2 \theta) + \rho \delta^* U \frac{dU}{dx} = \tau_0 = \alpha_1 \left(\frac{v}{U\theta}\right)^{1/n} \rho U^2$$

This can be written as:

$$\rho U^2 \frac{d\theta}{dx} + \theta \frac{d}{dx} (\rho U^2) + \rho H \theta U \frac{dU}{dx} = \alpha_1 \left(\frac{v}{U\theta}\right)^{1/n} \rho U^2$$

$$\frac{d\theta}{dx} + \theta \left[\frac{1}{\rho U^2} \frac{d(\rho U^2)}{dx} + H \frac{1}{U} \frac{dU}{dx} \right] = \alpha_1 \left(\frac{v}{U\theta}\right)^{1/n}$$

Again:

$$\frac{d}{dx} (m\theta) = mQ$$

where $Q = \alpha_1 \left(\frac{v}{U\theta}\right)^{1/n}$

and $m = e^{\int p dx}$

$$p dx = \left[\frac{d(\rho U^2)}{\rho U^2} + H \frac{dU}{U} \right]$$

$$m = \left(\frac{\rho U^2}{\rho_0 U_0^2} \right) \left(\frac{U}{U_0} \right)^H \quad \text{or} \quad \rho U^{H+2}$$

Hence, it is seen that:

$$(m\theta)^{1/n} \frac{d}{dx} (m\theta) = m \frac{n+1}{n} \alpha \left(\frac{v}{U} \right)^{1/n}$$

Integrating yields:

$$\left[(m\theta)^{\frac{n+1}{n}} \right]_{x_0}^x = \frac{\alpha(n+1)}{n} \int_{x_0}^x m \frac{n+1}{n} \left(\frac{v}{U} \right)^{1/n} dx \quad (\text{E-7b})$$

Inspection will also show that Equation (7b) could have been obtained directly from Equation (7), using the relationship between the two integrating factors, and between δ and θ . Note that $C_1 = 2(H+2)$.

Substituting for m in Equation (7b) yields:

$$(\rho U^{H+2} \theta)^{\frac{n+1}{n}} = \frac{n+1}{n} \alpha v^{1/n} \int_{x_0}^x \left(\frac{\rho U^{H+2}}{U^{1/n}} \right)^{\frac{n+1}{n}} dx + (\rho_0 U_0^{H+2} \theta_0)^{\frac{n+1}{n}}$$

This can be further simplified to either of two forms:

$$\theta^{\frac{n+1}{n}} = (\rho U^{H+2})^{-\frac{n+1}{n}} \left[\frac{n+1}{n} \alpha v^{1/n} \int_{x_0}^x \rho^{\frac{n+1}{n}} U^n dx + C_0 \right] \quad (\text{E-11})$$

$$\text{or} \quad \theta \left(\frac{U\theta}{v} \right)^{1/n} = \rho^{-\frac{n+1}{n}} U^{-n} \left[\frac{n+1}{n} \alpha \int_{x_0}^x \rho^{\frac{n+1}{n}} U^n dx + C_0' \right] \quad (\text{E-12})$$

$$\text{where} \quad \eta = (H+2) \frac{(n+1)}{n} - \frac{1}{n}$$

$$C_0 = (\rho U^{H+2} \theta)^{\frac{n+1}{n}} \quad @x = x_0$$

$$C_0' = C_0 / v^{1/2}$$

For the case of negligible density gradient Equation (E12) reduces to Equation (22.8) in Schlichting^(R2).

References

- R1) Launder, B.E. - "Laminarization of the Turbulent Boundary Layer by Acceleration" - Gas Turbine Laboratory Report #77 - M.I.T. November 1964.
- R2) Schlichting, H. - *Boundary Layer Theory* - McGraw-Hill

TABLE E1

x	A/A*	ρ/ρ_0	$(A/A^*)^{-8}$	$(\rho/\rho_0)^{-7}$	(F)	$\int_x^{x+\delta x} F dx$	$\int_x^x F dx$	(1/m)	K_0	δ^\dagger
					(4)x(5)			(2)/(6)	(8)x(9)	.0219(10) ^{1/2}
0	20	1	$1/256 \times 10^{-8}$	1	3.92×10^{-11}	1.58×10^{-11}				
.2	17.4	1	$1/84 \times 10^{-8}$	1	1.19×10^{-10}	3.52×10^{-11}	1.58×10^{-11}	14.6×10^{10}	2.31	.0333
.4	16.0	1	$1/42.9 \times 10^{-8}$	1	2.33×10^{-10}	3.97×10^{-10}	5.10×10^{-11}	6.86×10^{10}	3.50	.0410
.6	11.35	1	$1/2.68 \times 10^{-8}$	1	3.74×10^{-9}	2.82×10^{-8}	4.48×10^{-10}	3.04×10^9	1.36	.0256
.8	6.6	1	$1/3.6 \times 10^{-6}$	1	2.78×10^{-7}	1.70×10^{-5}	2.86×10^{-8}	2.38×10^7	.680	.0180
1.0	3.02	.978	$1/68.9 \times 10^{-2}$	1/.855	1.70×10^{-4}	1.62×10^{-2}	1.70×10^{-5}	1.78×10^4	.303	.0120
1.2	1.415	.875	1/16	1/.387	.162	1.64	1.62×10^{-2}	8.73	.142	.00825
1.4	1.020	.655	1/1.173	1/.0518	16.4	1.46	1.66	.0621	.103	.0070
1.46	1.000	.609	1	1/.0311	32.2	6.18	3.10	.0311	.097	.0068
1.6	1.04	.538	1/1.36	1/.0131	56.1	13.59	9.28	.0185	.172	.0091
1.8	1.170	.447	1/3.5	1/.00358	79.8	21.70	22.87	.0147	.336	.0127
2.0	1.321	.360	1/9.29	$1/7.84 \times 10^4$	137.2	32.62	44.57	.00963	.429	.0143
2.2	1.565	.2835	1/36	6800	189.0		77.19	.00827	.638	.0175

† $\delta^2 = \frac{30\mu}{\rho^* U^*} K_0 = 4.8 \times 10^{-4} K_0 \text{ in}^2$

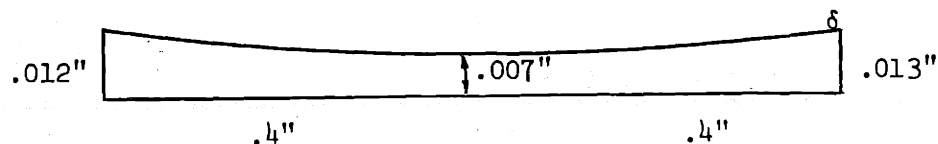
$\delta = .0219 \sqrt{K_0} \text{ in}$

APPENDIX FESTIMATED EFFECT OF DEPARTURE FROM 1-DIMENSIONAL FLOW ON
NOZZLE THROAT PRESSURE MEASUREMENTS

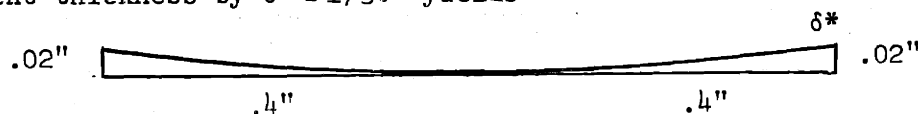
An observed discrepancy between measured density and pressure ratios occurred in the throat region, as mentioned in the text. Measured pressures at the throat tap were about 1.8" Hg higher than the value predicted from density measurements.

The boundary layer estimation presented in Appendix E indicates a relatively rapidly changing boundary layer thickness in the region of the throat. An order of magnitude analysis indicates that this departure from one-dimensionality, coupled with the sonic velocity of the mainstream, causes a considerable lateral pressure gradient, perpendicular to the flat side walls, of a magnitude which might account for the discrepancy.

The estimation of Appendix E yields a boundary layer with the following geometry at the throat



Approximating the curve as a segment of circular arc, and approximating displacement thickness by $\delta^* \approx 1/3\delta$ yields



The radius of displacement thickness curvature is approximately

$$R\theta = .4 = R \left(\frac{.02}{.4} \right)$$

$$R = 8''$$

The transverse pressure gradient across the streamlines is given by

$$\frac{1}{\rho} \frac{dp}{dn} = \frac{v^2}{R}$$

for which

$$V = 820 \text{ ft/sec.}$$

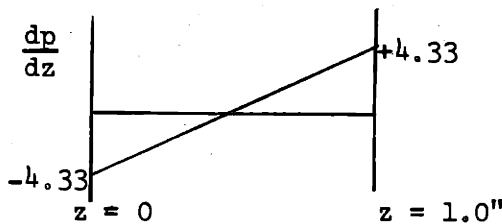
$$\rho = .25 \text{ lbm/ft}^3$$

$$R = .67 \text{ ft}$$

Hence, the estimated pressure gradient over the top of the boundary layer at the throat is

$$\frac{dp}{dn} = \frac{\rho V^2}{R} = 7500 \frac{\text{lbft}}{\text{ft}^3} = 4.33 \frac{\text{psi}}{\text{in}}$$

The side walls are approximately 1" apart. At a point midway between them, the pressure gradient is zero. Assuming the pressure gradient is linear,



$$\frac{dp}{dz} = -4.33 + 8.66z$$

And:



$$p = p_w - 4.33z + 4.33z^2$$

$$\therefore \bar{p} = \left[p_w z - \frac{4.33z^2}{2} + \frac{4.33z^3}{3} \right]_0^1$$

$$= p_w - .71$$

Hence: $p_w - \bar{p} = .71 \text{ psi}$

This is of sufficient magnitude to offer a possible explanation of the less than 1 psi difference between average mainstream and measured wall pressure at the throat.

It is noted that greater rates of curvature of the boundary layer occur upstream of the throat at relatively negligible velocities. Downstream, where velocities continue to increase the boundary layer has very little curvature.

APPENDIX GDISCUSSION OF INTERFEROMETRY APPLICATION TO TWO-DIMENSIONAL
NOZZLE FLOW

Extensive discussions of the theory behind interferometry techniques are numerous. References (14) and (36) are included for the reader who may desire additional detail.

Basically, an interferometer consists of a monochromatic source of light which is focused into a beam of nearly parallel rays. The beam is then split into two beams traveling separate paths of identical distance after which the beams are rejoined and focused on a viewing, or photographic, plate. An interference pattern of parallel light and dark bands, as seen in Fig. 12 is formed when the two beams are rejoined due to the fact that the various rays of each beam travel slightly different distances depending on the geometry of the mirror arrangement.

One beam is passed perpendicularly through the test section. To compensate for the change in optical path length caused by the glass side walls, "compensating" glasses of exactly the same thickness, must be placed in the path of the other beam. During testing, the only change which occurs is the density of the vapor in the test section which influences the velocity of light passing through it according to the relation, for two-dimensional flow:

$$\frac{S\lambda_0}{l} = n_1 - n_2$$

where n is the index of refraction of the gas in the test section, l is the width of test section through which light passes, λ_0 is the wave length of light being used, and S is the number of fringe shifts which occur at the point in question due to a change in the index from n_1 to n_2 .

The index of refraction is related to the density by the relationship

$$G\rho = n - 1$$

where G is the Gladstone-Dale constant, fixed for any gas.

The technique used in this investigation was to first photograph the interference fringe pattern for no flow and then take another photograph under test conditions. The fringes of each were then numbered from a common point which effectively represented stagnation conditions. For each distance x it was then a simple, though time consuming, matter to determine the fringe shift S and thence to calculate the density ratio. Photos used in calculating the density curves in Fig. 15(a), (b) and Fig. 16(a), (b) are shown in Figs. 11 and 12, respectively. A graphical illustration of the determination of S for test 1 (Fig. 15) is given in Fig. 13. Test 2 was done more precisely by measuring the distances to each fringe in the no-flow picture as measurements in the flow picture proceeded, since it was detected that slight departure from perfectly even spacing of the no-flow fringes occurs, probably due to minute differences in thickness of the optical glasses. (Note differences in Tables 3 and 4.)

Although interferometric methods did not succeed in producing measured effects of condensation, as mentioned in the text, the results obtained for non-condensing flow does offer a recommendation for possible further application in this direction. One important unfavorable aspect of it, however, is the extreme amount of time and effort required to reduce the photographs to meaningful data. Each of the two tests presented here require alignment of the interferometer with the nozzle (a process which may take as long as two days, after which, however, it is permanent), photography, development of negatives and prints (another day), measurements from prints, and calculations based on the measurements. If pressure measurements are taken, coordinating the location of pressure and density measurements also requires painstaking accuracy.

Such a laborious process in reducing the data is still predicated upon a two-dimensional nozzle and becomes prohibitively difficult for three-

dimensional flow. Reference 36 involves the analysis of *one* three-dimensional nozzle photograph.

APPENDIX HCOMPUTATIONAL PROGRAM

- Part 1: Comparison of Equations of State
- Part 2: Isentrope and Enthalpy Calculations
- Part 3: Normal Shock Calculations
- Part 4: Nucleation Contours Calculations
- Part 5: Condensation Calculations

PART 1

H2.

```

*M3851-3374,FMS,DEBUG,1,1,10,1
* XEQ
C COMPARISON OF EQUATIONS OF STATE
  READ 4, TO, VO
C CALCULATION USING BENEDICT WEBB RUBIN EQUATION OF STATE
  R= .08207
  V= VO*44./16.08
  T=TO/1.8
  AO=2.62392
  BO=0.052074
  CO=0.133670
  A=0.133333
  B=0.00396667
  C=14814.8
  ALPHA=0.0000890
  GAMMA=0.00557
  PBWR = R*T/V + (BO*R*T-AO-CO/(T*T))/(V*V) + (B*R*T-A)/(V**3) + A*A
  ALPHA/(V**6) + (C*(1. +GAMMA*(V*V))/(T*T*V**3))*EXPF(-GAMMA/(V*V))
  PBWR = PBWR*14.696
  PRINT 1, PBWR
C CALCULATION USING MARTIN AND HOU EQUATION OF STATE
  V = VO
  T = TO
  BV=.007495
  ATWO=-8.9273631
  BTWO=.005262476
  CTWO=-150.97587
  ATHRE=.18907819
  BTHRE=-.0000704617
  CTHRE=.0831424
  AFOUR=-.0002112459
  BFIVE=1.9565593*10.**(-5)
  TC=547.5
  R= .24381
  PMH = R*T/(V-BV) + (ATWO+BTWO*T+CTWO*EXPF(-5.475*T/TC))/((V-BV)**2
  1) + (ATHRE + BTHRE*T + CTHRE*EXPF(5.475*T/TC))/((V-BV)**3) + AFOUR
  2/((V-BV)**4) + BFIVE*T/((V-BV)**5)
  PRINT 2, PMH
C CALCULATION USING PLANK EQUATION OF STATE
C FIND LOCATION OF ZERO REMAINDER
  R= 1.8644
  T=TO/1.8
  J=1
  K=1
  PP=PBWR/14.696
  DELP=.1*PP
11 VP=R*T/PP+(.0825+.0012657*PP)*1000./((.01*T)**3)
  VP= VP/62.43
  IF (VP-V) 5,15,25
  IF (1.0001*VP-V) 6,6,15
  IF (J-2) 7,8,8
  J=2
  IF (K-2) 10,9,9
  DELP= .5*DELP
  PP= PP-DELP

```

H3.

```
GO TO 11
25 IF (.9999*VP-V) 15,26,26
26 IF (K-2) 27,28,28
27 K=2
28 IF (J-2) 30,29,29
29 DELP=.5*DELP
30 PP= PP+DELP
GO TO 11
15 PP= 14.696*PP
PRINT 3, PP
1 FORMAT (15H PRESSURE(BWR)=, F12.7)
2 FORMAT (15H PRESSURE(MH) =, F12.7)
3 FORMAT (15H PRESSURE(P) =, F12.7)
4 FORMAT (F5.1, F5.3)
END
```

PART 2

```

C   MAIN FOR ISENTROPE DECREASING P
    DIMENSION MARK(4),XOUT(200), Y(1), TOL(1), YMIN(1)
    1   ,DY(1)
    COMMON PZERO ,HZERO ,TZERO
    CALL ENT (P,T,H,4)
100  READ4,PZERO,TZERO,DELTAP,MP
    4   FORMAT (3F12.0,I4)
    X=0.
    CALL ENT (PZERO,TZERO,Y(1),3)
    HZERO=Y(1)
    TOL(1)=.0001
    YMIN(1)=10.
    H=DELTAP/3.
    XOUT(1)=X
    DO 2 I=2,MP
    2   XOUT(I)=XOUT(I-1)+DELTAP
    MARK(1)=1
    MARK(2)=MP
    MARK(4)=0
    CALL RUNGE (1,X,Y,TOL,YMIN,H,XOUT,MARK)
    GO TO 100
    END

```

0022

TOTAL 0022*

```

*   LABEL
C   DIFFEQ FOR ISENTROPE CALCULATION
    SUBROUTINE DIFFEQ (N,X,Y,DY)
    DIMENSION Y(1),DY(1)
    COMMON PZERO
    P=PZERO-X
    IF(P)1,2,2
    1   CALL EXIT
    2   CALL ENT (P,T,Y(1),2)
    CALL FOR RHO (P,T,RHO)
    DY(1)=-1./RHO
    RETURN
    END

```

0013

TOTAL 0013*

H5.

```
* LABEL
SUBROUTINE PRINT (N,XOUT,Y,DY,J)
C PRINT FOR ISENTROPE CALCULATION
DIMENSION XOUT(200),Y(1),DY(1)
COMMON PZERO,HZERO ,TZERO
P=PZERO-XOUT(J)
PRATIO=P/PZERO
CALL ENT (P,T,Y(1),2)
TRATIO=T/TZERO
CALL FORRHO (P,T,RHO)
CALL FOR RHO (PZERO,TZERO,RHOZER)
Z=P/(T*RHO*1.8644)
RRATIO=RHO/RHOZER
G=(P-PSAVE)*(T+TSAVE)/(T-TSAVE)/(P+PSAVE)
GAMMA=G/(G-1.)
GR=Z*GAMMA/(1.-(1.-Z)*GAMMA)
VEL=0.
W=2.*(HZERO-Y(1))*1033.*980.7
IF(W) 6,6,7
7 VEL=SQRTF(W)
6 H=Y(1)*.0242048+142.60
PSAVE=P
TSAVE=T
IF (J-1) 2,2,3
2 PRINT5,PRATIO,TRATIO,RRATIO,P,T,GAMMA,GR,H,Z,VEL
RETURN
3 PRINT1,PRATIO,TRATIO,RRATIO,P,T,GAMMA,GR,H,Z,VEL
5 FORMAT (12OH1 P/PO T/TO RHO/RHO0 P Z VEL
1 T GAMMA EFF GAMMA H Z P VEL
2 ,/36X,84H ATM DEG K
3 CAL/GM CM/SEC, //3F12.4,F12.3,F12.1,2F12.4,F12.2,
4 ,F12.4,F12.1)
1 FORMAT (3F12.4,F12.3,F12.1,2F12.4,F12.2,F12.4,F12.1)
RETURN
END
```

0035

TOTAL 0035*

```
* LABEL
SUBROUTINE FORRHO (P,T,RHO)
R=1.8644
V=R*T/P-(82.5+1.2657*P)/(0.01*T)**3.333
RHO=1./V
RETURN
END
```

0007

TOTAL 0007*

```

C   P IN ATM T IN DEG K  H IN ATM-CC/GM
    SUBROUTINE ENT (P,T,H,L)
    DIMENSION HZERO(130),TH(130)
    HOFPF(P,T)=4.333*(82.6*P+1.265*P*P)/(0.01*T)**3.333
    GO TO (1,2,3,4),L
4   J=0
7   J=J+1
C   HZERO IN BTU/LB MOLE  TH IN DEG R
    READ5,HZERO(J),TH(J)
5   FORMAT (2F10.0)
    TH(J)=TH(J)/1.8
    HZERO(J)=HZERO(J)*.52081
    IF(TH(J))6,6,7
C   NOW HZERO IS IN ATM-CC/GM AND T IS IN DEG K
C   ZERO H AT 0 DEG  GASEOUS
6   JEND=J-1
1   RETURN
3   DO 33 J=1,JEND
    IF(T-TH(J))32,33,33
33  CONTINUE
    GO TO 100
32  IB=J-1
    H=HZERO(IB)+(HZERO(IB+1)-HZERO(IB))/(TH(IB+1)-TH(IB))*(T-TH(IB))
1   -HOFPF(P,T)
    RETURN
2   DO 23 J=1,JEND,5
    H1=HZERO(J)-HOFPF(P,TH(J))
    IF(H1-H) 23,25,24
23  CONTINUE
    J=JEND
24  JH=J-5
    IF(JH) 100,100,29
29  DO 27 K=JH,J
    HA=HZERO(K)-HOFPF(P,TH(K))
    IF(HA-H) 27,28,28
27  HB=HA
    GO TO 100
28  IB=K-1
    T=TH(IB)+(TH(IB+1)-TH(IB))*(H-HB)/(HA-HB)
    RETURN
25  T=TH(J)
    RETURN
100 PRINT101,P,T,H
101 FORMAT (/42H T OR H IS OUT OF THE RANGE OF HZERO INPUT
1   ,/ 12X,2H P,12X,2H T,12X,2H H,/3F14.2)
    CALL EXIT
    END

```

0047

TOTAL 0047*

H7.

```
C   MAIN TO PUNCH ENTHALPY TABLES
    DIMENSION HH(6)
    CALL ENT(P,T,H,4)
    T1=30.
    DO 2 L=1,4
    T1=T1+60.
      T2 =T1+10.
    PUNCH7,T2
7   FORMAT (F17.1)
    P=0.
    DO 2 J=1,25
    P=P+.5
    T=T1
    DO 6 K=1,6
    T=T+10.
    CALL ENT (P,T,HH(K),3)
6   HH(K)=HH(K)*.0242048+142.60
C   H TO BE PUNCHE D TO AGREE WITH DIN I E   IC CAL/GM   O H AT O SOLID
    PUNCH3,P,HH
2   FORMAT (F6.1,6F11.2)
3   CALL EXIT
    END
```

0022

TOTAL 0022*

PART 3

```

* LABEL
  SUBROUTINE DIFFEQ (N,X,Y,DY)
  DIMENSION Y(2),DY(2)
  COMMON PZERO
  S=1.
  P=X
  GO TO (1,2),N
1  P=PZERO-X
  S=-1.
2  CALL ENT (P,T,Y(1),2)
  CALL FOR RHO (P,T,RHO)
  DY(1)=S/RHO
  DY(2)=1.
  RETURN
  END

```

0015

TOTAL 0015*

```

C MAIN FOR SHOCK CALCULATIONS
  CALL ENT (P,T,H,4)
  PRINT1
1  FORMAT (120H TOLL P01 T01 P1 T1
2  P2 T2 P02 T02 P02/P01 P1/P02
  CALL START(1)
  END

```

0008

TOTAL 0008*

```

* LABEL
  SUBROUTINE EQ1(V,REM)
  COMMON PZERO,TZERO,HZERO,TOLL,P2,T2,P1,T1,H1
  CALL FOR RHO (P1,T1,R1)
  U1=SQRTF(2.*(HZERO-H1))
  U2=U1*R1/V
  P2=P1+R1*U1*U1-V*U2*U2
  H2=HZERO-U2*U2*.5
  CALL ENT(P2,T2,H2,2)
  CALL FOR RHO (P2,T2,R2)
  REM=R2-V
  RETURN
  END

```

0013

TOTAL 0013*

```

* LABEL
SUBROUTINE ENT (P,T,H,L)
C P IN ATM T IN DEG K H IN ATM-CC/GM
DIMENSION HZERO(130),TH(130)
HOPPF(P,T)=4.333*(82.6*P+1.265*P*P)/(.01*T)**3.333
GO TO (1,2,3,4),L
4 J=0
7 J=J+1
C HZERO IN BTU/LB MOLE TH IN DEG R
READ5,HZERO(J),TH(J)
5 FORMAT (2F10.0)
TH(J)=TH(J)/1.8
HZERO(J)=HZERO(J)*.52081
IF(TH(J))6,6,7
C NOW HZERO IS IN ATM-CC/GM AND T IS IN DEG K
C ZERO H AT 0 DEG GASEOUS
6 JFND=J-1
1 RETURN
3 DO 33 J=1,JEND
IF(T-TH(J))32,33,33
33 CONTINUE
GO TO 100
32 IB=J-1
H=HZERO(IB)+(HZERO(IB+1)-HZERO(IB))/(TH(IB+1)-TH(IB))*(T-TH(IB))
1 -HOPPF(P,T)
RETURN
2 DO 23 J=1,JEND,5
H1=HZERO(J)-HOPPF(P,TH(J))
IF(H1-H) 23,25,24
23 CONTINUE
J=JEND
24 JH=J-5
IF(JH) 100,100,29
29 DO 27 K=JH,J
HA=HZERO(K)-HOPPF(P,TH(K))
IF(HA-H) 27,28,28
27 HB=HA
GO TO 100
28 IB=K-1
T=TH(IB)+(TH(IB+1)-TH(IB))*(H-HB)/(HA-HB)
RETURN
25 T=TH(J)
RETURN
100 PRINT101,P,T,H
101 FORMAT (/42H T OR H IS OUT OF THE RANGE OF HZERO INPUT
1 ,/ 12X,2H P,12X,2H T,12X,2H H,/3F14.2)
CALL EXIT
END

```

0048

TOTAL 0048*

H10.

```
SUBROUTINE PRINT (N,XOUT,Y,DY,J)
DIMENSION Y(2),DY(2),XOUT(1),R(3),REM(3)
COMMON PZERO,TZERO,HZERO,TOLL,P2,T2,P1,T1,H1
GO TO (3,4),N
3 P1=PZERO-XOUT(J)
CALL ENT (P1,T1,Y(1),2)
H1=Y(1)
C FIND FIRST GUESS AT RHO2
CALL FOR RHO(P1,T1,R(1))
CALL FOR RHO(PZERO,TZERO,RZERO)
R(1)=1.01*R(1)
R(2) = R(1)
DR=.1*(RZERO-R(1))
CALL EQ1 (R(1),REM(1))
11 R(2) = R(2) + DR
CALL EQ1 (R(2),REM(2))
IF(REM(1)*REM(2)) 10,10,11
10 R(3)=(R(1)+R(2))*0.5
CALL EQ1 (R(3),REM(3))
L=1
IF (REM(3)*REM(1)) 12,13,13
12 L=2
13 R(L)=R(3)
IF((R(2)-R(1))*2./R(1)-TOLL) 14,14,10
14 CONTINUE
CALL START(2)
4 IF (Y(1)-HZERO) 5,6,6
5 XB=Y(2)
HB=Y(1)
RETURN
6 P02=Y(2)-(Y(2)-XB)*(Y(1)-HZERO)/(Y(1)-HB)
CALL ENT (P02,T02,HZERO,2)
POUT=P02/PZERO
POUTA=P1/P02
PRINT7,TOLL,PZERO,TZERO,P1,T1,P2,T2,P02,T02,POUT,POUTA
7 FORMAT (F10.6,4(F10.3,F10.1),2F10.5)
CALL START(1)
END
```

0038

TOTAL 0038*

H 11.

```
SUBROUTINE START(N)
DIMENSION MARK(4),XOUT(200),Y(2),TOL(2),YMIN(2),DY(2)
COMMON PZERO,TZERO,HZERO, TOLL,P2,T2
H=.05
DO 1 J=1,2
MARK(J)=1
1 YMIN(J)=20.
GO TO(100,200),N
100 READ4, PZERO,TZERO,P1,TOLL
C SET CONSTANTS FOR RUNGE INTEGRATION DOWN THE ISENTROPE
X=0.
TOL(1)=TOLL
CALL ENT (PZERO,TZERO,Y(1),3)
HZERO=Y(1)
MARK(4)=0
4 FORMAT (4F12.0)
XOUT(1)=PZERO-P1
CALL RUNGE (1,X,Y,TOL,YMIN,H,XOUT,MARK)
CALL EXIT
200 X=P2
CALL ENT (P2,T2,Y(1),3)
MARK(2)=(PZERO-P2)*20.+20.
TOL(2)=1.
Y(2)=X
XOUT(1)=P2
MAR=MARK(2)
DO 7 K=2,MAR
7 XOUT(K)=XOUT(K-1)+.05
CALL RUNGE (2,X,Y,TOL,YMIN,H,XOUT,MARK)
CALL EXIT
END
```

0031

TOTAL 0031*

```
SUBROUTINE FORRHO (P,T,RHO)
R=1.8644
V=R*T/P-(82.5+1.2657*P)/(.01*T)**3.333
RHO=1./V
RETURN
END
```

0006

TOTAL 0006*

PART 4

```

* LABEL
C PROGRAM FOR RATE CONTOURS
C READ SECTION
  DIMENSION R(5), PP(5), FP(3), P(3)
101 READ1, RHOA,RHOB,SURFA,SURFB,WMOL
  1 FORMAT (5F12.0)
  READ1, TSTART,TEND,DELTAT
  READ40,R
40 FORMAT (5E12.2)
  PRINT22, RHOA,RHOB,SURFA,SURFB,WMOL,R
22 FORMAT (14H1RATE CONTOURS,/)
  1 6H RHOL=,F8.3, 2H -, F9.6,10H (T DEG C),/
  2 8H SIGMA =,F8.3,2H -,F9.6,10H (T DEG C),/
  3 7H WMOL =,F6.1,//
  4 24H TABLE CONTAINS P IN ATM,//
  5 19X,6H RATE=,E12.3,4E18.3,10H P INF ,/
  6 9H T DEG K ,/
  7 5H =,/ )
  M=(TEND-TSTART)/DELTAT
  T=TSTART-DELTAT
  DO 20 I=1,M
  T=T+DELTAT
C COMPUTATION
  RHOL=RHOA-RHOB*(T-273.16)
  SIGMA= SURFA-SURFB*(T-273.16)
  CALL PINFIN (T,PINF)
  IF (PINF) 20,20,74
74 C1=1.01325E6*1.0E16/(1.38*T) *PINF
  C1=LOGF(C1)
  C1=LOGF( SQRTF(WMOL*2.*SIGMA/(3.1416*6.025E23))/RHOL)+2.*C1
  C2=2.*SIGMA*WMOL/(82.062*1.01325E6*RHOL*T)
  C2=C2*C2*4.188*SIGMA*1.0E16/(1.38*T)
  DO 19 J=1,5
  IF(R(J)) 19,19,21
21 A=LOGF(R(J))-C1
  B=-2.
  C=C2
C CHOP FOR P
  P(3)=0.
  FP(1)=C
11 P(3)=P(3)+3.
  IF(P(3)-55.) 66,66,19
66 IF(FP(1)*(P(3)*P(3)*(A+B*P(3))+C))2,10,11
  2 P(1)=P(3)-3.
  P(2)=P(3)
  6 P(3)=(P(1)+P(2))*0.5
  IF (P(2)-P(1)-.005*P(2)) 10,10,9
  9 L=1
  FP(3)=P(3)*P(3)*(A+B*P(3))+C
  IF (FP(1)*FP(3)) 4,10,5
  4 L=2
  5 P(L)=P(3)
  GO TO 6
10 IF (P(3)-70.) 18,18,19
18 PP(J)=EXPF(P(3))*PINF

```


H13.

2

```
19 CONTINUE
20 PRINT 33, T, PP, PINF
33 FORMAT ( F10.2,9X,5E18.3,E11.3 )
GO TO 101
END
```

0060

TOTAL 0060*

C MAIN FOR CONDENSATION

```

DIMENSION Y(10),TOL(10),YMIN(10),XOUT(100),MARK(5)
COMMON PZERO, TZERO,WMOL, GAMMA, RHOL,
1HFG, SURFA, SURFB, XI, ALPHA, AMACH, X, AREA,
2DADX, P, T, RSTAR, TD, AMASS, AVGR, ASTAR,
3 SSAT, INTERP,Z ,YDROP,YRATE ,GAMA,GAMB,Y,NPART
4 ,RTIMES
INTERP=1
CALL AREAC(X,AREA,DADX)
100 READ 1, PZERO ATM
READ 1, TZERO DEG. C
READ 1, WMOL
READ 1, Z
READ 1, GAMA
READ 1, GAMB
READ 1, RHOL GM/CC
READ 1, HFG BTU/LBM
READ 1, SURFA DYNES/CM
READ 1, SURFB DYN/CM-C
READ 1, XI
READ 1, ALPHA
READ 1, RTIMES
READ 1, TOL(4)
READ 1, TOLL
READ 1, AMACH
READ 3, CNTAM PTS/CM3
READ 3, RZERO CM
1 FORMAT (F 20.0)
3 FORMAT (E11.3)
PRINT2, PZERO, TZERO, WMOL, Z,GAMA,GAMB,RHOL,HFG,SURFA
1,SURFB, XI, ALPHA, RTIMES, TOL(4), TOLL, AMACH, CNTAM, RZERO
2 FORMAT (25H1 CONDENSATION IN NOZZLES, //9H PZERO = ,
1 F10.3,/9H TZERO = , F10.2,/7HWMOL = , F12.2,/5H Z = ,F12.3,/7H
2 GAMA =,F12.2,/9H GAMB = ,F12.6,/8H RHOL = ,F12.3,/7H HFG = ,
3F12.2,/9H SURFA = , F10.2,/9H SURFB = , F11.3,/6H XI = , F16.5,/
48H ALPHA =,F14.5,/11H RATE*10.**F8.2,/9H TOL(4) =,F18.8,/7H TOLL
5=,F18.8,/9H AMACH1 =,F10.2,/8H CNTAM =,E12.3,/8H RZERO =,E12.3,/)
15 PZERO=2115.PZERO
TZERO=1.8*(TZERO+273.16)
INTERP=2
XOUT(1)=1.
XOUT(2)=AMACH *AMACH
XOUT(3)=2.*XOUT(2)
H=0.01
MARK(1)=1
MARK(2)=30
MARK(4)=0
DO 24 I=5,9
24 TOL(I)=TOLL
DO 81 I=1,3
81 TOL(I)=0.1
DO 25 I=1,9
Y(I)=0.
25 YMIN(I)=0.00001

```

```

WMOL=WMOL/Z
Y(1)=25.1327*62.4*CNTAM*      1544.*TZERO/(WMOL*PZERO)
Y(2)=Y(1)*RZERO
Y(3)=Y(2)*RZERO/2.
Y(5)=1.
Y(6)=1.
PZERO=PZERO/2115.
TZERO=TZERO/1.8-273.16
NPART=1
X=0.
N=9
CALL RUNGE (N, X, Y, TOL, YMIN, H, XOUT, MARK)
READ 77, L
77  FORMAT(I2)
    IF(L) 101,101,100
101  CALL EXIT
    END

```

0072

TOTAL 0072*

```

* LABEL
C SUBROUTINE TO COMPUTE NUCLEATION RATE
  SUBROUTINE RATEC(PRESS,TEMP, SIGMA, SSAT, RATE)
  DIMENSION Y(10)
  COMMON PZERO, TZERO,WMOL, GAMMA, RHOL,
1HFG, SURFA, SURFB, XI, ALPHA, AMACH, X, AREA,
2DADX, P, T, RSTAR, TD, AMASS, AVGR, ASTAR, SSAT
3 ,INTERP,Z,YDROP,YRATE,GAMA,GAMB,Y,NPART,RTIMES
  A=RSTAR
  B=10.**16/(1.380*TEMP)
  C=-4.1887*SIGMA*A*A*B
13  D=PRESS*1.01325E6*B
14  E=WMOL/(RHOL*6.025E23)
  EE=2.*SIGMA/(3.1416*WMOL)*6.025E23
  AA=2.*LOGF(D)+ LOGF(E) +.5*LOGF(EE)+ C
  AA=AA+2.303*16.
  IF(AA) 16,16,17
16  RATE=0.0
  GO TO 12
17  CONTINUE
  IF(AA-85.0) 18,18,19
19  AA=85.0
18  RATE=EXPF(AA)
12  RETURN
  END

```

0025

TOTAL 0025*

```

* LABEL
C SUBROUTINE TO COMPUTE DERIVATIVES
  SUBROUTINE DIFFEQ (N, X, Y, DY)
  DIMENSION Y(10),DY(10)
  COMMON PZERO, TZERO,WMOL, GAMMA, RHOL,
  1HFG, SURFA, SURFB, XI, ALPHA, AMACH, X, AREA,
  2DADX, P, T, RSTAR, TD, AMASS, AVGR, ASTAR,
  3 SSAT, INTERP,Z ,YDROP,YRATE ,GAMA,GAMB,Y,NPART
55 TEMP=Y(6)*(TZERO+273.16)
  R=.08478/WMOL
  GAMMA=GAMA-GAMB*(TEMP-273.16)
  FAC=1./(1.+(GAMMA-1.)*(1.-Z))
  GAMMA=GAMMA*FAC
  GO TO (1,2),NPART
  1 DO 3 I=1,9
  3 DY(I)=0.
  DY(5)=-Y(5)/(2./GAMMA+X*(GAMMA-1.)/GAMMA)
  DY(8)=R*TEMP*DY(5)/Y(5)
  DY(6)=Y(6)*(GAMMA-1.)*DY(5)/(GAMMA*Y(5))
  RETURN
  2 CALL PINFIN (TEMP,PINF)
  PRESS=Y(5)*PZERO
  SSAT=PRESS/PINF
  IF (SSAT-1.) 30, 30, 31
30 RATE=0
  RSTAR=0
  DY(9)=0.
  DROPG=0
  GO TO 32
31 SIGMA=SURFA-SURFB*(TEMP-273.16)
  RSTAR=2.*SIGMA*WMOL/(82.062*1.01325E6*RHOL*TEMP*LOGF(SSAT))
  IF (Y(1)-25.1327) 65,65,66
65 AVGR=1.3*RSTAR
  GO TO 67
66 AVGR=SQRTF(2.*Y(3)/Y(1))
67 CALL RATEC(PRESS, TEMP, SIGMA, SSAT, RATE)
  CALL DROPGC(PRESS, TEMP, SSAT, AVGR, DROPG)
  6 DROPG=DROPG/(Y(7)*SQRTF(GAMMA*8.314E7/WMOL*TEMP))
  VEL=SQRTF (-2.*Y(8)*980.7E6)
  DY(9)=1./VEL
32 CALL AREAC(X, AREA, DADX)
  CONLAM=(GAMMA-1.0)/GAMMA*HFG*WMOL/(1544.*1.8*TEMP)*778.
  DY(1)=25.1327* RATE*AREA
  DY(2)=Y(1)*DROPG+DY(1)*RSTAR
  DY(3)=Y(2)*DROPG+12.56637* RATE*AREA*RSTAR*RSTAR
  YDROP=RHOL/AMASS*Y(3)*DROPG
  YRATE=RHOL/AMASS*4.1888*RATE*AREA*RSTAR**3
  DY(4)=YDROP+YRATE
  DO 444 I=1,4
444 DY(I)=0.
  DY(5)=Y(5)*(((CONLAM-1.)/(1.-Y(4)))*DY(4)-DADX)/(1. (1.-Y(4))*
  1 ((GAMMA-1.)/GAMMA+1./GAMMA*Y(7)*Y(7) ))
  DY(6)=Y(6)*(CONLAM*DY(4)+(GAMMA-1.)/GAMMA*(1.-Y(4))*DY(5)/Y(5))
  DY(7)=Y(7)*(-(1.-Y(4))*DY(5)/(GAMMA*Y(7)*Y(7)*Y(5))-
  1 .5/Y(6)*DY(6) )

```

```
DY(8)=R*TEMP*DY(5)/Y(5)
RETURN
END
```

```
C   PINFIN FOR CO2    0 TO 240 DEG K
C   BELOW 93  PINF=C*EXPF(-HFG/R/T) WAS USED AND PINF AT 93 USED TO GET C
C   ABOVE 93 AN EQUATION OF THE FORM P=C*EXPF(A/T) WAS USED TO INTERPOLATE
C   BETWEEN DATA POINTS.    DATA TAKEN FROM HANDBOOK OF PHYSICS AND
C   CHEMISTRY, INTERNATIONAL CRITICAL TABLES, AND MATHESON GAS DATA
```

```
SUBROUTINE PINFIN (T,PINF)
  IF (T-93.) 1,1,2
1  A=6.033
  B=-1263.
  GO TO 10
  IF (T-140.) 3,3,4
2  A=7.492
3  B=-1430.
  GO TO 10
  IF (T-160.) 5,5,6
4  A=7.0851
5  B=-1373.
  GO TO 10
  IF (T-195.) 7,7,8
6  A=6.8355
7  B=-1333.
  GO TO 10
  IF (T-216.6) 9,9,11
8  A=7.028
9  B=-1367.
  GO TO 10
11 A=4.727
  F=-870.1
10 PINF=10.**(A+B/T)
  RETURN
  END
```

```

* LABEL
C SUBROUTINE TO PRINT
  SUBROUTINE PRINT(N, XOUT, YOUT, DY, J)
  DIMENSION XOUT(1), YOUT(7), Y(10), DY(1)
  COMMON PZERO, TZERO, WMOL, GAMMA, RHOL,
  1HFG, SURFA, SURFB, XI, ALPHA, AMACH, X, AREA,
  2DADX, P, T, RSTAR, TD, AMASS, AVGR, ASTAR,
  3 SSAT, INTERP, Z, YDROP, YRATE, GAMA, GAMB, Y, NPART
  GAMMA=GAMA-GAMB*YOUT(6)*(TZERO+273.16)
  GAMMA=GAMMA/(1.+(GAMMA-1.)*(1.-Z))
  IF (J-2) 21,22,32
21 AMASS=ASTAR*PZERO*YOUT(5)*2115.*SQRTF(GAMMA*WMOL/(32.2*1544.
  1 *(TZERO+273.16)*YOUT(6)*1.8))
  AMASS=32.2*454.6*AMASS/(30.48*30.48)
  PRINT10
  PSTAR=YOUT(5)
  TSTAR=YOUT(6)
  GSTAR=GAMMA
  RETURN
22 NPART=2
  DO 26 I=1,9
26 Y(I)=YOUT(I)
  DO 27 I=1,3
27 Y(I)=Y(I)*AMASS
  Y(7)=AMACH
  A=PSTAR/(Y(5)*AMACH)*SQRTF(Y(6)*GSTAR/(TSTAR*GAMMA))
  INTERP=3
  AREA=A*ASTAR
  CALL AREAC(X, AREA, DADX)
  INTERP=2
  XOUT(3)=X
  DO 25 I=3,63
25 XOUT(I+1)=XOUT(I)+.2
32 CALL AREAC(XOUT(J), AREA, DADX)
  AREA=AREA/ASTAR
  TEMP=YOUT(6)*(TZERO+273.16)
  CALL PINFIN(TEMP, PINF)
  PRESS=YOUT(5)*PZERO
  SSAT=PRESS/PINF
  SIGMA=SURFA-SURFB*(TEMP-273.16)
  IF(SSAT-1.) 69,69,67
67 CALL RATEC(PRESS, TEMP, SIGMA, SSAT, RATE)
  IF(YOUT(1)-25.1327) 69,69,68
68 AVGR= SQRTF(2.*YOUT(3)/YOUT(1))
  CALL DROPGC(PRESS, TEMP, SSAT, AVGR, DROPG)
  DTD=TD-YOUT(6)*(TZERO+273.16)
  PPSF=2115.*PZERO
  TDEGR=1.8*(TZERO+273.16)
  TOTALN=YOUT(1)*WMOL*PPSF/(25.1327*62.4*AMASS*1544.*TDEGR)
69 PRINT11, XOUT(J), AREA, YOUT(5), YOUT(6), SSAT, YOUT(7), YOUT(4),
  1 YDROP, YRATE, DTD, AVGR, RSTAR, RATE, TOTALN
  RETURN
10 FORMAT (12OH X A/A* P/PO T/T0 S SAT MACH MOIST BY GROWTH
  1Y GROWTH, NEW PART TD-T AVGR RSTAR NRATE TOTALN
  2 ,//)

```

11 FORMAT (F7.3,F8.3,2F7.4,F8.3,F7.3,F8.5,2E10.3,F7.2,4E10.3)
END

0057

TOTAL 0057*

```

* LABEL
SUBROUTINE DROPGC(PRESS,TEMP, SSAT, AVGR, DROPG)
C SUBROUTINE TO COMPUTE DROP GROWTH
COMMON PZERO, TZERO,WMOLV,GAMMAV,RHOL,
1HFG, SURFA, SURFB, XI, ALPHA, AMACH, X, AREA,
2DADX, P, T, RSTAR, TD, AMASS, AVGR, ASTAR,
3SSAT, INTERP
J=1
P=PRESS*1.01325E6
T=TEMP
R=AVGR
L=0
D(1)=0
D(2)=0
TD=T-1.
1 TD=TD+1.
5 CALL PINFIN(TD, PINF)
PD=1.01325E6*PINF*EXPF(RSTAR*T/(TD*R)*LOGF(SSAT))
GASCON=8.314E7/WMOL
CONLAM=(GAMMA-1.)/GAMMA*HFG*778./(1544.45*1.8*T:MP)*WMOL
BETA=P/SQRTF(6.2832*GASCON*T)
BETAD = PD/SQRTF(6.2832*GASCON*TD)
DROPG=XI/RHOL*(BETA-BETAD)
AA = 1. - BETAD*TD/(BETA*T)
AAA=.5*(CONLAM-1.)*GAMMA/(GAMMA-1.)*(1.-BETAD/BETA)
A = AA+AAA - (1./XI - 1.) *ALPHA*(TD/T-1.)
GO TO (8,9),J
8 J=2
IF(A) 10,10,9
10 DROPG=0.
PRINT11, PD,P,T,A,AA,AAA ,X,Y(4)
11 FORMAT(8E12.3)
RETURN
9 I=1
IF(A) 2,2,3
2 I=2
3 D(I)=TD
D3= D(1)*D(2)
IF(D3) 4,1,4
4 TD=.5*(D(1)+D(2))
L=L+1
IF(L-20) 5,5,60
60 IF(DROPG) 10,6,6
6 RETURN
END

```

```

* LABEL
C
C FIRST ORDER DIFF. EQ. ROUTINE--ADJUSTS STEP SIZE
C
SUBROUTINE RUNGE(N, X, Y, TOL, YMIN, H, XOUT, MARK)
DIMENSION Y(1), YMIN(1), TOL(1), SUB(50), XOUT(1), MARK(1)
DIMENSION DY(50), YA(50), FA(50), FB(50), FC(50), YKEEP(50)
KBTWN = 1
KBIG = 1
KLOW = 1
NCOUNT = 15
J = MARK(1)
MAX = MARK(2)
L = MARK(4)
IF (L) 210, 210, 220
210 LTEST = 1
GO TO 230
220 LTEST = 2
NUM = L
230 DO 250 I = 1, N
250 SUB(I) = TOL(I)/32.0
10 IF (MAX - J) 20, 30, 30
20 RETURN
30 A = XOUT(J) - X
B = ABSF(1.E-7 * X)
IF (A + B) 40, 35, 35
35 IF (A - B) 50, 50, 60
40 J = J + 1
GO TO 10
50 CALL PRINT(N, XOUT, Y, DY, J)
J = J + 1
GO TO 10
60 IF (A - 1.5*H) 70, 70, 80
70 H = A
L = L + 1
GO TO 1000
80 IF (A - 3.*H) 90, 1000, 1000
90 H = .5*A
C
C DO RUNGE-KUTTE-MERSON INTEGRATION
C
1000 XA = X + H/3.
XB = X + .5*H
CALL DIFFEQ(N, X, Y, DY)
X = X + H
DO 1030 I = 1, N
YKEEP(I) = Y(I)
FA(I) = H*DY(I)
1030 YA(I) = Y(I) + FA(I)/3.
CALL DIFFEQ(N, XA, YA, DY)
DO 1040 I = 1, N
1040 YA(I) = Y(I) + FA(I)/6. + H*DY(I)/6.
CALL DIFFEQ(N, XA, YA, DY)
DO 1050 I = 1, N
FB(I) = H*DY(I)

```



```

1050 YA(I) = Y(I) + .125*FA(I) + .375*FB(I)
      CALL DIFFEQ(N, XB, YA, DY)
      DO 1060 I = 1, N
      FC(I) = H*DY(I)
1060 YA(I) = Y(I) + .5*FA(I) - 1.5*FB(I) + 2.*FC(I)
      CALL DIFFEQ(N, X, YA, DY)
      DO 1130 I = 1, N
      Y(I) = Y(I) + FA(I)/6. + .666666667*FC(I) + H*DY(I)/6.
      J = Y(I)
      IF (ABSF(U) - YMIN(I)) 1130, 1090, 1090
1090 KLOW = 2
      E = .2*ABSF(U - YA(I) )
      IF ( E - ABSF(TOL(I)*U) ) 1110, 1100, 1100
1100 KBIG = 2
      GO TO 1130
1110 IF ( E - ABSF(SUB(I)*U) ) 1130, 1120, 1120
1120 KBTWN = 2
1130 CONTINUE
      GO TO (100, 1135), KLOW
1135 GO TO (1180, 1140), KBIG
1140 NCOUNT = NCOUNT - 1
      IF (NCOUNT) 1150, 1150, 1170
1150 PRINT 1160, X, H
      PRINT 1165, (I, Y(I), DY(I), I = 1, N)
      RETURN
1160 FORMAT (58H4STEP SIZE HALVED 15 TIMES CONSECUTIVELY SINCE LAST PRI
INT /29H PROGRAM TERMINATED AT X = , E16.8, 8H, H = , E16.8,
2//3H I, 13X, 4HY(I), 16X, 5HDY(I),//)
1165 FORMAT (13, 7X, 2(E16.8, 4X))
1170 KBIG = 1
      IF (H - B) 1176, 1172, 1172
1172 X = X - H
      H = .5*H
      DO 1174 I = 1, N
1174 Y(I) = YKEEP(I)
      KBTWN = 1
      KLOW = 1
      GO TO 1000
1176 M = 15 - NCOUNT
      PRINT 1178, M, X, H
      PRINT 1165, (I, Y(I), DY(I), I = 1, N)
      RETURN
1178 FORMAT (41H4STEP SIZE BECAME TOO SMALL FOR COMPUTER./20H IT HAS BE
1EN HALVED , 12, 21H TIMES CONSECUTIVELY./29H PROGRAM TERMINATED AT
2 X = , E16.8, 8H, H = , E16.8, //3H I, 13X, 4HY(I), 16X,
35HDY(I),//)
1180 NCOUNT = 15
      GO TO (1190, 1200), KBTWN
1190 H = 2.*H
1200 KBTWN = 1
      KLOW = 1
C
C CHECK FOR INTERMEDIATE PRINT OUT
C
100 GO TO (10, 110), LTEST

```

H 22.

```
110 IF (L) 120, 120, 150
120 PRINT 130, X, H
    PRINT 140, (I, Y(I), DY(I), I = 1, N)
    L = NUM
    GO TO 10
130 FORMAT (5H X = , E16.8, 4X, 4HH = , E16.8, 11X, 1HI, 13X, 4HY(I),
116X, 5HDY(I)/)
140 FORMAT (55X, I3, 7X, 2(E16.8, 4X))
150 L = L - 1
    GO TO 10
    END
```

```

* LABEL
C INTERPOLATION ROUTINE FOR COMPUTING AREA
C DADX IS CONTINUOUS
C SUBROUTINE AREAC(XX,AREA,DADX)
COMMON PZERO, TZERO, WMOL, GAMMA, RHOL,
1HFG, SURFA, SURFB, XI, ALPHA, AMACH,XX, AREA,
2DADX,P,T,RSTAR,TD,AMASS,AVGR,ASTAR,
3SSAT, IINTERP
DIMENSION DD(50),X(50),A(50),D(50),DA(50)

C
C
C AREAC PART 1
C
C INTERP=1, READ AREA X AND ASTAR
C SET X,DADX TO CORRESPOND TO ASTAR
C ASTAR MUST BE IN AREA DATA LIST
GO TO (1,2,3,4), INTERP
1 I=0
11 I=I+1
READ10, X(I),A(I)
10 FORMAT(2F15.0)
IF(A(I)) 11,12,11
12 READ10, XX,ASTAR
IEND=I-2
C IEND = LAST VALUE OF I USED MINUS 1
AREA=ASTAR
DADX=0.
C FIND IZERO
I=0
13 I=I+1
IF(X(I)-XX) 13,14,14
14 IZERO=I
D(IZERO)=0.
DO 15 I=IZERO,IEND
15 D(I+1) = 2.*(A(I+1)-A(I))/(X(I+1)-X(I))-D(I)
DO 16 I=2,IZERO
J=IZERO-I+1
16 D(J)=2.*(A(J+1)-A(J))/(X(J+1)-X(J))-D(J+1)
DO 17 I=2,IEND
17 DD(I) = (D(I)-D(I-1))/(X(I)-X(I-1))
C PLUG IA INTO DD
RETURN
C
C
C AREAC PART 2
C
C GIVEN X OUTPUT IS AREA AND DADX
2 IF(XX-X(I)) 20,23,22
20 I=I-1
IF(XX-X(I)) 20,23,23
23 IB=I
IA=I+1
GO TO 24

```

```

22  I=I+1
    IF (XX-X(I)) 25,23,22
25  IA=I
    IB=I-1
C   FIND AREA AND DADX
24  AREA=A(IB) + (XX-X(IB))*DD(IA)
    1 *(XX-X(IB))*0.5 + D(IB)
302 DADX=(DD(IA)*(XX-X(IB))+D(IB))/AREA
    RETURN
C
C
C   AREAC PART 3
C
C   GIVEN AREA FIND X AND DADX
C   IF MACH IS LESS THAN 1 LOOK BEFORE THROAT
C   IF MACH IS GREATER THAN 1 LOOK AFTER THROAT
3   I=IZERO
    IF (AMACH-1.) 30,31,31
30  I=I-1
    IF (AREA-A(I)) 32,32,30
32  IB=I
    IA=I+1
    GO TO 34
31  I=I+1
    IF (AREA-A(I)) 35,32,31
35  IA=I
    IB=I-1
C   FIND X AND DADX
34  IF (D(IA)-D(IB)) 36,37,34
36  SIGN=1.
301 XX= (-D(IB)+SIGN* SQRTF(D(IB)*D(IB) -2.*DD(IA)*(A(IB)-AREA)))
    1 /DD(IA) + X(IB)
    IF (XX-X(IB)) 38,39,39
38  SIGN=-1.
    GO TO 301
39  IF (XX-X(IA)) 302,302,38
37  XX=(AREA-A(IB))/D(IB) + X(IB)
    DADX=D(IB)/AREA
4   RETURN
    END

```

```
SUBROUTINE AREAC (X, AREA, DADX)
COMMON PZERO, TZERO, WMOL, GAMMA, RHOL, HFG, SURFA, SURFB, XI, AL, AM, XX, AREA
1A, DADX, P, T, RSTAR, TD, AMASS, AVGR, ASTAR, SSAT, INTERP
GO TO (1,2,3), INTERP
1 CONTINUE
  ASTAR=1.
  X=.55
  RETURN
C NOZZLE TWO B
2 IF (X-1.45) 10,11,11
10 AREA=1.+0.00889*(X-.55)
  DADX=.00889/AREA
  RETURN
11 IF (X-4.85) 12,13,13
12 AREA=1.008+.0218*(X-1.45)
  DADX=.0218/AREA
  RETURN
13 AREA=1.082+.0133*(X-4.85)
  DADX=.0133/AREA
  RETURN
3 IF (AREA-1.008) 30,30,31
30 X=(AREA-1.)*112.5+.55
  DADX=.00889/AREA
  RETURN
31 X=(AREA-1.008)/.0218+1.45
  DADX=.0218/AREA
  RETURN
END
```

0028

TOTAL 0028*

APPENDIX IESTIMATION OF EXPERIMENTAL ERRORTEMPERATURE MEASUREMENTS

Estimated error (difference between measured and actual temperature) on temperature readings except where otherwise noted is $+ 0.5^{\circ}$, $- 1.5^{\circ}$ F.

This was determined after the following measurements and observations.

- 1) Temperature of various portions of the ice bath of the reference junction were found to vary by as much as 1° F from the freezing point, 32.2° F, despite its containment in an insulated thermos.
- 2) A calibration of the potentiometer (Wheatstone bridge type) used for measurements, compared exactly with those readings of the standard copper-constantan conversion tables at each end (32° F and 212° F) of the calibration and showed a maximum variation of $+ 1.0^{\circ}$ F between.
- 3) The time constant of the thermocouple was measured with the aid of a Sanborn Recorder capable of recording a 50 cps signal with no distortion. Subjecting the thermocouple to various step changes in temperature, it was found that for still water $\tau = .15$ sec, for still air, $\tau = 1.4$ sec, and for response to the variation of human breath, $\tau = .6$ sec. The measured time constant of the potentiometer was $.9$ sec $\pm .2$ sec.

Based on these observations, a reference temperature of 32.2° F was *assumed* for all measurements and the variation in ice bath temperature allowed for in the estimated larger possible negative error.

Assuming a linear temperature transient over a 1 minute period, a variation from 190° F to $- 50^{\circ}$ F would result in a rate change of $- 4.0^{\circ}$ F/sec. Hence, for the non-condensing curves, this effect alone could contribute an error of about 5° F, in the thermocouple ($\tau = .6$) and potentiometer circuit ($\tau = .9$ sec). Hence, in the non-condensing curves, an error of $+ 4.5^{\circ}$ F, $- 1.5^{\circ}$ F is estimated. In measurements involving condensation, care was taken to let temperature readings reach a relatively constant level before data (photos) were taken. No transient effects are estimated for those cases.

PRESSURE

TEMPERATURE MEASUREMENTS

Pressure readings taken by the mercury manometer board are estimated accurate within $\pm .1$ " Hg, this would amount to $\pm 1.25\%$ error in the pressure ratios near station 18 on the figures for Nozzle I.

Minimum pressure readings for Nozzle II were in the vicinity of 28" Hg, well beyond the region of condensation. Hence, pressure ratios in this vicinity are estimated accurate to within .5%.

In the region of condensation (station 10) pressure levels range near 80" Hg. Hence, error in pressure ratios in this region is estimated at $\pm .125\%$, two orders of magnitude less than the pressure variation caused by condensation at this point.

Error has been introduced into the values of stagnation pressure wherever they have not been directly measured by the manometer board owing to the high pressure level, or the stagnation tank pressure gauge, as occurred several times for Nozzle I. General observations of the behavior of the pressure ratio at the throat have shown that although its value remained remarkably close to .535 for all pressure levels, it had a slight tendency to decrease with increasing pressure. Based on these observations (and others with air, where average p/p_0 measured .523 and the same tendency was noted) it is estimated that the pressure ratio at the throat could have been lowered to a minimum value of .525 at the highest pressure levels. Hence, calculated stagnation pressures are estimated to have an error of + 1%, - 2%.

Measurements in Nozzle II used the stagnation pressure gauge for all determinations of stagnation pressure after the gauge was calibrated and found to be accurate to within 1/2 psi at all pressures within the range of experimentation. Consequently, all stagnation pressure readings for Nozzle II are estimated accurate to within 1/2 psi and static pressure readings within .1" Hg.

DENSITY

Distance between optical glass side walls in the interferometric measurements was .956 inches. At the wall the boundary layer was about .006" at the throat and somewhat larger downstream (See Figure 12). Within the boundary layer densities are lower than in the mainstream, due to temperature recovery effects. This will cause a small error in the measured interferometric fringe shift data when applied to determination of density in the mid-stream. An upper limit on error in density measurements was estimated by assuming a thickness of the order of the displacement thickness (also given an upper limit of $\delta^* = 1/3 \delta$) to be of temperature equal to the stagnation temperature.

Near the throat, assuming $\delta^* = .002''$

$$2\delta^* = .004''$$

$$l = .956'' \approx 1.0''$$

$$\frac{T_{\text{stream}}}{T_{\delta}} = .8$$

$$\therefore \frac{\rho_{\delta}}{\rho_{\text{stream}}} = .8$$

Hence,

$$\rho_s - \rho_{\delta} \approx .2\rho_s$$

$$\text{also, } \rho_o - \rho_s \approx .6\rho_s$$

The fringe shift due to difference in density over length l is

$$S = \frac{lG}{\lambda} (\rho_1 - \rho_2)$$

Hence,

$$\frac{S_{\delta}}{S} = \frac{\delta^* (\rho_s - \rho_{\delta})}{l (\rho_o - \rho_s)} = \frac{.004 (.2\rho_s)}{.96 (.6\rho_s)} \approx .13\%$$

Similar estimates further downstream indicated that maximum error in density measurements probably do not exceed .2%.